Skoltech

Skolkovo Institute of Science and Technology

Skolkovo Institute of Science and Technology

PROPERTIES AND CHARACTERISTICS OF THE CrFeCoNi HIGH-ENTROPY ALLOYS AND ITS MODIFICATIONS PRODUCED BY ADDITIVE MANUFACTURING TECHNIQUE

Doctoral Thesis
by

YULIA O. KUZMINOVA

DOCTORAL PROGRAM IN MATHEMATICS AND MECHANICS

Supervisor
Associate Professor, Igor V. Shishkovsky

Co-Supervisor
Assistant Professor, Stanislav A. Evlashin

Moscow - 2023

I hereby declare that the work presented in this thesis was carried out by myself at Skolkovo Institute of Science and Technology, Moscow, except where due acknowledgement is made, and has not been submitted for any other degree.

Yulia Kuzminova (Candidate)

Prof. Igor Shishkovsky (Supervisor)

Prof. Stanislav Evlashin (Co-Supervisor)

Abstract

For centuries, humans have sought ways to enhance material quality, dating back to the Bronze Age. They discovered that mechanical deformation, like forging, or alloying metals, such as adding tin to copper, could boost material strength. Yet, with every progress leap, new materials were necessary. The Industrial Revolution spurred steel development as a construction material in the 18th and 19th centuries. In the 20th century, the creation of jet engines necessitated new alloys with high-strength properties at elevated temperatures, leading to the development of nickel superalloys. Lastly, the Information Revolution would not have been possible without semiconductors. Today, we are living in the 4th Industrial Revolution requiring the development of new materials for new technologies such as 3D printing, robotics, and Big Data.

The new frontier in Materials Science has emerged with the introduction of High-entropy Alloys (HEAs) or Multi-principal Element Alloys. Unlike traditional alloying approaches, HEAs involve designing alloys with multiple main elements, expanding the range of possible material properties. The first published CrFeCoNiMn HEA has demonstrated exceptional strength-ductile characteristics at cryogenic temperatures and offers potential for microstructure design. Additionally, HEAs with high melting point elements, Refractory High-entropy Alloys, have the potential to replace costly nickel-based alloys in high-temperature applications. However, it is crucial to explore these new materials using innovative production technologies that can contribute to their unique characteristics.

Additive Manufacturing (AM) is a rapidly expanding technology that enables the production of intricate parts while reducing time and material usage. Due to the technological specifics of AM, metals and alloys produced through this process possess unique characteristics such as elongated structures along the building direction, fine substructures, strong residual stress, and defects like pores or unmelted powder particles. Therefore, it is necessary to adjust the chemical composition and/or post-treatments of printed materials to account for these properties. Combining AM with new materials like HEAs can offer unique combinations of properties. Additionally, developing HEA compositions specifically for AM applications would be a logical step forward.

This study explores a new alloy design approach using additive technologies, focusing on the Cr-Fe-Co-Ni-based system produced by powder bed fusion (PBF) AM technology. The first part of the study investigates the printed CrFeCoNi alloy synthesized using pre-alloyed powder, examining its structural and phase evolutions in response to heat treatments, mechanical properties at as-built and annealed states, and the significance of the AM process for structural evolution during high-pressure torsion. The second part considers the structural and phase evolutions of printed CrFeCoNiAl alloys synthesized using a premix of CrFeCoNi and Al powders, depending on the aluminum content. Finally, the study demonstrates the structural and mechanical behavior of CrFeCoNi(Al,Ti) alloys synthesized using a premix of three powders (CrFeCoNi, Al, and Ti). The main finding of the study is the successful synthesis of PBF CrFeCoNi(Al,Ti) alloys using powder blends, which show promising mechanical characteristics after selected heat treatment.

Publications

1. **Kuzminova Y.***; Firsov D.; Dudin A.; Sergeev S.; Zhilyaev A.; Dyakov A.; Chupeeva A.; Alekseev A.; Martynov D.; Akhatov I.; Evlashin S. *The effect of the parameters of the powder bed fusion process on the microstructure and mechanical properties of CrFeCoNi medium-entropy alloys*. Intermetallics. 2020. doi:10.1016/j.intermet.2019.106651.

2. Zhao, Wenrui; Han, Jae-Kyung; **Kuzminova, Yulia O.**; Evlashin, Stanislav A.; Zhilyaev, Alexander P.; Pesin, Alexander M.; Jang, Jae-il; Liss, Klaus-Dieter; Kawasaki, Megumi*. *Significance of grain refinement on micro-mechanical properties and structures of additively-manufactured CoCr-FeNi high-entropy alloy*. Materials Science and Engineering A. 2021. doi:10.1016/j.msea.2021.140898.

3. **Kuzminova Y.O.***; Firsov D.G.; Dagesyan S.A.; Konev S.D.; Sergeev S.N.; Zhilyaev A.P.;Kawasaki M.; Akhatov I.S.; Evlashin S.A. *Fatigue behavior of additive manufactured CrFeCoNi medium-entropy alloy*. Journal of Alloys and Compounds. 2021. doi:10.1016/j.jallcom.2021.158609.

4. **Kuzminova, Yulia***; Shibalova, Anastasia; Evlashin, Stanislav; Shishkovsky, Igor; Krakhmalev, Pavel. *Structural effect of low Al content in the in-situ additive manufactured CrFeCoNiAlx high-entropy alloy*. Materials Letters. 2021. doi:10.1016/j.matlet.2021.130487.

5. Xiaojing Liu; Jae-Kyung Han; Yusuke Onuki; **Yulia O. Kuzminova**; Stanislav A. Evlashin; Megumi Kawasaki; Klaus-Dieter Liss*. *In Situ Neutron Diffraction Investigating Microstructure and Texture Evolution upon Heating of Nanostructured CoCrFeNi High-Entropy Alloy*. Advanced Engineering Materials. 2022. doi:10.1002/adem.202201256.

6. **Kuzminova, Yulia O.***; Kudryavtsev, Egor A.; Han, Jae-Kyung; Kawasaki, Megumi; Evlashin, Stanislav A. *Phase and structural changes during heat treatment of additive manufactured CrFeCoNi high-entropy alloy*. Journal of Alloys and Compounds. 2022. doi:10.1016/j.jallcom.2021.161495.

7. **Kuzminova, Yulia O.**; Firsov, Denis G.; Shibalova, Anastasia A.; Evlashin, Stanislav A.; Shishkovsky, Igor V.; Dautov, Stanislav S.* *The oxidation behavior of the CrFeCoNiAlx (x = 0, 1.0, and 5.0 wt%) high-entropy alloy synthesized with Al elemental powder via powder bed fusion technique at high temperatures.* Micron. 2023. doi:10.1016/j.micron.2022.103399.

8. **Kuzminova, Yulia O.***; Firsov, Denis G.; Shibalova, Anastasia A.; Kudryavtsev, Egor A.; Krakhmalev, Pavel; Klimova-Korsmik, Olga G.; Shishkovsky, Igor V.; Evlashin, Stanislav A.; *Structural and mechanical properties of the CrFeCoNi(Al,Ti) high-entropy alloys produced by additive manufacturing technique using elemental powder blends.* [Under review]

Conferences

1. **Y. Kuzminova**, S. Evlashin, D. Firsov. *The application of the 3D-printing technology to the CrFeCoNi medium-entropy alloy* . Conference and school for young scientists "ADDITIVE TECHNOLOGIES IN DIGITAL MANUFACTURING. METALS, ALLOYS, COMPOSITES", October 2-4, 2019, MISiS, Moscow, Russia.

2. **Y. Kuzminova**, D. Firsov, S. Evlashin. *The effect of the 3D-printing parameters on the structural and mechanical properties of the CrFeCoNi medium-entropy alloys* School of young scientists "Structure and properties of high-entropy alloys and coatings", October 9-11, 2019, BelSU, Belgorod, Russia.

3. **Y. Kuzminova**, A. Shibalova, S. Evlashin, I. Shishkovsky, P. Krakhmalev. *Structural effect of low Al content in the in-situ additive manufactured CrFeCoNiAlx high-entropy alloy*. The 5th conference «Magnitogorsk Materials Week», April, 2021, MSTU, Magnitogorsk, Russia.

4. **Y. Kuzminova**, A. Shibalova, S. Evlashin, I. Shishkovsky, P. Krakhmalev. *In-situ manufacturing of CrFeCoNiAlx high-entropy alloy by powder bed fusion technology*. International conference «Beam Technologies and Laser Applications», September 20-22, 2021, Saint-Petersburg, Russia.

5. **Y. Kuzminova**, I. Shishkovsky, P. Krakhmalev, S. Evlashin. *Effect of Al Presence in the CrCoNiFeAl High-entropy Alloy Synthesized via an In Situ Additive Manufacturing Technique*. The 13th International Conference on Key Engineering Materials (ICKEM 2023), March 24-26, 2023, Istanbul, Türkiye.

Acknowledgments

I would like to express my gratitude to Denis Firsov and Oleg Dubinin, my colleagues who played an active role in this project and provided valuable assistance in its completion. Moreover, I am thankful to my family for their enthusiastic support of my decision to pursue academic education. Lastly, I would like to pay tribute to Professor Alexander Zhiliaev, who served as a model of professionalism and creativity for me.

Contents

Chapter 1

Introduction

Multiprincipal element alloys (MPEAs) or High-entropy alloys (HEAs) were discovered in 2004 in two simultaneously published studies [8, 80]. Yeh *et al.* suggested that the high concentration of each element will provide a high configurational entropy which in turn gives the stable solid solution and they presented the single-phase CrFeCoNiMn alloy. However, further works demonstrated that such an approach was wrong, most HEAs contain at least two phases [47, 21]. Nevertheless, a new direction in Material Science was developed due to the new approach of alloy design creating alloy compositions with several main elements.

The Cr-Fe-Co-Ni-Mn system was mainly interesting due to the five elements in equiatomic portions which is a lower required number of elements in the system according to Yeh's definition. Meanwhile, the four-component Cr-Fe-Co-Ni system represents similar mechanical properties [18]. Both alloys demonstrated high strength and ductility at cryogenic temperatures and ordinary characteristics at room temperatures. The properties are changed dramatically with the aluminum addition to the system. It was presented that physical and mechanical properties are changed with a growth of the Al concentration in the Cr-Fe-Co-Ni-(Mn)-Al systems. Aluminum presence changes the face-centered cubic (*f.c.c.*) crystal structure to the body-centered cubic (*b.c.c.*) changing physical and mechanical properties [12, 26]. Since it was concluded that the single-phase HEAs do not guarantee the exceptional properties for engineering applications (particularly, the CrFeCoNi-based system is not appropriate for the high-temperature applications) [46, 2], more attention was

paid to the multiple-phase alloys. In these terms, the Cr-Co-Ni-Al-Ti looks like one of the most interesting due to the high specific strength values at middle temperatures [20].

The discussed above alloys were produced by conventional techniques such as cast alloying or arc alloying with further treatments. One of the new techniques allowing to produce the metallic parts is additive manufacturing (AM) or 3D printing. AM actively grows due to the possibility to perform the parts with complex geometry saving time and feedstock material. One of the well-developed AM techniques is powder bed fusion (PBF). PBF is a popular technique for metal 3D printing that offers parts with smooth surfaces and intricate shapes allowing the production of multiple parts in a single print. The printed materials have unique mechanical and physical characteristics due to the fine microstructure formation. However, this technique requires metal powder as a feedstock material. The production of metal powder for AM is time and energy costs. It limits the application of new materials such as HEAs for AM. As a solution, the *in situ* AM approach can accelerate the implementation of HEA for the 3D printing process by using metal powder blends. In this work, the *in situ* AM is considered as the *in situ* alloying process assisted using AM technologies. It assumes the creation of the solid material the chemical composition of which is formed during the printing in the melting pool as a reaction between feedstock materials [33]. Such the definition does not limit the use the elemental powders only but also considers the use of the prealloyed powders. This approach enables the avoidance of complex and costly prealloying procedures intended for the production of raw materials for AM. Today, plenty of works demonstrated the possibility to print HEA parts using metal powder blends. In addition to the complex geometry and unique structural characteristics provided by the AM process, tweaking the printing parameters can yield complex multi-phase compositions in HEA, as was demonstrated for the PBF high-nitrogen steel, where the chess *f.c.c.+b.c.c.* phase structure was achieved by regulating laser input energy [1]. However, since the AM affects the printed material properties, the *in situ* AM brings more specific characteristics to the final material such as inhomogeneous element distribution in printed material and/or printing defects related to nonoptimal printing parameters

for one of the used powders. Therefore, it is essential to estimate the effect of the AM process on the material properties and further consider the effects of the *in situ* printing taking into account the results from the previous steps of the investigation.

The present work can be divided into two main sections. The first section provides a comprehensive investigation of the PBF CrFeCoNi alloy, and its properties in an as-built state and after post-treatments. The second section considers the effect of the different Al and Ti additions to the Cr-Fe-Co-Ni system by using the blend of aluminum, titanium, and CrFeCoNi powders at the PBF process.

Aim and objects of the work: Reveal the structural and property specifics of the CrFeCoNi-based HEAs produced by the PBF AM technique and define their evolution after the further post-treatments.

In order to achieve these results the following steps were planned to be done: i) find the PBF parameters for the CrFeCoNi alloy, and analyze the obtained structure, phase composition, and mechanical properties; ii) define the annealing temperature effect on the structural and phase compositions of the PBF CrFeCoNi alloy and changes in mechanical characteristics after heat treatment; iii) reveal the PBF impact on the CrFeCoNi alloys hardening behavior by comparing the structure evolution of the cast and printed alloys after the high-pressure torsion (HPT) process (the choice of the HPT process is discussed in Chapter 5); iv) analyze the aluminum effect on the structural changes at middle temperatures of the PBF CrFeCoNiAl$_x$ alloys; v) define the structural specifics of the PBF CrFeCoNi(Al,Ti) alloys synthesized using powder blends and reveal their mechanical properties.

Novelty: The work represents the comprehensive study of the PBF CrFeCoNi alloy and systematic investigation of the effects of aluminum and titanium on the CrFeCoNi alloy synthesized via the PBF technique:

- The printing parameters providing the best mechanical characteristics and lowest porosity for the PBF CrFeCoNi alloy were found. It was shown that the PBF process provides the same or better mechanical properties for CrFeCoNi alloy as the conventional process (arc-melting $\rightarrow$ 1000°C homogenization $\rightarrow$ hot-rolling at 1000°C with the total reduction in thickness of 92%) while the yield strength properties stay higher (up to 500 MPa) even after the heat

treatment at 750°C.

- The PBF CrFeCoNi alloy behavior under the cycling loads highly depends on the presence of the defects formed during the printing at the near-surface area. Additionally, it was discussed that the additional deformation mechanisms occur under the tensile load compared to a lower cycling load. The twinning deformation mechanism may take place at the later stage of the tensile deformation, while dislocation slip dominates at cycling loads of 480 MPa.

- According to the *in situ* neutron diffraction analysis, it was revealed that the PBF CrFeCoNi alloy demonstrates lower temperatures of the recovery process (600°C) compared with the cast alloy. The recrystallization process occurs at 700°C according to the microstructure analysis. The formation of the intermetallic phase was not observed up to 1000°C, while the M_2N precipitates form at the temperatures of 700-800°C due to nitrogen presence in the initial powder.

- PBF printing with powder blends can be successfully used for printing solid samples. The synthesized CrFeCoNi(Al,Ti) alloys demonstrate the changes in mechanical properties due to the new phase formations. However, the inhomogeneity in the chemical composition was observed for all samples printed using powder blends limiting the mechanical property gains. The post-heat treatment at high temperatures may be considered as an additional step uniforming the element distribution and improving the material properties.

- The alloying with aluminum of the PBF CrFeCoNi alloy improves the oxidation resistance of material at the elevated temperatures of 800°C and 1000°C due to the prevention of the oxide scale delamination. The aluminum reacts with the oxygen forming the Al_2O_3 along the columnar boundaries under the top Cr_2O_3 layer.

Scientific significance: The study reveals the systematized research of the PBF Cr-Fe-Co-Ni-based alloys. The analysis of the printing process - structure composition - mechanical properties links provides a comprehensive understanding

of the HEA applications as AM materials and indicates the future steps to be done to achieve non-ordinary material properties using new alloys and technologies.

1.1 General Concepts of High-entropy Alloys

Yeh *et al.* provided an intriguing explanation for investigating alloys containing five or more elements in near-equiatomic proportions [80]. They theorized that having multiple elements in these alloys would increase the configurational entropy of mixing (eq. 1.1 - 1.3), which could prevent the formation of potentially damaging intermetallic compounds. As well-known, phase formation depends on the relative free energy:

$$\Delta G_{mix} = \Delta H_{mix} - T\Delta S_{mix} \tag{1.1}$$

where the ΔG_{mix}, ΔH_{mix}, and ΔS_{mix} are the Gibbs free energy, enthalpy, and entropy of mixing, correspondingly, and T is the absolute temperature. In its turn, the ΔS_{mix} consists of the several items:

$$\Delta S_{mix} = \Delta S_e + \Delta S_m + \Delta S_v + \Delta S_{conf} \tag{1.2}$$

where ΔS_e is a electronic entropy, S_m is a magnetic entropy, ΔS_v is a vibrational entropy, and ΔS_{conf} is a configurational entropy. For the equiatomic element composition, the ΔS_{conf} can be calculated as:

$$\Delta S_{conf} = R \ln n \tag{1.3}$$

where R is the absolute gas constant, and n is the number of elements.

This view went against the conventional understanding, which suggested that the more elements in a concentrated alloy, the greater likelihood of new phase forming. This hypothesis was unusual because traditional binary phase diagrams typically showed solid solutions at the ends of the spectrum and compounds in the center, but Yeh's group believed that their alloy entropy would deter intermetallic formation.

In 2004, Yeh *et al.* simultaneously with Cantor's group presented the single

phase FeCrMnNiCo alloy having all elements in equiatomic portions [80, 8]. However, further investigations demonstrated the decomposition of this phase structure at elevated temperatures [51]. Most investigated HEAs also have multi-phase composition rather the single-phase solid solution [47]. Ultimately, the theoretical concept was not proved by practice, but it was an interesting and novel idea of using several principal elements for the alloy design. To date, there are suggestions for alternative names for HEA, such as compositionally complex alloys and multi-component alloys, but it looks like the name "high-entropy alloys" is more popular in the literature.

Since the HEAs were discovered, the questions of choosing elements and their amounts immediately arose. Using the periodic table of elements alone, over 5 million new five-element HEAs having equal parts of each element can be made. If the alloys with different numbers of elements or with different amounts of each element are added, the number of potential new alloys becomes almost limitless. The question then becomes, how is effectively searching through such a vast number of potential alloys possible? To date, this question is still open. However, there are methods for screening potential alloys. George *et al.* suggest three approaches for navigation in the uncharted HEA space [21]: Calculation of Phase Diagrams (CALPHAD) approach, Combinatorial experimental approach, and Mechanism-based approach. They also can be adapted together as a systematic search of alloy composition depending on required properties as was discussed by Miracle *et al.* [46]. Below, these three approaches are briefly discussed in the order of possible application for searching a required composition.

CALPHAD approach is a calculating phase diagrams method using Gibbs-Helmholtz free-energy formulations. This thermodynamic model analyzes the free-energy approximations for each phase in an alloy system based on concentration and temperature at constant pressure. By identifying the equilibrium phase for each temperature through energy minimization, software such as ThermoCalc or CompuTherm is used to calculate the phase diagram. This method enables identifying co-existing phases, their compositions, and volume fractions. CALPHAD methods are useful for extrapolating into unexplored areas of composition, but unexpected intermetallic phases often arise. Its predictive power is limited outside of

fitted ranges, and for cases where competing intermetallic phases are unknown [23]. Moreover, the CALPHAD approach has limitations, as it is based on thermodynamics and may not detect meta-stable or transient phases present in successful alloys. Additionally, equilibrium approaches alone cannot determine important characteristics such as microstructure, morphology, and orientation of phases, which are critical for determining the mechanical and structural properties of alloys. Therefore, the CALPHAD method is a good approach for screening the pool of the possible alloy composition and choosing the most prospective ones.

Combinatorial experimental approach involves creating and analyzing several alloy compositions at once, using techniques like high-throughput synthesis such as bulk prototyping by casting; diffusion couples; thin-films [66, 84]. Additive manufacturing is an effective combinatorial method allowing for the creation of chemical gradient samples on a micro to centimeter scale [35]. By metallurgical or XRD characterization of these samples, primary information about phases and microstructures can be obtained. Combinatorial approaches are useful in eliminating impractical materials and identifying potential materials for larger-scale evaluations. It can be especially effective based on the CALPHAD method results. Metal properties like tensile strength and impact are also estimated through these approaches. In comparison to bulk rapid alloy prototyping or combinatorial thin-film materials, additive manufacturing is an essential method to explore significant portions of compositional space. Overall, combinatorial approaches enable efficient evaluation of potential materials that could be utilized in real-world applications.

Mechanism-based approach can be considered as the next step of alloy design. After an alloy composition choosing, the microstructure-based and mechanism-based design approach can be involved to achieve the required mechanical or functional properties. Since the required chemical composition is identified, further processes, such as intensive plastic deformation or forming incoherent precipitates in the matrix, can be applied to involve the Hall-Petch or Orowan mechanisms to strengthen the material. FeCrNi-based stainless steels and FeMnC-based twinning induced plasticity steels are examples of materials that undergo this treatment. These alloys are similar to *f.c.c.* HEAs and are strengthened through various mechanisms

such as solid-solution and precipitation strengthening, deformation twinning, and the formation of ϵ-martensite and α-martensite phases [54]. The combination of design approaches and HEA compositions provides a wide playground for alloy design targeted for specific use conditions, Fig.1-5.
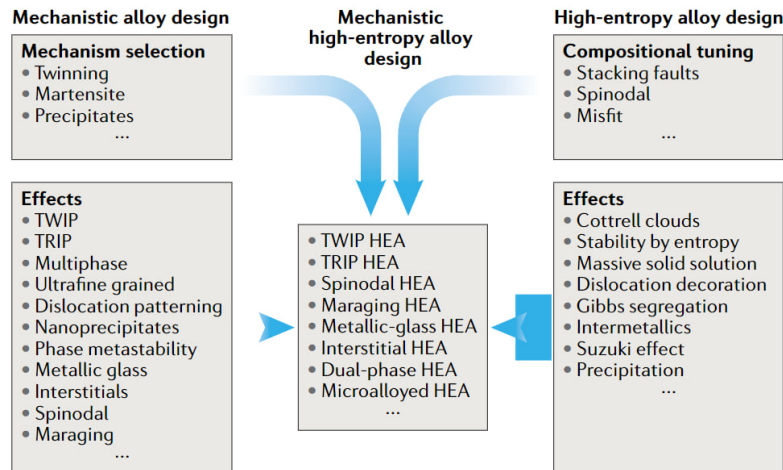

Figure 1-1: Mechanistic approaches to the HEA design [21].

Other approaches. The approaches described above are well-known and they have already demonstrated their effectiveness by finding the Ti-Zr-Hf-Hb-Ta [60, 15] and Al-Cr-Nb-Ti-V-Zr HEA systems [83, 82] for high-temperature applications. However, new techniques for searching for new alloy compositions are actively applied and demonstrate the prospective results.

One approach actively applied to the prediction and analysis of HEAs is density functional theory (DFT). DFT is a theoretical approach that models the electronic structure of materials and can describe the qualitative and quantitative changes of the lattice parameters with alloying in a wide compositional range rather accurately. A recent example is the prediction of the PtPd-based HEA as catalytic material using DFT analysis and an artificial neural network [56].

The way of applying machine learning to predict the HEA composition is actively developing today. Recent work demonstrated the possibility to design the new HEA based on the phenomenological properties of used elements [63]. According to the modernized random forest classifier method developed in the work, the $Ni_{25}Cu_{18.75}Fe_{25}Co_{25}Al_{6.25}$ alloy was predicted and successfully synthesized. Another

work represents the promising results of HEA prediction based on the analysis of the scientific publications [53]. The prospective of such an approach were proved by predicting the CrFeCoNiMn alloy based on the literature till the 2004 year.

1.2 Cr-Co-Ni-based System

The searching of the new HEA compositions providing the unique characteristics is occurring for about twenty years. As was said above, there were developed the promising systems for the high-temperature applications as a single *b.c.c.* phase Ti-Zr-Hf-Nb-Ta system (a tensile yield strength of 1303 MPa and ϵ=1.9) [60] or a multiple-phase Al-Cr-Nb-Ti-V-Zr system (a compressive yield strength of 1535 MPa and ϵ=0.6) [82]. Both systems have a high strength characteristics but the ductility at room temperature is low which limits their application. Meanwhile, the first published CrFeCoNiMn alloy is still interesting [21]. Especially, the compositions based on the Cr-Co-Ni system demonstrate the prospective replacement of the nickel superalloys [65]. Due to a wide play-ground for material property modifications, this work is focused on the Cr-Co-Ni-based CrFeCoNi alloy, which includes the iron decreasing the cost of the material.

Starting from the beginning, the five-element CrMnFeCoNi alloy was discovered as a single-phase *f.c.c.* structure. The subsequent studies showed that it decomposes into two additional phases, metallic *b.c.c.*-Cr and intermetallic L10-NiMn and B2-FeCo, below 800°C [51]. Wu *et al.* studied the temperature dependence of the mechanical properties for the equiatomic *f.c.c.* alloys [76]. It reveals the non-linear dependency of the yield strength on the element number in the alloy indicating the importance of the right choice of alloying elements rather than its number (Fig.1-2).

The four-component CrFeCoNi alloy demonstrates similar mechanical characteristics as CrMnFeCoNi alloy, Fig.1-3, and the properties of the three-component CrCoNi alloy even exceed the CrMnFeCoNi ones showing the 890 MPa ultimate tensile strength and 73 % elongation [57, 18, 22]. All these alloys demonstrate a strong temperature dependency, which is not typical for pure *f.c.c.* metals. Comparing the CrMnFeCoNi and CrCoNi alloys, a similar deformation mechanism is observed
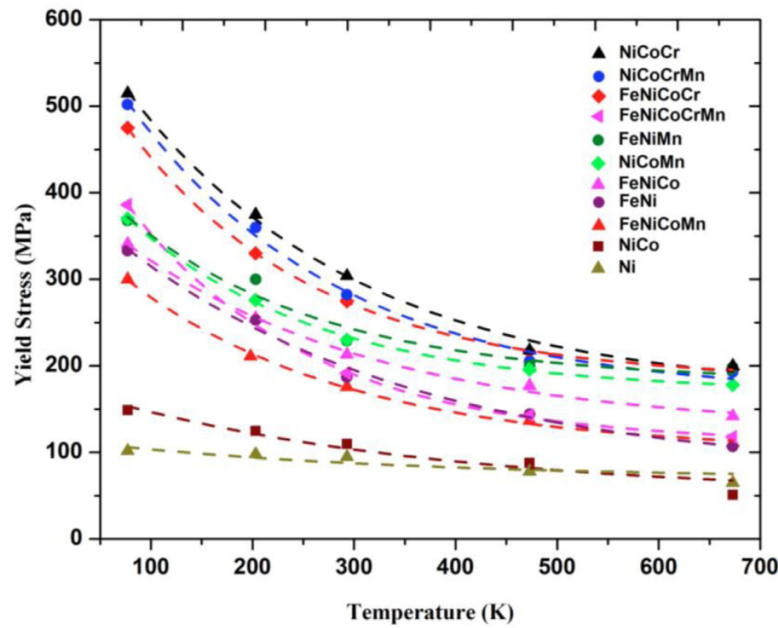
Figure 1-2: Yield strength of the *f.c.c.* CrCoNi family and Ni-based alloys versus testing temperature [76, 20].

at a temperature range of 293-77 K [76, 22]. For the CrMnFeCoNi alloy, the initial plasticity, up to tensile strains of about 2 %, occurs exclusively by the planar glide of $1/2\langle110\rangle$ dislocations on the {111} planes. At higher strains, at room temperature and above, slip becomes more homogeneous, and cell structures develop. At the temperature of 77 K, nanoscale twinning was observed as an additional deformation mode during the plastic flow, but not shortly after yielding [76]. The same behavior is observed for the CrCoNi alloy at cryogenic temperature while the nano-twinning is observed even at room temperature (which is not observed for the five-component alloy). It becomes the major deformation mode with the temperature decrease [22]. The activation of the nano-twinning mechanism strengthens the material and postpones the onset of necking instability by work hardening increase. It makes the CrCoNi-based alloys the most prospective materials for low-temperature applications. However, the mechanical properties of these alloys dramatically drop at elevated temperatures which encourages the further searching of the alloy compositions.

The first years published works consider the alloying with aluminum the CrCoNi-based alloys. They demonstrated the transformation of the *f.c.c.* crystal structure
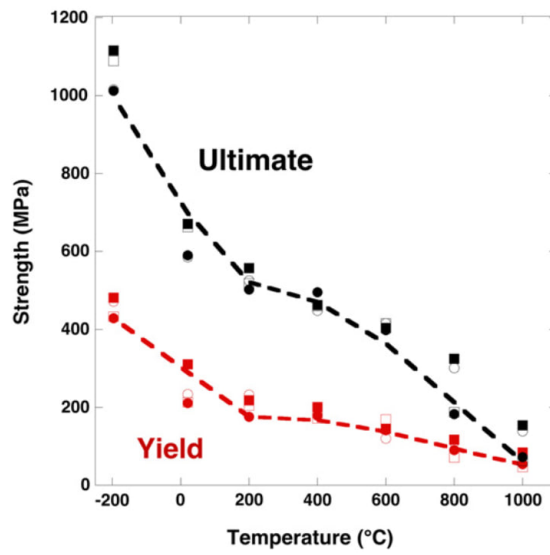
Figure 1-3: Yield and ultimate strengths for CrFeCoNi (squares) and CrFeCoNiMn (circles) alloys tensile tested at strain rates of 10^{-1} s^{-1} (open symbols) and 10^{-3} s^{-1} (filled symbols) versus test temperature [18].

to the *b.c.c.* with an increase of the aluminum content [42]. The phase composition of the CrFeCoNiAl$_x$ alloy is not limited by two phases. Bloomfield *et al.* presented a complex phase transformation behavior of the alloy considering CrFeCoNiAl$_{0.5}$ and CrFeCoNiAl compositions, Fig.1-4 [5]. This transformation correlates with the physical and mechanical property changes, Table 1.1 [12, 30, 74]. Indeed, the alloying with aluminum increases the strength characteristics of the CrCoNi-based system significantly. However, the softening increase of CrFeCoNiAl$_x$ alloys occurs at 600°C ($0.5T_m$ in K) limiting alloy application at elevated temperatures [74].

Table 1.1: The tensile properties of the HEAs at room temperature.

Composition	YTS, MPa	UTS, MPa	ϵ, %	Ref.
Hot-rolled CoCrFeNi	300	671	42	[18]
Arc melted Al$_{0.3}$CoCrFeNi*	275	528	37	[44]
Arc melted Al$_{0.6}$CoCrFeNi	412	932	21	[2]
Cold-rolled Al$_{0.5}$CoCrCuFeNi	1284	1344	7.6	[70]
Arc melted Al$_{0.5}$CoCrFeNiTi$_{0.15}$	1098	1415	5	[2]

*alloying elements are labeled with a molar ratio

Slone *et al.* note that "Load-bearing applications at temperatures from approximately 650-900°C typically utilize polycrystalline Ni-base superalloys" strengthened via precipitation of Ni$_3$(Al,Ti,Nb) γ' or γ" phases [64]. Having a similar elemental
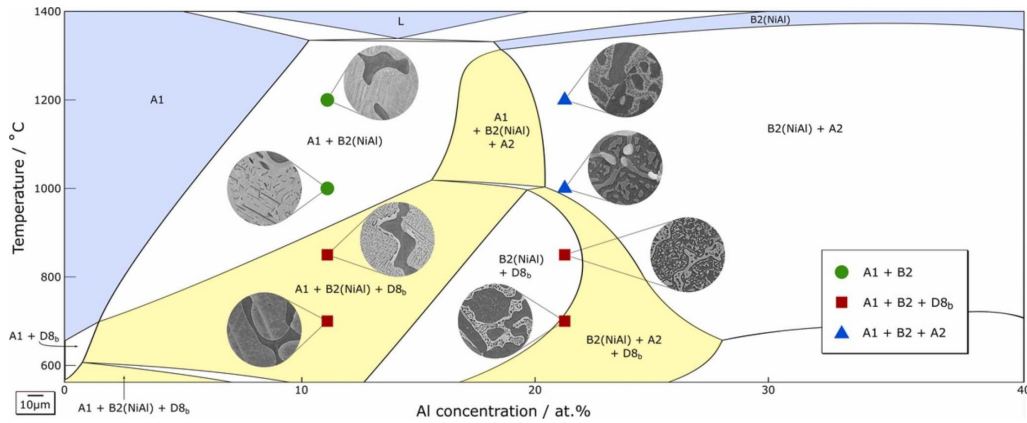
Figure 1-4: Thermodynamic phase diagram calculated with CALPHAD for Al_xCrFeCoNi alloys with related structural images [5].

composition, the CrCoNi-based HEAs can also be strengthened by alloying with aluminum and titanium aiming for the new phase formation. Indeed, the γ' phase was observed in the $CrCoNiAl_{0.13}Ti_{0.07}Nb_{0.03}$ alloy after aging at 700-900°C, while at the fully recrystallized condition, this material represents the *f.c.c.* phase only [64]. However, the mechanical tests at elevated temperatures confirm the strength property improving at elevated temperatures, yield strength of 530 MPa and elongation of >55% at 700°C for the $Al_{0.5}CoCrFeNiTi_{0.15}$ composition revealing the *f.c.c.* and *b.c.c.* phases [2]. The earlier study also represents the A2 Fe-Cr and B2 Al-Ni *b.c.c.* phases in the $AlCoCrFeNiTi_{0.5}$ alloy [81]. It can be concluded that the aluminum and titanium stabilize the hard *b.c.c.* phase in the AlCoCrFeNiTi system which mainly contributes to the strength properties of the material. Moreover, the alloying with aluminum and titanium the CrCoNi-system promotes comparably high specific strength making this system interesting for further development for the structural applications at high temperatures, Fig.1-5.

There is a particular interest in applying additive manufacturing processes for HEAs. It is discussed below in section 1.5: High-entropy Alloys as Additive Manufacturing Materials, after a review of the AM processes and materials.
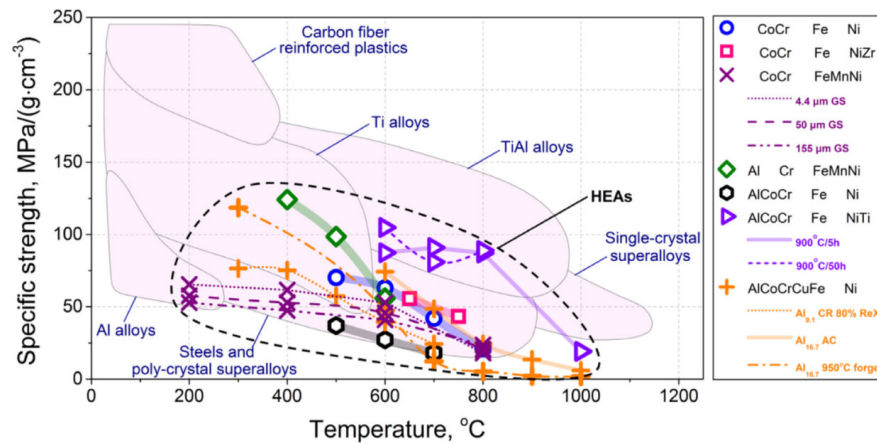
Figure 1-5: Specific strength vs. temperature of MPEA reported in the literature, shown with respect to conventional high-temperature materials [20].

1.3 Metal Additive Manufacturing Techniques

AM is a process of building the three dimension parts by adding the source material layer by layer according to the digital model. AM techniques increase the design flexibility of the parts allowing to apply the topological optimization and building complex geometries that are difficult or impossible to produce with conventional manufacturing techniques. It also reduces costs associated with tooling, setup, and assembly, as many parts can be printed in one operation, and increase the cost-effectiveness using fewer materials. Additionally, the important advantage of the AM, especially for the medical field, is geometry individualization in a cost-effectively way. Note that here and further, the metal AM processes are discussed only.

As feedstock material for the AM a wire or powder is typically used, and as the heat source a laser or electron energy can be applied. The combination of the material type and a heat source provides plenty of the title for the AM process. However, all of them can be categorized into several groups: i) PBF; ii) direct metal deposition (DMD); iii) sheet lamination; iv) binder (or material) jetting; material extrusion [14]. Each of these technologies has its unique advantages and disadvantages, and the choice of technology will depend on several factors including material requirements, part complexity, and cost. The binder jetting and material extrusion techniques use polymers to create a part form. It requires further polymer removal

process and sintering of the metal powder which do not provide the appropriate mechanical characteristics since the metal powder is not melted. The sheet lamination technique involves the bounding together of the metal sheets using ultrasonic welding. It limits the geometry of the parts and makes them unsuitable for structural use. Only two AM techniques (PBF and DMD) offer mechanical properties comparable with the conventional techniques and allow *in situ* mixing of the materials during the printing.

DMD technology involves the use of a high-powered laser that melts metal powder or wire in the stream of the shield gas and deposits it in precise layers to form a three-dimensional part (Fig.1-6a). DMD combines computer numerical control machining and metal deposition techniques, allowing parts to be built with complex geometries while maintaining dimensional accuracy. The main advantages of DMD technology are the possibility of printing a continuous part using different metal powders simultaneously and printing large parts, Fig.1-6b.
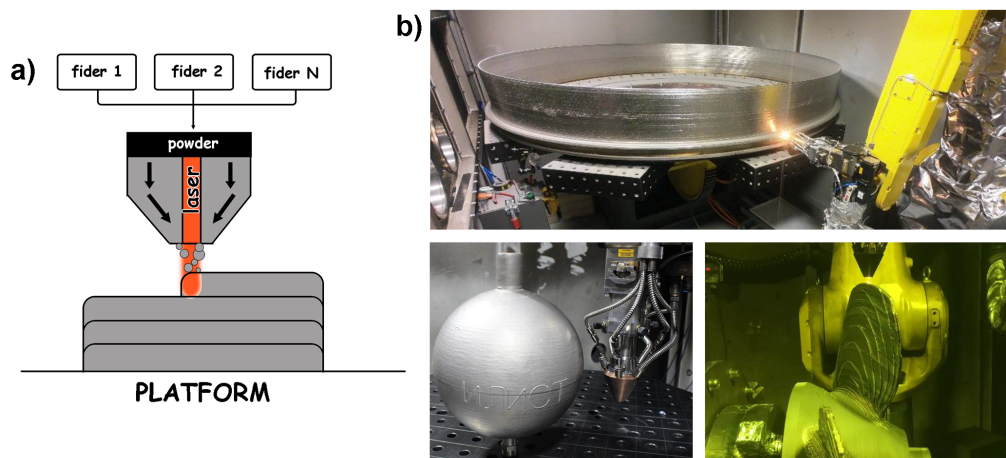

Figure 1-6: (a) The scheme of the DMD process; (b) examples of the DMD items printed in the Institute of Laser and Welding Technologies.

PBF additive manufacturing technology involves creating 3D objects by building up layers of material, one at a time. A thin layer of powder is spread across a build plate, and a laser or electron beam selectively melts or sinters the powder in the inert atmosphere according to a digital model (Fig.1-7a). This process is repeated layer by layer until the object is complete. PBF technology offers significant advantages such as creating complex geometries, reducing material waste, and allowing

for customized and low-volume production. The main advantages of the process are the high accuracy of the printed parts, low roughness, and the possibility to print complex geometry, mainly provided by the small laser spot diameter and the possibility to print overhanging structures in a powder bed (or print support structures), Fig.1-7b.
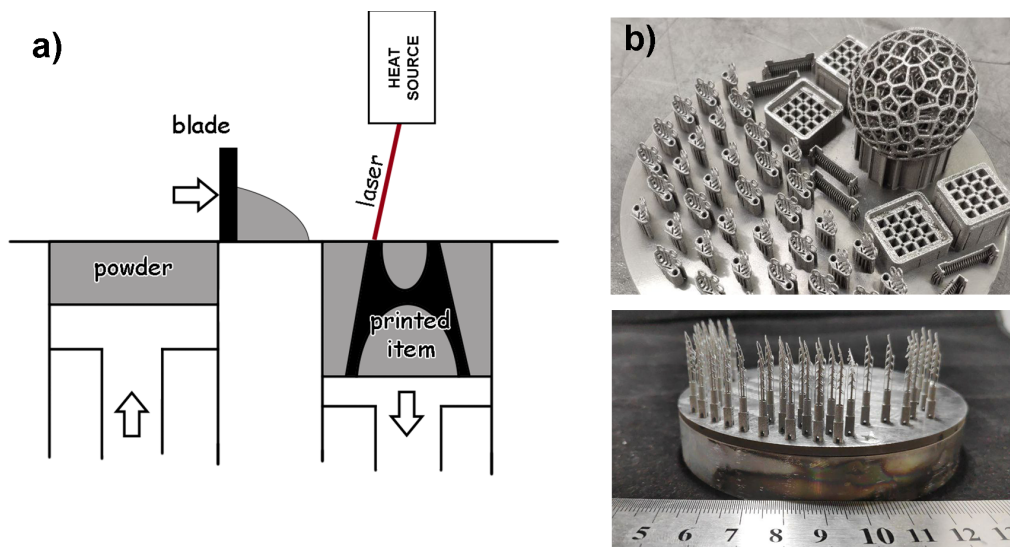
Figure 1-7: (a) The scheme of the PBF process; (b) examples of the PBF items printed in the Skoltech Additive Manufacturing Lab.

The application of the *in situ* AM technique often involves the DMD process due to its simple implementation in the DMD. Meanwhile, the PBF technique is actively used to print items for aerospace and medical applications requiring high accuracy, weight minimization, and complex geometry. It makes PBF printing interesting for new material applications, and, particularly, for the printing process using powder blends. There is a limited number of publications considering the use of powder blends in the PBF process which makes new investigations in this direction more valuable.

1.4 Specific Properties of Additive Manufactured Alloys

The metal materials obtained via AM technologies are characterized by fine microstructure and anisotropic structure (texture) along the build direction. The fine substructure occurs due to the high cooling rate. It also provides residual stress in the as-built material which limits the application of the 3D printed materials and often requires additional post-treatments. Due to the heating gradient from the heated top to the cooled bottom, the elongated microstructure along the build direction is observed for all materials. Below, the AM material characteristics are indicated and the improvement ways are discussed.

Printing Defects

One of the main challenges for printed material applications is the minimization of printed defects. The <u>loss of elements</u> taking place at high temperatures is one of them. Selective vaporization can lead to alterations in the overall composition of an alloy due to variations in the volatility of certain elements [49]. This can have detrimental effects on the microstructure solidification, mechanical properties, and corrosion resistance, ultimately hindering the production of high-quality components. Despite limited literature on the subject, several studies have demonstrated noteworthy changes in composition. Plenty of works report the loss of aluminum during the PBF process (electron beam source), Fig.1-8 [6, 19, 31].

Modeling works reveal the exponential dependence of element vapor flux on temperature highly depending on the computed temperature distribution [14, 49, 59]. During laser processing, alloying elements vaporize from the molten pool's surface, even though they are depleted from the entire volume of the well-mixed liquid pool. Therefore, the surface area-to-volume ratio is a significant factor in determining the extent of composition change [69]. Accurate estimations of both the temperature field and molten pool geometry are essential for understanding composition changes during AM. The most important variables that impact alloying element vaporization during AM are those that affect molten pool geometry and temperature distributions, such as power, scanning speed, feed-stock feed rate, and
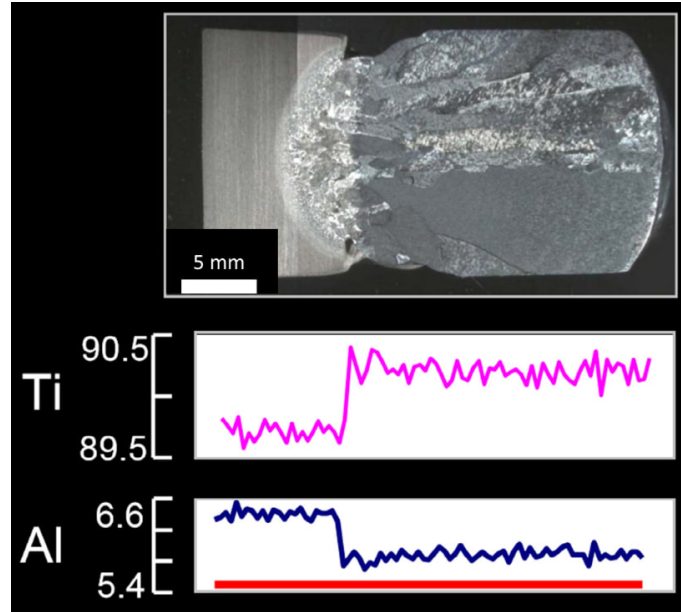
Figure 1-8: Measured chemical composition along the build height for a Ti-6Al-4V sample fabricated by PBF-EB showing depletion in Al concentration [31].

beam diameter. Through the manipulation of these parameters, it is possible to impact the element vapor flux intensity. However, the adjusting of the alloy chemical compositions for AM looks more prospective.

Another challenge for the printing process is porosity and lack of fusion defects. Defects such as porosity and lack of fusion voids are frequently found in AM. It is crucial to minimize or eliminate these defects as they have adverse effects on mechanical properties [9]. Researchers have identified three primary mechanisms responsible for these effects. The first mechanism occurs when some AM processes are operated at high power density, leading to deposition or melting in keyhole mode [34, 45]. If keyhole mode melting is not carefully controlled, the keyholes can become unstable and repeatedly form and collapse, resulting in entrapped vapor and voids inside the deposit [34]. Those porosities are almost spherical in shape. It was shown that the keyhole forms especially at the melt pool turns where the laser impact is the highest [45]. Therefore, the minimization of keyhole defects can be achieved through the optimization of the laser strategy [39]. Additionally, it is possible to decrease the laser input energy. As was shown in the studies, the volumetric input energy (or laser input energy), (E_v, J/m^3), can be estimated through the equation [62, 11]:

$$E_v = P/h \cdot l \cdot v \tag{1.4}$$

where P is laser power (W), h is hatch space (m), l is layer thickness (m), and v is laser speed (m/s). This equation does not have a strong thermodynamic base but it provides the possibility to estimate appropriate regimes for printing the specific material. Cherry et al. demonstrate the parabolic dependency of the defect volume and volumetric energy for PBF 316L steel, Fig.1-9 [11]. The high E_v leads to the overheating of the material forming the keyholes while the low E_v does not provide enough energy to melt the powder and leads to the second defect type, lack of fusion defects. Instead of the keyhole pores the lack of fusion defects have an irregular shape and commonly include the unmelted particles due to not enough penetration between the neighbor molten pool tracks or between the layers, Fig.1-9. Additionally, gas defects can also occur. Gas can be entrapped inside the powder particles during the powder atomization process [14]. These entrapped gases result in microscopic spherical gas pores. In addition, gas pores may also be formed due to the entrapment of the shielding gas or alloy vapors inside the molten pool.

Adjusting the printing process parameters it is possible to manipulate the volume of defects. Hot Isostatic Pressing (HIP) can also be helpful to improve the material properties. It especially demonstrates the promising results for AM Ti6Al4V alloy having a brittle martensitic phase at an as-built state. HIP allows to stabilize the phase composition and heal pores. It increases ductility and plays a decisive role in the fatigue properties of PBF Ti6Al4V alloy (Fig.1-10a) while for initially ductile PBF 316L steel, it was not so significant (Fig.1-10b).

The defects such as pores and voids impact a crucial role in the material fatigue behavior. As far as author knowledge the AM material properties under the cycling load do not exceed (and usually are much lower) compared with their analogs produced by conventional techniques. As was presented above, HIP can be an effective technique for improving the fatigue properties of AM alloys while it is not so effective for ductile materials. Moreover, it does not allow to "close" the opened pores. The near-surface porosity and surface roughness play a more significant role in the material properties under the cycling load (the examples of defects presented
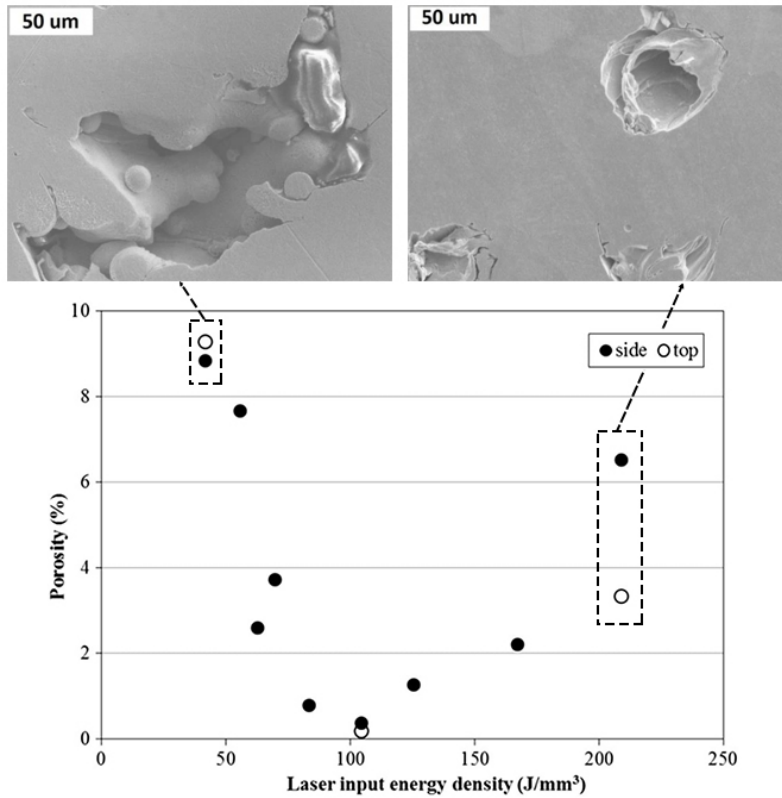
Figure 1-9: Porosity versus E_v for PBF 316L steel measured using an optical microscope with typical pore defects for energies of 42 and 209 J/mm^3 [11].

in Fig.1-11) [79, 78, 77]. It was demonstrated that the central defects do not contribute to the fatigue behavior of the PBF 316L steel [72], presumably, due to the compressive residual stress in the inner material zone [16]. At the same time, removing the near-surface porosity, which usually has higher density rather than the inner porosity due to edge effects, by a simple machining process increases the fatigue life [78, 77]. Panov *et al.* also demonstrate an effective way to improve the PBF material fatigue life by laser polishing which remelts the surface and removes near-surface porosity and roughness [52].

Residual Stress and Distortion

Residual stresses have the potential to cause various issues in the fabricated part. These include part distortion, loss of geometric tolerance, and delamination of layers during the deposition process. Additionally, the fatigue performance and fracture resistance of the part can be compromised due to the presence of residual stresses. The three types of residual stresses are distinguished: i) Macro stress involves the
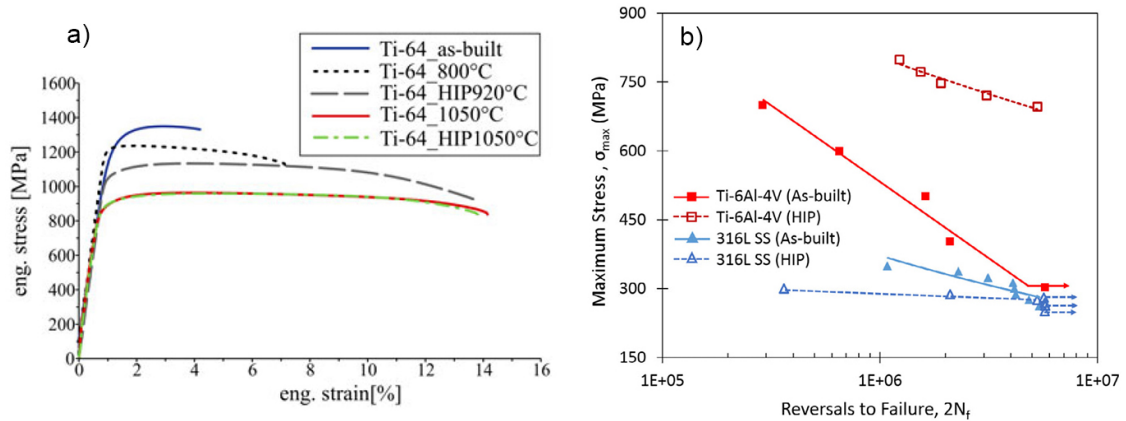
Figure 1-10: Effect of the common heat treatment and HIP on the PBF Ti6Al4V tensile properties (a) and comparison of the PBF Ti6Al4V and PBF 316L alloy behavior under cycling load without heat treatment and after HIP (b) [41, 78].
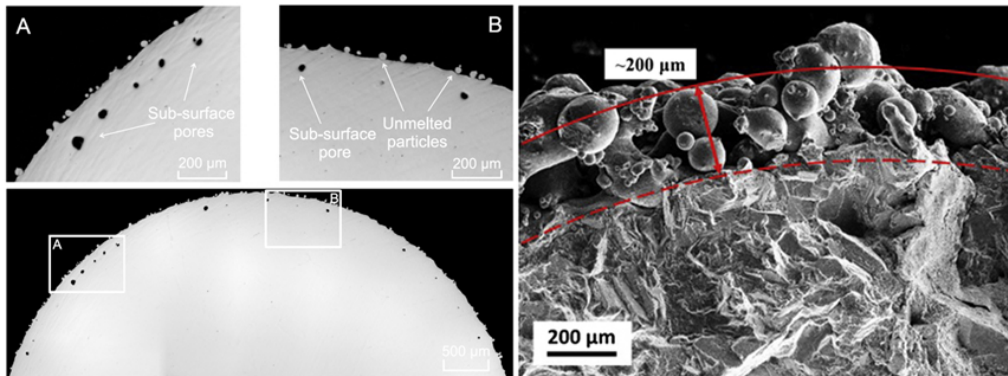
Figure 1-11: Inner porosity observed for PBF 316L steel (left) and surface roughness for PBF Inconel718 alloy (right) [52, 78].

interaction between several grains. This stress impacts the macroscopic material dimension. It is estimated through the destructive hole-drilling method; ii) Micro stress is considered in one grain; iii) Sub-micro stress is developed within several atomic distances of the grain. It includes the effects of crystalline defects such as vacancies, dislocations, etc. All three types can be estimated using non-destructive X-ray or neutron diffraction techniques, even it is challenging to apply neutron diffraction for a sub-micro stresses measurements. However, in real life, materials have all the residual stress types.

There are several important physical factors that contribute to the development of residual stresses in AM. These factors include the following: 1) the presence of a temperature gradient in the material caused by localized heating and cooling due

to the movement of the heat source; 2) the thermal expansion and contraction of the material resulting from the changes in temperature during the AM process; 3) the uneven distribution of inelastic strains, which leads to strain compatibility issues. Debroy *et al.* considered the classic bar-frame problem during the welding adapted to explain the residual stresses in AM material [14]. They identified the main factors of residual stresses during the printing: 1) Thermal gradient. The non-uniform heating and cooling process do not allow the frame and center parts of the workpiece to expand and contract freely. It leads to the compressed stresses in the middle and tensile stresses on the edges; 2) Thermal expansion. The thermal strain can exceed the elastic strain limit, resulting in the accumulation of plastic strain upon further heating/cooling. Moreover, when dissimilar metals are used (having different thermal expansion coefficients), it can result in the formation of residual stresses even when they are heated and cooled down uniformly; 3) Plasticity and flow stress. The speed of the heating-cooling process should also be taken into account. The speed of stress waves in metals is significantly faster than the rate of heat conduction. However, whenever a new temperature distribution is established, the stresses are simultaneously redistributed in order to attain a new state of static equilibrium.

Finite-element Analysis of the steel bar printing process was experimentally verified and it demonstrates similar conclusions, Fig.1-12 [16]. There is well-seen compression stress in the bar center and tensile stress closer to the edge region Fig.1-12c. It leads to the difference in the plastic deformation history for the vertically and horizontally printed bars which may be responsible for the difference in the elastic deformation flow during the testing Fig.1-12d.

The analysis of residual stresses is highly important to build the parts of the required geometry. There are softwares, such as MSC Simufact Additive or Oqton Amphyon, providing the turnkey solutions to recalculate the initial geometry and to obtain the required one for the printed part. Another approach allows us to calculate the stress field in the printed part and totally modify the geometry (add stiffening ribs, topologically optimize, choose the printing strategy allowing to compensate oppositely directed stresses) [36]. In practice, these approaches reduce the itera-
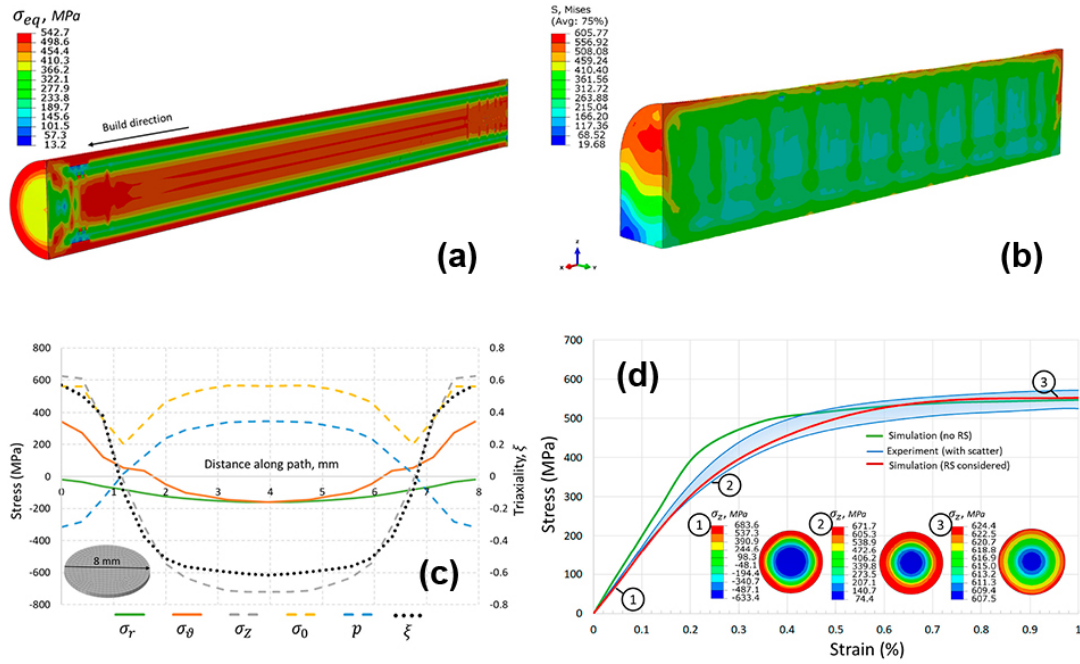
Figure 1-12: The calculated von Mises residual stress distributions in the bars printed along the build direction (a) and transversely (b). The cross-section of the vertical build bar also consists of the inhomogeneous stress distribution (c). The simulation of the deformation behavior of the materials with (red line) and without (green line) residual stress under the tensile loading reveals the difference in the elastic zone and in the beginning of the plastic zone (d). The experimental data (blue area) have a good match with modeling taking onto account the residual stress impact [16].

tion number reaching the required geometry but do not minimize them completely. Therefore, the residual stress in AM material is still an actual topic today.

Structure and Texture

AM methods often produce structures closely resembling those in multipass welds since they use the same heat sources as in traditional welding processes. The same as for the welding process, the several critical parameters affecting the solidification process can be identified such as the temperature gradient G, solidification velocity R, and undercooling ΔT [14]. Based on the first two parameters, the solidification map can be constructed, Fig.1-13a [37]. The ratio G/R determines the mode of solidification while the product GR governs the scale of the solidification microstructure. The solidification microstructures can be planar, cellular, columnar dendritic, or equiaxed dendritic with decreasing G/R values. The dimension of all

four solidification microstructures decreases with increasing cooling rate GR.

During AM of single crystal alloys, the desired solidification microstructures consist of columnar dendrites that grow epitaxially from the single crystal substrate, without the presence of equiaxed dendrites. When a single crystal deposit is formed through additive processes, its microstructural characteristics can be assessed using such parameters as the solidification growth rate and temperature gradient. Depending on the specific values of these parameters, the solidification structure can undergo changes, transitioning from columnar to equiaxed, experiencing oriented-to-misoriented transitions, or forming stray grains. Desired solid microstructures can be reached by referring to the solidification maps plotted based on the known temperature gradient G and solidification rate R. For the AM metallic materials, the columnar and equiaxed structures are the most common observed solidification microstructures. At the same time, the specific solidification conditions may form an equiaxed structure. The undercooling (ΔT) is the main dendrite growth driving force. The total undercooling is estimated as the difference between the equilibrium liquidus temperature and the local dendrite tip temperature. As an example, the dependency between the undercooling and dendrite growth velocity for the Inconel 718 Ni-based alloy is demonstrated in Fig.1-13b [28]. It is seen that ΔT increases significantly dendrite growth velocity. Summarizing, the solidification structure in AM is influenced by a few key parameters. Understanding the relationship between the process and structure can be enhanced by correlating the processing parameters with these key solidification parameters. Apart from the dendritic microstructure mentioned earlier, the solidification microstructure in AM can also include a significant presence of precipitates, particularly in precipitation-strengthened alloys like Ni-base superalloys. This is primarily due to the rapid cooling that occurs in the localized melt pool during AM, leading to a non-equilibrium solidification condition.

The grain structure orientation has a stronger dependency on the shape and size of the melt pool which in turn are affected by the process parameters, material properties, and cooling conditions. During solidification, columnar grains typically grow from the boundary towards the melt pool center. The grain growth direction is aligned to the maximum heat flow direction, which is perpendicular to the so-
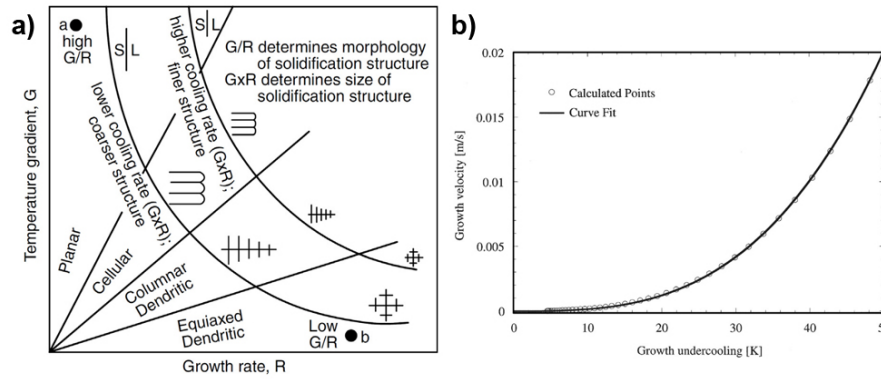
Figure 1-13: (a) Effect of temperature gradient G and growth rate R on the morphology and size of solidification microstructure; (b) Dendrite growth velocity as a function of undercooling for Inconel 718 alloy [14, 37, 28].

lidifying surface of the melt pool for polycrystalline materials. Depending on the crystal structure the easy growth directions are determined (for example, <1 0 0> for *f.c.c.* and *b.c.c.* structures, <1 0 $\overline{1}$ 0> for hexagonal-close-packed crystal structures, which are the epitaxial growth directions for these crystal structures) [37]. Such preferable grain growth orientation results in a strong texture along the build direction. Although, the geometry (or depth) of the melt pool impacts the heat flow direction, as can be illustrated in Fig.1-14a, comparing the melt pools during the PBF and DMD processes. The small volume and high speed of the melt pool during the PBF process form near "vertical" (along the build direction) heat flow providing the codirectional grain growth. The moving of the DMD melt pool is slower forming the strongest thermal gradient from the melt pool front center to the melt pool back bottom. The melt pool geometry also can be manipulated within one process, for example, through the laser scanning speed Fig.1-14b. However, generally, the PBF is characterized as a higher cooling rate process compared with DMD ($<10^{-8}$ *vs.* $<10^{-3}$ K/s), which provides the finer microstructure [27].

The further layer-by-layer printing results in the remelting of the previous layers forming the heat gradient from the top to the bottom of the work-peace. The texture for the specific crystal structure is variable depending on the printing process conditions, but not in the wide limits. Therefore, for all AM materials, the strong texture is observed along the building direction forming the anisotropy of physical and mechanical material properties. The homogeneous heat treatment of HIP may

remove the structural texture. However, Voisin *et al.* demonstrated the thermal structural stability of the PBF 316L steel compared with its conventional analog [71]. It indicates the specific of AM structure behavior requiring the revision of the known techniques affecting the structure of AM materials.
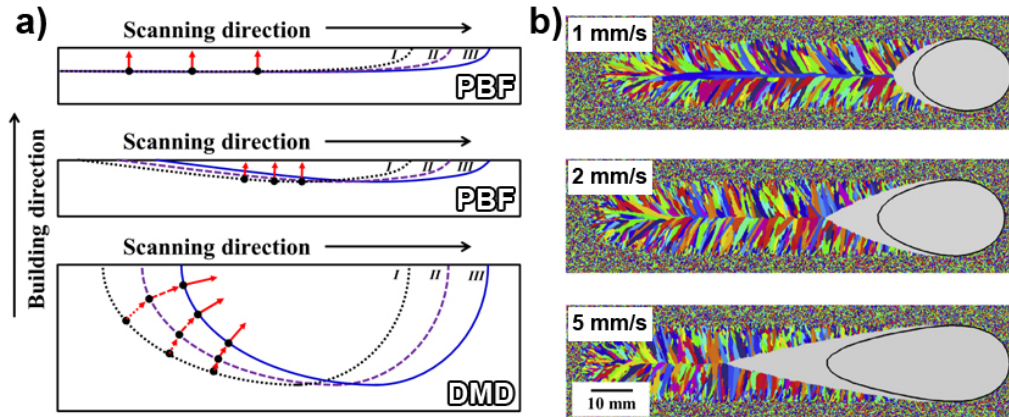

Figure 1-14: (a) Illustration of the growth direction of the columnar grains [14]; (b) Simulated grain structure for a single linear pass for different scanning speed [10].

Mechanical Properties

As previously mentioned, printing defects have a notable impact on the mechanical properties of AM materials. Many post-processing methods aim to reduce these defects through heat or surface treatments, but this can result in unfavorable alterations to the microstructure that affect the material mechanical traits. Ultimately, all process steps (including printing parameters and conditions, as well as post-processing techniques like HIP or machining) are selected with the goal of achieving the desired final material properties.

The AM materials compared with the conventional analogs have their strengths and weaknesses in terms of mechanical characteristics. The AM material properties do not exceed the conventional material ones under the cycling load while they represent the same or even higher strength values at the static load. Although, each material has its own specifics affecting the final properties. For example, the properties of AM austenitic steel depend on the microstructure component size and defect volume. At the same time, the multi-phase Inconel718 and Ti6Al4V alloys are more impacted by the thermal history. For the multi-phase material such as Ti6Al4V alloy, the difference in the thermal history for different layers forms the

inhomogeneous phase composition along the part height. It results in the mechanical characteristics difference for each zone along the height. However, it is possible to indicate the contributors to mechanical properties typical for all AM materials.

The main contributor is the fine microstructure providing the high strength properties for all AM materials according to the Hall-Petch law [75, 4]. The strong residual stress also contributes to the strength properties of AM alloys. Commonly, the residual stress removal allows the yield stress to decrease and increase ductility [71].

There is also a difference in the mechanical properties of the AM materials tested along the build direction and transversely. The summarized tensile properties for AM austenitic steels in Fig.1-15 demonstrate that there is anisotropy of strength while the difference in elongation is less pronounced. It can be explained by the strong structural texture along the build direction [55, 14], preferable crystallographic direction [61], and difference in residual stress distribution for specimens cut/printed in different directions [16]. All these factors can result in the mechanical property anisotropy. The contribution of each of them is discussable. Additionally, the phase composition should be taken into account. However, it should be noted a minor difference in mechanical properties in two directions for the dual Ti6Al4V alloy even after the phase stabilization heat treatment [43].

All these specifics should be taken into account for the understating of the AM material applications and/or creating the specific post-treatments.
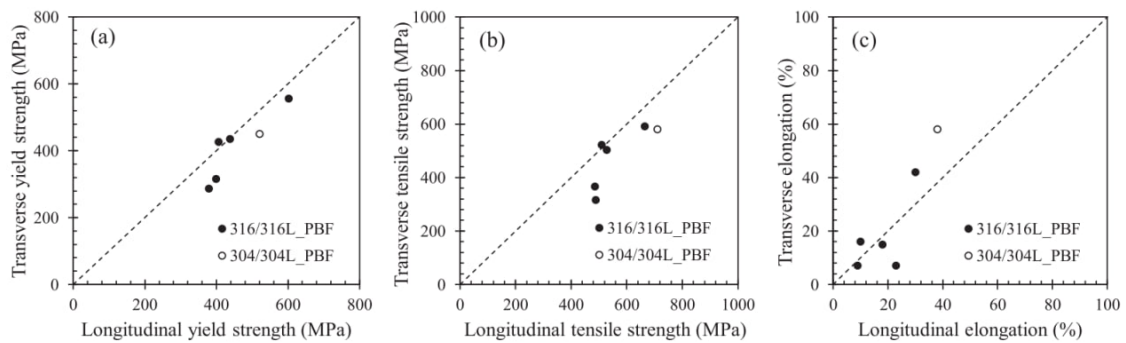

Figure 1-15: The tensile yield strength (a), ultimate strength (b), and elongation (c) for PBF austenitic stainless steels along the transverse direction (tension along the z-axis) versus the longitudinal direction (along the y-axis) [14].

1.5   High-entropy Alloys as Additive Manufacturing Materials

DMD and PBF show great potential in developing HEA products. The focused high-energy beam used melts powders and creates near-fully dense products, while the ultrafast cooling rates prevent the formation of unwanted intermetallic compounds and element diffusion, and also lead to microstructure refinement. However, the rapid solidification process causes residual stresses and cracks, requiring the alloy compositions adapted for crack resistance and counteracted residual stresses to improve printability. It can limit the direct usage of the known alloys for AM and require their composition modifications. As materials for AM, HEAs can be adapted for AM applications at the chemical composition developing step. Moreover, HEAs can be developed using the AM technical capabilities. Both DMD and PBF can use pre-alloyed HEA powders made through gas or water atomization or mechanical alloying to achieve product homogeneity. DMD allows *in situ* alloying with elemental powders and PBF allows the use of element powder blends, avoiding the lengthy process of developing HEA powders. Other benefits of DMD and PBF including design freedom and the potential for non-assembly required also may accelerate the application of HEA products for industrial uses.

Many publications consider the DMD for *in situ* printing with elemental powders and/or for creating graded HEA materials using pre-alloyed HEA powders. Joseph *et al.* successfully synthesized the DMD Al_xCoCrFeNi alloy using elemental powders [29]. Li *et al.* represented the phase evolution printing the same Al_xCoCrFeNi alloy considering the wide range of aluminum content [42]. There are also reports considering HEAs with high-melting temperature elements. The promising DMD printing of Mo-Nb-Ta-W HEAs was demonstrated in the work [48]. Authors note that not only the chemical composition affects the printed material properties, but manipulating with printing process parameters through the cooling rate it possible to affect the HEA phase composition. Kunce *et al.* found that a high-power laser source (1 kW) produced a *b.c.c.* phase in TiZrNbMoV HEAs, whereas, a low-power laser source (300 W) generated *b.c.c.* + NbTi4-type phases with Zr-rich precipitates

[38]. It should be noted that most of the publications considering the *in situ* DMD technique represent the trivial geometry of the printed parts (cubes, cylinders, etc.). One of the prospective AlCoCrFeNiTi HEA was printed using the DMD technique but only for structural analyses without mechanical test results [3]. At the same time, PBF allows printing more complex HEA parts Fig.1-16.
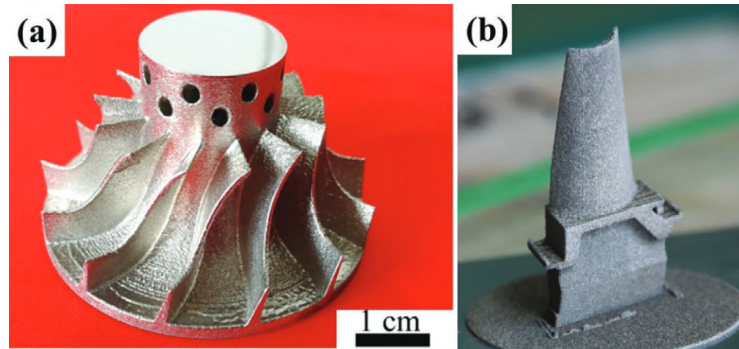

Figure 1-16: Examples of PBF HEA parts: a) an $Al_{0.5}CoCrFeNi$ turbine blade, and b) an WNbTaMo blade [85, 24].

Since the PBF technique requires high powder quality, it complicates the use of elemental powder blends. Therefore, most of the works introduce printing HEA products using the developed HEA powders. For example, Brif *et al.* initiated the work on PBF-printed CoCrFeNi HEA products with a combination of high strength and ductility [7]. Comparison of the PBF and DMD techniques for the CoCrFeNiTi-based high-entropy alloy represents the higher strength characteristics for the PBF alloy (ultimate strength of 1178 MPa vs. 932 MPa and elongation of 26 % vs. 4 % for the PBF and DMD materials, respectively) [17]. As was mentioned above, the PBF provides cooling rates and thermal history different from the DMD forming other structures. It should be taken into account for developing the HEA composition specifically for the PBF process.

However, the manufacturing process of high-quality powders with unique chemical compositions is costly. It forces the PBF printing with powder blends. There are works reporting the use of powder blends for PBF printing the Co-Cr-Fe, Ti-Al, Ni-Ti, Ti-Mo-Zr-Fe, and other systems [67, 68, 25, 32, 50, 73, 13]. According to the published reports, the following main challenges can be indicated: i) the evaporation of elements with lower melting points changing the chemical composition of printed

material compared with the initial powder blend [73]; ii) the chemical inhomogeneity formed due to the difference of Marangoni effect on the different elements [13]; iii) the thermal reactions between the elements during the melting process affecting the melt pool stability [73]. The described factors impact the structural and mechanical properties of the final material. Comparison of the PBF $Al_{0.5}CoCrFeNi$ alloys printed using pre-alloyed powder and powder blends reveals the significantly lower ductility of the powder blended HEA (22% vs. 10%) [85, 68], while strength properties are similar or higher. It can be associated with aluminum inhomogeneity in the material noted in the study. The additional process steps may help to improve the properties of the material produced from the powder blend. The mechanical alloying of powder blend may prevent a significant change in the chemical composition of printed material. For example, it prevents the aluminum evaporation printing Ti-Al system [50]. However, the irregular particle shape may cause defects. Adjusting the scanning strategy (double scanning) demonstrates the promising results to homogenize the element distribution for the CoCrFeMnNi system [32]. The homogenizing as a post-treatment process may also have uniform material properties. The choice of treatment procedure is highly dependent on the used chemical compositions and should be considered accordingly.

It can be concluded that the PBF technique has the potential for the HEA application for printing structural items. Using the pre-alloyed HEA powders provides homogeneous chemical and phase distributions comparable with the cast alloys. Meanwhile, printing with powder blends has limitations and may request additional procedures to improve material properties. Additionally, PBF provides the benefits of AM materials to the printed HEA items. However, it should be noted that the defects typical for AM materials are also observed in AM HEAs.

1.6 Applied Methods and Techniques

The present work considers the PBF alloys analyzing the mechanical, structural, and phase properties. Since each chapter includes information about the applied methods in detail, a brief discussion about the choice of the analytical methods and

specific their application is presented below.

Commercial powders of the CrFeCoNi (Polema Inc.), Al (RusAl Inc.), and Ti (AP&C Inc.) were used for all presented studies. All solid parts were printed with these powders using the PBF Trumpf 1000 3D metal printer. The parts were cut for further analyses and tests, if needed, with preliminary heat treatment conducted in the air and cooling into the water.

For the mechanical tests, the Instron machines were used. During the study, the common one-axis tensile and fatigue tests were realized according to ASTM E8 and ISO 1099, correspondingly. The microhardness tests were conducted with the appropriate load of 0.3 kgf.

Since the printed materials have a strong structural texture, the structural analyses were conducted in two directions, along and transversely to the build direction. The structural analysis includes such techniques as Scanning Electron Microscopy (SEM), Energy Dispersive X-ray (EDX) analysis, Electron Backscatter Diffraction (EBSD), Differential Scanning Calorimetry (DSC), X-ray (XRD), and Neutron Diffractions. Structural estimations were complemented with phase analyses using Transmission Electron Microscopy (TEM) diffraction and XRD with the Crystallography Open Database. The chemical composition of the printed materials including the qualitative analysis of the light elements was estimated using the EDX technique, while for the quantitative analysis of the light elements the combustion technique was used. The printed material porosity was estimated using optical microscopy according to ASTM E1245.

1.7   Thesis Structure and Author's Contribution

The present Ph.D. thesis includes 10 chapters. Chapter 1 is an introduction section where the problem statement and the goals of the thesis are presented.

In chapter 2, the first results for the CrFeCoNi alloy printed with PBF technique are discussed. At the beginning, I analyzed the morphology, particle distribution, and chemical composition of the initial powder using the SEM methods. As a next step, I was needed to choose the printing process parameters for the material.

Since the literature for these alloys is limited and each printer may contribute its own specifics to the printing procedure, the samples were printed varying the laser power and speed. Based on the porosity measurements by the optical images and microhardness responses, I chose the printing process parameters for the CrFeCoNi alloy. I conducted the tensile tests at the temperature range of -150°C - 300°C and compared the results with the hot-rolled material having the same chemical composition. Additionally, I applied the annealing at 750°C to remove the material residual stress and investigated its effect on the mechanical properties at the same temperature range.

Since the understanding of a material behavior during the heating is essential for its application limits, I deiced to investigate the structure and phase evaluations at different temperatures up to 1000°C in chapter 3. For these proposes, I annealed the printed CrFeCoNi alloy at different temperatures for 24 hours with further cooling in water to fix the material structure at investigated temperature. Using the microscopy and XRD techniques, I observed the formation of new phase at the specific temperature range and cellular structure transformation associated with the recrystallization process beginning.

In chapter 4, I focused on the CrFeCoNi alloy behavior under the cycling load due to its importance for structural application. The fatigue properties of the AM materials present lower characteristics compared with their conventionally produced analogs. Therefore, I also considered the ways improving the fatigue strength of the considered PBF CrFeCoNi alloy such as heat treatment (HT) and surface machining.

Chapters 5 and 6 consider the HPT process effect on the PBF CrFeCoNi alloy in comparison to the cast CrFeCoNi alloy. In chapter 5 the specifics of the strain hardening capability of the PBF CrFeCoNi alloy are discussed through the nanoindentation and microhardness results and microstructure analysis. In chapter 6, the structural and phase evolutions of the CrFeCoNi alloy under the heating are considered using the *in situ* neutron diffraction technique. It extend the knowledge about the PBF CrFeCoNi structure transformation during the heating discussed in chapter 3 and demonstrated the changes of the structure evolution during the heating after the HPT process. For both chapters, my contribution is limited by the providing

the PBF CrFeCoNi material and conducting the SEM analysis.

In chapter 7, the CrFeCoNi system is modified with aluminum by using the CrFeCoNi and Al powders blend for the PBF process. I started from the small aluminum concentrations in the $CrFeCoNiAl_x$ system (up to 2 at%) due to the limited literature for this aluminum volume. Moreover, it allowed consequentially analyzing the transformations in the $CrFeCoNiAl_x$ alloy with the aluminum concentration increase. In this chapter, I analyzed the effect of the aluminum presence in the material on the porosity formation, microhardness response, and structural changes including new phase formation.

To analyze the potential application of the PBF $CrFeCoNiAl_x$ alloy at elevated temperatures, I analyzed the oxidation behavior of the material at temperatures of 800°C and 1000°C in chapter 8. Based on the previous results, I prepared the $CrFeCoNiAl_x$ composition with an aluminum content of 2 at% and the second one with an aluminum concentration of 7 at% and compared them with the four-component system. I used to analyze sample weight changes during the 500 hours and analyzed near-surface chemical compositions and microhardness responses after the HT.

Chapter 9 presents the structural and mechanical properties of the PBF CrFeCoNi(Al,Ti) alloys printed using the CrFeCoNi, Al, and Ti powder blends. At the final stage of my research, I investigated the possibility of the simultaneous alloying the CrFeCoNi system with aluminum and titanium. I analyzed the structural and mechanical properties at as-built and annealed at 800°C states. Additionally, I discussed the effect of the high-temperature post-treatment on the elemental distribution in the alloys.

The last chapter 10 includes the conclusions made based on thesis results together with outlooks of future application of the PBF CrFeCoNi(Al,Ti) alloys printed using the powder blends.

Chapter 2

The effect of the parameters of the powder bed fusion process on the microstructure and mechanical properties of CrFeCoNi medium-entropy alloys

In this chapter, the alloy produced by the PBF technique with CrFeCoNi powder is considered. The powder analysis and choice of process parameters are described. The structure and phase composition analyses of the as-built CrFeCoNi alloy are conducted. Additionally, the effect of the annealing at 750°C on the tensile properties of the material in the temperature range of -150 - 300°C is described.

In this stage of work, two main printing parameters were varied, laser power and laser speed, to minimize the optical porosity and maximize the microhardness of the printed material. As a result, the laser power of 150 W and the laser speed of 600 mm/s were chosen. These printing process parameters also provide the material texture indicating the fully melted powder. The EDX mapping analysis demonstrated the homogeneous element distribution in the material. Unfortunately, we should admit the incorrect results of the quantitative elemental analysis due to technical

reasons discovered after work publication. The same as in further chapters the correct chemical compositions were $Cr_{24}Fe_{25}Co_{26}Ni_{25}$ and $Cr_{25}Fe_{26}Co_{24}Ni_{25}$ (at%) for the used powder and printed with chosen printing parameters alloy, respectively. The structure of the material is the typical *f.c.c.* material with elongated grains and strong texture along the build direction. The XRD analysis also presented that the material has an *f.c.c.* phase. Note that in the publication the formation of additional *b.c.c.* FeCr and CrNi phases in the as-built CrFeCoNi alloy were discussed since some XRD peaks were associated with those phases. However, such conclusion cannot be made by only one XRD peak for each phase without additional proof (for example, TEM diffraction analysis) which was not presented. The phase analysis results provided in Chapter 3 demonstrated the *f.c.c.* phase only at the as-built state of the material which was also true for the material in the present chapter since the same powder and printing process parameters were used. After HT at 750°C, which was applied to remove the residual stress, the new phase precipitates were observed on the grain boundaries. They were misidentified as sigma-phase formation (note, the further more comprehensive investigations presented in Chapter 3 identified these precipitates as nitrides, according to the EDX and TEM diffraction analyses). The tensile tests at temperatures in the range of -150 - 300°C of the as-built CrFeCoNi alloy demonstrated similar mechanical characteristics as for hot-rolled material having the same chemical composition, except the yield strength values which were higher by about 300 MPa. The HT did not change significantly the ultimate strength but decreased the yield strength by 100 MPa. It also slightly increased the ductility of the material at room temperature and above and dramatically dropped it at cryogenic temperature. Such an effect was associated with new phase formation on the grain boundaries.

Contribution: I contributed to the development of the structural and phase analyses of the material, the sample preparation process, the mechanical testing, the original draft, the final writing, and the editing of the manuscript. I would like to thank all the authors for their valuable contributions to the development of this paper.

Typos and clarifications: The article contains typos indicated after publica-

tion. The list of typos is presented below:

- The "top" and "front" labels indicate the cross-sections perpendicular to the build-direction and scan-direction, respectively.

- Correct label for Fig. 5 is "Backscattered electron images of PBF CrFeCoNi alloy from the (a, b) top side and (c, d) front side of the sample".

- Due to the high ductility of the tensile tested material, the elongation at fracture measurements was conducted by the strain-to-failure method.
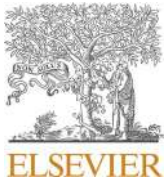
The effect of the parameters of the powder bed fusion process on the microstructure and mechanical properties of CrFeCoNi medium-entropy alloys

Y. Kuzminova [a,*], D. Firsov [a], A. Dudin [d], S. Sergeev [c], A. Zhilyaev [b,c], A. Dyakov [a], A. Chupeeva [e], A. Alekseev [e], D. Martynov [e], I. Akhatov [a], S. Evlashin [a]

[a] *Center for Design, Manufacturing & Materials, Skolkovo Institute of Science and Technology, Moscow, Russia*
[b] *Magnitogorsk State Technical University, Magnitogorsk, Russia*
[c] *Institute for Metals Superplasticity Problems of Russian Academy of Science, Ufa, Russia*
[d] *Institute of Nanotechnologies of Microelectronics of the Russian Academy of Sciences, Moscow, Russia*
[e] *JSC Polema, Tula, Russia*

A B S T R A C T

Multi-principal elemental alloys, referred to as high- or medium-entropy alloys, are a new class of materials with properties that can be predicted according to their compositional combinations. CrFeCoNi alloys are considered as a potential material for high-temperature application. In this work, we investigate the structural and mechanical properties of 3D-printed CrFeCoNi alloys produced by powder bed fusion. The porosity, microhardness and mechanical properties of the printed parts were studied. The samples demonstrate mechanical properties that are better than those previously reported. In the temperature range from $-150\,°C$ to $300\,°C$, the yield strength of printed samples is twice as high as that of traditional manufacturing techniques. Annealing at $750\,°C$ leads to formation of a sigma phase and changes in mechanical properties. This research estimates the potential application of CrFeCoNi medium-entropy alloys in the field of additive manufacturing.

1. Introduction

In recent years, considerable attention has been focused on high- and medium-entropy alloys (HEAs and MEAs). According to the composition-based definition, HEAs are alloys with five or more principal elements in equimolar rations with concentrations of each element 5–35 at. %, for MEAs, the number of these elements is at most four [1,2]. Varying the composition configuration of the HEAs and MEAs changes over their physical and mechanical properties. Previous articles have demonstrated the thermal properties of AlCoCrFeNi, AlCrFeMnNiMo, and CoCrFeMnNi systems [3–5]. The impact of Al on the electrical properties of the AlCoCrFeNi alloy has been investigated [6–8]. For instance, an increase in Al content leads to the transformation of the structure from face-centred cubic (fcc) to body-centred cubic (bcc), resulting in a non-monotonic temperature dependence of the electrical resistivity [9]. The magnetic properties of a HEA were studied in another work [7]. However, most researchers have investigated the mechanical properties of HEAs, especially the middle entropy system CrFeCoNi, in

isolation and with additional elements such as Al, Mn, Si, and V [8,10,11].

The HEA definition suggests at least five principal elements, but sometimes ternary CoCrNi and quaternary CoCrFeNi and CoCrMnNi alloys provide the same or better mechanical properties than those of CoCrFeMnNi [9]. For the Co–Cr–Fe–Mn–Ni system, the strength properties depend mostly on elements rather than the number of components. For instance, removing Cr obviously reduces the ultimate and yield strengths in the low-temperature range [12].

Additionally, the structural composition of the alloy has a high impact on its mechanical properties, and can control its deformation. The mechanical and structural properties of CrFeCoNi alloys were investigated after hot-rolling [10]. The yield and ultimate strength of the hot-rolled alloy approximately increase by a factor of 1.5 and 1.2, respectively, compared to casted alloys [11].

The mechanical characteristics of metal can be improved by additive manufacturing (AM), which is one of the modern methods of metal processing. AM allows the production of complex parts with lower

Table 1
Printer process parameters.

PBF parameter	Values
Laser power	60, 90, 120, 150 W
Laser spot diameter	55 μm
Hatch spacing	50 μm
Layer thickness	20 μm
Scan strategy	chess X–Y, 4 mm
Laser scan speed	100, 300, 600, 900, 1200, 1500 mm/s
Gas speed (Ar)	2.5 m/s
Oxygen level	<0.3 at. %
Pressure in chamber	1 bar

number of conventional processing steps. Moreover, the strength properties of austenitic stainless steels, titanium, and aluminium alloy AM parts are higher than those of their traditionally processed counterparts [13].

Brif et al. considered the application of MEAs in the AM field [14]. The solid parts were produced with CrFeCoNi alloys by powder bed fusion (PBF). The yield strength of PBF alloys (600 MPa) is much higher than that of hot-rolled alloys (300 MPa). However, the mechanical properties of the AM-made CrFeCoNi alloy were considered at room temperature only. The optimal printing parameters for MEA alloys have yet to be determined.

In the current study, we investigated the structural and mechanical properties of printed CrFeCoNi alloys. The mechanical properties of printed material were provided in the temperature range from $-150\,°C$ to $300\,°C$ for as-printed and annealed samples. The phase composition was considered before and after annealing.

The $750\,°C$ annealing for 12 h was demonstrated to reduce the residual stress for CrFeCoNi MEAs [14]. The reduction of the strength results into the stress relief. No changes in grain size were observed for heat treatments up to $800\,°C$ [10]. At the same time, for similar alloys, CrMnFeCoNi HEAs, the Cr-rich particles formation on the grain border was presented after heat treatments with temperatures up to $700\,°C$ [15, 16], which can embrittle the material. On the other hand, heat treatments at $800\,°C$ and higher indicate a stable solid solution for the same HEAs [15,17]. All considered, the $750\,°C$ heat treatment for 12 hours was chosen as an optimal.

2. Material and methods

2.1. Material

The $Cr_{21}Fe_{21}Co_{23}Ni_{35}$ (at.) MEAs powder, produced by the spraying method, was provided by Joint Stock Company Polema, Russia. The powder morphology is considered in the "Results and Discussion" chapter.

2.2. Sample preparation

The solid parts were produced by PBF technology (Trumpf TruPrint

1000, Germany) with laser heat source. Laser power (P) and scan speed (V) were variable parameters. During the manufacturing process no preheating of powder or platform was applied. A study of the MEA printing process and detailed characterization of the printed parts were carried out. First, the printing conditions that provide the best combination of microhardness and porosity were found. Second, the mechanical and structural properties and the ultimate composition of the parts printed under certain conditions were investigated.

The cylindrical parts were printed with a diameter of 5 mm and a height of 20 mm. The laser power and scan speed were varied in the range of 60–150 W and 100–1500 mm/s, respectively. Other printing conditions were set according to the suggested manufacturer protocol for stainless steel. The scan strategy had a chess form with a square side length of 4 mm, and the laser direction between neighbouring squares was normal. All the process parameters are summarized in Table 1. For simplicity, each sample is identified by the values of the laser power and speed used to print it. For instance, the sample manufactured using P = 60 W and V = 300 mm/s is referred to as S60_300.

2.3. Structural analysis

The powder particle size was measured using a laser particle size analyser (Fritsch Analysette 22 NanoTec, Germany) and Fritsch MaS control software. The standard procedure for particle size characterization was used.

Porosity was investigated according to the American Society for Testing and Materials (ASTM) E1245-03. Manufactured cylindrical samples were cut along the transverse to the built direction plane, mounted and polished with polishing diamond suspension (particle size of 3 μm). The relative porosity was determined by optical microscopy (Carl Zeiss, Axio Scope.A1, Germany) and Thixomet Pro software (Russia).

For scanning electron microscopy (SEM) and electron backscatter diffraction (EBSD) analyses the surface of the samples was additionally polished with silica oxide suspension (particle size of 40 nm) and followed by electrochemical polishing in an electrolyte of 900 ml of butanol C_4H_9OH + 100 ml of perchloric acid $HClO_4$. Polishing was carried out at room temperature, the voltage was 40 V, and the current did not exceed 1.1 A. The process lasts no more than 30 seconds. SEM (Carl Zeiss Supra 40, Germany) was used to characterize the printed parts. The SEM microscope was equipped with an energy dispersive X-ray (EDX) (Octane Elect EDS System) detector to obtain the elemental distribution and mapping at the center of sample surface from the square area with side of 200 μm.

For the crystallographic texture intensity analysis, an EBSD (Tescan Mira 3) system was employed. The pole figures and EBSD maps were acquired for the top and front sides of the printed sample. The scanning step size for the EBSD map was 2 μm, and the minimum boundary misorientation was 2°.

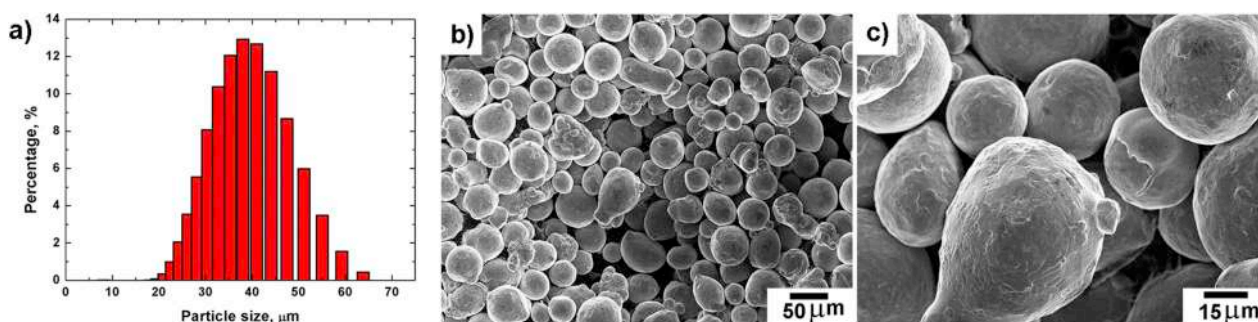The powder and printed parts were measured by X-ray diffraction (XRD) using a Bruker D8 ADVANCE (Massachusetts, USA)

Fig. 1. The powder used for printing: a) size distribution of the powder; b) and c) SEM images of the powder at different magnifications.
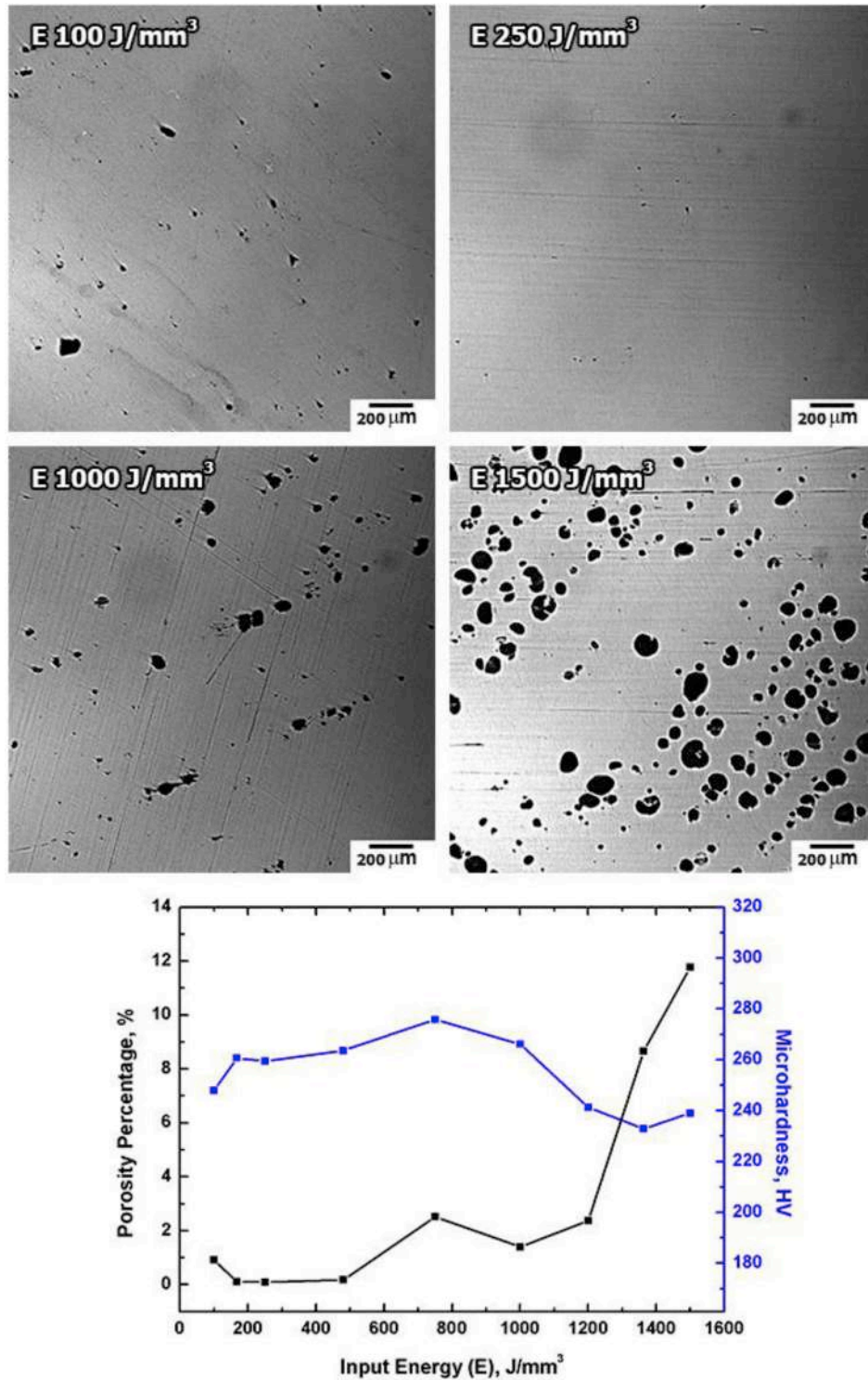
Fig. 2. Optical images of different PBF samples and evolution of the porosity volume and hardness via the input energy.

diffractometer with CuKα radiation (wavelength = 1.5418 Å). The diffraction peaks considered were in the range $2\theta = [20°; 100°]$ from the top view of the samples. The incremental step size was equal to $\Delta(2\theta) = 0.01°$, and the step time was equal to 0.15 s. The peaks were indexed using Diffrac EVA software (Bruker, Bellerica, Massachusetts, USA). The powder and S90_900, S150_900, S150_600, and S150_600 + annealing samples were investigated with $\Delta(2\theta) = 0.005°$ and a step time of 3.5 s in the above mentioned 2θ range.

2.4. Mechanical testing

The specimens were printed along the build direction under optimal printing conditions. The main objective was to achieve the best tensile strength properties. The thermal gradient forms the anisotropic structure in the printed materials. For austenitic stainless steel and nickel-based alloys, which have fcc structures similar to the CrFeCoNi MEAs, the yield and ultimate tensile strengths in the longitudinal direction are equal to or greater than those in the transverse direction [13].
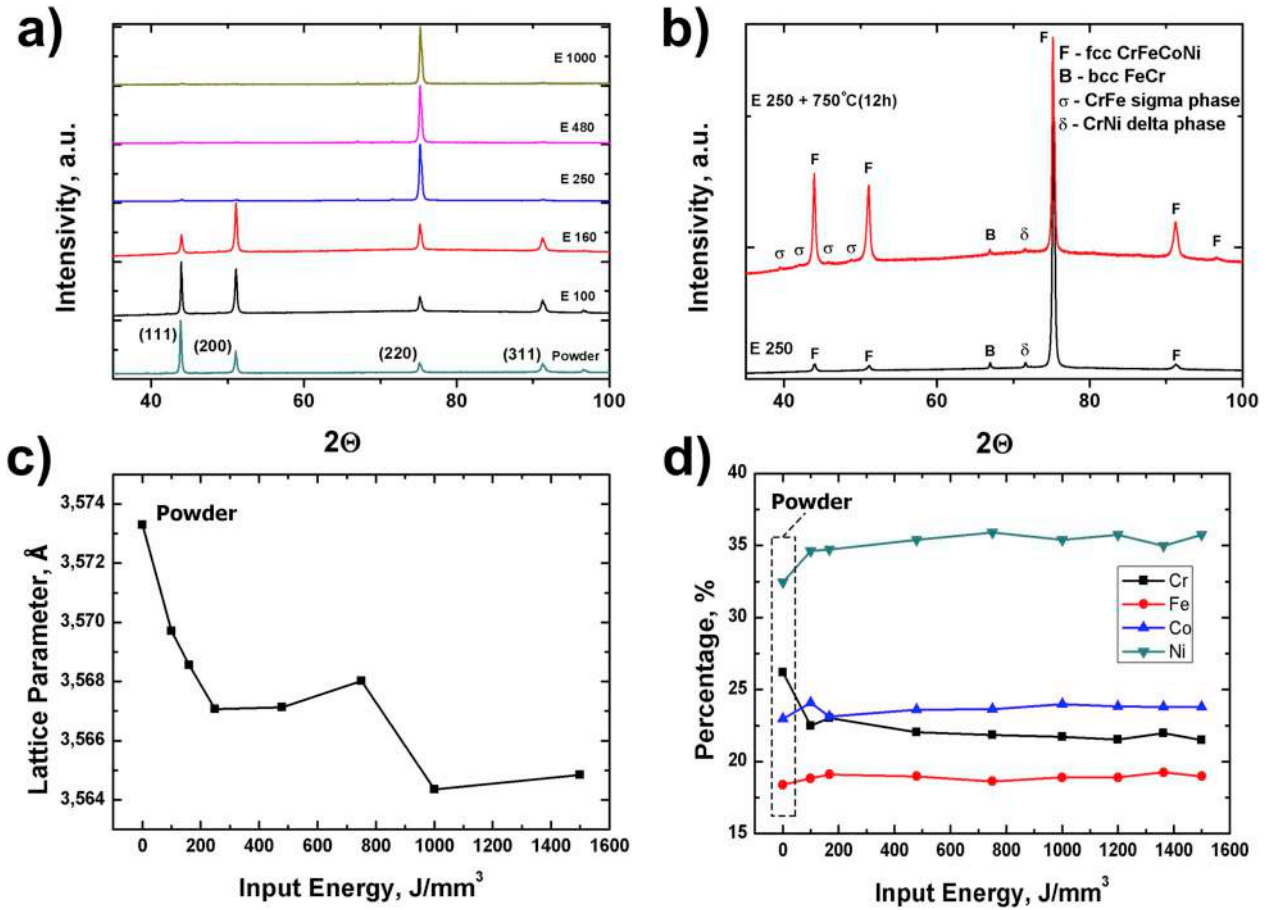
Fig. 3. XRD and EDX analyses of the printed samples: (a, b) XRD patterns of the PBF manufactured CrFeCoNi alloys; c) dependence of the lattice parameter on the input energy; d) atomic composition of the alloy at different input.
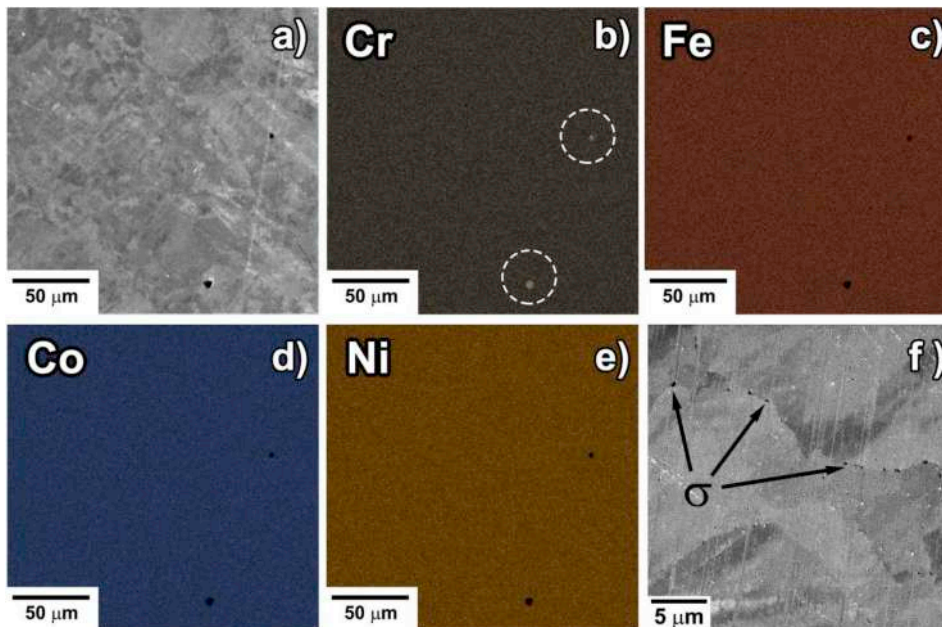
Fig. 4. (a–e) EDX map of the printed sample after annealing; f) backscattered electron image of annealed MEA.

The printed samples underwent tensile testing using an Instron testing machine 8801 (Massachusetts, USA). The tensile tests were carried out in the temperature range from −150°C to 300°C with a strain rate of 10^{-3} s^{-1}. The geometry of the specimens was determined according to the ASTM-E8 procedure.

The heat treatment at 750°C was applied to reduce the residual
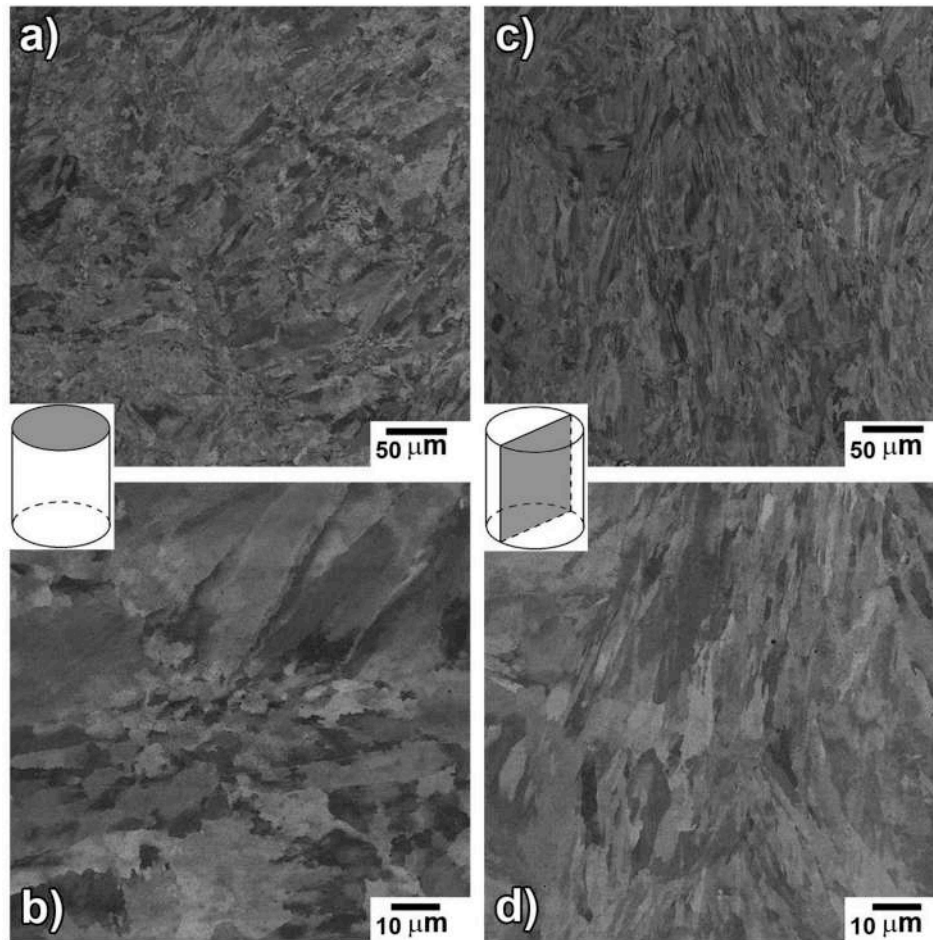
Fig. 5. Backscattered electron images of PBF CrFeCoNi alloy from the (a, b) front side and (c, d) top side of the sample.

stress. After the specimens underwent tensile testing at the same temperature range, the microhardness was measured using a Nanovea PB 1000 with a load of 200 g for at least 10 measurements per sample.

3. Results and discussion

3.1. Powder morphology

Fig. 1 demonstrates the particle size distribution and morphology of the powder. The size distribution ranges from approximately 20-65 μm with a mean particle size of 38 μm (Fig. 1a). SEM images of the powder indicate that most of the particles are nearly spherical (Fig. 1b). The small satellites are observed. The powder shape has a roughness (Fig. 1c).

### 3.2. Porosity and hardness

The optical micrographs in Fig. 2 demonstrate the effects of the input energy on porosity and pore morphology. The laser input energy (E) can be estimated as:

$$E = P / (V \cdot h \cdot l), \qquad (1)$$

where P is the laser power (W), V is the scan speed (mm/s), h is the hatch spacing (mm), and l is the layer thickness (mm) [18].

The increase in the input energy from 100 J/mm^3 to 160 J/mm^3 decreases the porosity from 1% to less than 0.5%, which also works for the input energy in the range from 160 to 480 J/mm^3. The low porosity value is achieved with E = 250 J/mm^3 and is equal to 0.09%. The

porosity increases up to 11.8% with increasing input energy from 480 J/mm^3 to 1500 J/mm^3.

The same dependence between the porosity and input energy is observed for the stainless steel [18] and Mg alloy [19]. The forms of the pores are analysed for different input energies (E = 100 J/mm^3 and E = 1500 J/mm^3) (see Fig. 2). The pores with irregular forms at a low density of laser input energy can be explained by the small melting pool, which is not large enough to melt the powder [20]. On the other hand, a high density of laser input energy mostly leads to spherical pores as a result of gas voids and solidification shrinkage [20]. The presence of moisture and contamination on the powder surface can lead to the formation of gaseous porosity [21].

The porosity value of the printed material impacts the material hardness [18]. In Fig. 2, an increase in hardness from 247 to 276 HV is observed for the samples produced with input energies in the range of 100–750 J/mm^3. With increasing input energy, the porosity impact also increases, which leads to hardness decreasing from 276 HV (750 J/mm^3) to 233 HV (1500 J/mm^3).

To summarize the results of the porosity and hardness analysis, the samples that demonstrated minimum porosity (less than 0.5%) and high hardness were chosen for tensile testing at room temperature. Sample S150_600 displayed the most favourable strength-strain characteristics among the selected samples.

3.3. Phase analysis

The XRD analysis from the top plane of the samples demonstrates that the structural composition of the alloy changes with increasing laser input energy (Fig. 3a). The intensity of peak (220) hkl becomes
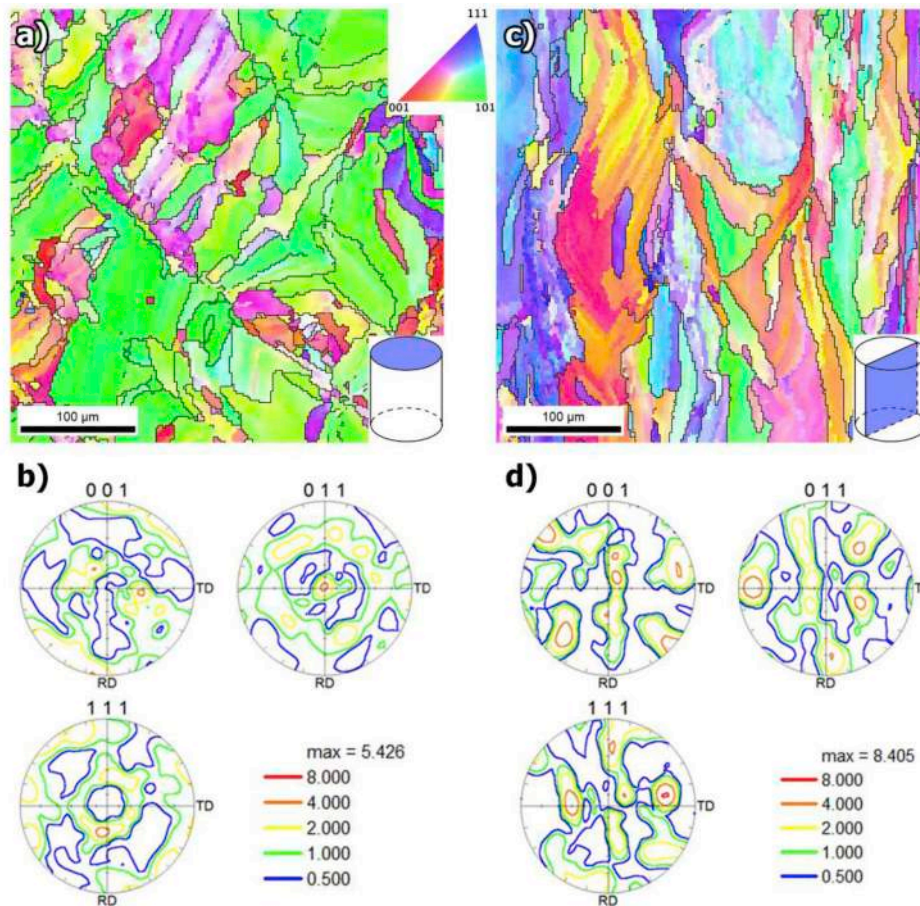
Fig. 6. EBSD maps and pole figures of the (a, b) top side and the (c, d) front side of the samples.

Table 2
Mechanical properties of the CrFeCoNi alloys at room temperature.

Manufacturing	σ_y, MPa	σ_{uts}, MPa	ε, %	E, GPa
As-cast [11]	140	488	83	–
Hot-rolled [10]	300	671	42	–
PBF printed [14]	600	745	32	–
PBF printed + 750 °C annealing [14]	495	695	30	–
PBF, S150_600 (present work)	596	691	38	135
PBF, S150_600 + 750 °C annealing (present work)	495	672	42	203

dominant instead of (111) hkl, which is in line with specimens with $E \geq 250 \text{ J/mm}^3$. This finding demonstrates the structural changes in the material, where peak (220) starts to prevail in the build direction after a specific value of the heat input. In contrast, previous work [14] demonstrates no changes in the XRD results for the printed MEA parts, but which sides of the samples were used for XRD analysis were not specified. The annealing (Fig. 3b) of S150_600 leads to the formation of uniform crystalline structures.

Two new peaks are observed for the printed parts via XRD analysis. The 2θ peak of 66.9° presents the bcc FeCr phase (peak B, Fig. 3b) with a lattice parameter of 2.79 Å. The next peak at 2θ = 71.6° presents the fcc CrNi phase (peak δ, Fig. 3b) with a lattice parameter of 4.56 Å. For CoCrFeNiMn alloy, the Mn-, Ni- and Cr-rich regions are observed after the manufacturing process [22]. Ether, Praveen et al. investigated HEAs synthesized by mechanical alloying (MA) and spark plasma sintering (SPS) [23]. These researchers observed the fcc and bcc structures for CoCrFeNi after MA and the fcc and sigma phase after SPS at 900 °C. Two

bcc phases (FeCr and NiAl) were observed with a lattice parameter of 3.01 Å for FeNiCrCo$_{0.3}$Al$_{0.7}$ alloy [24].

The EDX spectroscopy mapping is presented in Fig. 4a–e. The dotted area can be Cr-rich particles or pores. It could be either imprint from removed Cr-rich particles or pores formed as a result of Cr vaporization. Yet, no Cr-rich pores or imprints are observed in as-printed samples. After annealing, the precipitations along the grain borders can be observed (Fig. 4f). For CrMnFeCoNi alloys after annealing at 700 °C the formation of Cr-rich sigma phase along the grain borders was described [15]. We suggest that precipitations in Fig. 4f present the Cr-rich sigma phase, which correlates with results of XRD pattern of annealed sample (Fig. 3b). It indicates the CrFe crystal structure with space group P42/mnm and lattice parameters a = 8.8 Å and c = 4.544 Å.

The results of the XRD analysis indicate a decrease in the alloy lattice parameter (Fig. 3c). The CoCrFeNiMn HEA exhibited a decrease in the lattice parameter due to Mn removal during the printing process, as explained in Ref. [22]. In that case, the removal of Mn occurred because it had the lowest vaporization point, the lowest vaporization heat and the highest atomic diameter of all the alloy elements. However, in the current research, the element with the lowest vaporization point and lowest smallest vaporization heat is Cr. The EDX results (Fig. 3d) show that the Cr content in the alloy decreases during the printing process.

3.4. Microstructural analysis

Figs. 5 and 6 show the microstructures and crystallographic texture of the manufactured alloy. In the top view (Fig. 5a and b), the melt track is clearly observed. However, the EBSD result from the same view provides the massy structure (Fig. 6a). Low-angle boundaries constitute 70% of all the boundaries. The high stress in the AM material is formed
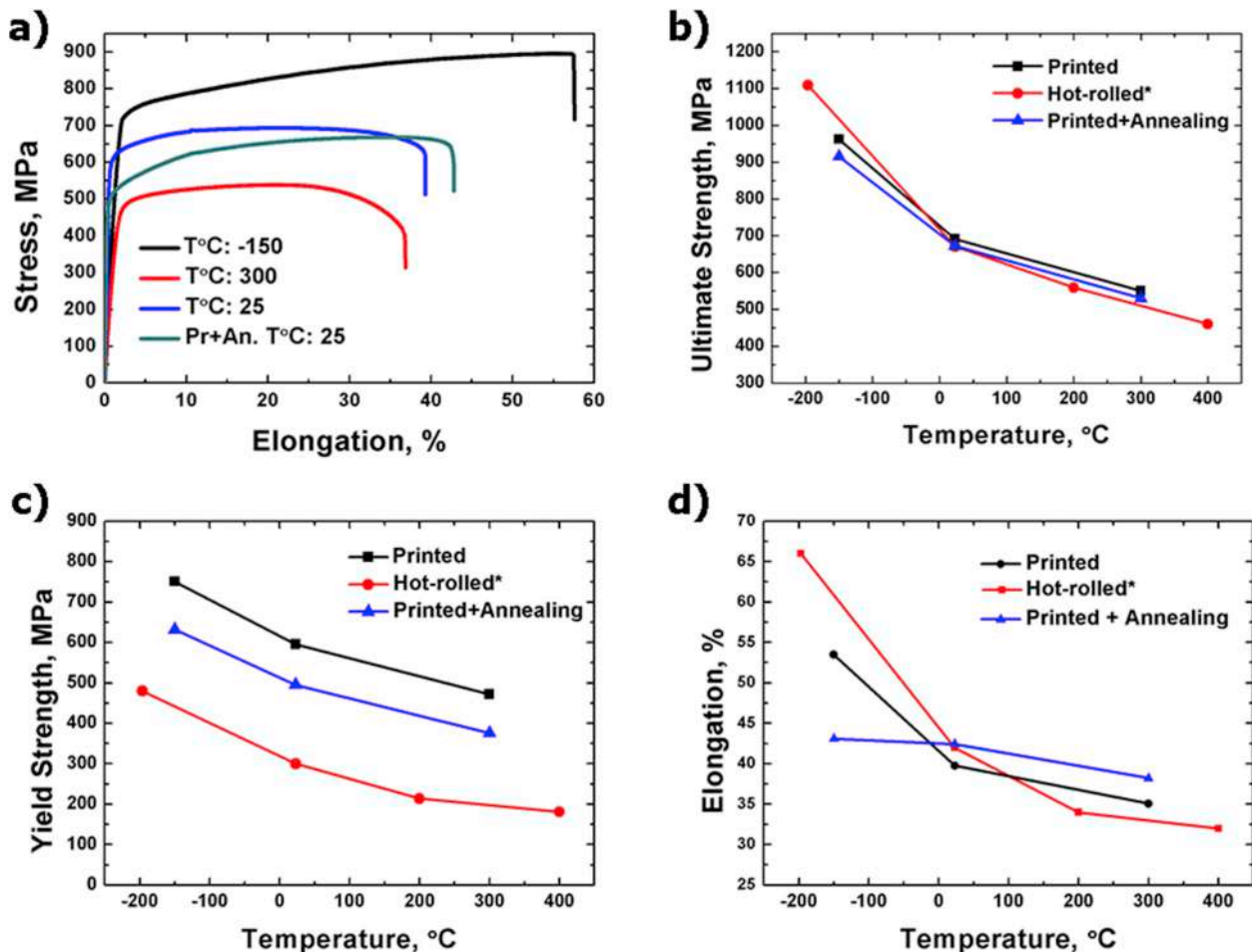
Fig. 7. The mechanical properties of the PBF CrFeCoNi alloy in the studied temperature range: a) typical engineering stress-strain curves; b) ultimate strength; c) yield strength; and d) elongation. *Red line: the results of hot-rolled MEA from Ref. [10].

by the high velocity of cooling, which is created by a thermal gradient [13]. The pole figures demonstrate the fibre texture in the <011> direction along the build direction (Fig. 6b).

In the front view, columnar grains along the build direction are observed (Fig. 5c and d) as a result of the heat transfer [13]. The fraction of the low-angle boundaries was also high, reaching 75%. The texture does not have a dominant crystallographic direction (Fig. 6c), although the <001> and <011> directions are extended in the build direction, and <111> has the strongest signal (8.405 a.u.) in the normal direction (Fig. 6d).

The mean grain size for the top view is 12 μm, and that for the front view is 13 μm. The bimodal structure is observed in both views. The dispersion of the grain size has peaks of 23 and 52 μm for the top view and 42 and 90 μm for the front view.

3.5. Mechanical properties

Table 2 summarizes the tensile test results for CrFeCoNi alloy produced by the casting, hot-rolling and PBF methods [10,11,14].

The typical engineering stress-strain curves for printed and annealed samples are presented in Fig. 7a. The tensile test results at room temperature demonstrated an ultimate strength of 691 MPa and a yield strength of 600 MPa. The ductility of the samples was 38%. The yield strength correlated with the results of other research groups [14] and is approximately twice that of hot-rolled alloy [10] and three times that of casted alloy [11]. On the other hand, the ultimate strength is 50 MPa less than that reported in another study, and the strain is 8% higher than that in the other study [14].

Brif et al. used an input energy of 600 J/mm^3; regarding Eq. (1), a change in the laser input energy may affect the strength material properties. Heat energy impacts the material structure and therefore the mechanical properties [13]. However, no trends between the yield or ultimate tensile strength and the input energy were found for austenitic stainless steel [13].

Additionally, the strength properties of the CrFeCoNi alloy were obtained at temperatures of −150 °C, 25 °C, and 300 °C. The ultimate strength of the PBF material is comparable to that of the hot-rolled material [10] over a wide range of temperatures (Fig. 7b). However, the yield strength of the PBF material is 300 MPa higher than that of the hot-rolled material at each temperature point (Fig. 7c) due to the high internal stress of the material.

Annealing at 750 °C reduces the yield strength by ~100 MPa in the temperature range from −150 °C to 300 °C, as shown in Fig. 7c, but the ultimate strength is slightly changed to 672 MPa at room temperature (Fig. 7b).

An increase in material strength with decreasing temperature is typical for several binary fcc solid solution alloys. This effect was considered for the CoCrFeMnNi HEA [25]. Otto et al. showed that plasticity is realized by dislocation glide and nanoscale twinning at low temperatures. This effect increase the ductility and the strength properties. The same effects were reported for CoCrFeNi [10].

In the present work, the ductility slightly increases after annealing at room temperature and higher temperatures but decreases by 10% at cryogenic temperature compared to that of the unannealed material (Fig. 7d). For the hot-rolled alloys the ductility decrease is not observed at cryogenic temperatures [10]. Gali and George applied the 900 °C

annealed for 1 h to the mechanical test samples to remove the stress. The annealing at 900 °C does not lead to formation of intermetallic particles [15]. At the same time, the formation of sigma phase was observed for annealed samples in present work. As known from Refs. [9,11], the volume of intermetallic phases, such as sigma phase, affects the ductility properties. Presence of sigma phase is observed along with ductility decrease [9]. To summarize, we suggest that the sigma phase formation in CrFeCoNi alloys after annealing at 750 °C decreases ductility at cryogenic temperatures.

4. Conclusions

In this work, CrFeCoNi alloy was printed using PBF technique. Printing conditions were chosen according to the analysis of the porosity and microhardness. Samples produced with a laser energy of 150 W and a scan speed of 600 mm/s demonstrate the best combination of porosity and microhardness. The XRD results show the formation of new phases of bcc FeCr and fcc NiCr for AM alloys. The ultimate strength and ductility properties of as-printed alloys are comparable to hot-rolled alloys in the temperature range from −150 °C to 300 °C. The yield strength reaches the value of 596 MPa and decreases with increasing testing temperature. The annealing at 750 °C decreases the yield properties by 100 MPa and does not affect the ultimate strength in the considered temperature range. The ductility of annealed samples increases slightly at room temperature and above. The annealing reduces the ductility of printed alloys by 10%. Presumably, formation of sigma phase influences ductility. The microstructure of the printed alloy demonstrates a bimodal grain distribution: peaks at 23 and 52 μm from the top view and 42 and 90 μm from the front view.

Acknowledgements

Appendix A. Supplementary data

Supplementary data to this article can be found online at https://doi.org/10.1016/j.intermet.2019.106651.

References

[1] J.W. Yeh, S.K. Chen, S.J. Lin, J.Y. Gan, T.S. Chin, T.T. Shun, C.H. Tsau, S.Y. Chang, Nanostructured high-entropy alloys with multiple principal elements: Novel alloy design concepts and outcomes, Adv. Eng. Mater. 6 (2004) 299–303+274, https://doi.org/10.1002/adem.200300567.

[2] J.W. Yeh, Y.L. Chen, S.J. Lin, S.K. Chen, High-entropy alloys – a new era of exploitation, Mater. Sci. Forum 560 (2009) 1–9. https://doi.org/10.4028/www.scientific.net/msf.560.1.

[3] C. Li, J.C. Li, M. Zhao, Q. Jiang, Effect of aluminum contents on microstructure and properties of AlxCoCrFeNi alloys, J. Alloy. Comp. 504 (2010) S515–S518, https://doi.org/10.1016/J.JALLCOM.2010.03.111.

[4] C.-L. Lu, S.-Y. Lu, J.-W. Yeh, W.-K. Hsu, Thermal expansion and enhanced heat transfer in high-entropy alloys, J. Appl. Crystallogr. 46 (2013) 736–739, https://doi.org/10.1107/s0021889813005785.

[5] G. Laplanche, P. Gadaud, O. Horst, F. Otto, G. Eggeler, E.P. George, Temperature dependencies of the elastic moduli and thermal expansion coefficient of an equiatomic, single-phase CoCrFeMnNi high-entropy alloy, J. Alloy. Comp. 623 (2015) 348–353, https://doi.org/10.1016/J.JALLCOM.2014.11.061.

[6] H.-P. Chou, Y.-S. Chang, S.-K. Chen, J.-W. Yeh, Microstructure, thermophysical and electrical properties in AlxCoCrFeNi (0 ≤ x ≤2) high-entropy alloys, Mater. Sci. Eng. B 163 (2009) 184–189, https://doi.org/10.1016/J.MSEB.2009.05.024.

[7] Y.-F. Kao, S.-K. Chen, T.-J. Chen, P.-C. Chu, J.-W. Yeh, S.-J. Lin, Electrical, magnetic, and Hall properties of AlxCoCrFeNi high-entropy alloys, J. Alloy. Comp. 509 (2011) 1607–1614, https://doi.org/10.1016/J.JALLCOM.2010.10.210.

[8] T.T. Zuo, R.B. Li, X.J. Ren, Y. Zhang, Effects of Al and Si addition on the structure and properties of CoFeNi equal atomic ratio alloy, J. Magn. Magn. Mater. 371 (2014) 60–68, https://doi.org/10.1016/J.JMMM.2014.07.023.

[9] D.B. Miracle, O.N. Senkov, A critical review of high entropy alloys and related concepts, Acta Mater. 122 (2017) 448–511, https://doi.org/10.1016/j.actamat.2016.08.081.

[10] A. Gali, E.P. George, Tensile properties of high- and medium-entropy alloys, Intermetallics 39 (2013) 74–78, https://doi.org/10.1016/j.intermet.2013.03.018.

[11] G.A. Salishchev, M.A. Tikhonovsky, D.G. Shaysultanov, N.D. Stepanov, A. V. Kuznetsov, I.V. Kolodiy, A.S. Tortika, O.N. Senkov, Effect of Mn and v on structure and mechanical properties of high-entropy alloys based on CoCrFeNi system, J. Alloy. Comp. 591 (2014) 11–24, https://doi.org/10.1016/j.jallcom.2013.12.210.

[12] Z. Wu, H. Bei, G.M. Pharr, E.P. George, Temperature dependence of the mechanical properties of equiatomic solid solution alloys with face-centered cubic crystal structures, Acta Mater. 81 (2014) 428–441, https://doi.org/10.1016/j.actamat.2014.08.026.

[13] T. DebRoy, H.L. Wei, J.S. Zuback, T. Mukherjee, J.W. Elmer, J.O. Milewski, A. M. Beese, A. Wilson-Heid, A. De, W. Zhang, Additive manufacturing of metallic components – process, structure and properties, Prog. Mater. Sci. 92 (2018) 112–224, https://doi.org/10.1016/j.pmatsci.2017.10.001.112–224.

[14] Y. Brif, M. Thomas, I. Todd, The use of high-entropy alloys in additive manufacturing, Scr. Mater. 99 (2015) 93–96, https://doi.org/10.1016/j.scriptamat.2014.11.037.

[15] F. Otto, A. Dlouhý, K.G. Pradeep, M. Kuběnová, D. Raabe, G. Eggeler, E.P. George, Decomposition of the single-phase high-entropy alloy CrMnFeCoNi after prolonged anneals at intermediate temperatures, Acta Mater. 112 (2016) 40–52, https://doi.org/10.1016/j.actamat.2016.04.005.

[16] M.V. Klimova, D.G. Shaysultanov, S.V. Zherebtsov, N.D. Stepanov, Effect of second phase particles on mechanical properties and grain growth in a CoCrFeMnNi high entropy alloy, Mater. Sci. Eng. A 748 (2019) 228–235, https://doi.org/10.1016/j.msea.2019.01.112.

[17] B. Schuh, F. Mendez-Martin, B. Völker, E.P. George, H. Clemens, R. Pippan, A. Hohenwarter, Mechanical properties, microstructure and thermal stability of a nanocrystalline CoCrFeMnNi high-entropy alloy after severe plastic deformation, Acta Mater. 96 (2015) 258–268, https://doi.org/10.1016/J.ACTAMAT.2015.06.025.

[18] J.A. Cherry, H.M. Davies, S. Mehmood, N.P. Lavery, S.G.R. Brown, J. Sienz, Investigation into the Effect of process parameters on microstructural and physical properties of 316L stainless steel parts by selective laser melting, in: Advanced Sustainable Manufacturing Technologies (ASTUTE), Digital Technium, College of Engineering, 2014.

[19] B. Zhang, H. Liao, C. Coddet, Effects of processing parameters on properties of selective laser melting Mg–9%Al powder mixture, Mater. Des. 34 (2012) 753–758, https://doi.org/10.1016/J.MATDES.2011.06.061.

[20] L. Hao, S. Dadbakhsh, O. Seaman, M. Felstead, Selective laser melting of a stainless steel and hydroxyapatite composite for load-bearing implant development, J. Mater. Process. Technol. 209 (2009) 5793–5801, https://doi.org/10.1016/j.jmatprotec.2009.06.012.

[21] M.A. Taha, A.F. Yousef, K.A. Gany, H.A. Sabour, On selective laser melting of ultra high carbon steel: effect of scan speed and post heat treatment, Mater. Werkst. 43 (2012) 913–923, https://doi.org/10.1002/mawe.201200030.

[22] R. Li, P. Niu, T. Yuan, P. Cao, C. Chen, K. Zhou, Selective laser melting of an equiatomic CoCrFeMnNi high-entropy alloy: processability, non-equilibrium microstructure and mechanical property, J. Alloy. Comp. 746 (2018) 125–134, https://doi.org/10.1016/j.jallcom.2018.02.298.

[23] S. Praveen, B.S. Murty, R.S. Kottada, Alloying behavior in multi-component AlCoCrCuFe and NiCoCrCuFe high entropy alloys, Mater. Sci. Eng. A 534 (2012) 83–89, https://doi.org/10.1016/J.MSEA.2011.11.044.

[24] W. Chen, Z. Fu, S. Fang, H. Xiao, D. Zhu, Alloying behavior, microstructure and mechanical properties in a FeNiCrCo0.3Al0.7 high entropy alloy, Mater. Des. 51 (2013) 854–860, https://doi.org/10.1016/J.MATDES.2013.04.061.

[25] F. Otto, A. Dlouhý, C. Somsen, H. Bei, G. Eggeler, E.P. George, The influences of temperature and microstructure on the tensile properties of a CoCrFeMnNi high-entropy alloy, Acta Mater. 61 (2013) 5743–5755, https://doi.org/10.1016/j.actamat.2013.06.018.

Chapter 3

Phase and structural changes during heat treatment of additive manufactured CrFeCoNi high-entropy alloy

Previous Chapter 2 represented the effect of the HT on mechanical characteristics. It demonstrated the importance of understanding the material structure evolution under heating. Therefore, in this chapter the effect of annealing at different temperatures on the structure and phase changes in the PBF CrFeCoNi alloy. The annealings were conducted at temperatures of 400 - 1000°C with a step of 100°C for 24 hours. Additionally, the material was analyzed up to 1200°C using the DSC method.

The main structural changes occur starting from the 700°C annealing causing the distortion of the cell structure and dropping of the microhardness. The formation of a new phase on the grain boundaries was observed at the temperature range of 700 - 800°C. It was recognized as an M_2N crystal structure according to the TEM diffraction analysis. Its formation was associated with the impurity of the initial powder having up to 0.1 wt% of nitrogen (earlier it was misrecognized as a sigma phase). Except for nitrides, no other phase formation was revealed. The heating of the up to 1000°C leads to the formation of small equaxial grains instead of the

cellular substructure while the texture along the build direction is still observed. The heat treatments at temperatures lower than 700°C do not provide the significant structural changes according to the microscopy observation. The presented in article conclusion about the temperature range of the recrystallization beginning at 600-700°C was not accurate. Based on the *in-situ* neutron diffraction analysis results presented in Chapter 6, it is possible to clarify the temperature range of the beginning of the recrystallization process for the PBF CrFeCoNi alloy as about 800°C. At the temperature of 700°C the coalescence of the cell structure is seen according to the TEM observation. It can be associated with a discontinuous recovery process since the nonuniform grains are observed with the BSE imaging. After annealing at temperature of 800°C and above, the small grains can be recognized as new in the BSE images which can be associated with the continuous recrystallization process. However, to clearly recognize the occurred processes, additional investigations are required since it is challenging in some cases to distinguish recovery and recrystallization processes overlapping at some temperatures. The increase of the microhardness is observed for the short heat treatments up to one hour at 500°C and 600°C which was associated with a reduction of crystal defects possibly on the cellular grain boundaries. The DSC analysis also demonstrates the endothermic peaks at temperatures of 500°C and 600°C. At the same time, the formation of secondary phase (nitrindes), which can contribute to the material strengthening, is observed only after a long HT at 600°C for 21 days.

Contribution: I contributed to the development of the structural and phase analyses of the material, the sample preparation process, the formal analysis, the original draft, the final writing, and editing of the manuscript. I would like to thank all the authors for their valuable contributions to the development of this paper.

Typos:

- Fig. 11c. The right axis should be labeled as "Dislocation density, 10^{14} m^{-2}".

- Fig. 8. The TEM images were obtained from the sample plane transversal to the building direction.
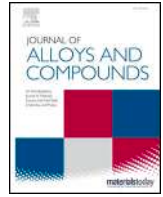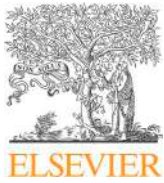
Phase and structural changes during heat treatment of additive manufactured CrFeCoNi high-entropy alloy

Yulia O. Kuzminova [a,*], Egor A. Kudryavtsev [b], Jae-Kyung Han [c], Megumi Kawasaki [c], Stanislav A. Evlashin [a]

[a] Center for Design, Manufacturing & Materials, Skolkovo Institute of Science and Technology, Moscow 121205, Russia
[b] The Joint Research Center of Belgorod State National Research University «Technology and Materials», Belgorod 308015, Russia
[c] School of Mechanical, Industrial & Manufacturing Engineering, Oregon State University, Corvallis, OR 97331, USA

ARTICLE INFO

ABSTRACT

Additive manufacturing (AM) of high-entropy alloys (HEAs) is a new challenge in the Material Science and Advanced Manufacturing fields. In the AM processing procedure, heat treatments after fabrication are often beneficial to stabilize microstructure and properties, while limited reports are available for AM HEAs. In the current study, the effect of a post-printing heat treatment at 400–1000 ℃ for 24 h and for 21 days on the changes in structures and phase compositions of an AM CrFeCoNi alloy prepared by the laser powder bed fusion AM technique is presented to better understand a heat treatment-microstructure-property relationship of the AM HEA. Heating up to 600 ℃ demonstrated the polygonization process in the alloy. Grain growth was observed in the alloy upon heating over 700 ℃, while a preferred texture is observed along the build direction after annealing at 900 ℃ for 24 h. The formation of the secondary phase was revealed, and it is associated with the impurities of the initial CrFeCoNi powder. The AM CrFeCoNi system demonstrates excellent phase stability inthe solid solution for all annealing temperatures.

© 2021 Elsevier B.V. All rights reserved.

1. Introduction

High-entropy alloys (HEAs) have received great attention in materials science due to their new alloy-design approach in comparison with the conventional alloy developments. Earlier terminology of HEA was used for expressing a single solid solution [1,2]. However, Miracle and Senkov reviewed that the essential group of HEAs contains at least two phases [3]. The presence of secondary phases provides a tangible impact on the mechanical and physical properties of HEAs. For example, a B2/body-centered cubic (bcc) phase formed by the presence of Al increases the strength characteristics [4–6] as well as the thermal and electrical properties [7] in AlCoCrFeNi alloys. Moreover, precipitations of the σ-phase nucleated at elevated temperatures of 600–800 ℃ increase strength in $Al_{0.5}CoCrFeMnNi$ and CoCrFeMnNi alloys [8,9]. A detailed investigation in the phase stability of a CoCrFeMnNi alloy demonstrated the formation of a Cr-rich bcc phase, Fe-Co phase, and Ni-Mn $L1_0$ structure at a temperature range of 500–600 ℃ [9–11]. A stable face-centered cubic (fcc) solid solution of a CoCrFeMnNi alloy is observed only at temperatures higher than 800 ℃ [11], while an ultrafine-grained CoCrFeNi alloy without Mn provides a stable solid solution after heating up to ~730 ℃ [12]. By contrast, Sathiyamoorthi et al. observed the evolution of Cr_7C_3 particles in a CoCrFeNi alloy at 600 ℃ up to 1000 ℃ [13] and the observed phase was expected as the σ-phase [14].

HEAs are actively constructed through the application of the modern manufacturing techniques such as Additive Manufacturing (AM) [15,16]. For the AM process, post-printing heat treatment of the as-built materials is often applied to remove residual stresses, but it leads to structural changes including recrystallization and secondary phase formations [17–19]. Synthesis of CoCrFeMnNi alloys is common by the AM process due to their nature with a ductile fcc structure as matrix, which provides stable printability [19–21]. A CrFeCoNi alloy also demonstrates the same or even better properties than the five-component alloy [22–25]. The four-component system is actively explored for composition modification by the AM process [26,27]. However, the results obtained from structural and phase analyses are contradictory for the quaternary CoCrFeNi alloy, while the microstructural and phase thermal stabilities are well investigated for the CoCrFeMnNi alloys. Therefore, a comprehensive understanding of the influence of temperature in the post-printing

---

* Correspondence to: Skolkovo Institute of Science and Technology, Bolshoy Boulevard 30, bld. 1, Moscow 121205, Russia.
E-mail address: yulia.kuzminova@skoltech.ru (Y.O. Kuzminova).

Table 1
The chemical composition of CrFeCoNi powder in wt%.

Cr	Fe	Co	Ni	O	N	C
24.65	25.09	25.47	24.55	0.129	0.095	0.015

heat treatment on CoCrFeNi alloy is required for the development of the desirable HEAs having stable structure produced by the current AM techniques.

Accordingly, the present research demonstrates a comprehensive study of structural evolution during post-printing heat treatment of an AM CrFeCoNi alloy over a wide temperature range of 400–1000 °C.

2. Material and methods

2.1. Material

The CrFeCoNi powder (JSC Polema, Russia) with purity of > 99.7 wt% obtained through a spraying technique was used in the study. Table 1 summarizes the full chemical composition of the powder. Fig. 1 presents (a) the low and (b) high magnifications of the powder morphology. According to previous powder analysis, the particle size distribution poses in a range of 10–60 μm with average size of 27 μm [23]. The particles were predominantly spherical, while some particles had irregular shapes.

2.2. Printing process

The CrFeCoNi alloy was performed using the widely used laser powder bed fusion (L-PBF) additive manufacturing technique. TruPrint 1000 metal 3D printer (TRUMPF) was used in the current work to manufacture the samples with the selected printing process parameters according to the results from the previous study [18]. A full list of the applied parameters is shown in Table 2. The samples were printed with the chess X-Y scan strategy with a square side of 4 mm (detailed information of the applied scan strategy is described

Table 2
A list of the applied printing process parameters.

L-PBF parameter	Values
Laser power	150 W
Laser spot diameter	55 μm
Hatch spacing	80 μm
Layer thickness	20 μm
Laser scan speed	600 mm/s
Gas speed (Ar)	2.5 m/s
Oxygen level	< 0.3 at%
Pressure in chamber	1 bar

elsewhere [28]). Totally, 10 cylindrical samples were printed with a diameter and a height of 10.0 mm and 10.0 mm, respectively. The printing process was conducted without platform preheating.

2.3. Heat treatment process

The printed samples were annealed at different temperatures in the range of 400–1000 °C with a step of 100 °C in air. The cylindrical samples were disposed of in the furnace SNOL 6.7-1300 (AB UMEGA GROUP) preheated to the required temperature. Each sample was annealed for 24 h with the following cooling in water. Additionally, the long heat treatment in air was applied to the as-built samples at temperatures of 600 and 700 °C for 21 days.

2.4. Differential scanning calorimetry

Thermal stability of the CrFeCoNi powder and the as-built CrFeCoNi sample was studied using differential scanning calorimetry (DSC) analysis using the thermal analyzer STA 449 F3 Jupiter (NETZSCH) with a heating speed of 20 K/min up to 900 °C in Ar atmosphere.

2.5. Microhardness testing

Top sample surfaces were prepared for the microhardness tests with the 2000-grit SiC papers. A Vickers microhardness testing
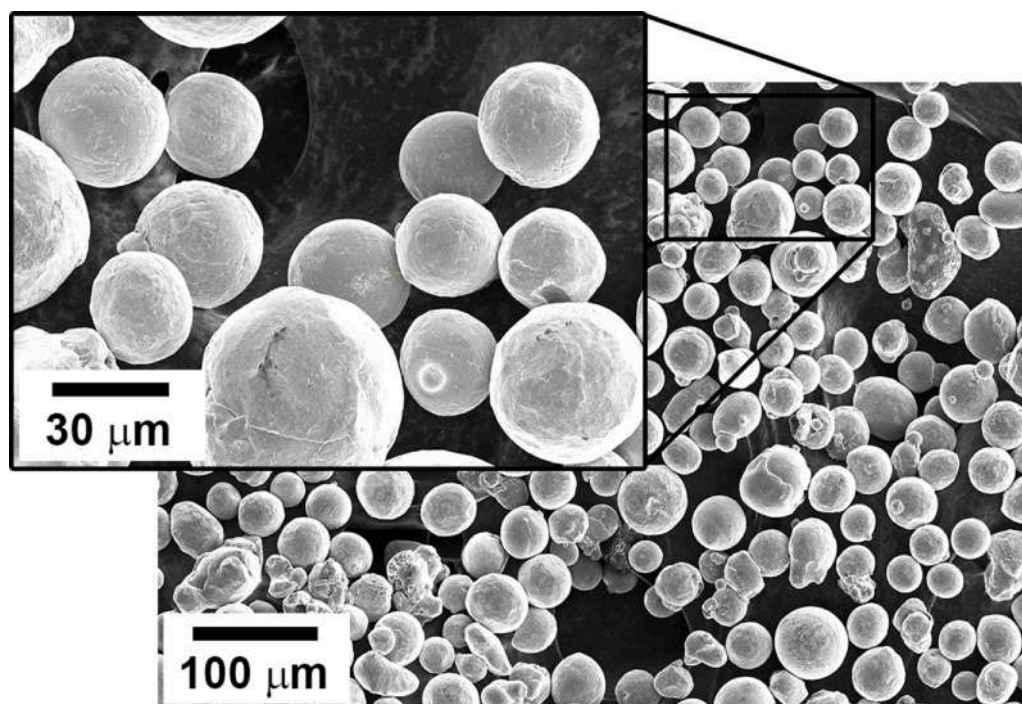

Fig. 1. SEM images of the CrFeCoNi powder at low and high magnifications.

machine ITV-1-AM (Metrotest, Russia) was used for the micro-hardness tests under a load of 300 g for at least 10 measurements per sample.

2.6. Structural and phase analyses

Structural analysis was performed using a scanning electron microscope Quattro S (Thermo Fisher Scientific Inc., USA) equipped with an energy dispersive X-ray (EDX) detector. The samples were cut perpendicularly to the build direction, ground using the SiC grinding papers up to 2000-grit, and polished with a diamond suspension (up to 3 μm) and silica oxide suspension (up to 40 nm). A transmission electron microscope (TEM) JEM-2100 (JEOL, Japan) was used for the microstructural and phase analyses with the accelerating voltage of 200 kV. The samples were prepared by cutting transversely to the build direction and thinned up to 100 μm using the SiC grinding papers. The mixture of 95% CH_3COOH and 5% $HClO_4$ at the 25 V potential was applied for the twin-jet electropolishing using TenuPol5 machine (Struers, Denmark). To minimize the edge effect, all structural investigations were made in the sample centers. The analysis of light elements was performed using determinators LECO TC-136 and LECO SC-144 (LECO Corporation, USA). The structural calculations from images were made using the open source software ImageJ developed by National Institute of Health (USA).

Bruker D8 ADVANCE (Bruker, USA) diffractometer with CoKα radiation (wavelength = 1.79026 Å) was applied for performing the X-ray diffraction (XRD) analysis. The top surfaces of the samples was polished with the 2000-grit SiC grinding paper, polished with the final silica oxide suspension of 40 nm, and electropolished with LectroPol-5 (Struers, Denmark) using a solution of 900 ml C_4H_9OH + 100 ml $HClO_4$ at the ~28 V potential. The XRD patterns were obtained in the 2θ range from 47°–125° with a step size of 0.07° and an incremental time of 2.0 s.

3. Results

3.1. Thermal analysis and hardness evolution of CrFeCoNi alloy

Fig. 2 presents the DSC traces from 200 ℃ to 900 ℃ for the powder and the bulk as-built samples of the CrFeCoNi alloy. The curve for the as-built sample has two endothermic peaks at ~500 ℃ and ~610 ℃ overlapping each other. The first peak begins at 400 ℃ with a peak at 500 ℃, and it switches to the next peak with the
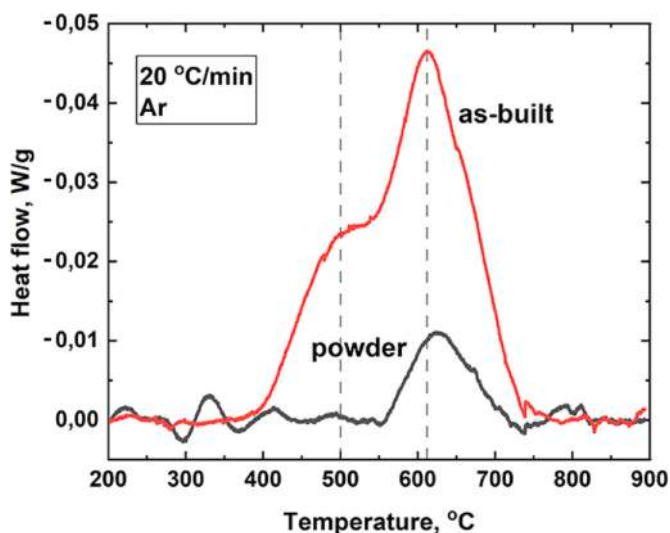
Fig. 2. DSC thermograms obtained for the powder and as-built sample of AM CrFeCoNi at heating rate 20 ℃/min in an argon atmosphere.
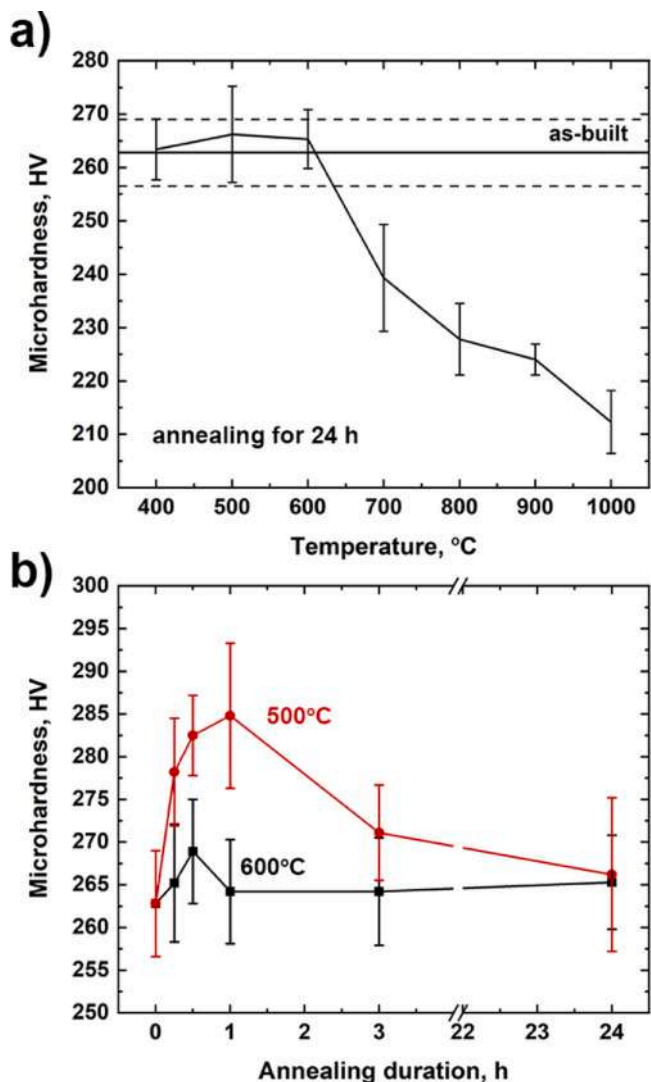
Fig. 3. Effect of (a) temperature and (b) duration of annealings at 500 and 600 ℃ on microhardness of AM CrFeMnNi alloy. The microhardness of as-built CrFeMnNi alloy in Fig. 3a is presented as the horizontal line and its standard deviation error as dotted lines.

highest at 610 ℃ and a finish at 740 ℃. The powder sample shows only one peak starting at 550 ℃ and a finish at 740 ℃, where the single peak seems consistent with the second peak of the as-built sample but with less intensity.

The connected first and second peaks of the exothermic peaks may be attributed to the recovery and recrystallization of the as-built CrFeCoNi alloy. Specifically, the first peak is related to the recovery process. The second peak for the as-built sample and the only distinguishable peak for the powder are associated with the recrystallization process. The highly strained as-built sample may provide the thermal peak shifting to lower temperatures in comparison to the powder sample. It is worth noting that an ultrafine-grained conventionally-manufactured CrFeCoNi alloy demonstrated the exothermic DSC peaks at 407 ℃ and 597 ℃ [12]. Considering the highly strained ultrafine-grained condition leading to the lower DSC peaks, the present as-built CrFeCoNi alloy demonstrated reasonable thermal characteristics. The integration of the thermal peak area yields 4.8 J/g for the powder and 6.8 J/g and 22.5 J/g for the first and the second peaks, respectively, for the as-built sample according to Gaussian peaks fitting.

Fig. 3 shows the effect of (a) annealing temperature for 24 h of heating and (b) duration of annealings at 500 and 600 ℃ for 24 h on

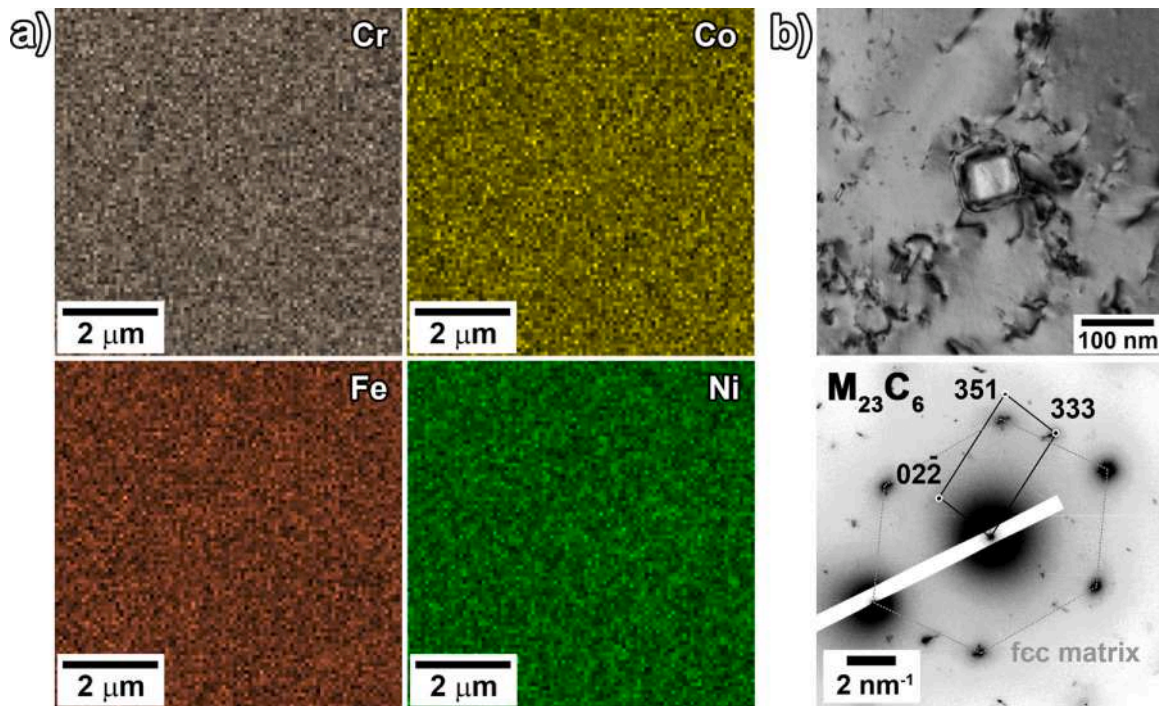**Fig. 4.** (a) The homogeneous element distribution and (b) TEM image of $M_{23}C_6$ precipitate with a corresponding diffraction in the as-built CrFeCoNi alloy. (For interpretation of the references to color in this figure legend, the reader is referred to the web version of this article.)

microhardness of the AM CrFeCoNi alloy. Hardness of the as-built sample before annealing is ~263 HV that is denoted with a solid horizontal line with the error values with the dotted-lines in Fig. 3a. After annealing at 400 °C, the hardness is similar compared with the as-built sample, and it reaches 267 HV at 500-600 °C which is higher than the as-built condition. Thereafter, hardness showed a continuous drop towards ~212 HV with increasing annealing temperature to 1000 °C. The short annealing at 500 °C increases the material hardness which achieves the highest value of ~285 HV after 1 h and further decreases toward 267 HV after 24 h, Fig. 3b. The hardness measurements during annealing at 600 °C demonstrate the highest microhardness value after 30 min and a slight decrease after 1 h, which is then maintained consistent up to 24 h of annealing.

3.2. Microstructural evolution upon the annealing

Fig. 4 represents (a) the homogeneous element distributions taken by EDX analysis with no proof of secondary phase in the as-built CrFeCoNi alloy, while (b) the TEM image with corresponding TEM diffraction is indicating a presence of nano-scale $M_{23}C_6$ precipitates [29] in the material. Fig. 5 consists of the backscattered electron (BSE) images transversally to the build direction (BD) with two different magnifications of (a, b) the as-built CrFeCoNi alloy before annealing and after annealing at (c, d) 400 °C and (e, f) 500 °C for 24 h, and the TEM images of the CrFeCoNi alloy in (g) an as-built condition and (h) after annealing at 400 °C. The as-built sample demonstrates the bimodal grain size distributions (Fig. 5a) where there are coarse grains with lengths of ~50 μm and widths of ~8 μm elongated transversally to the moving of the melt pool and a fine-grained structure between the neighboring melt tracks. The domains in the fine structure consist of subgrains (Fig. 5b) where a cellular substructure consists of elongated subgrains having a width of ~450 nm and a length of ~700 nm (Fig. 5g). Such cellular structure is responsible for higher strength characteristics in AM materials [30–32]. Note that the subgrains form a columnar structure following the build direction, where the elongation indicates their

growth oblique to the build direction [33]. The microstructure remained reasonably consistent after annealing at 400 °C (Fig. 5c) where both elongated and fine grains are still visible and the consistent substructure with average size of ~480 nm is observed with the formation of dislocation walls (Fig. 5d and h). After annealing at 500 °C for 24 h, the square domains with sizes of ~35 μm appear and the elongated structure appears to be ambiguous (Fig. 5e), while the cell substructure after annealing at 500 °C remains consistent with the materials in as-built and as-annealed at 400 °C (Fig. 5f).

Fig. 6 shows the microscopic images of the AM CrFeCoNi alloy after annealing at (a, b) 600 °C, (c, d, e) 700 °C, and (f) 800 °C for 24 h. Annealing at 600 °C leads to the polygonization process. In practice, the polygonized domains with smooth borders appear next to the fine structure (Fig. 6a), while the cellular substructure with cells of ~450 nm is formed within the domains (Fig. 6b). Note, the size of such domains having the length of ~55 μm and thickness of ~7 μm is similar to as-built structure. An increase in the annealing temperature towards 700 °C shows recrystallized grains in the entire fine grain regions with average size of ~1.5 μm, while the melt track with the elongated grains is inherited in some local regions (Fig. 6c). In higher magnification, secondary phase precipitates are observed at grain borders and these are denoted by white arrows (Fig. 6d). The TEM image presents a degradation of cellular structure and dislocation-free grains in the regions where recrystallization occurs (Fig. 6e). The dislocation walls of the substructure are degraded, and, instead, the dislocations migrate to grain borders and some subgrains coalesce. The BSE image of the AM CrFeCoNi alloy annealed at 800 °C reveals the further developed recrystallization process and the impedance of the grain borders coalescence by the secondary phase precipitates that are marked by white arrows (Fig. 6f). After 800 °C annealing, the grain size of the substructure is in the range of 0.5–3.3 μm. It should be mentioned that due to high irregularity of the microstructure after annealing at 700 and 800 °C, the estimation of the precise grain sizes is complicated.

Fig. 7 presents the BSE images of the AM CrFeCoNi alloy followed by annealing for 24 h at (a) 900 °C and (b, c) 1000 °C, and (d) a TEM
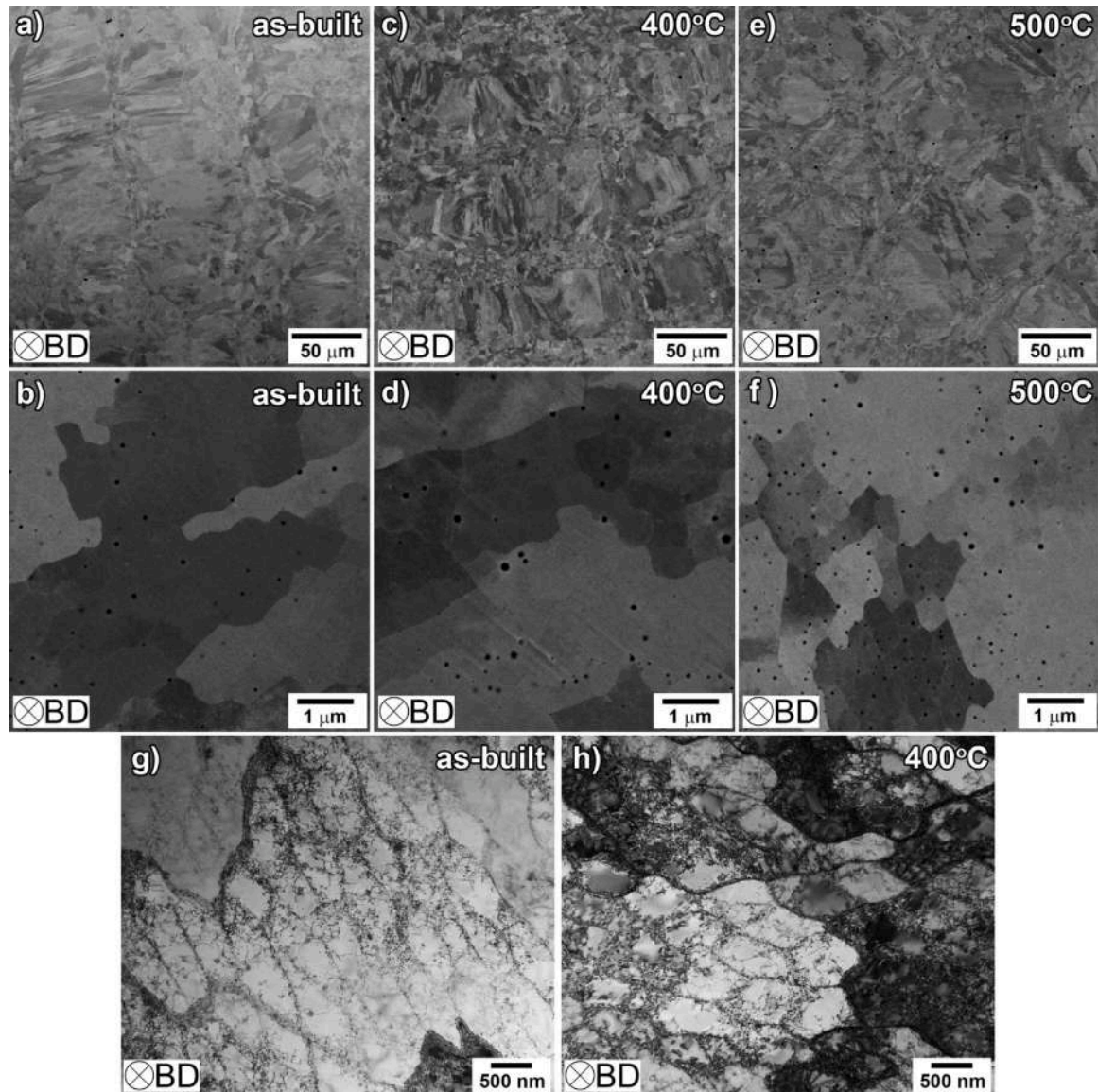
Fig. 5. BSE images of (a, b) as-built CrFeCoNi alloy and after annealing at (c, d) 400 and (e, f) 500 ℃ for 24 h and TEM images of (g) as-built and (h) annealed at 400 ℃ CrFeCoNi alloy.

image of the as-annealed alloy at 900 ℃. After annealing at 900 ℃, newly formed large grains with size of 5–10 μm are visible in the formally fine-grained region (Fig. 7a). As seen in the depicted image in Fig. 7a, the formation of recrystallized small grains also occurs (marked by white arrows). The domain walls are formed by the dissolved subgrain borders consisting of dislocations, which are visible in the TEM micrographs where the dissolved subgrain borders promote dislocation pile-ups and intragranular dislocations are visible in the observed region of the alloy after annealing at 900 ℃ (Fig. 7d). After 900 ℃ annealing, the average size of microstructure is ~1260 nm. The bimodal microstructure is still observed after annealing at 1000 ℃ in the AM CrFeCoNi alloy (Fig. 7b), while the high magnification micrograph shows a replacement of the fine structure to the equiaxed recrystallized grains with sizes of ~0.5–2.5 μm (Fig. 7c).

In previous works, the precipitates observed in a CrFeCoNi microstructure after annealing at 750 ℃ and 800 ℃ are considered as the σ-phase [18,23]. In order to examine detailed structure of the secondary phase in the alloy heated at different temperatures and treatment time, TEM diffraction analysis was performed for the alloy

after annealing for 24 h. Fig. 8 shows TEM diffractions for the precipitates observed in the AM CrFeCoNi alloy after annealing at (a) 700 ℃ and (b) 900 ℃. The analysis reveals that the consistent M_2N structure [34] presents in both samples. The presence of the secondary phase is further confirmed by a long-term heat treatment at 700 ℃ for 21 days leading to the coarsening of the precipitates in the as-built CrFeCoNi alloy and it is available by EDX analysis as shown in Fig. 9a. It was determined that the precipitates are rich in Cr (up to 50 at%) with an equal value of other elements and high values of N and O. Table 3 presents the detailed composition of spots presented in Fig. 9a. Moreover, the as-built CrFeCoNi alloy was also heat treated at 600 ℃ for 21 days to evaluate the presence of the secondary phase with the M_2N structure during the recrystallization process at 600 ℃, and a BSE image of the CrFeCoNi sample is shown in Fig. 9b. The formation of Cr-rich precipitates were visible along grain boundaries after the long heat treatment at 600 ℃. Note that the formation of the secondary phase may affect the recrystallization behavior of the as-built CrFeCoNi alloy. The analysis of N content was performed using a combustion method due to the low effectiveness of EDX method for the analysis of light elements. As it was presented in
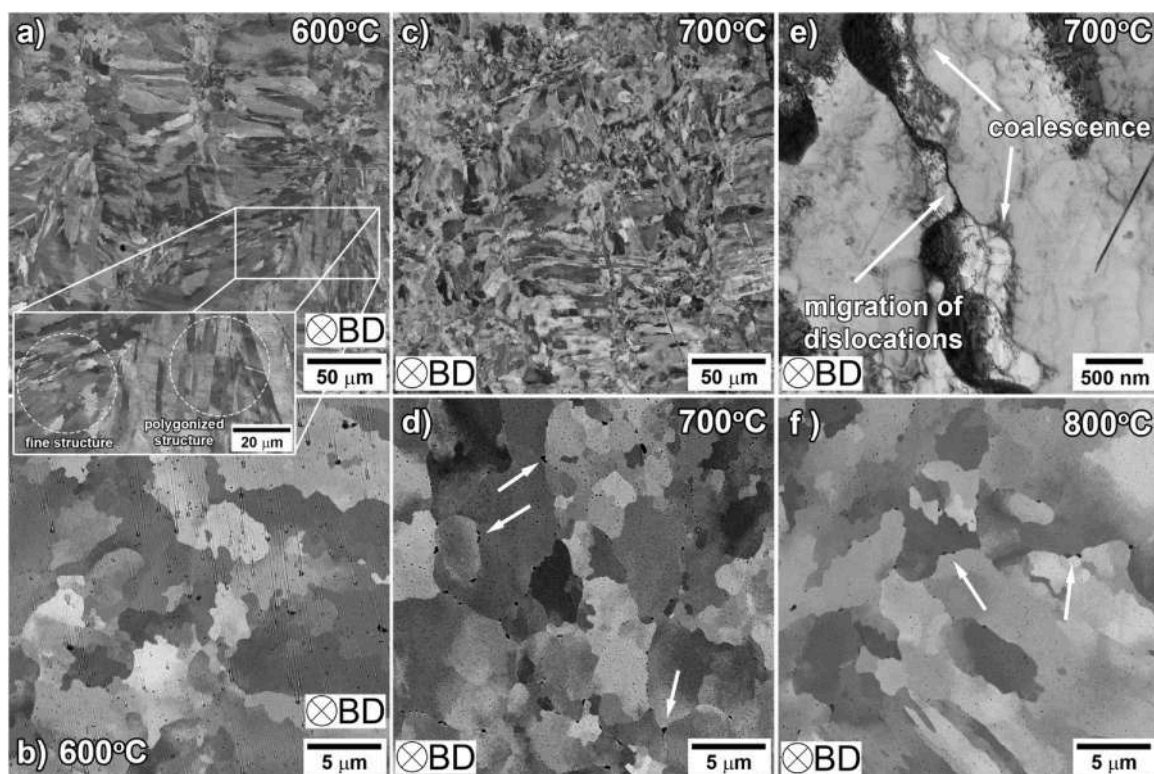
Fig. 6. The images of CrFeCoNi structures after annealing at temperatures of (a, b) 600 °C, (c, d, e) 700 °C, and (f) 800 °C. All images are BSE except the 6e which is represented as a TEM micrograph.
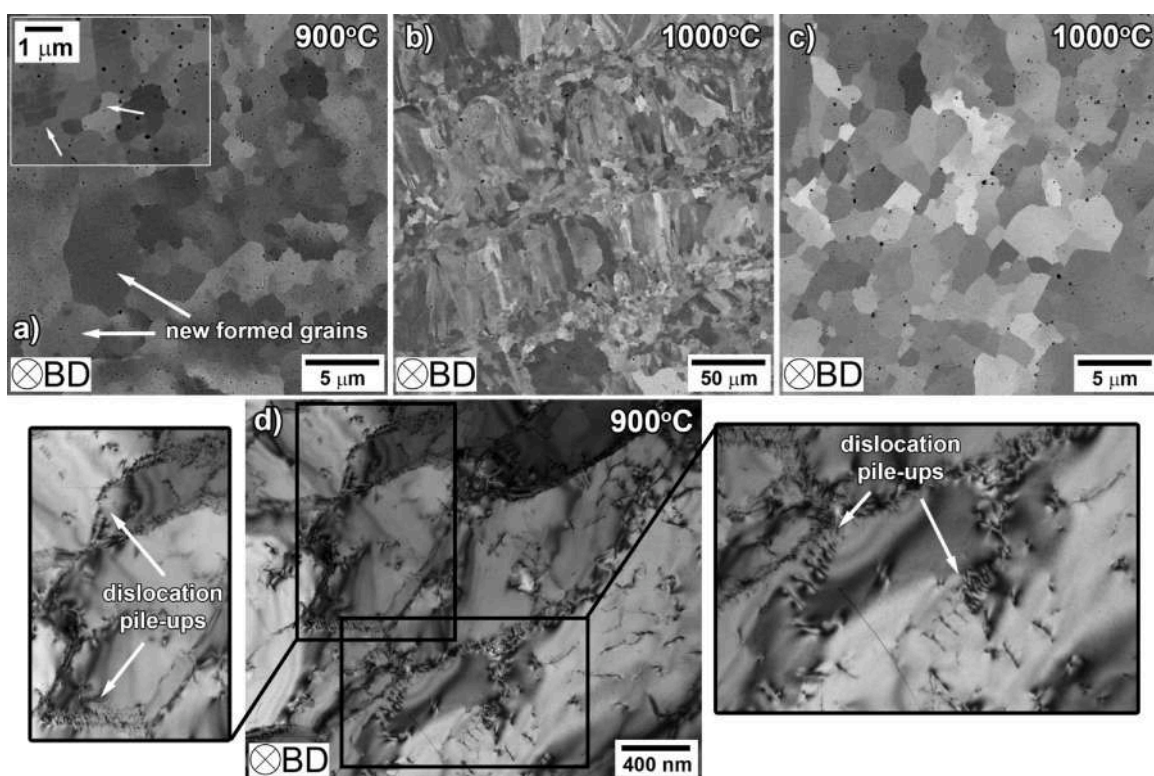
Fig. 7. BSE images of AM CrFeCoNi alloy after annealing at (a) 900 and (b, c) 1000 °C and (d) the TEM image of as-annealed at 900 °C CrFeCoNi alloy.
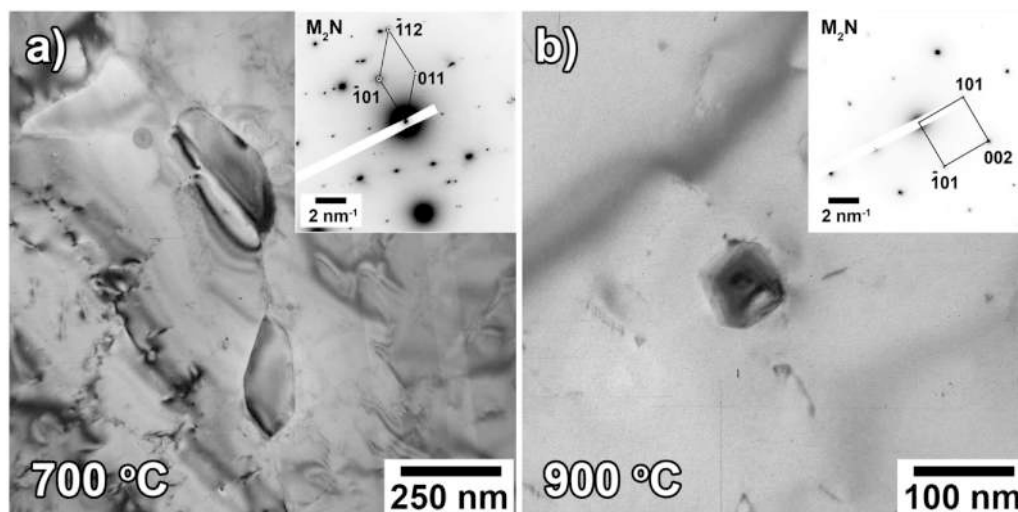
Fig. 8. TEM diffraction of precipitates found at the AM CrFeCoNi after annealing at (a) 700 and (b) 900 °C.
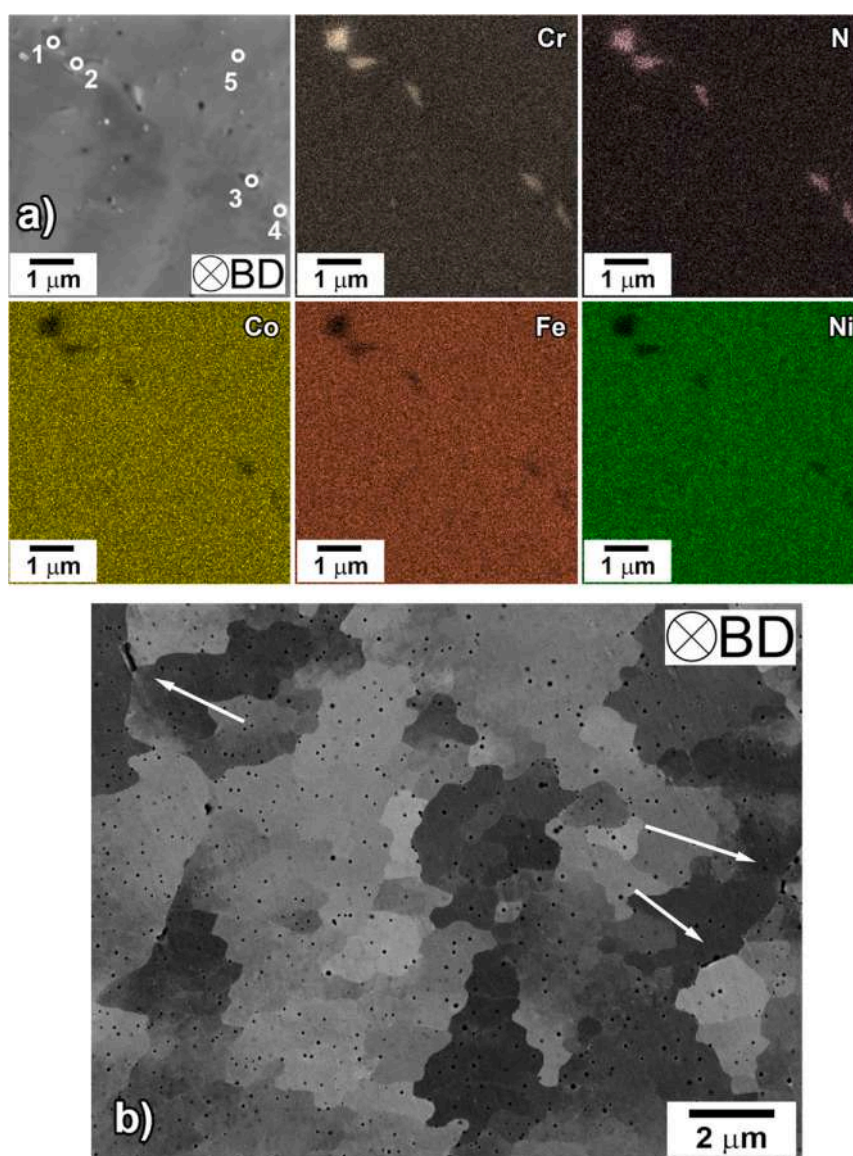
Fig. 9. (a) EDX result of AM CrFeCoNi alloy annealed at 700 °C for 21 days; (b) BSE image of AM CrFeCoNi alloy annealed at 600 °C for 21 days. (For interpretation of the references to color in this figure legend, the reader is referred to the web version of this article.)

Table 3
The chemical composition (in wt%) of CrFeCoNi alloy annealed at 700 °C for 21 days estimated with EDX. The number of points corresponds to the locations with the consistent numbers in Fig. 9a.

	C	O	N	Cr	Fe	Co	Ni
spot 1	7.42	**13.53**	**4.76**	**48.20**	9.79	8.61	7.69
spot 2	7.60	**11.94**	**4.28**	**40.10**	13.08	12.07	10.93
spot 3	6.58	**10.36**	**4.28**	**33.92**	16.01	15.12	13.73
spot 4	7.45	**9.13**	**4.16**	**29.98**	17.33	16.44	15.51
spot 5	7.32	1.22	2.89	22.73	22.77	21.99	21.08

Table 1, 0.095 wt% of N in the powder was determined. There is relatively the same content of N (~0.085 wt%) in the printed samples before heat treatment and after annealing at 700 °C for 24 h as well as 21 days. After printing, the contents of O and C in the material also drop toward ~0.115 and ~0.004 wt%, respectively, and stay at approximately the same level after the annealing at 700 °C up to 21 days.

Fig. 10 presents (a) the X-ray profiles of the powder, the as-built CrFeCoNi alloy before and after annealing at 400, 700, and 900 °C for 24 h and the BSE images of CrFeCoNi alloy at (b) as-printed and (c) as-annealed at 1000 °C for 24 h conditions. According to XRD analysis, all samples present a pure fcc structure, Fig. 10a. The dotted lines indicate the interplanar distance for corresponding planes for the crystal structure with a lattice parameter of 3.58 Å. In contrast to compositional analysis, no additional phases such as $M_{23}C_6$ precipitates and Cr-rich precipitates with M_2N structure were determined both before and after annealing due to their small contents below ~5 vol%, which is the XRD detection limit. Only the powder profile reveals the dominant (111) peak, while all other profiles for as-built samples demonstrate the strong texture of < 100 > and < 110 > toward the build direction. It is reported for the 316l stainless steel having an fcc structure the < 110 > crystal texture alignments with the build direction and the < 100 > crystal texture with the laser track [33]. In the current study with the CrFeCoNi alloy, the difference in the XRD peak intensity is associated with the texture variety between the < 100 > and < 110 > along the printed sample heights, and the tendency is maintained after annealing at 900 °C for 24 h. As can be seen in Fig. 10b and c, the preferable texture is observed even after 1000 °C annealing for 24 h.

4. Discussion

4.1. Structural evolution

DSC analysis demonstrates two endothermic peaks for the as-built CrFeCoNi alloy at 500 and 610 °C. The first peak is associated with the recovery process in the material, which agrees with the results of SEM analysis revealing no structural changes up to 600 °C. The second DSC peak at 610 °C ending at 740 °C is associated with the following two processes. The first process is related to the beginning of the recrystallization of the material. At 700 °C, the grains grow and degradation of dislocation walls are observed in the material. The second process is associated with the secondary phase formation, where TEM and EDX analyses demonstrated the appearance of the Cr-rich precipitates with M_2N structure at the temperature range of 700–800 °C after heating for 24 h. It should be noted that the long heat treatment at lower temperature can also form the nitrides in CrFeCoNi alloy, as shown in Fig. 9b. Thus, the contributions of the recrystallization process and the secondary phase formation process to the second DSC peak can be influenced by the heat treatment conditions. Note, Sathiyamoorthi et al. performing the DSC analysis on mechanically alloyed CoCrFeNi powder observed the exothermic peak at 600 °C, which was associated with the appearance of Cr_7C_3 precipitates [13]. In the present study, the carbides with $M_{23}C_6$ structure were observed in the as-built condition (Fig. 4b). Shun and Du considered the decomposition of the Cr_7C_6 carbide to $Cr_{23}C_6$ in $Al_{0.3}CoCrFeNiC_{0.1}$ alloy at temperatures of 800–1000 °C [35]. The presence of both carbide types is possible in the current AM CrFeCoNi. However, in contrast to the studies [13,35], the present XRD analysis failed to reveal any additional phases formation and decomposition except the main fcc structure. Further studies are required for the significance of the small volume of different secondary phases to the recrystallization process in the AM CrFeCoNi alloy.

Nevertheless, structural changes with heating of the AM CrFeCoNi alloy can be visible by utilizing the XRD line profiles. The obtained XRD line profiles were analyzed using a William-Hall (W-H) method. The W-H plots with the full width at half maximum (FWHM) against a scattering vector for the CrFeCoNi powder and the AM CrFeCoNi alloy before and after annealing at 400, 700, and 900 °C are presented in Fig. 11a. Table 4 summarizes the obtained results by the XRD analysis as well as subgrain size and dislocation density
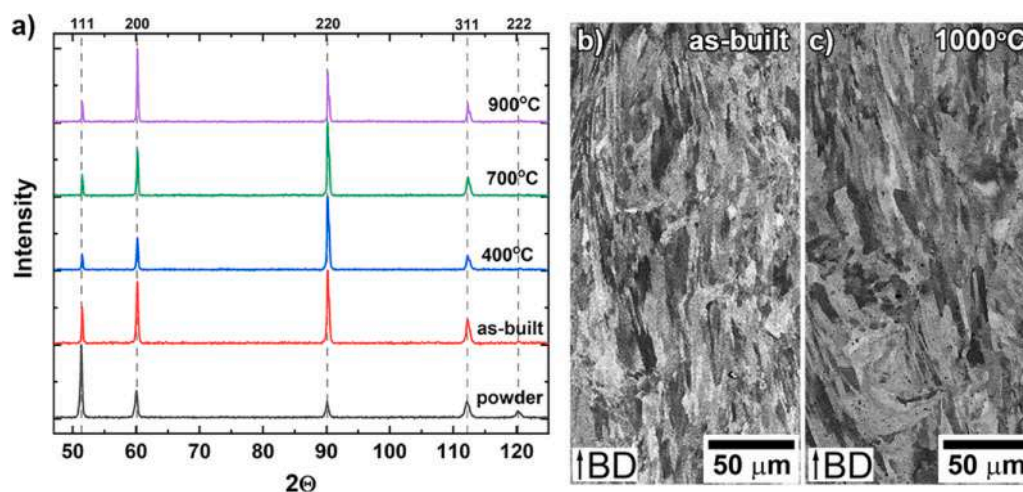

Fig. 10. (a) XRD profiles of the powder and AM CrFeCoNi alloy at as-built condition and annealed at temperatures of 400, 700, and 900 °C for 24 h obtained with a Co-tube; the front view BSE images of (b) as-printed CrFeCoNi alloy and (c) annealed at 1000 °C for 24 h.
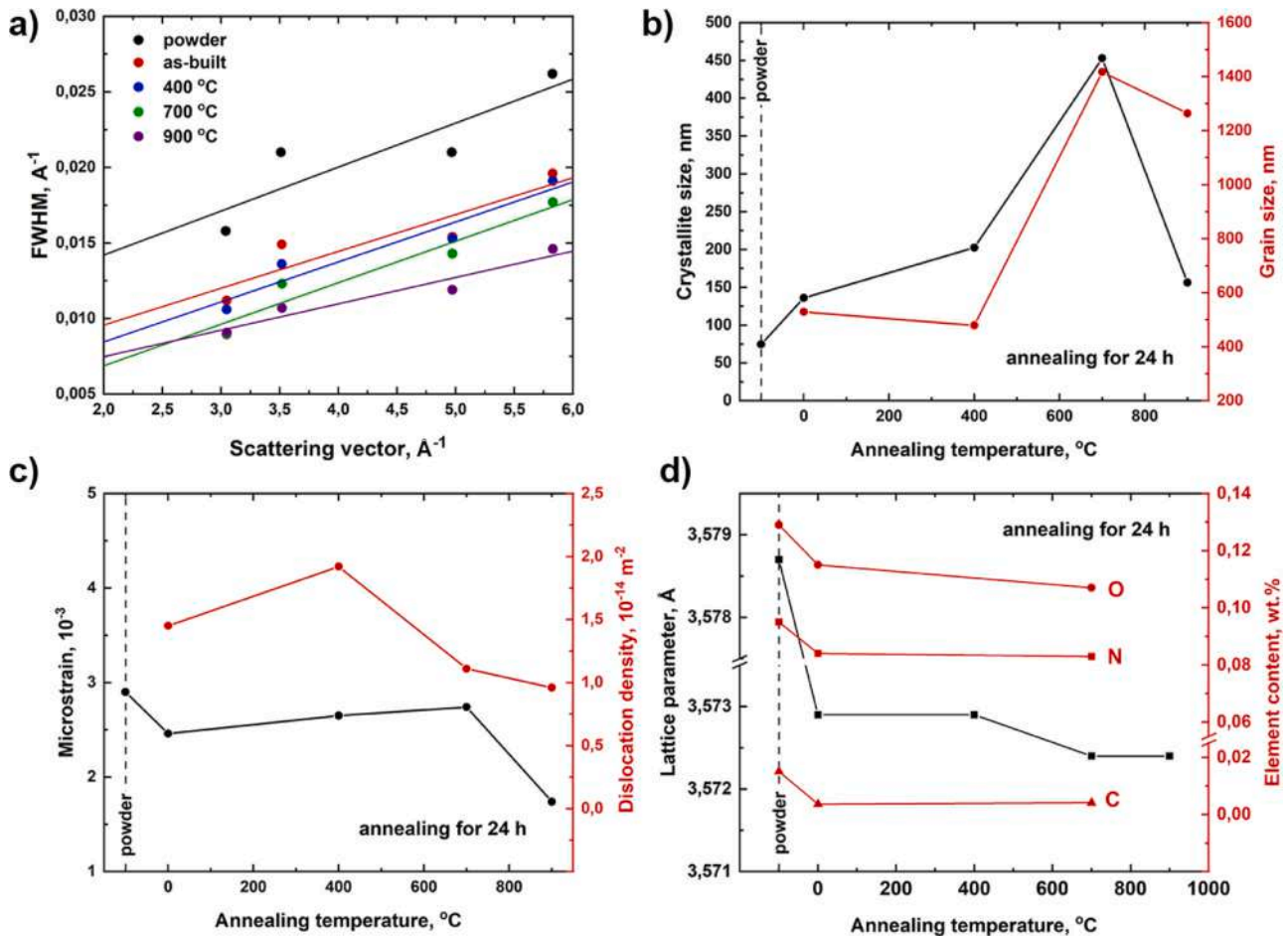
Fig. 11. (a) Williamson-Hall plot with the full width at half maximum (FWHM) against a scattering vector for the CrFeCoNi alloy powder, and the AM CrFeCoNi alloy at as-built and as-annealed at 400, 700, and 900 °C conditions; (b) the crystallite size according to W-H analysis and the grain size and (c) the microstrain calculated from XRD profiles and dislocation density for the powder and AM CrFeCoNi alloy at as-built and as-annealed for 24 h conditions; (d) the lattice parameter and light element content in the CrFeCoNi alloy at different conditions. (For interpretation of the references to color in this figure legend, the reader is referred to the web version of this article.)

Table 4
Results of XRD profiles according to W-H method and calculations from TEM analysis.

	Crystallite size, nm	Microstrain	Lattice constant, Å	Dislocation density, $\times 10^{-14}$ m^{-2}	Grain size, nm
powder	74.56	0.00290	3.5787 ± 0.0010	–	–
as-built	136.05	0.00246	3.5729 ± 0.0025	1.45	530
annealed at 400 °C	202.44	0.00265	3.5729 ± 0.0019	1.92	480
annealed at 700 °C	452.75	0.00274	3.5724 ± 0.0025	1.11	1420
annealed at 900 °C	156.24	0.00174	3.5724 ± 0.0032	0.96	1260

estimated by direct microstructural measurements by TEM for the CrFeCoNi alloy. XRD and TEM analyses demonstrate a consistent tendency for the structural sizes to evolve as shown in Fig. 11b. Specifically, similar structural sizes of crystallite and grain size are observed for the as-built and as-annealed samples heated at 400 °C. These increase dramatically at 400–700 °C, where the recrystallization process proceeds, and slightly decrease at 900 °C, which associates with the appearance of recrystallized small grains in the material at 900 °C. During the recrystallization, following microstructural evolution was observed: i) the cellular substructure transforms to large domains by degradation of the dislocation walls as the subgrain boundaries; and ii) some subgrain boundaries transform to the high-angle boundaries by dislocation absorption. It is worth noting that, although the general trend of the structural sizes is consistent in these two different analyses procedures, the differences often appear due to involved examination sizes, areas,

and volumes where XRD oversees the global sizes and textures, while TEM analysis limits the local microstructures. It is important to note that according to the XRD and microstructure analyses, the texture in the material is observed along BD after annealing at 900–1000 °C (Fig. 10). Only after 1200 °C annealing, the full recrystallized structure with non-textured equiaxed grains is observed for L-PBF CrFeCoNi alloy [36]. Similar to L-PBF 316l stainless steel [33], the L-PBF CrFeCoNi alloy demonstrates relative structural stability at intermediate temperatures of 800–1000 °C, which is associated with the features of L-PBF materials. However, additional investigations are required to better understand the grain boundary transformation during the middle- and high-temperature anneals.

Annealing at 400 °C leads to an increase in dislocation density as shown in Fig. 11c, and it agrees with the thermal analysis revealing the beginning of the "recovery" peak. At this temperature, the dislocations move from dislocation walls in the subgrain bodies

towards more equilibrium states, resulting in a slight increase of its density. There is an apparent decrease in the microstrain during the heat treatment at 700 and 900 °C, and the reduction of the dislocation density is observed at 700 °C (Fig. 11c). These results confirm the occurrence of a recrystallization process with microstructural relaxation followed by grain growth during heating at 700–900 °C in the AM CrFeCoNi alloy.

4.2. Post printing heating and strengthening

In the present work, effect of annealing temperature on microhardness of the AM CrFeCoNi alloy microhardness was demonstrated in Fig. 3a. A slight increase of microhardness is seen at temperatures of 500–600 °C. Schuh et al. showed a similar hardness behavior for an ultrafine-grained CoCrFeMnNi alloy [10], where the maximum hardness was recorded after annealing at 450 °C for one hour. They suggested there are two possible contributions to the strengthening of the alloy. First, the formation of two new secondary phases having the intermetallics character leads to promotion in strength of the ultrafine-grained CoCrFeMnNi alloy, while the mechanical characteristics were not determined due to a difficulty caused by their small size. Second, there is a reduction of dislocation density upon annealing. The same strengthening behavior was observed in the cold-worked CoCrFeMnNi alloy after one hour annealing at 600 °C which was associated with the bcc and σ particles precipitation [9]. In the present study, increasing hardness during annealing at 500–600 °C for 1 h is presented in Fig. 3b, while the annealing at 600 °C formed the secondary phase only after the long-time heat treatment for 21 days, where the cellular structure persists during heating (Fig. 9b). Moreover, according to DSC analysis, the first endothermic peak for as-built CrFeCoNi alloy associated with the recovery process is observed at 500 °C, where the hardness increases by ~22 HV for the first hour of annealing. It allows the statement that strengthening after short annealing (up to one hour) is initiated due to absorption of dislocations participated in the plastic deformation to grain boundaries and annihilation of dislocations without activating the new dislocation sources. This process puts the dislocations to a more equilibrium statement which requires the additional stress effort to continue the plastic flow. It must be significant in the pre-strained materials, such as AM materials and ultrafine-grained materials.

4.3. Secondary phase formation

It was mentioned earlier that two precipitate types having the $M_{23}C_6$ and M_2N structures were determined in the AM CrFeCoNi alloy through TEM analysis. The $M_{23}C_6$ was observed in several studies for the CrFeCoNi systems at different temperatures [13,35], while no study has described the M_2N for a CoCrFeNi alloy. Hung et al. reveal only the main fcc structure without any additional phases for a CoCrFeNi alloy with > 99.9 wt% purity [12]. The purity of > 99.5 wt% in a CoCrFeNi alloy provides the oxides and carbides [13,37,38]. In the present study, the purity of the CoCrFeNi powder is > 99.7 wt% with the N impurity of ~0.1 wt%. The analysis of a pseudo-binary CoCrFeMnNi−N phase diagram shows the formation of a Cr_2N structure in the fcc matrix starting at ~0.024 wt% at room temperature [39]. Other works also demonstrate the Cr_2N formation in CoCrFeMnNi alloy systems with at least ~0.25 wt% N content and its strengthening effect on the material [40–43]. Due to the similar behavior of CoCrFeMnNi and CrFeCoNi alloys, the N content of ~0.1 wt% is enough for the formation of an M_2N structure. Because of the high cooling rate during the printing process, such structure does not appear at the as-built condition, but, instead, it precipitates during post-printing heat treatment at 700–800 °C and stops at

~900–1000 °C. In practice, the decrease of the N content up to ~0.085 wt% occurs in the material at the printing process with no changes during the heat treatments. However, it can be seen that the O and C contents are also lower in the printed material compared with the powder, Fig. 11d, due to a lower surface area for the solid sample compared with powder. The decrease of the CrFeCoNi lattice parameter after the printing process can be associated with lower contents of light elements in material as shown in Fig. 11d. The further decrease of the lattice parameter after annealings at 700 and 900 °C is explained by the nitrides formation and the N depletion of solid solution.

The effect of secondary phase formation on the mechanical properties was discussed in earlier studies [18,23], where the M_2N precipitates were recognized as a σ-phase. It reveals dramatic effects on the ductile characteristics of the material at cryogenic temperatures and on strengthening under cycling loading. However, the formation of the M_2N precipitates observed at 700 °C annealing does not lead to any strengthening in the present study, as seen from the microhardness test results, due probably to its low content in the bulk samples.

From the present experiments, the following three comments should be noted for further studies. First, the presence of N as an impurity element in the powder leads to the formation of M_2N precipitates in the CrFeCoNi alloy at the temperature range of 700–800 °C, influencing the material properties even if the formation of the precipitates is not significant. Second, no σ-phase was observed in the AM CoCrFeNi alloy after heat treatment up to 1000 °C. As was discussed in the study [12], the solid solution can be achieved as a stable state at higher temperatures up to 1000 °C in the AM CrFeCoNi alloy due to the Mn absence, unlike the CoCrFeMnNi system, where the σ-phase formation initiates at temperatures of 600–900 °C [9–11]. Third, the printing process may decrease the N content. Possibly, the N content in the as-built material can be reduced by manipulating the printing process parameters, as it was demonstrated for high nitrogen steel [44].

5. Conclusions

The analysis of the AM CrFeCoNi alloy with post-printing heat treatment at 400–1000 °C for 24 h and longer time duration was performed in the present work. According to the results, the following statements can be made:

1. The recovery process without recrystallization was observed after heating over 400 °C, and the maximum hardness was observed after one hour annealing at 500 °C. Such hardening is due to the polygonization process beginning when dislocations migrate into grain borders.
2. The recrystallization process followed by grain growth began at and above 600–700 °C, where the hardness drops continuously at 700–1000 °C, while the cellular substructure is observed after long-time heat treatment for 21 days at 600 °C. The structural changes continue with increasing annealing temperature, and the strong texture in the material is observed even after annealing at 900–1000 °C for 24 h.
3. The presence of the nitrogen (~0.09 wt%) in the as-built CrFeCoNi sample tends to form Cr-rich precipitates with an M_2N structure on the grain boundaries after annealing at 700–800 °C, which may affect the mechanical properties of the material, while the microhardness measurement failed to demonstrate additional hardening in the present AM alloy. The long-time heat treatment as low as 600 °C can also lead to secondary phase formation.
4. No σ-phase formation was observed at all investigated temperatures, demonstrating the stable solid solution of the CrFeCoNi system at temperatures up to ~1000 °C.

CRediT authorship contribution statement

Yulia O. Kuzminova: Conceptualization, Methodology, Writing – original draft, Investigation. **Egor A. Kudryavtsev:** Investigation. **Jae-Kyung Han:** Formal analysis. **Megumi Kawasaki:** Writing – review & editing. **Stanislav A. Evlashin:** Resources, Writing – review & editing.

Declaration of Competing Interest

The authors declare that they have no known competing financial interests or personal relationships that could have appeared to influence the work reported in this paper.

Acknowledgments

References

[1] J.W. Yeh, S.K. Chen, S.J. Lin, J.Y. Gan, T.S. Chin, T.T. Shun, C.H. Tsau, S.Y. Chang, Nanostructured high-entropy alloys with multiple principal elements: novel alloy design concepts and outcomes, Adv. Eng. Mater. 6 (2004) 299–303, https://doi.org/10.1002/adem.200300567 (+274).

[2] B. Cantor, I.T.H. Chang, P. Knight, A.J.B. Vincent, Microstructural development in equiatomic multicomponent alloys, Mater. Sci. Eng. A 375–377 (2004) 213–218, https://doi.org/10.1016/j.msea.2003.10.257

[3] D.B. Miracle, O.N. Senkov, A critical review of high entropy alloys and related concepts, Acta Mater. 122 (2017) 448–511, https://doi.org/10.1016/j.actamat.2016.08.081

[4] M.A. Hemphill, T. Yuan, G.Y. Wang, J.W. Yeh, C.W. Tsai, A. Chuang, P.K. Liaw, Fatigue behavior of Al 0. 5 CoCrCuFeNi high entropy alloys, Acta Mater. 60 (2012) 5723–5734, https://doi.org/10.1016/j.actamat.2012.06.046

[5] B.B. Bian, N. Guo, H.J. Yang, R.P. Guo, L. Yang, Y.C. Wu, J.W. Qiao, A novel cobalt-free FeMnCrNi medium-entropy alloy with exceptional yield strength and ductility at cryogenic temperature, J. Alloy. Compd. 827 (2020) 153981, https://doi.org/10.1016/j.jallcom.2020.153981

[6] D. Liu, X. Jin, N. Guo, P.K. Liaw, J.W. Qiao, Non-equiatomic FeMnCrNiAl high-entropy alloys with heterogeneous structures for strength and ductility combination, Mater. Sci. Eng.: A 818 (2021) 141386, https://doi.org/10.1016/j.msea.2021.141386

[7] H.-P. Chou, Y.-S. Chang, S.-K. Chen, J.-W. Yeh, Microstructure, thermophysical and electrical properties in AlxCoCrFeNi (0 ≤ x ≤2) high-entropy alloys, Mater. Sci. Eng. B 163 (2009) 184–189, https://doi.org/10.1016/J.MSEB.2009.05.024

[8] T.S. Reddy, I.S. Wani, T. Bhattacharjee, S.R. Reddy, R. Saha, P.P. Bhattacharjee, Intermetallics Severe plastic deformation driven nanostructure and phase evolution in a Al 0. 5 CoCrFeMnNi dual phase high entropy alloy, Intermetallics 91 (2017) 150–157, https://doi.org/10.1016/j.intermet.2017.09.002

[9] M.V. Klimova, D.G. Shaysultanov, S.V. Zherebtsov, N.D. Stepanov, Effect of second phase particles on mechanical properties and grain growth in a CoCrFeMnNi high entropy alloy, Mater. Sci. Eng. A 748 (2019) 228–235, https://doi.org/10.1016/j.msea.2019.01.112

[10] B. Schuh, F. Mendez-Martin, B. Völker, E.P. George, H. Clemens, R. Pippan, A. Hohenwarter, Mechanical properties, microstructure and thermal stability of a nanocrystalline CoCrFeMnNi high-entropy alloy after severe plastic deformation, Acta Mater. 96 (2015) 258–268, https://doi.org/10.1016/J.ACTAMAT.2015.06.025

[11] F. Otto, A. Dlouhý, K.G. Pradeep, M. Kuběnová, D. Raabe, G. Eggeler, E.P. George, Decomposition of the single-phase high-entropy alloy CrMnFeCoNi after prolonged anneals at intermediate temperatures, Acta Mater. 112 (2016) 40–52, https://doi.org/10.1016/j.actamat.2016.04.005

[12] P.T. Hung, M. Kawasaki, J.-K. Han, J.L. Lábár, J. Gubicza, Microstructure evolution in a nanocrystalline CoCrFeNi multi-principal element alloy during annealing, Mater. Charact. 171 (2021) 110807, https://doi.org/10.1016/j.matchar.2020.110807

[13] P. Sathiyamoorthi, J. Basu, S. Kashyap, K.G. Pradeep, R. Sankar, Thermal stability and grain boundary strengthening in ultra fine-grained CoCrFeNi high entropy

alloy composite, Mater. Des. 134 (2017) 426–433, https://doi.org/10.1016/j.matdes.2017.08.053

[14] S. Praveen, B.S. Murty, R.S. Kottada, Alloying behavior in multi-component AlCoCrCuFe and NiCoCrCuFe high entropy alloys, Mater. Sci. Eng. A 534 (2012) 83–89, https://doi.org/10.1016/j.msea.2011.11.044

[15] C. Juan, M. Tsai, C. Tsai, C. Lin, W. Wang, C. Yang, S. Chen, S. Lin, J. Yeh, Intermetallics Enhanced mechanical properties of HfMoTaTiZr and HfMoNbTaTiZr refractory high-entropy alloys, Intermetallics 62 (2015) 76–83, https://doi.org/10.1016/j.intermet.2015.03.013

[16] H. Chen, A. Kauffmann, S. Laube, I. Choi, R. Schwaiger, Y. Huang, K. Lichtenberg, F. Mu, Contribution of lattice distortion to solid solution strengthening in a series of refractory high entropy alloys, n.d., doi: 10.1007/s11661-017-4386-1.

[17] A. Riemer, S. Leuders, M. Thöne, H.A. Richard, T. Tröster, T. Niendorf, On the fatigue crack growth behavior in 316L stainless steel manufactured by selective laser melting, Eng. Fract. Mech. 120 (2014) 15–25, https://doi.org/10.1016/j.engfracmech.2014.03.008

[18] Y. Kuzminova, D. Firsov, A. Dudin, S. Sergeev, A. Zhilyaev, A. Dyakov, A. Chupeeva, A. Alekseev, D. Martynov, I. Akhatov, S. Evlashin, The effect of the parameters of the powder bed fusion process on the microstructure and mechanical properties of CrFeCoNi medium-entropy alloys, Intermetallics 116 (2020) 106651, https://doi.org/10.1016/j.intermet.2019.106651

[19] R. Li, P. Niu, T. Yuan, P. Cao, C. Chen, K. Zhou, Selective laser melting of an equiatomic CoCrFeMnNi high-entropy alloy: processability, non-equilibrium microstructure and mechanical property, J. Alloy. Compd. 746 (2018) 125–134, https://doi.org/10.1016/j.jallcom.2018.02.298

[20] Y. Chew, G.J. Bi, Z.G. Zhu, F.L. Ng, F. Weng, S.B. Liu, S.M.L. Nai, B.Y. Lee, Microstructure and enhanced strength of laser aided additive manufactured CoCrFeNiMn high entropy alloy, Mater. Sci. Eng. A 744 (2019) 137–144, https://doi.org/10.1016/j.msea.2018.12.005

[21] C. Haase, F. Tang, M.B. Wilms, A. Weisheit, B. Hallstedt, Combining thermodynamic modeling and 3D printing of elemental powder blends for high-throughput investigation of high-entropy alloys – towards rapid alloy screening and design, Mater. Sci. Eng. A 688 (2017) 180–189, https://doi.org/10.1016/j.msea.2017.01.099

[22] Y. Brif, M. Thomas, I. Todd, The use of high-entropy alloys in additive manufacturing, Scr. Mater. 99 (2015) 93–96, https://doi.org/10.1016/j.scriptamat.2014.11.037

[23] Y.O. Kuzminova, D.G. Firsov, S.A. Dagesyan, S.D. Konev, S.N. Sergeev, A.P. Zhilyaev, M. Kawasaki, I.S. Akhatov, S.A. Evlashin, Fatigue behavior of additive manufactured CrFeCoNi medium-entropy alloy, J. Alloy. Compd. 863 (2021) 158609, https://doi.org/10.1016/j.jallcom.2021.158609

[24] W. Zhao, J.-K. Han, Y.O. Kuzminova, S.A. Evlashin, A.P. Zhilyaev, A.M. Pesin, J. Jang, K.-D. Liss, M. Kawasaki, Significance of grain refinement on micro-mechanical properties and structures of additively-manufactured CoCrFeNi high-entropy alloy, Mater. Sci. Eng.: A 807 (2021) 140898, https://doi.org/10.1016/j.msea.2021.140898

[25] D. Lin, L. Xu, Y. Han, Y. Zhang, H. Jing, Structure and mechanical properties of a FeCoCrNi high-entropy alloy fabricated via selective laser melting, Intermetallics 127 (2020) 106963, https://doi.org/10.1016/j.intermet.2020.106963

[26] J. Joseph, T. Jarvis, X. Wu, N. Stanford, P. Hodgson, D.M. Fabijanic, Comparative study of the microstructures and mechanical properties of direct laser fabricated and arc-melted AlxCoCrFeNi high entropy alloys, Mater. Sci. Eng. A 633 (2015) 184–193, https://doi.org/10.1016/j.msea.2015.02.072

[27] M. Li, J. Gazquez, A. Borisevich, R. Mishra, K.M. Flores, Evaluation of microstructure and mechanical property variations in AlxCoCrFeNi high entropy alloys produced by a high-throughput laser deposition method, Intermetallics 95 (2018) 110–118, https://doi.org/10.1016/j.intermet.2018.01.021

[28] A.M. Filimonov, O.A. Rogozin, D.G. Firsov, Y.O. Kuzminova, S.N. Sergeev, A.P. Zhilyaev, M.I. Lerner, N.E. Toropkov, A.P. Simonov, I.I. Binkov, I.V. Okulov, I.S. Akhatov, S.A. Evlashin, Hardening of additive manufactured 316L stainless steel by using bimodal powder containing nanoscale fraction, Materials 14 (2020) 115, https://doi.org/10.3390/ma14010115

[29] A. Bowman, G. Arnold, E. Storms, N. Nereson, The crystal structure of Cr23C6, Acta Crystallogr. Sect. B Struct. Crystallogr. Cryst. Chem. 28 (10) (1972) 3102–3103, https://doi.org/10.1107/S0567740872007526

[30] Y.M. Wang, T. Voisin, J.T. McKeown, J. Ye, N.P. Calta, Z. Li, Z. Zeng, Y. Zhang, W. Chen, T.T. Roehling, R.T. Ott, M.K. Santala, P.J. Depond, M.J. Matthews, A.V. Hamza, T. Zhu, Additively manufactured hierarchical stainless steels with high strength and ductility, Nat. Mater. 17 (2018) 63–71, https://doi.org/10.1038/nmat5021

[31] R. Wu, M. Zaiser, Cell structure formation in a two-dimensional density-based dislocation dynamics model, Mater. Theory 5 (2021) 3, https://doi.org/10.1186/s41313-020-00025-x

[32] R. Wu, D. Tüzes, P.D. Ispánovity, I. Groma, T. Hochrainer, M. Zaiser, Instability of dislocation fluxes in a single slip: deterministic and stochastic models of dislocation patterning, Phys. Rev. B 98 (2018) 054110, https://doi.org/10.1103/PhysRevB.98.054110

[33] T. Voisin, J.-B. Forien, A. Perron, S. Aubry, N. Bertin, A. Samanta, A. Baker, Y.M. Wang, New insights on cellular structures strengthening mechanisms and thermal stability of an austenitic stainless steel fabricated by laser powder-bed-fusion, Acta Mater. 203 (2021) 116476, https://doi.org/10.1016/j.actamat.2020.11.018

[34] J. Cabana, C.D. Ling, J. Oró-Solé, D. Gautier, G. Tobías, S. Adams, E. Canadell, M.R. Palacín, Antifluorite-type lithium chromium oxide nitrides: synthesis, structure, order, and electrochemical properties, Inorg. Chem. 43 (2004) 7050–7060, https://doi.org/10.1021/ic049138z

[35] T.-T. Shun, Y.-C. Du, Age hardening of the Al0.3CoCrFeNiC0.1 high entropy alloy, J. Alloy. Compd. 478 (2009) 269–272, https://doi.org/10.1016/j.jallcom.2008.12.014

[36] Y. Kuzminova, A. Shibalova, S. Evlashin, I. Shishkovsky, P. Krakhmalev, Structural effect of low Al content in the in-situ additive manufactured CrFeCoNiAlx high-entropy alloy, Mater. Lett. 303 (2021) 130487, https://doi.org/10.1016/j.matlet.2021.130487

[37] S. Praveen, B.S. Murty, R.S. Kottada, Phase evolution and densification behavior of nanocrystalline multicomponent high entropy alloys during spark plasma sintering, JOM 65 (2013) 1797–1804, https://doi.org/10.1007/s11837-013-0759-0

[38] S. Praveen, J. Basu, S. Kashyap, R. Sankar, Exceptional resistance to grain growth in nanocrystalline CoCrFeNi high entropy alloy at high homologous temperatures, J. Alloy. Compd. 662 (2016) 361–367, https://doi.org/10.1016/j.jallcom.2015.12.020

[39] Igor Moravcik, Jan Cizek, Larissa dA. Gouvea, Jan Cupera, Ivan Guban, Ivo Dlouhy, Nitrogen interstitial alloying of CoCrFeMnNi high entropy alloy through reactive powder milling, Entropy 21 (4) (2019) 363, https://doi.org/10.3390/e21040363

[40] F. Xiong, R. Fu, Y. Li, D. Sang, Effects of nitrogen alloying and friction stir processing on the microstructures and mechanical properties of CoCrFeMnNi high-entropy alloys, J. Alloy. Compd. 822 (2020) 153512, https://doi.org/10.1016/j.jallcom.2019.153512

[41] D. Edgard, J. Park, B. Straumal, N. Park, Investigation on the precipitate formation and behavior in nitrogen-containing equiatomic CoCrFeMnNi high-entropy alloy, Mater. Lett. 258 (2020) 126806, https://doi.org/10.1016/j.matlet.2019.126806

[42] D. Edgard, J. Park, N. Park, Strengthening of ultrafine-grained equiatomic CoCrFeMnNi high-entropy alloy by nitrogen addition, Mater. Lett. 258 (2020) 126772, https://doi.org/10.1016/j.matlet.2019.126772

[43] M. Klimova, D. Shaysultanov, A. Semenyuk, S. Zherebtsov, G. Salishchev, N. Stepanov, Effect of nitrogen on mechanical properties of CoCrFeMnNi high entropy alloy at room and cryogenic temperatures, J. Alloy. Compd. 849 (2020) 156633, https://doi.org/10.1016/j.jallcom.2020.156633

[44] A. Arabi-hashemi, X. Maeder, R. Figi, C. Schreiner, S. Griffiths, C. Leinenbach, 3D magnetic patterning in additive manufacturing via site-specific in-situ alloy modification, Appl. Mater. Today 18 (2020) 100512, https://doi.org/10.1016/j.apmt.2019.100512

Chapter 4

Fatigue behavior of additive manufactured CrFeCoNi medium-entropy alloy

In this chapter, the fatigue life of the PBF CrFeCoNi alloy is considered since it is one of the important properties of AM materials. The fatigue properties were measured with a frequency of 25 Hz and a stress ratio of 0.1. The printed material at as-built and annealed at 800°C states were tested to analyze the effect of the residual stress removal on the fatigue strength. Additionally, the as-built and machined samples were prepared for tests to estimate the near-surface defect impact on the material life under the cycling loads.

One of the conclusions made in the study was: "The twinning deformation mechanism takes place at the tensile deformation, while dislocation slip dominates at cycling loads of 480 MPa". This conclusion should be clarified since it is not fully correct in this state. The observed deformation slips (Fig. 9a and 9b, Chapter4) were recognized as twins similar to those observed in the CrFeCoNiMn alloy after intensive deformation [58]. However, the TEM analysis is needed to prove this statement. Additionally, Laplanche *et al.* indicated the critical stress of 720 MPa at which twins appear in the CrFeCoNiMn alloy at 77 K [40]. Indeed, they observed twins in the material tensile tested at room temperature after the true stress reached 820 MPa (usually, such stress is reached close to fracture) [40]. The same as Cantor's

alloy, the CrFeCoNi alloy may involve the planar slip deformation mechanism as the main at earlier stages while twinning may appear at the later deformation stages. According to the present results, it can be argued that twins are not observed in the material after cyclic loading up to 480 MPa involving the dislocation slip deformation mechanism only, while the tensile-tested samples may consist of twins, but additional analyses are needed. The near-surface defects play a crucial role in the fatigue life of the PBF CrFeCoNi alloy. Both, as-built and annealed materials, demonstrated a significant increase in fatigue strength after removing the defects. At the same time, the annealing effect on the fatigue properties is more arguable. It predictably decreases the fatigue at the low cycle fatigue zone, but does not improve it at the high cycle fatigue, possibly, due to the nitride formations on the grain boundaries discussed in Chapter 3.

Contribution: I contributed to the development of the structural and phase analyses of the material, the sample preparation process, the mechanical testing, the original draft, the final writing, and editing of the manuscript. I would like to thank all the authors for their valuable contributions to the development of this paper.

Clarification: The tensile and fatigue tests were conducted along the samples produced along the build direction.

Fatigue behavior of additive manufactured CrFeCoNi medium-entropy alloy

Y.O. Kuzminova [a,*], D.G. Firsov [a], S.A. Dagesyan [b], S.D. Konev [a], S.N. Sergeev [c], A.P. Zhilyaev [c,d], M. Kawasaki [e], I.S. Akhatov [a], S.A. Evlashin [a]

[a] Center for Design, Manufacturing & Materials, Skolkovo Institute of Science and Technology, Moscow 121205, Russia
[b] Department of Physics, M. V. Lomonosov Moscow State University, Moscow 119991, Russia
[c] Institute for Metals Superplasticity Problems of Russian Academy of Science, Ufa 450001, Russia
[d] Magnitogorsk State Technical University, Magnitogorsk 455000, Russia
[e] School of Mechanical, Industrial & Manufacturing Engineering, Oregon State University, Corvallis, OR 97331, USA

ARTICLE INFO

ABSTRACT

High-entropy alloys (HEAs) are considered to be prospective materials for operation in harsh environments. These materials often demonstrate high strength during static tests. However, a limited number of studies describe the fatigue properties of HEAs. Most of them focused on the two systems of CoCrFeMnNi or AlCoCrFeNi produced by arc or induction meltings. In this paper, the fatigue behavior of CrFeCoNi medium-entropy alloys (MEAs) produced by additive manufacturing was investigated to extend the understanding of the HEA applications. The fatigue test is conducted at a frequency of 25 Hz, and the stress ratio of 0.1. The changes in fatigue and tensile properties are studied through structural and phase analysis. Special emphasis was placed on evaluating the impact of machining and heat treatment on the fatigue characteristics of the MEA samples.

© 2021 Elsevier B.V. All rights reserved.

1. Introduction

High-entropy alloys (HEAs) demonstrate unique physical and mechanical properties in a wider range of temperatures than the general engineering alloys. In practice, HEAs show excellent strength at ambient temperatures, e.g., a cold-rolled $Al_{0.5}CoCrFeNi$ HEA demonstrates high yield and ultimate strengths of 1284 and 1344 MPa, respectively [1]. Moreover, HEAs containing elements with high melting points have been studied and developed for high-temperature applications. Refractory HEA materials demonstrate high strength at high temperatures [2–4]. The compression yield strengths of MoNbTaW and MoNbTaVW reached the values of 548 and 842 MPa, respectively, and achieved the compression strain of ~15% at a temperature of 1000 °C, while the ductility did not exceed 3% at room temperature (RT) [2].

The basic concept behind the design of HEAs containing five or more principal elements does not guarantee remarkable properties. In practice, mechanical properties of the elevated entropy alloys mostly depended on the element composition rather than the element number. Ternary CoCrNi and quaternary CoCrFeNi and FeMnCrNi medium-entropy alloys (MEAs) demonstrated equal or higher strengths than CoCrFeMnNi HEAs [5,6]. In other words, careful selection of additional elements to MEAs can improve their mechanical properties, such as improved strengths of MEAs by adding a small amount of alloying elements of Al or Nb [7,8]. In addition, the manufacturing procedure also influences the static mechanical properties of HEAs. The yield and ultimate strengths of CoCrFeNi alloys obtained by different fabrication techniques, such as arc melting with further intensive plastic deformation, and additive manufacturing (AM) [9–14], vary from 140 to 600 MPa and from 488 to 695 MPa, respectively.

Most materials are exploited at loads much lower than the yield strength, which does not lead to destruction upon a single load application. For the practical purposes of examining the sustainability of materials, it is essential to understand the behavior of materials under cycling loading. To the best of our knowledge, limited studies are focused on the fatigue properties of HEAs [1,15–21]. More studies are required for better understanding of the fatigue behavior of HEAs produced through different techniques including the modern techniques of AM technologies so as to evaluate the property-processing relationship of HEAs. Influence of the processing routes on the mechanical properties can vary depending on the

---

material. For instance, the ultimate tensile strength of 316L stainless steel produced by AM was reasonably similar to the cast materials [22,23], while the fatigue life of AM non-ferrous alloys is much lower compared to that for conventional analogs due to the formation of voids and defects during the printing process [24,25]. Despite the essential effect of the pore presence in AM materials on fatigue properties, printing parameters influence the material fatigue behavior. The higher fatigue strength was demonstrated for AM 316L and AM 17-4 PH stainless steels printed in a horizontal direction, which correlates with tensile properties [26,27]. Preheating of the build platform reduces the fatigue properties of AM 316L stainless steel due to its effect on microstructure [28]. Moreover, the initial material properties also impact the effect of further post-treatments. Hot-isostatic pressing plays a crucial role in a brittle AM Ti6Al4V alloy improving its fatigue properties, while it reduces the fatigue resistance of a ductile AM 316L stainless steel at low-cycle fatigue (LCF) regime [29]. It should be noted that most of the works considering the fatigue behavior of AM materials are focused on the traditional alloy compositions, while the number of work investigating the fatigue properties of AM HEAs is limited.

In the present work, fatigue properties of CrFeCoNi MEA produced by AM were studied. The research was initiated due to the lack of reports on the fatigue properties of CrFeCoNi alloys, while CrFeCoNi alloys demonstrate excellent mechanical properties at cryogenic temperatures [14] and are used as a base material for the production of CrFeCoNiMn, AlCoCrFeNi, and AlCoCrCuFeNi [5]. In the present study, annealing was applied to the MEA samples to release the residual stress after the manufacturing process. The influence of the heat treatment on the tensile strength and fatigue properties was evaluated for the AM CrFeCoNi alloy.

2. Materials and methods

2.1. Materials

Scanning electron microscopy (SEM) micrographs of the $Cr_{24}Fe_{25}Co_{26}Ni_{25}$ (at%) powder (JSC Polema, Russia) produced by the spraying method and used in the current work are presented at the low and high magnifications in Fig. 1a and b, respectively. A particle size distribution is depicted in Fig. 1a. The size distribution of the MEA powders was in the range from 15 to 65 μm with the average particle size of 32 μm. The particles were predominantly spherical, while some particles had irregular shapes.

2.2. Printing process

The powder bed fusion technique with a laser heat source (L-PBF) was applied to print the MEA samples. A 3D TruPrint 1000 metal printer (TRUMPF Inc., Germany) was used for the process. The processing parameters were chosen according to our previous research [14]. Thus, the processing was operated at the laser power and laser speed of 150 W, 600 mm/s, respectively. The samples were printed with a laser spot diameter of 55 μm, hatch spacing of 80 μm, and a layer thickness of 20 μm. The chess X-Y scan strategy with the square side of 4.0 mm was applied. The shift of the laser pattern between the layers was 2.76 mm and 3.25 mm, along X and Y directions, respectively. The printing process was performed in an argon atmosphere with gas flow velocity of 2.5 m/s and chamber pressure of 1 bar. The level of oxygen did not exceed 0.3 at%. The samples were printed with geometry according to ASTM E8 and ISO 1099:2006(E). All samples were printed in the vertical direction without preheating of the platform.

2.3. Mechanical testing

Half of the AM-built MEA samples were annealed at 800 °C for 12 h, followed by water quenching to remove the residual stress. This
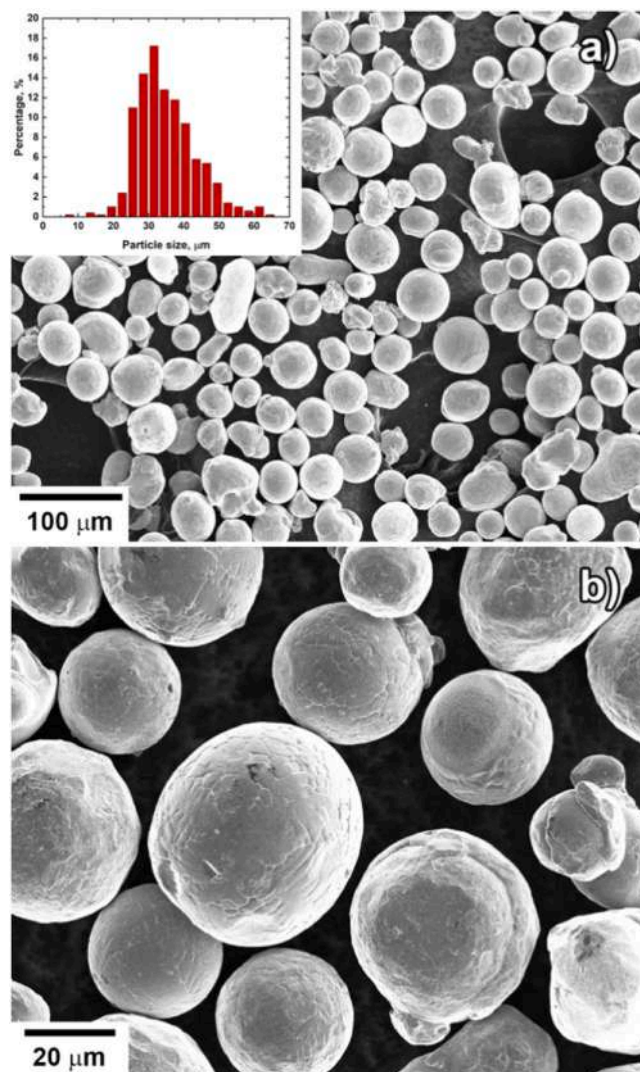
Fig. 1. SEM images of the CrFeCoNi powders were taken at the low (a) and high (b) magnifications.

temperature prevents the recrystallization processes [11] and produces a stable solid solution state in the similar CrMnFeCoNi alloys [30], while an earlier study showed that annealing at 750 °C leads to the σ phase formation which decreases the strength at cryogenic temperatures [14]. Half of the as-built samples without annealing and the annealed samples were turning processed (further, "machined samples") to investigate the fatigue properties of the AM MEA after different treatments.

An Instron 5985 testing machine (Instron, USA) was used for tensile testing. The testing was performed at RT at a strain rate of 1.0×10^{-3} s^{-1} using an extensometer according to ASTM E8. The round-shape samples had a gauge length of 16.0 mm and a diameter of 4.0 mm. The fatigue tests were performed according to ISO 1099:2006(E) using an Instron 8801 testing machine (Instron, USA) at RT. The stress-controlled fatigue testing procedure was performed at a frequency of 25 Hz and at stress ratio (R) of 0.1. The test procedure was interrupted after 10^7 cycles or sample fracture. The samples with a circular cross-section were applied, and the gauge cross-section had a diameter of 4.0 mm with a gauge radius of 12.0 mm. The gauge length of the machined samples was polished with a rotary tool. A Nanovea PB 1000 (NANOVEA, USA) was used for the microhardness measurements with a load of 200 g for at least 10 measurements per sample.

2.4. Structural and phase analyses

Optical microscope (Carl Zeiss, Axio Scope.A1, Germany) and Thixomet Pro software (Thixomet, Russia) were used to determine the porosity of the AM-built samples in the horizontal direction, which is perpendicular to the 3D building direction.

The samples were cut in vertical and horizontal directions to evaluate the microstructure using SEM with electron backscatter diffraction (EBSD) analyses. Up to 2000-grit SiC grinding papers were used for the initial sample polishing process followed by a polishing procedure with a diamond suspension (3 μm) and silica oxide suspension (40 nm). The samples were further electropolished in an electrolyte comprising 900 ml of butanol (C_4H_9OH) plus 100 ml of perchloric acid ($HClO_4$) with a voltage of 40 V for 30 s. The SEM images were obtained with a Carl Zeiss Supra 40 microscope (Carl Zeiss AG, Germany) with an energy dispersive X-ray (EDX) detector. Tescan Mira 3 microscope (TESCAN, Czech Republic) equipped with an EBSD system was used for EBSD analysis. A step size of 0.5 μm and a minimum boundary misorientation of 2° was applied for the EBSD maps according to the inverse pole figure (IPF). X-ray diffraction (XRD) analysis was performed with a Bruker D8 ADVANCE (Bruker, USA) diffractometer with CuKα radiation (wavelength = 1.5418 Å) measured from the top surfaces of the as-built as well as further treated samples. The diffraction patterns were obtained for a 2θ angle in the range from 30° to 100° with a step size of 0.005° and incremental time of 3 s

3. Results

3.1. Consolidation

The consolidated powder samples had low porosity with less than 0.1% of the total sample volume determined by the standard procedure (ASTM E1245-03) using an optical microscope. The relative density of the fabricated samples was determined as 7.92 g/cm^3 by the Archimedes' principle, while the density of the MEA powders before consolidation was 8.02 g/cm^3. It estimates nanoscale inner porosity with 1.25% of the powder volume, which cannot be observed by the optical methods. The roughness of the AM-built MEA samples was 4.6 μm (R_a) and 26.2 μm (R_z) from the front surfaces. After machining and polishing procedures, it did not exceed 0.4 μm and 1.9 μm, for R_a and R_z, respectively.

3.2. Microstructure

Fig. 2 shows the backscattered electron (BSE) images of the as-built and annealed CrFeCoNi alloys, where the images represent the top view (a, b, and c) and the front view (d, e, and f), and the top view of the misorientation maps are shown for the as-built (g [14]) and as-annealed alloy. Fig. 2a shows the duplex microstructure comprising the elongated domains, which length correlates with the laser beam width of 50 μm, and a fine structure in the middle between neighboring melt tracks. This appearance can be the result of the overlapping of neighboring laser tracks, remelting, and recrystallization. A typical cellular substructure for the printing material is displayed with elongated grains (600 and 1300 nm) from the top view of the as-built samples, as shown in Fig. 2b (dotted area). Annealing of the as-built sample forms "square domains" at the sample top surface with sizes from 40 to 45 μm (Fig. 2c). A fine grain structure is still observed around the square domains.

The BSE image of the as-built alloy in the front view shows columnar grains elongated along the build direction, as shown in Fig. 2d. The characteristic size of the grains varies between ~10 and 60 μm, while some irregular small grains are also observed. Annealing leads to the formation of a less regular structure with the texture along the building direction, which remains the same

(Fig. 2e). The higher magnification shows twins-like grains having a width of ~2 μm, which are not observed in the as-built material, with fine grains of ~1 μm (Fig. 2f). Comparison of the misorientation of grains in the as-built CrFeCoNi alloy (Fig. 2g [14]) and the annealed alloy (Fig. 2h) exhibits a removal of the residual stress that is confirmed by the decrease in an average structure misorientation coefficient from 1.4 to 0.7 measured with OIM Analysis software (EDAX, AMETEK Inc., USA). Fig. 3 shows the EBSD IPF maps for (a) as-built and (b) as-annealed samples and (c) their grain boundary character distributions, which present the changes in boundary characteristics after annealing. While the misorientation is reduced and is accumulated in the vicinity of boundaries, the fraction of high-angle boundaries is increased from 0.2 to up to 0.3 (Fig. 3c).

3.3. Phase properties

Fig. 4a shows the X-ray diffraction (XRD) line profiles for the initial powder and as-built and annealed CrFeCoNi alloys. There are three important findings in the analysis. First, it is apparent that all sample conditions show the peak intensities indicating an fcc structure. The intensity at the (220) peak is dominant in the as-built and annealed samples, while high intensity was observed at the (111) peak in the powder. Second, the position of the (111) peak shifts in the as-built material where the enlarged peaks for the (111) plane were shown in Fig. 4b, while the annealed sample showed the (111) peak at the same position as the powder material. The shifting of the peak to the left in the profile is due to the high microstrain in the structure of the as-built alloy, thereby indicating residual stress. The existence of residual stress after printing and removal after annealing in the XRD analysis reasonably agrees with the observed microstructure shown in Fig. 2g and h. Third, the XRD profiles reveal two additional phases in the samples before and after annealing at 800 °C, which are indicated with yellow and purple dotted lines in Fig. 4a. Earlier reports on the CrMnFeCoNi alloy described the presence of the Cr-rich secondary phases, including bcc Fe-Cr and cubic Cr-rich compounds [14,30–32], while the EDX analysis on the present as-built CrFeCoNi alloy demonstrates homogeneous elemental distributions as shown in Fig. 5. The peak positions of secondary phases indicate the formation of two other fcc phases with lattice parameters of 3.954 Å (orange dotted line) and 3.729 Å (purple dotted line), but it is expected these compounds are under the detective limit of EDX analysis. Figs. 4c and 4d show the BSE images of the samples before and after annealing, respectively, which demonstrate the presence of precipitates on the grain boundaries after annealing. Although the present XRD analysis does not provide enough phase information due to the limited concentrations of these additional phases in the CrFeCoNi alloy, from the references of the CrMnFeCoNi alloys, Cr-rich particles with a Cr-Fe-type σ phase may be anticipated after heat treatment [31,32].

3.4. Tensile properties

Fig. 6a demonstrates the typical engineering stress-strain curves for the as-built and annealed CrFeCoNi alloys. It is evident that the annealing reduces the yield strength of the alloy from 551.0 MPa to 456.3 MPa, while the ultimate tensile strength is maintained without significant change, such as 658.3 MPa before annealing and 637.5 MPa after annealing. The ductility of the material increases after annealing by ~13% (from 51.4% to 64.8%). The microhardness is also reduced by annealing from 259 HV to 209 HV. These changes in mechanical properties of the CrFeCoNi alloy after annealing are attributed to the changes in the substructural characteristics from the total cellular to the irregular substructure (Fig. 2b and f). The results of mechanical testing are summarized in Table 1.

Fig. 6b presents the true stress-strain curves of the CrFeCoNi alloy before and after annealing, where both sample conditions
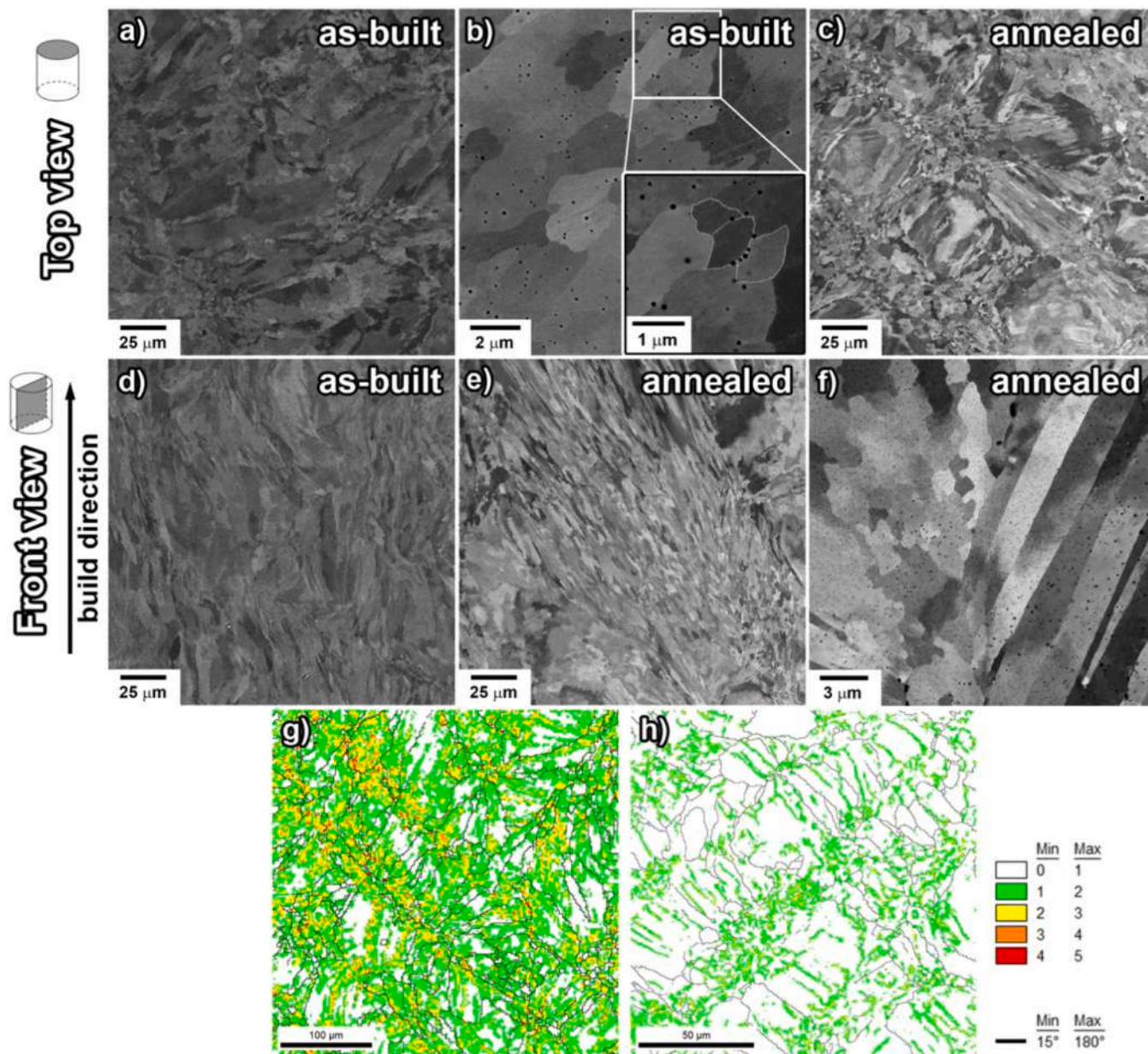
Fig. 2. Backscattered electron images of the CrFeCoNi alloy: top view (a, b, and c) and front view (d, e, and f). Misorientation maps for as-built CrFeCoNi alloy (g [14]) and annealed alloys (h) from the top view.
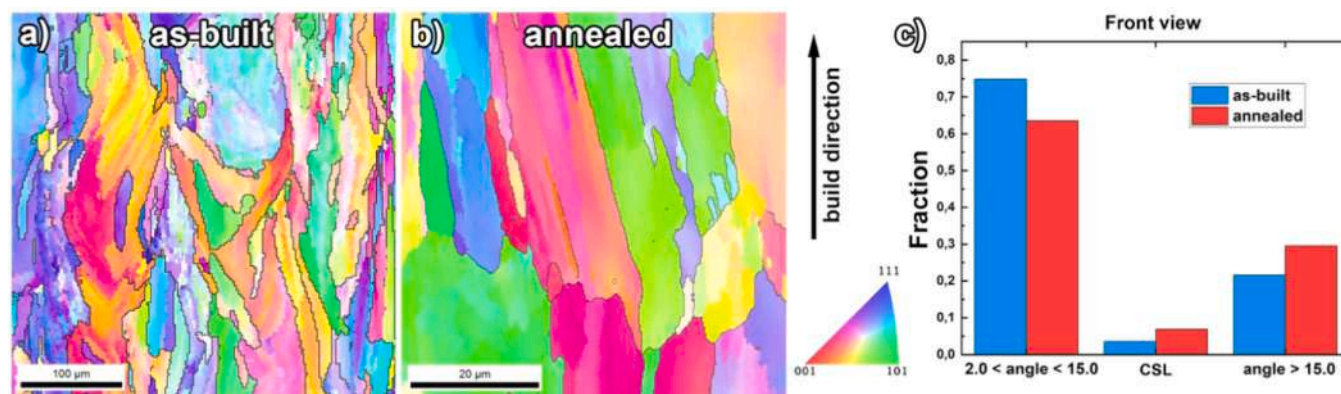
Fig. 3. EBSD IPF maps of the as-built [14] (a) and annealed CrFeCoNi alloy (b), and grain boundary character distribution for them (c).
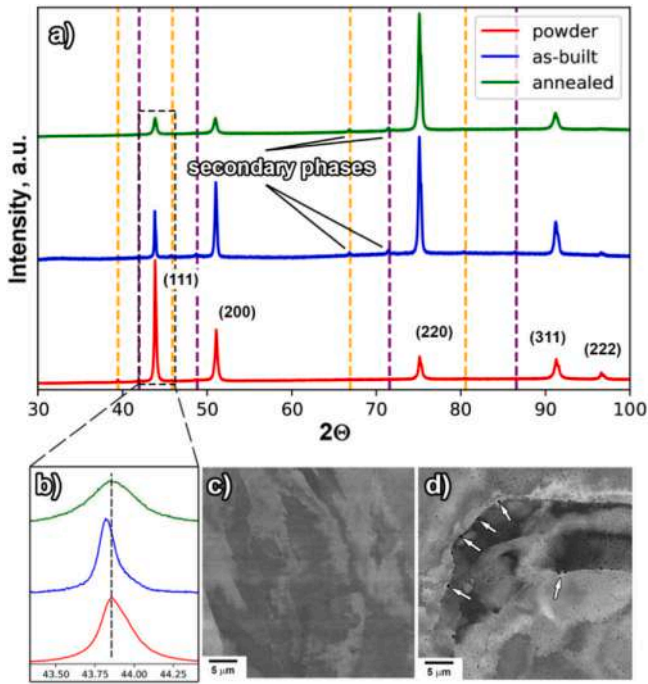
Fig. 4. X-ray diffraction patterns of the CrFeCoNi alloy (a, b) and backscattered electron images of the 3D printed CrFeCoNi alloy before (c) and after (d) annealing at 800 ℃. (For interpretation of the references to color in this figure legend, the reader is referred to the web version of this article.)

Table 1
Tensile test results of the CrFeCoNi alloy.

	σ_y, MPa	σ_{uts}, MPa	ε, %	Microhardness, HV
As-built	551.0 ± 9.6	658.3 ± 9.0	51.4 ± 10.9	259 ± 8
Annealed at 800 ℃	456.3 ± 9.9	637.5 ± 14.4	64.8 ± 3.7	209 ± 12

display the monotonic hardening process during the tensile loading. The strain hardening in the material after heat treatment is developed further due to its less dislocation density, as discussed earlier in terms of misorientation. The damage initiation in true stress is equal to 1016 and 1032 MPa for as-built and annealed MEA, respectively.

3.5. Fatigue properties

Fig. 7a and b demonstrate the S-N curves of the printed CrFeCoNi alloy in as-built and after annealing conditions (a) without turning process (machining) and (b) with machining. The machined samples demonstrate a much higher fatigue resistance for both samples in as-built and as-annealed conditions. The as-built samples without annealing are able to withstand 10^7 cycles at maximum fatigue stress of 414 MPa (stress amplitude (σ_a) of 186.3 MPa) after machining, in contrast to the unmachined samples showing maximum fatigue stress of 138 MPa (σ_a = 62.1 MPa). The heat treatment tends to improve the fatigue life in the high cycle fatigue conditions for the alloy both with/without machining. Despite the fact that the machined samples achieved 10^7 cycles at cycle loads of 414 MPa
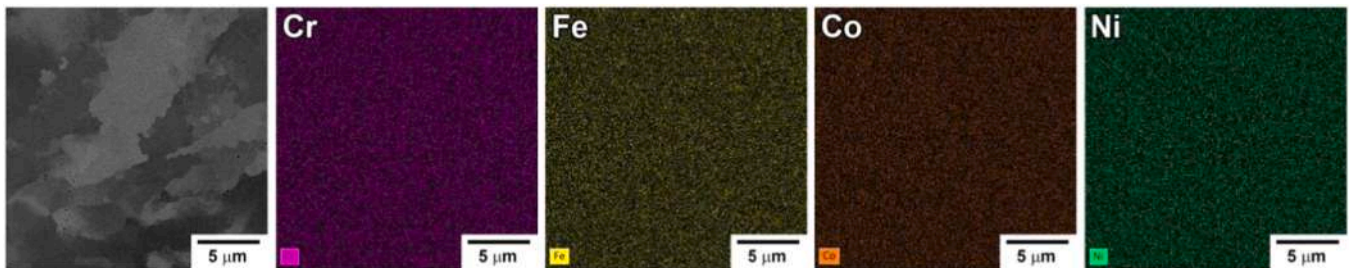
Fig. 5. EDX results for the as-built CrFeCoNi alloy in top view.
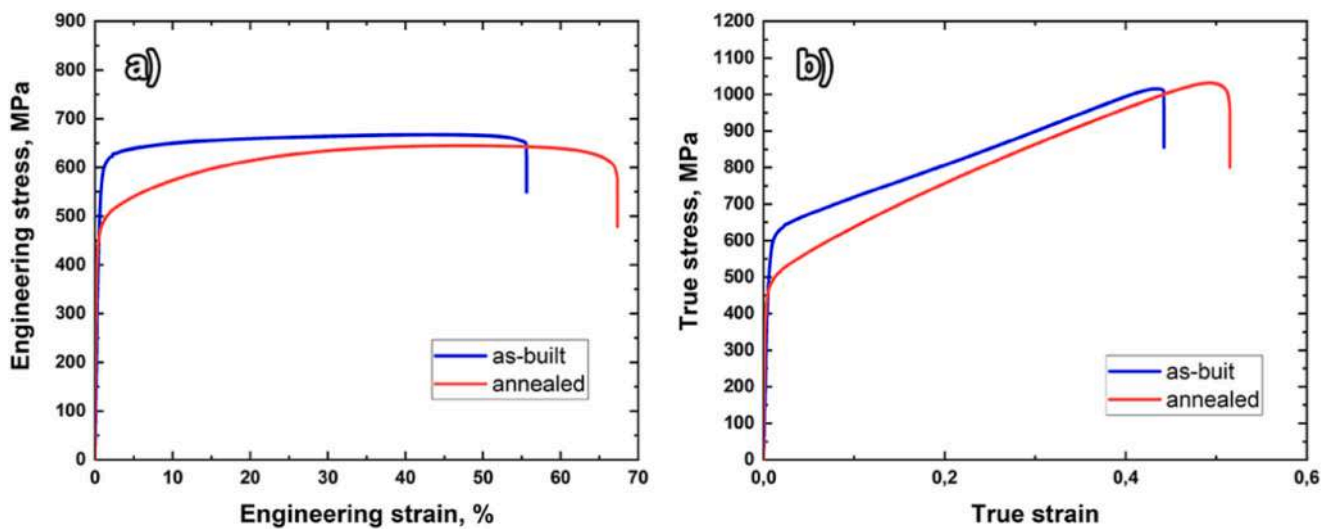
Fig. 6. Engineering and true stress-strain curves of the CrFeCoNi alloy.
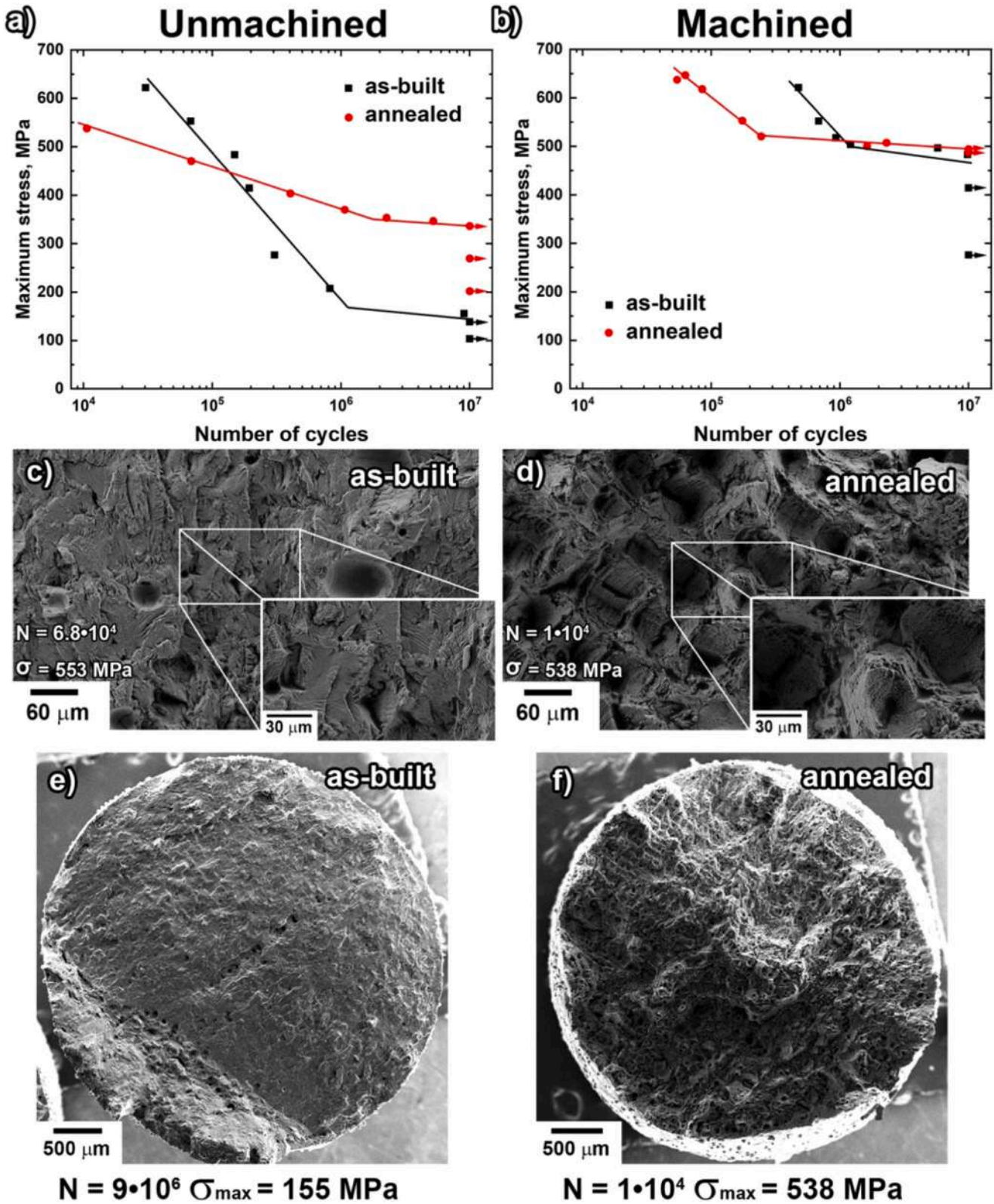
Fig. 7. The S-N curves of the CrFeCoNi alloy in as-built and after annealing conditions (a) without machining and (b) with machining. The fracture surfaces of (c) and (e) as-built (d) and (f) annealed samples without machining.

and 494 MPa (σ_a = 222.3 MPa) before and after annealing, respectively, the machined as-built sample withstood close to 10^7 cycles (9.8×10^6) and failed at the load of 483 MPa. Thus, the heat treatment provides more contribution to the fatigue strengths from 138 MPa up to 336 MPa (σ_a = 151.2 MPa) after annealing in the

unmachined samples. The detailed fatigue results are summarized in Table 2.

Figs. 7c–f characterize the fracture surfaces of the as-built and annealed samples without machining. The as-built sample has a brittle fracture surface with brittle faceted regions, which can be

Table 2
Summary of the fatigue test results.

	Unmachined		Machined	
	σ_{max}, MPa	N, cycles	σ_{max}, MPa	N, cycles
As-built (no annealing)	621.9	30,343	621.0	476,027
	552.8	67,972	552.0	6,83,116
	483.7	149,227	517.5	9,31,293
	414.6	193,695	503.7	1,207,982
	276.4	304,583	496.8	5,743,441
	207.3	819,884	483.0	9,830,569
	155.5	9,041,019	414.0	10^7
	138.2	10^7	276.0	10^7
	103.7	10^7	–	–
Annealed at 800 ℃	537.6	10,618	646.8	62,915
	470.4	68,799	637.0	54,323
	403.2	404,854	617.5	85,198
	369.6	1,069,877	552.5	174,391
	352.8	2,259,636	520.0	244,577
	346.1	5,511,310	507.0	2,305,909
	336.0	10^7	500.5	1,627,070
	268.8	10^7	494.0	10^7
	201.6	10^7	487.5	10^7

recognized in the image with higher magnification in Fig. 7c. Additionally, it is anticipated to observe the voids on the fracture surface. The annealed sample presents more ductile fracture behavior. It has dimple-like square features with a size of ~50 µm, as shown in Fig. 7d. It should be noted that brittle and ductile areas are observed for both the as-built and annealed samples. However, for some as-built samples, a fully brittle fracture mode is typical, while a completely ductile fracture behavior is possible for the annealed samples (Figs. 7e and f).

Fig. 8 shows the crack initiation sites for the as-built samples (a) without and (b) with the machining procedure. The cracks are initiated in the voids and pores near the sample surface of the as-built sample without machining, which can be seen in the magnified image (Fig. 8a), in contrast to the machined sample where the crack starts from inner defects (Fig. 8b).

3.6. Microstructure evolution under loading

Fig. 9 demonstrates the BSE images of the microstructure of (a, c, and e) the as-built and (b, d, and f) annealed CrFeCoNi alloys fractured at different loads. Fig. 9a and b present the microstructure after damage at tensile load. It is seen that the microstructure is full of the slip lines crossing over the columnar grains for both sample conditions. Fig. 9c and d present the microstructure after the failure of the as-built and as-annealed at the cycling loads of 518 MPa and 520 MPa, respectively. These show the changes of the deformation mechanism compared with those failed during tensile load. Specifically, the deformation bands are clearly observed for as-built and annealed materials, which are denoted by dotted lines. The distance between the lines in the as-built material of ~150 µm is wider than ~90 µm for the annealed one. Fig. 9e and f demonstrate the microstructure of as-built and as-annealed samples after cycling loading at 483 MPa and 488 MPa, respectively. The as-built microstructure flows along the slip planes and changes the direction (dotted lines in Fig. 9e), while the deformation bands can be seen in the annealed material.

Fig. 10a–d present the EBSD IPF maps and corresponded misorientation maps of (a, b) the printed and (c, d) annealed CrFeCoNi samples after fracturing under cyclic loads at 483 MPa and 455 MPa, respectively. It demonstrates the dislocation density (or misorientation) concentrating along the slip traces in grains with the {001} orientations for as-build and annealed samples, while the cellular dislocation structure is formed in the grains with the {111} orientations in Fig. 10a and ~{211} orientations in Fig. 10d. Fig. 10e
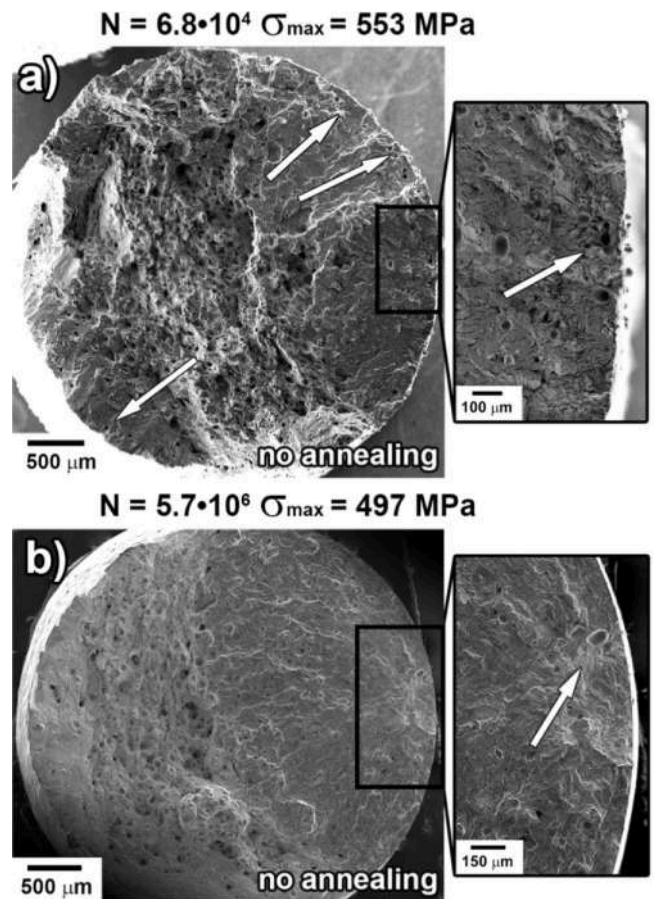
Fig. 8. Fatigue fracture surfaces and crack initiation sites for (a) the unmachined and (b) machined sample of the printed alloy without annealing.

shows the intersection of slip traces. The as-built material shows the microstructure involving some regions free of dislocations (Fig. 10b), while it was full of misorientation before the deformation (Fig. 2g). Fig. 10f represents the distributions of grain boundary misorientation for as-built and annealed CrFeCoNi alloy. It demonstrates high fractions of boundary misorientation below 10° and no grain boundary with misorientation of 60° for both as-built and annealed alloys after cycling loading at 483 MPa and 488 MPa, respectively.

4. Discussion

4.1. Tensile properties

The present as-built CrFeCoNi alloy demonstrates an ultimate strength and ductility similar to the hot-rolled CrMnFeCoNi and CrFeCoNi alloys [11]. However, the yield strength of the material in the present research is higher, which is typical for printed fcc materials [33]. Wang et al. explained that the yield strength for printed austenitic steel increased due to the formation of a fine cellular microstructure leading to strengthening explained by the Hall-Petch relationship [34]. In the present study, Fig. 2b demonstrates a similar microstructure. It can be concluded that the high yield strength of the as-built sample can be contributed by the fine microstructure. After heat treatment, the mechanical properties are significantly changed. A slight decrease in ultimate strength by ~20 MPa was observed, and the presence of the fine structure next to large domains expected as annealing twins (Fig. 2f) implies the beginning of the recrystallization process. These are consistent with the misorientation maps confirming the occurrence of recovery in the material after annealing at 800 ℃. The annealing twins were observed
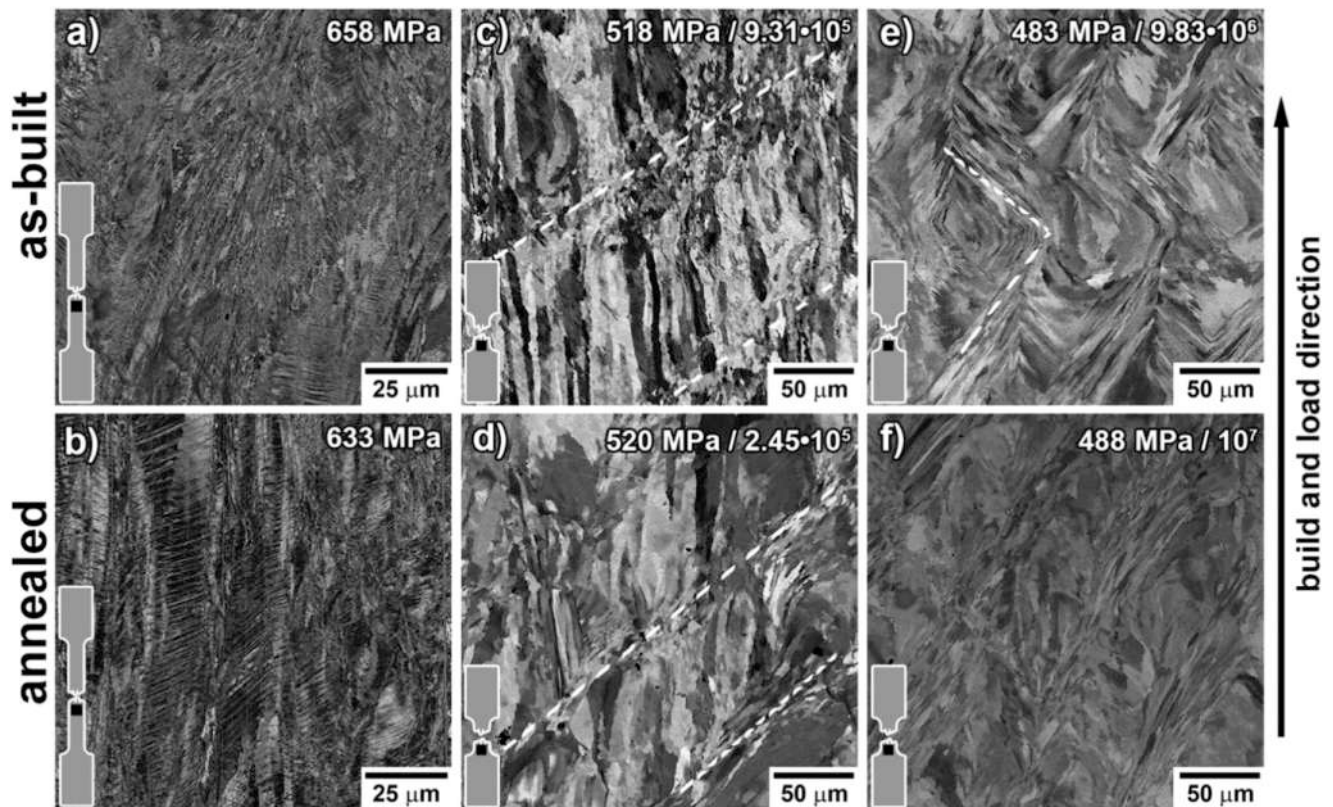
Fig. 9. BSE images were taken close to the neck of damage of as-printed (upper raw) and as-annealed (lower raw) CrFeCoNi alloy after tensile fracture (a, b) and after cycling loading at different stresses (c–f). The failure loads and numbers of cycles before damage are on the upper left in each image. Left-down inserts demonstrate the position of the presented area.

in CrMnFeCoNi alloys after annealing at 800 °C [32] and in CrMnFeCoNi and CrFeCoNi alloys after recrystallization at 900 °C [11]. Both alloys are characterized by low stacking fault energies, 20–25 mJ/m^2 [35]. Other studies that investigated similar CrMnFe-CoNi alloys [30,32,36] postulated that the recrystallization process starts at 600 °C. Moreover, due to the low stacking fault energy, the CrMnFeCoNi alloys are deformed at tensile load through the de-formation twinning process [21,37]. Such mechanism is suitable for the present CrFeCoNi alloys.

4.2. Machining impact

The fatigue strength of the machined CrFeCoNi alloy is two to three times higher than the as-built and unmachined conditions. In general, the samples with higher surface roughness have stress concentrators that facilitate crack initiation [38]. DebRoy et al. de-scribed surface roughness as the main issue limiting the fatigue performance of AM components [33]. Yadollahi and Shamsaei sug-gested that the near-surface defects formed during the printing process enable the initiation of cracks under cycling loading [25]. Other works also consider the irregular near-surface voids as the main reason for limiting the fatigue life of AM alloys [25,27,37,39]. The near-surface defects are explained through the contact of the melt pool with the powder bed resulting in the thermal/fluidic edge effects [25]. However, the comprehensive explanation of the nature of such voids and pores is still unclear. In the present work, the additional laser tracks were applied along the perimeter of the cross-section on each layer to decrease the surface roughness of the samples. However, such remelting procedures can increase the near-surface porosity. Thus, the machining process removes the surface layer with voids, which improves the fatigue life of the AM pro-cessed CrFeCoNi alloy. Several crack site initiations are observed in

the unmachined samples in Fig. 8a, typical for LCF. The high fraction of initiated cracks during LCF (or higher stress loads) enables the formation of several cracks [25]. During high cycle fatigue (HCF), the contribution of one severe defect initiates the crack, which leads to damage of the sample.

4.3. Impact of the annealing on the fatigue properties

The fatigue strength of the unmachined CrFeCoNi samples is increased after annealing at 800 °C, but it presents lower values during LCF. The machined samples demonstrate the higher fatigue resistance properties at LCF before heat treatment and the same fatigue strength at HCF before and after annealing.

Dislocation structures influence the fatigue resistance of mate-rials, and their impact can be indirectly estimated through the ten-sile strength [38]. The annealing process decreases the yield stress of materials and increases the ratio of the yield stress to ultimate tensile strength, $k = \sigma_{uts}/\sigma_y$. For the as-built CrFeCoNi alloy, k is less than 1.2, and it may be considered as a cyclically work-softened material. The yield strength is decreased after annealing, and k in-creased up to 1.4, which is expected due to its cyclically work-hardening. Application of heat treatment to a printed 316L stainless steel increases k from 1.2 to 1.6, which in turn improves the fatigue limits [40,41]. Similar fatigue behavior is observed for the CrFeCoNi alloy, but it occurred only for the unmachined samples. As far as time for crack initiation decreases due to the presence of the voids in the unmachined samples, the contribution of the time for crack propagation to the total fatigue life increases.

The absence of near-surface defects raises the significance of the presence of the secondary phases to fatigue behavior of the CrFeCoNi alloy. The formation of the σ phase could facilitate the crack pro-pagation in the material due to the embrittlement of the material
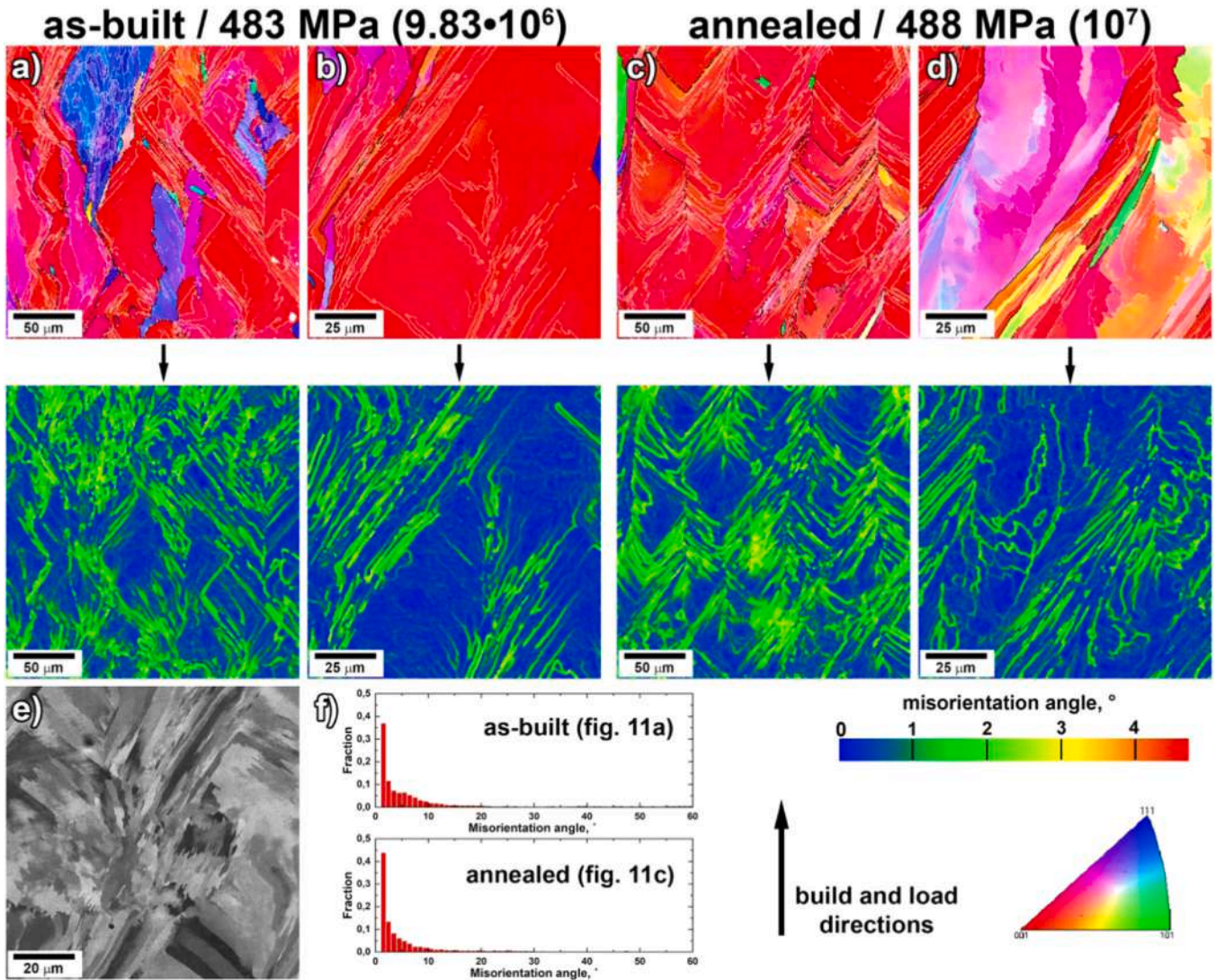
Fig. 10. EBSD IPF and misorientation maps of printed CrFeCoNi alloy fractured under cyclic loads at (a, b) 483 MPa and (c, d) 455 MPa; (e) BSE image of the as-built microstructure; (f) boundary distributions of as-built and annealed material.

Table 3
Comparison of yield strength, ultimate strength, fatigue strength, and fatigue ratio of L-PBF CrFeCoNi alloy with other HEAs and other L-PBF alloys performing in the vertical direction.

	R	σ_y, MPa	σuts, MPa	σ_{af}, MPa	Fatigue ratio
CrFeCoNi (machined, no annealing) [present work]	0.1	565	658	186	0.28
CrFeCoNi (machined, annealed at 800 ℃) [present work]	0.1	458	637	222	0.35
CoCrFeMnNi [21]	0.1	293	626	126	0.20
$Al_{0.3}$CoCrCuFeNi [19]	-1	900	1074	450	0.42
$Al_{0.5}$CoCrCuFeNi [16]	0.1	1284	1344	383	0.29
$Al_{0.7}$CoCrCuFeNi [20]	-1	780/1050	1040/1400	410/460	0.39/0.33
17–4 pH stainless steel [27]	-1	580	940	282	0.30
316L stainless steel [46]	0.1	479	565	124	0.22
Inconel 718 [39]	0.1	1170	1380	297	0.22

[5,14]. The higher fatigue resistance at HCF regime is expected for the ductile materials after annealing [29]. However, the same fatigue strength is observed for the as-built and annealed CrFeCoNi samples, which is explained by σ phase presence in the annealed alloy facilitating the crack propagation due to incoherent grain border formation. The absence of the boundaries with the misorientation of 60° in the as-built and annealed samples damaged under the cycling load (Fig. 10f) shows that the deformation process is mostly going through the planar slips. The same conclusion was reported for the

CoCrFeMnNi alloys having similar low stacking fault energy [21,35,37].

4.4. Comparison with other alloys

To date, only a few studies present the results on fatigue endurance of HEAs [42]. Most of them reported on the Al-added HEAs [1,16,18–20]. Others focus on fatigue crack growth behavior [17,43–45]. Generally, HEAs demonstrate high σ_{af} in relation to the

ultimate strengths [1,15,16], where σ_{af} is fatigue strength. The AM CrFeCoNi alloys demonstrate the fatigue ratios (σ_{af}/σ_{uts}) comparable with those of other conventional alloys (Table 3). In these terms, the fatigue properties of the printed CrFeCoNi alloy are even better than high-strength Al$_{0.5}$CoCrCuFeNi alloys [16] and Cantor's alloys [21]. It should be noted that AM provides lower fatigue characteristics than those the equivalent alloys that are produced with traditional procedures [25]. Adding Al to CrFeCoNi alloys increases the material strength (including the fatigue strength) by the formation of the hard B2 phase [20]. Such phase leads to a reduction in ductility. Based on the existing results, Li et al. conclude that the HEAs are not good candidates for replacing conventional alloys [42]. Nevertheless, the CrFeCoNi alloys can be a good material for modifications and applications in the additive technology field due to the stable solid solution during the printing process, high ductility, and excellent printability. More results on the fatigue studies are required to conclude the feasibility of HEAs.

5. Conclusion

In the present work, the influence of post-treatments on the fatigue properties of L-PBF CrFeCoNi alloy has been studied. Following conclusions can be made:

- The L-PBF technique forms the material with cellular structure leading to increased yield strength up to 551 MPa. Annealing at 800 °C removes the residual stress and initiates the recrystallization process that reduces the yield strength by 100 MPa. Heat treatment does not change the ultimate strength significantly (658 MPa and 637 MPa before and after annealing, respectively), but increases the ductility by 13%.
- The twinning deformation mechanism takes place at the tensile deformation, while dislocation slip dominates at cycling loads of ~480 MPa.
- The machining process plays a critical role in the fatigue properties of the AM alloys by removing of near-surface defects in the samples. It increases the total fatigue life by the complication of the crack initiation.
- Annealing does not improve the fatigue characteristics of the material due to the formation of the σ phase that facilitates crack propagation. Despite the measured fatigue strength for unannealed samples of 414 MPa, which is by 80 MPa lower than for annealed samples, they withstand close to ~10^7 cycles at a cycling load of 483 MPa.

CRediT authorship contribution statement

Y.O. Kuzminova: Writing - original draft, Conceptualization, Methodology, Investigation, Data curation. **D.G. Firsov:** Investigation. **S.A. Dagesyan:** Investigation. **S.D. Konev:** Investigation. **S.N. Sergeev**: Investigation. **A.P. Zhilyaev**: Resources; **M. Kawasaki**: Writing- reviewing & editing. **I.S. Akhatov**: Resources. **S.A. Evlashin**: Supervision, Writing - review & editing.

Declaration of Competing Interest

The authors declare that they have no known competing financial interests or personal relationships that could have appeared to influence the work reported in this paper.

Acknowledgements

References

[1] M.A. Hemphill, T. Yuan, G.Y. Wang, J.W. Yeh, C.W. Tsai, A. Chuang, P.K. Liaw, Fatigue behavior of Al 0.5 CoCrCuFeNi high entropy alloys, Acta Mater. 60 (2012) 5723–5734, https://doi.org/10.1016/j.actamat.2012.06.046

[2] O.N. Senkov, G.B. Wilks, J.M. Scott, D.B. Miracle, Mechanical properties of Nb25Mo25Ta25W25 and V20Nb20Mo20Ta20W20 refractory high entropy alloys, Intermetallics 19 (2011) 698–706, https://doi.org/10.1016/j.intermet.2011.01.004

[3] O.N. Senkov, J.K. Jensen, A.L. Pilchak, D.B. Miracle, H.L. Fraser, Compositional variation effects on the microstructure and properties of a refractory high-entropy superalloy AlMo0.5NbTa0.5TiZr, Mater. Des. 139 (2018) 498–511, https://doi.org/10.1016/j.matdes.2017.11.033

[4] N.D. Stepanov, N.Y. Yurchenko, E.S. Panina, M.A. Tikhonovsky, S.V. Zherebtsov, Precipitation-strengthened refractory Al0.5CrNbTi2V0.5 high entropy alloy, Mater. Lett. 188 (2017) 162–164, https://doi.org/10.1016/j.matlet.2016.11.030

[5] D.B. Miracle, O.N. Senkov, A critical review of high entropy alloys and related concepts, Acta Mater. 122 (2017) 448–511, https://doi.org/10.1016/j.actamat.2016.08.081

[6] B.B. Bian, N. Guo, H.J. Yang, R.P. Guo, L. Yang, Y.C. Wu, J.W. Qiao, A novel cobalt-free FeMnCrNi medium-entropy alloy with exceptional yield strength and ductility at cryogenic temperature, J. Alloy. Compd. 827 (2020) 153981, https://doi.org/10.1016/j.jallcom.2020.153981

[7] D. Li, C. Li, T. Feng, Y. Zhang, G. Sha, J.J. Lewandowski, P.K. Liaw, Y. Zhang, High-entropy Al 0.3 CoCrFeNi alloy fibers with high tensile strength and ductility at ambient and cryogenic temperatures, Acta Mater. 123 (2017) 285–294, https://doi.org/10.1016/j.actamat.2016.10.038

[8] F. He, Z. Wang, P. Cheng, Q. Wang, J. Li, Y. Dang, J. Wang, C.T. Liu, Designing eutectic high entropy alloys of CoCrFeNiNbx, J. Alloy. Compd. 656 (2016) 284–289, https://doi.org/10.1016/j.jallcom.2015.09.153

[9] T.W. Zhang, S.G. Ma, D. Zhao, Y.C. Wu, Y. Zhang, Z.H. Wang, J.W. Qiao, Simultaneous enhancement of strength and ductility in a NiCoCrFe high-entropy alloy upon dynamic tension: micromechanism and constitutive modeling, Int. J. Plast. 124 (2020) 226–246, https://doi.org/10.1016/j.ijplas.2019.08.013

[10] G.A. Salishchev, M.A. Tikhonovsky, D.G. Shaysultanov, N.D. Stepanov, A.V. Kuznetsov, I.V. Kolodiy, A.S. Tortika, O.N. Senkov, Effect of Mn and V on structure and mechanical properties of high-entropy alloys based on CoCrFeNi system, J. Alloy. Compd. 591 (2014) 11–24, https://doi.org/10.1016/j.jallcom.2013.12.210

[11] A. Gali, E.P. George, Tensile properties of high- and medium-entropy alloys, Intermetallics 39 (2013) 74–78, https://doi.org/10.1016/j.intermet.2013.03.018

[12] Z. Wu, H. Bei, G.M. Pharr, E.P. George, Temperature dependence of the mechanical properties of equiatomic solid solution alloys with face-centered cubic crystal structures, Acta Mater. 81 (2014) 428–441, https://doi.org/10.1016/j.actamat.2014.08.026

[13] Y. Brif, M. Thomas, I. Todd, The use of high-entropy alloys in additive manufacturing, Scr. Mater. 99 (2015) 93–96, https://doi.org/10.1016/j.scriptamat.2014.11.037

[14] Y. Kuzminova, D. Firsov, A. Dudin, S. Sergeev, A. Zhilyaev, A. Dyakov, A. Chupeeva, A. Alekseev, D. Martynov, I. Akhatov, S. Evlashin, The effect of the parameters of the powder bed fusion process on the microstructure and mechanical properties of CrFeCoNi medium-entropy alloys, Intermetallics 116 (2020) 106651, https://doi.org/10.1016/j.intermet.2019.106651

[15] P.Y. Chen, C. Lee, S.Y. Wang, M. Seifi, J.J. Lewandowski, K.A. Dahmen, H.L. Jia, X. Xie, B.L. Chen, J.W. Yeh, C.W. Tsai, T. Yuan, P.K. Liaw, Fatigue behavior of high-entropy alloys: a review, Sci. China Technol. Sci. 61 (2018) 168–178, https://doi.org/10.1007/s11431-017-9137-4

[16] Z. Tang, T. Yuan, C.W. Tsai, J.W. Yeh, C.D. Lundin, P.K. Liaw, Fatigue behavior of a wrought Al < inf > 0.5 </inf > CoCrFeNi two-phase high-entropy alloy, Acta Mater. 99 (2015) 247–258, https://doi.org/10.1016/j.actamat.2015.07.004

[17] K.V.S. Thurston, B. Gludovatz, A. Hohenwarter, E.P. Laplanche, E.P. George, R.O. Ritchie, Effect of temperature on the fatigue-crack growth behavior of the high-entropy alloy CrMnFeCoNi, Intermetallics 88 (2017) 65–72, https://doi.org/10.1016/j.intermet.2017.05.009

[18] S. Shukla, T. Wang, S. Cotton, R.S. Mishra, Hierarchical microstructure for improved fatigue properties in a eutectic high entropy alloy, Scr. Mater. 156 (2018) 105–109, https://doi.org/10.1016/j.scriptamat.2018.07.022

[19] K. Liu, M. Komarasamy, B. Gwalani, S. Shukla, R.S. Mishra, Fatigue behavior of ultra fine grained triplex Al0.3CoCrFeNi high entropy alloy, Scr. Mater. 158 (2019) 116–120, https://doi.org/10.1016/j.scriptamat.2018.08.048

[20] K. Liu, B. Gwalani, M. Komarasamy, S. Shukla, T. Wang, R.S. Mishra, Effect of nano-sized precipitates on the fatigue property of a lamellar structured high entropy alloy, Mater. Sci. Eng. A 760 (2019) 225–230, https://doi.org/10.1016/j.msea.2019.06.012

[21] Y. Kim, G. Ham, H. Seop, K. Lee, High-cycle fatigue and tensile deformation behaviors of coarse-grained equiatomic CoCrFeMnNi high entropy alloy and

unexpected hardening behavior during cyclic loading, Intermetallics 111 (2019) 106486, https://doi.org/10.1016/j.intermet.2019.106486

[22] D. Herzog, V. Seyda, E. Wycisk, C. Emmelmann, Additive manufacturing of metals, Acta Mater. 117 (2016) 371–392, https://doi.org/10.1016/J.ACTAMAT.2016.07.019

[23] A. Röttger, K. Geenen, M. Windmann, F. Binner, W. Theisen, Comparison of microstructure and mechanical properties of 316 L austenitic steel processed by selective laser melting with hot-isostatic pressed and cast material, Mater. Sci. Eng. A 678 (2016) 365–376, https://doi.org/10.1016/J.MSEA.2016.10.012

[24] T.M. Mower, M.J. Long, Mechanical behavior of additive manufactured, powder-bed laser-fused materials, Mater. Sci. Eng. A 651 (2016) 198–213, https://doi.org/10.1016/J.MSEA.2015.10.068

[25] A. Yadollahi, N. Shamsaei, Additive manufacturing of fatigue resistant materials: challenges and opportunities, Int. J. Fatigue 98 (2017) 14–31, https://doi.org/10.1016/J.IJFATIGUE.2017.01.001

[26] R. Shrestha, J. Simsiriwong, N. Shamsaei, S.M. Thompson, L. Bian, Effect of build orientation on the fatigue behavior of stainless steel 316L manufactured via a laser-powder bed fusion process, in: Solid Free. Fabr. 2016 Proc. 27th Annu. Int. Solid Free. Fabr. Symp. - An Addit. Manuf. Conf. SFF 2016, 2016, 605–616.

[27] A. Yadollahi, N. Shamsaei, S.M. Thompson, A. Elwany, L. Bian, Effects of building orientation and heat treatment on fatigue behavior of selective laser melted 17-4 PH stainless steel, Int. J. Fatigue 94 (2017) 218–235, https://doi.org/10.1016/j.ijfatigue.2016.03.014

[28] S. Siddique, M. Imran, E. Wycisk, C. Emmelmann, F. Walther, Influence of process-induced microstructure and imperfections on mechanical properties of AlSi12 processed by selective laser melting, J. Mater. Process. Technol. 221 (2015) 205–213, https://doi.org/10.1016/j.jmatprotec.2015.02.023

[29] S. Leuders, T. Lieneke, S. Lammers, T. Tröster, T. Niendorf, On the fatigue properties of metals manufactured by selective laser melting – the role of ductility, J. Mater. Res. 29 (17) (2014) 1911–1919, https://doi.org/10.1557/jmr.2014.157

[30] B. Schuh, F. Mendez-Martin, B. Völker, E.P. George, H. Clemens, R. Pippan, A. Hohenwarter, Mechanical properties, microstructure and thermal stability of a nanocrystalline CoCrFeMnNi high-entropy alloy after severe plastic deformation, Acta Mater. 96 (2015) 258–268, https://doi.org/10.1016/J.ACTAMAT.2015.06.025

[31] F. Otto, A. Dlouhý, K.G. Pradeep, M. Kuběnová, D. Raabe, G. Eggeler, E.P. George, Decomposition of the single-phase high-entropy alloy CrMnFeCoNi after prolonged anneals at intermediate temperatures, Acta Mater. 112 (2016) 40–52, https://doi.org/10.1016/j.actamat.2016.04.005

[32] M.V. Klimova, D.G. Shaysultanov, S.V. Zherebtsov, N.D. Stepanov, Effect of second phase particles on mechanical properties and grain growth in a CoCrFeMnNi high entropy alloy, Mater. Sci. Eng. A 748 (2019) 228–235, https://doi.org/10.1016/j.msea.2019.01.112

[33] T. DebRoy, H.L. Wei, J.S. Zuback, T. Mukherjee, J.W. Elmer, J.O. Milewski, A.M. Beese, A. Wilson-Heid, A. De, W. Zhang, Additive manufacturing of metallic components – process, structure and properties, Prog. Mater. Sci. 92 (2018) 112–224, https://doi.org/10.1016/j.pmatsci.2017.10.001

[34] Y.M. Wang, T. Voisin, J.T. McKeown, J. Ye, N.P. Calta, Z. Li, Z. Zeng, Y. Zhang, W. Chen, T.T. Roehling, R.T. Ott, M.K. Santala, P.J. Depond, M.J. Matthews, A.V. Hamza, T. Zhu, Additively manufactured hierarchical stainless steels with high strength and ductility, Nat. Mater. 17 (2018) 63–71, https://doi.org/10.1038/nmat5021

[35] A.J. Zaddach, C. Niu, C.C. Koch, D.L. Irving, Mechanical properties and stacking fault energies of NiFeCrCoMn high-entropy alloy, JOM 65 (2013) 1780–1789, https://doi.org/10.1007/s11837-013-0771-4

[36] Z. Wu, H. Bei, F. Otto, G.M. Pharr, E.P. George, Recovery, recrystallization, grain growth and phase stability of a family of FCC-structured multi-component equiatomic solid solution alloys, Intermetallics 46 (2014) 131–140, https://doi.org/10.1016/j.intermet.2013.10.024

[37] M. Jin, A. Piglione, B. Dovgyy, E. Hosseini, P.A. Hooper, S.R. Holdsworth, M. Pham, Cyclic plasticity and fatigue damage of CrMnFeCoNi high entropy alloy fabricated by laser powder-bed fusion, Addit. Manuf. 36 (2020) 101584, https://doi.org/10.1016/j.addma.2020.101584

[38] R.I. Stephens, A. Fatemi, R.R. Stephens, H.O. Fuchs, Metal Fatigue in Engineering, second ed., Wiley, 2000.

[39] A. Yadollahi, M.J. Mahtabi, A. Khalili, H.R. Doude, J.C. Newman, Fatigue life prediction of additively manufactured material: effects of surface roughness, defect size, and shape, Fatigue Fract. Eng. Mater. Struct. 41 (2018) 1602–1614, https://doi.org/10.1111/ffe.12799

[40] S. Leuders, T. Lieneke, S. Lammers, T. Tröster, T. Niendorf, On the fatigue properties of metals manufactured by selective laser melting – the role of ductility, J. Mater. Res. 29 (17) (2014) 1911–1919, https://doi.org/10.1557/jmr.2014.157

[41] A. Riemer, S. Leuders, M. Thöne, H.A. Richard, T. Tröster, T. Niendorf, On the fatigue crack growth behavior in 316L stainless steel manufactured by selective laser melting, Eng. Fract. Mech. 120 (2014) 15–25, https://doi.org/10.1016/j.engfracmech.2014.03.008

[42] W. Li, S. Chen, P.K. Liaw, Discovery and design of fatigue-resistant high-entropy alloys, Scr. Mater. 187 (2020) 68–75, https://doi.org/10.1016/j.scriptamat.2020.05.047

[43] M. Seifi, D. Li, Z. Yong, P.K. Liaw, J.J. Lewandowski, Fracture toughness and fatigue crack growth behavior of As-cast high-entropy alloys, JOM 67 (2015) 2288–2295, https://doi.org/10.1007/s11837-015-1563-9

[44] W. Li, X. Long, S. Huang, Q. Fang, C. Jiang, Elevated fatigue crack growth resistance of Mo alloyed CoCrFeNi high entropy alloys, Eng. Fract. Mech. 218 (2019) 106579, https://doi.org/10.1016/j.engfracmech.2019.106579

[45] B. Guennec, V. Kentheswaran, L. Perrière, A. Ueno, I. Guillot, J. Couzinié, G. Dirras, Analysis of the fatigue crack growth mechanisms in equimolar body centered cubic HfNbTaTiZr high-entropy alloy: discussions on its singularities and consequences on the crack propagation rate properties, Intermetallics 110 (2019) 106459, https://doi.org/10.1016/j.intermet.2019.04.002

[46] B. Voloskov, S. Evlashin, S. Dagesyan, S. Abaimov, I. Akhatov, I. Sergeichev, Very high cycle fatigue behavior of additively manufactured 316L stainless steel, Materials 13 (2020) 3293, https://doi.org/10.3390/ma13153293

Chapter 5

Significance of grain refinement on micro-mechanical properties and structures of additively-manufactured CoCrFeNi high-entropy alloy

Further research is being conducted on AM HEA materials to explore the effects of post-treatments on their properties. One particular focus is on grain refinement, which has proven to be a successful method for enhancing strength characteristics. Additionally, the analysis of the printed material properties and behavior after a high loading allows a better understanding of its possible structural application conditions and ways of property improvement, particularly, by grain refinement. Various techniques can be used to create fine-grained materials, including multiple forging, equal-channel angular pressing, and HPT. For this study, the HPT method was chosen as the most suitable option due to its ability to maintain the sample shape and easily achieve high deformations without damaging the material having comparably low ductility.

The process of HPT is illustrated in Fig.5-1. By applying pressure to the upper

plunger and controlling the rotation of the lower plunger, the desired level of deformation can be easily attained. Moreover, the HPT method can be considered as an effective process in minimizing defects such as pores or uneven element distribution in AM metal materials, particularly when used for *in situ* printing.
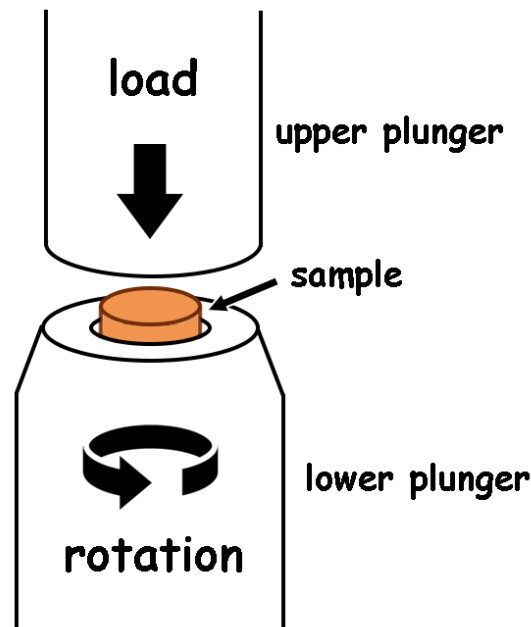
Figure 5-1: The scheme of the HPT process.

In this chapter, the effects of grain refinement on a CoCrFeNi HEA fabricated through the PBF technique in comparison with the as-cast material is studied, which underwent HPT grain refinement. It reveals that Vickers microhardness indicates an increase in strain hardenability of printed HEA, while nanoindentation shows enhanced plasticity. This suggests the potential for high ductility in the material. Additionally, XRD analysis of an AM CoCrFeNi HEA prepared using laser PBF and subsequent HPT at room temperature reveals structural evolution with grain refinement in the HEA, providing an insight into the rate-controlling mechanism of grain boundary-mediated dislocation activity. These findings highlight the significance of grain refinement in advancing the AM technology of HEAs.

Contribution: I contributed to the development of the microstructural analyses and related sample preparation procedures and the editing of the manuscript. I would like to thank all the authors for their valuable contributions to the development of this paper.
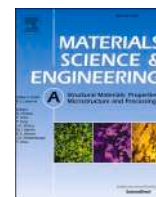
Significance of grain refinement on micro-mechanical properties and structures of additively-manufactured CoCrFeNi high-entropy alloy

Wenrui Zhao [a], Jae-Kyung Han [a], Yulia O. Kuzminova [b], Stanislav A. Evlashin [b], Alexander P. Zhilyaev [c,d], Alexander M. Pesin [c], Jae-il Jang [e], Klaus-Dieter Liss [f,g,c], Megumi Kawasaki [a,c,*]

[a] School of Mechanical, Industrial and Manufacturing Engineering, Oregon State University, Corvallis, OR, 97331, USA
[b] Center for Design, Manufacturing & Materials, Skolkovo Institute of Science and Technology, Moscow, 143026, Russia
[c] Laboratory of Mechanics of Gradient Nanomaterials, Nosov Magnitogorsk State Technical University, Magnitogorsk, 455000, Russia
[d] Institute for Metals Superplasticity Problems, Ufa, 450001, Russia
[e] Division of Materials Science and Engineering, Hanyang University, Seoul, 04763, Republic of Korea
[f] Materials and Engineering Science Program, Guangdong Technion - Israel Institute of Technology, Shantou, Guangdong, 515063, China
[g] Technion - Israel Institute of Technology, Haifa, 32000, Israel

ARTICLE INFO

ABSTRACT

Grain refinement is an effective approach to improve mechanical properties of conventionally-manufactured high entropy alloys (HEAs). Additive manufacturing of HEAs is a new materials challenge and increasing reports are available for exploring the optimal processing parameters and post-manufacturing treatments to advance the physical and mechanical properties of additively-manufactured (AM) HEAs. At the current stage of the development of AM HEAs, it is necessary to investigate the significance of grain refinement on their mechanical properties and structures. In the present study, a CoCrFeNi HEA is manufactured by a laser powder-bed fusion technique using pre-alloyed HEA powders on which grain refinement was conducted by high-pressure torsion for up to 8 turns under 6 GPa at room temperature. The results from nanoindentation and Vickers microhardness testing demonstrate high strain hardening capability and increased plasticity, thus potentially high ductility, in the nanostructured AM CoCrFeNi HEA. X-ray diffraction analysis demonstrates the structural evolution with decreasing crystallite size, increasing microstrain and expanding lattice parameter with grain refinement in the HEA. The structural changes justify the estimation by nanoindentation of the rate-controlling mechanism of the grain boundary-mediated dislocation activity for the nanostructured AM HEA. This study provides advantages of nanostructuring for current developments in the AM technology of HEAs.

1. Introduction

A breakthrough of traditional alloy design involving a principle element with additions of minor elements was achieved by an introduction of high-entropy alloys (HEAs) having multiple principle elements with equiatomic or near equiatomic configurations that often lead to a simple crystalline structure [1–3]. Numerous research studies in the last decade described the superior mechanical properties of HEAs and their structural changes at a wide range of temperatures, and these intensive studies yielded several reviews in literature. Specifically, several reviews placed their special focuses on physical properties including magnetic, electrical and thermal properties [4], structure and

phase balance [5,6] and the thermodynamic concepts [7] of HEAs, while additional reviews focus more on general mechanical properties and deformation mechanisms [8,9] as well as fracture and magnetization [10] and corrosion resistance [11] of HEAs. Moreover, a recent report summarized the mechanical behavior of HEAs having heterogeneous microstructures [12].

Bulk HEAs have been produced by a conventionally-manufactured (CM) approach of melting and casting as well as solid-state techniques of mechanical alloying [13,14]. Thin film deposition and sputtering of HEAs are also developed for coating purposes [15,16]. Nevertheless, the majority of the research and applications use bulk HEAs and processing of nanocrystalline HEAs has become one of the major topics in the

society. Applications of severe plastic deformation is a well-recognized procedure for processing of bulk nanocrystalline metals and alloys [17], and it was utilized for nanocrystallization of bulk HEAs. Specifically, as far as CM HEAs with an *f.c.c.* single phase or an *f.c.c.* major phase, equal-channel angular pressing (ECAP) was conducted on a CoCrFeNiMn alloy [18], and high-pressure torsion (HPT) was applied on CoCrFeNi alloy [19], CoCrFeNiMn alloys [20–28], $Al_{0.1-0.3}$CoCrFeNi alloys [29,30] and a $(CoCuFeNi)_{1-x}Ti_xAl_x$ alloy [19]. Moreover, HPT was applied for sintering of mechanically-alloyed powders leading to an HPT-induced CoCrFeNiMn alloy [31]. Grain refinement at the surfaces of HEAs are reported by applying an ultrasonic surface mechanical attrition treatment (SMAT) on CM CoNiCrMn and FeCoNiCrMn–Al HEAs [32].

Additive manufacturing of HEAs is a new materials challenge and earlier representative studies were reported in 2015 [33,34]. Increasing reports are available in the last five years for exploring the optimal AM processing parameters to advance the physical and mechanical properties of additively-manufactured (AM) HEAs and the several summaries are published elsewhere [35–39]. Although advantages of high efficiency of additive manufacturing in the metal production processes attracted much attentions to AM HEAs, the post-treatments for surface hardening by laser shock peening on an AM CoCrFeMnNi alloy [40] and aerosol deposition on an AM $Fe_{40}(CoCrMnNi)_{60}$ alloy [41] reveal the necessity of post-manufacturing treatments in the current AM HEAs as well as the feasibility of grain refinement on cultivating the existing good mechanical properties in the AM HEAs.

Accordingly, at the current early stage of development in AM HEAs, it is indispensable to investigate the significance of grain refinement in bulk volume on mechanical properties and structural changes. The present study demonstrates an improved strain hardenability by Vickers microhardness and enhanced plasticity by nanoindentation, thereby a potential for exhibiting high ductilities, and the detailed structural changes at different processing stages of AM and grain refinement by X-ray diffraction analysis of an AM CoCrFeNi HEA prepared by a laser powder-bed fusion technique followed by HPT at room temperature. This study informs the importance of grain refinement in the current advancement for the AM technology of HEAs.

2. Materials and experimental procedure

The CoCrFeNi HEA powders with the atomic fractions of 24 at.% Co, 26 at.% Cr, 25 at.% Fe, and 25 at.% Ni were produced by the atomization spraying method leading to powders with spherical morphology [38, 42]. Additive manufacturing of the bulk CoCrFeNi HEA was conducted by the Powder Bed Fusion (PBF) technology with a laser heat source (PBF-L) using a metal 3D printer, Trumpf TruPrint 1000. The bar-shaped cylindrical samples were printed (or built), where the lengths of the bars of ~8.5 cm is along the build direction and a diameter of the cross-section is 12.0 mm. The applied parameters for the printing process were set at a laser power of 150 W, a laser speed of 600 mm/s, a laser spot diameter of 55 μm, hatch spacing of 80 μm, and a layer thickness of 20 μm. The printing process was performed in an inert atmosphere (Ar) with a gas feed velocity of 2.5 m/s at a chamber pressure of 1 bar. The oxygen level was kept within 0.3 at.%. Detailed procedures of additive manufacturing for the HEA are described in an earlier study, where an average particle size of the HEA powders is 35–40 μm [43]. For comparison purposes, a conventionally-manufactured (CM) cast $Co_{25}Cr_{25}Fe_{25}Ni_{25}$ HEA was prepared in this study. A billet of the CM CoCrFeNi HEA was produced by vacuum induction melting of the alloy components having purity of >99.9 wt% followed by drop-casting. The cast ingot was subjected to hot-rolling at 1050 °C with a thickness reduction ratio of 64% and then annealing at 1100 °C for 1 h to achieve a homogenized microstructure. An earlier study showed that the solutionized CM CoCrFeNi HEA has an average grain size of ~57 ± 20 μm [26].

The prepared bars of the AM CoCrFeNi HEA were machined to have a

cross-section diameter of 10 mm and sliced into disks with thicknesses of ~0.85 mm by wire-cut electrical discharge machining. A set of disks was polished down to have final parallel thicknesses of ~0.83 mm and processed by HPT under quasi-constrained conditions at room temperature. The disks were processed under a compressive pressure of 6.0 GPa and a rotational speed of 1 rpm for total numbers of revolution, *N*, of 1/ 2, 1, 2, 4 and 8 turns for the AM HEA samples. These HPT-processed disks were cut into halves along the diameters and these were mold for polishing their vertical cross-sections. The surfaces were mechanically polished with 0.5 μm alumina powders with ethanol and 0.05 μm silica suspension to obtain mirror-like surfaces. Consistent sample preparations were applied for the CM HEA and the sample was processed for 1/2 and 5 HPT turns.

Vickers microhardness measurements were conducted to profile the hardness variations along the disk diameters on the polished vertical cross-sections of both CoCrFeNi HEA before and after HPT. The Vickers microhardness values, H_V, were recorded using a Mitutoyo HM-200 with an applied load of 100 gf and a dwell time of 10 s. The structural evolution of the AM HEA was examined at the conditions of initial powders, as-built without HPT and after HPT processing by X-ray powder diffraction (XRD) employing a Bruker D8 ADVANCE, using Cu K_α radiation at an incremental time of 3.0 s and a step size of 0.005° on slightly polished disk surfaces.

Microstructural examinations were conducted using scanning electron microscopy (SEM) for the AM HEA in an as-built condition and using transmission electron microscopy (TEM) after HPT processing. An as-built surface vertical to the building direction of the AM CoCrFeNi HEA was mechanically polished with 40 nm silica suspension followed by electrochemical polishing in an electrolyte of 900 ml of butanol C_4H_9OH + 100 ml of perchloric acid $HClO_4$ at room temperature. SEM analysis was conducted using Carl Zeiss Supra 40. The TEM observations were conducted by high resolution TEM, HRTEM-Philips CM200 and Philips C2100, at an accelerating voltage of 200 kV. Conventional mechanical polishing was applied to prepare the TEM samples. The AM HEA after HPT was first cut and then ground to a thickness of lower than 100 μm using grade 1000 abrasive paper. A series of 3 mm disks were punched out at *r* of ~3.5 mm in each disk sample, where *r* is the radius from the disk center. Using diamond paste, the punched samples were then polished and ion milled for thinning in the final step.

The micro-mechanical properties were examined at the disk edges of the AM and CM CoCrFeNi HEA before after HPT using a nanoindentation facility, Nanoindenter-XP, with a three-sided pyramidal Berkovich indenter having a center-line-to-face angle of 65.3°. More than 15 indentations were conducted at each testing condition for all samples to achieve statistically valid data. All measurements were conducted under a predetermined maximum applied load of P_{max} = 50 mN at constant indentation strain rates, $\dot{\varepsilon}_i$, of 0.0125, 0.025, 0.05, and 0.1 s^{-1}, which are equivalent to general strain rates, $\dot{\varepsilon}$, of 1.25×10^{-4}, 2.5×10^{-4}, 5.0×10^{-4}, and 1.0×10^{-3} s^{-1}, respectively, by taking account of the empirical relation of $\dot{\varepsilon} \approx 0.01\dot{\varepsilon}_i$ [44].

3. Experimental results

3.1. Hardness development

Fig. 1 shows the Vickers microhardness distributions along the radius of the disks of (a) AM HEA and (b) CM HEA before and after HPT processing. The plots represent the hardness variations over the disk surfaces, since, as defined by the principles of HPT processing [45], the evolution of hardness is generally with radial symmetry in the HPT-processed disks. The dashed horizontal line in each plot denotes the initial average hardness value of $H_V \approx 260$ and ~160 for the AM and CM CoCrFeNi HEA, respectively. These measured hardness values in the present study are in a reasonable range with the reported values of H_V = 238 and 118 for a CoCrFeNi HEA manufactured by a powder-bed AM technique and a CM technique by casting, respectively [34]. A higher
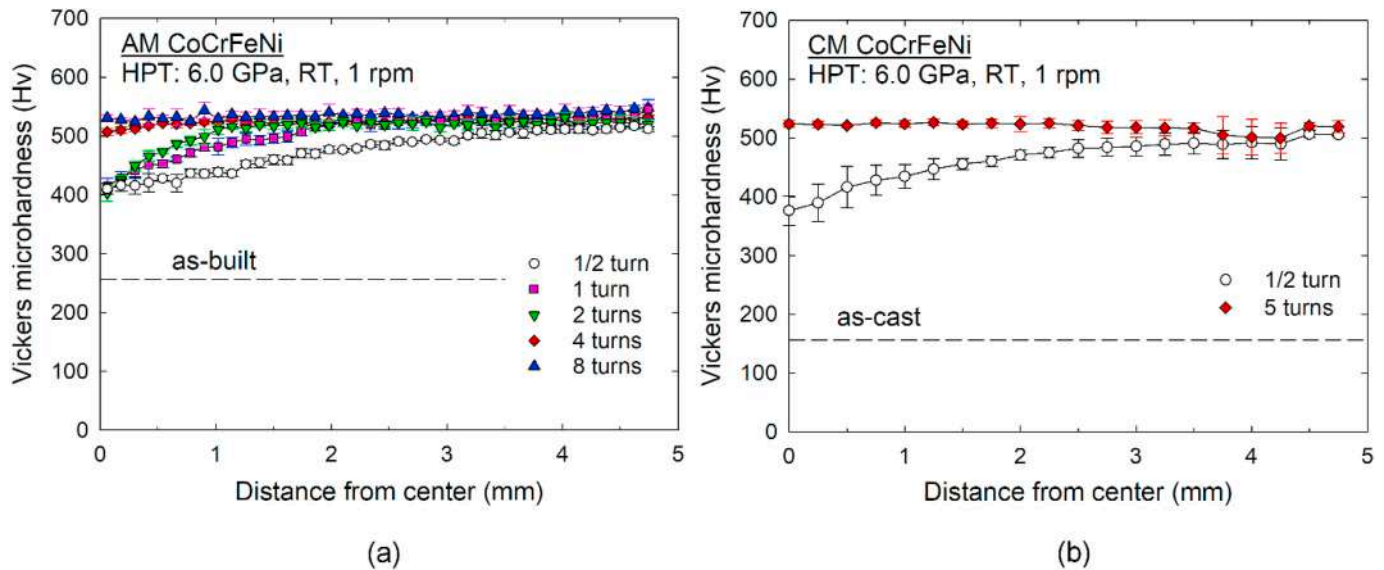
Fig. 1. Vickers microhardness distributions along the radius of the disks of (a) AM CoCrFeNi HEA and (b) CM CoCrFeNi HEA before and after HPT processing.

hardness of the AM HEA than the CM HEA is attributed to the different microstructures introduced by the different processing routes. The result is in good agreement with an earlier report demonstrating significantly higher yield strengths of ~500–510 MPa in an as-built CoCrFeNiMn alloy through selective laser melting with different laser scanning speeds than ~200 MPa for the as-cast CoCrFeNiMn alloy [46]. The high strength in the as-built alloy was attributed to the processing procedure enabling the formation of hierarchical cellular microstructure that led to a large contribution to dislocation strengthening.

The AM HEA shows a significant hardness increase to $H_V = 400$ at the center of the disk after 1/2 turn by HPT and the hardness gradually increases to ~510 towards the disk edge as shown in Fig. 1(a). Increasing numbers of HPT turns to 1 and 2, the central region of the disk having low hardness shrinks and the region with high hardness of $H_V = 525$ extends at $r > 2.0$ mm. Ultimately, the hardness value reaches saturation at $H_V = 525$ throughout the disk diameter after 4 and 8 HPT turns of grain refinement. A consistent trend of hardness evolution was observed in the CM HEA after HPT for 1/2 turn as shown in Fig. 1(b), where the hardness value increases to $H_V = 375$ at the disk center and further increases to 500 towards the disk edge. Homogeneously distributed high hardness of $H_V = 525$ in saturation was observed across the disk radius after 5 HPT turns. The results suggest that the CoCrFeNi HEA manufactured by the different procedures enable the demonstration of a consistent upper hardness limit at $H_V = 525$ after severe deformation by sufficient HPT turns of over 4–5. It should be noted that a hot-isostatic processed $Al_{0.1}CoCrFeNi$ alloy after mechanical alloying of powders processed by HPT for 2 turns showed a significant increase in hardness from $H_V = 135$ to 482 [30]. Moreover, reasonably similar high hardness was proclaimed in several CM HEAs having an *f.c.c.* crystal structure after HPT: an $Al_{0.3}CoCrFeNi$ alloy ($H_V \approx 530$ after 8 turns [29]), CoCrNiFeMn alloys ($H_V \approx 520$ after 5 turns [20], 486 ± 15 at the disk edge after 2 turns [21], and 450 after 10 turns [22]), and a $(FeNiCoCu)_{86}Ti_7Al_7$ alloy ($H_V = 525$ after 10 turns [19]).

3.2. Microstructural evolution

Fig. 2 shows the XRD patterns measured at the overall mid-thickness disk surfaces of the AM CoCrFeNi HEA disks in the conditions of, from top, atomized powders, as-built, and after HPT for 1/2, 1, 2, 4, and 8 turns. There are three notable features in Fig. 2. First, all major peaks in each sample condition are determined as a pure *f.c.c.* structure, such as 111, 200, 220, 331, and 222 (indexed in red), thereby implying a
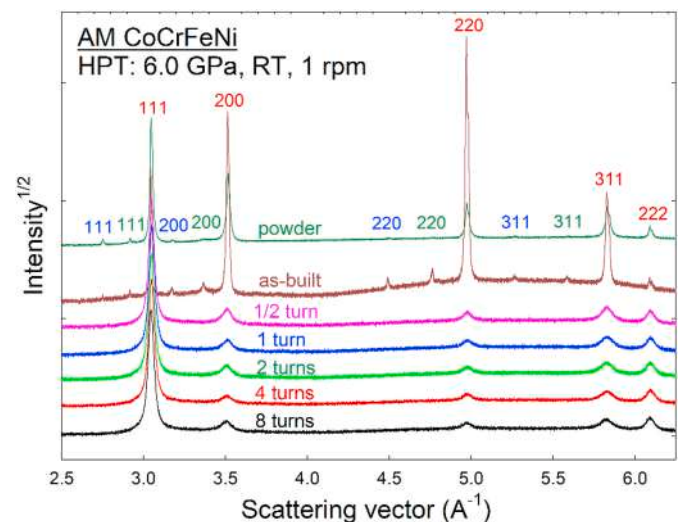
Fig. 2. XRD patterns taken at overall disk surfaces at the mid-thickness of the CoCrFeNi HEA disks in the conditions of, from the top, atomized powders, as-built, and after HPT for 1/2, 1, 2, 4, 8 turns.

presence of an *f.c.c.* primary phase. Second, two additional sets of weak *f.c.c.* peaks (noted in blue and green) are detected for the CoCrFeNi HEA in powders and an as-built condition, whereas there remains only the *f.c.c.* primary phase in the HEA after HPT processing. Due to the weak relative intensity of the additional sets of the *f.c.c.* peaks, it is estimated that the volume fractions of these minor *f.c.c.* phases are close to the detection limit of XRD of ~5 vol.%. Peak position analysis provided the lattice parameters of $a = 3.572$ Å for the primary *f.c.c.* phase and 3.729 Å and 3.954 Å for the two minor *f.c.c.* phases with peaks indexed in green and blue, respectively, for the HEA in a powder condition. The measured lattice parameters for the minor *f.c.c.* phases confirm these are neither the commonly observed phases, such as *b.c.c.* phase and σ phase involving Cr, for the *f.c.c.* CoCrFeNi-based HEAs manufactured by mechanical alloying and sintering at 600–900°C [47,48] nor any possible oxides. A possibility of the additional *f.c.c.* phases may be attributed to the heterogeneous distributions of the HEA elements in powders and an as-built condition, where non-equimolar CoCrFeNi-based HEAs show variations in lattice parameter from $a = 3.58$ Å for equimolar CoCrFeNi-based HEAs [27,49,50]. Third, there is apparent peak

broadening after HPT in each major *f.c.c.* peak in comparison with those for the powders and as-built HEA indicating a refined crystallite size with defects. The peak broadening becomes further augmented with increasing numbers of HPT turns.

Fig. 3 shows representative backscattered electron (BSE) images in (a) low and (b) high magnifications of the as-built sample, and the TEM bright-field images of the AM CoCrFeNi alloy after HPT for (c) 1 turn and (d) 8 turns. These BSE micrographs were taken on the sample surfaces normal to the building direction. The TEM images include the corresponding selected-area diffraction (SAED) patterns. It is apparent from Fig. 3(a) that there is a duplex microstructure consisting of the elongated phases with 50–55 μm lengths which are associated with the laser spot diameter. Between the neighboring tracks, nearly equiaxed microstructures having a phase size of <10 μm is observed and it is due to the overlaps of the neighboring laser tracks leading to re-melting and recrystallization of the as-built phase. A typical granular configuration in the as-built materials is displayed with cellular sizes of ~1.0 μm as shown in Fig. 3(b). The observed as-built microstructure is well consistent with that of the Cantor alloy manufactured by the laser additive manufacturing methods [39].

The TEM micrographs describe the significant grain refinement in the microstructure of the AM HEA by severe plastic deformation. In practice, the grains are reasonably equiaxed even after 1 HPT turn in Fig. 3(c) and the ultrafine-grained microstructure continues through 8 HPT turns in Fig. 3(d), while the severe deformation introduces many dislocations around grain boundaries. The estimated average spatial grain sizes of the HEA are $d \approx 105$ nm and ~90 nm after 1 and 8 turns, respectively. The TEM observation was conducted at $r \approx 3.5$ mm, and it is reasonable to conclude that the microstructure was severely refined and saturated at $r \approx 3.5$ mm even after 1 HPT turn. The result is fully consistent with the saturated Vickers microhardness value after 1 turn at $r \approx 3.5$ mm as shown in Fig. 1(a). The SAED patterns for both 1 and 8 turns confirm the presence of a single *f.c.c.* phase within the inspected regions. It should be noted that the observed ultrafine grain sizes of the

AM HEA are in good agreement with the earlier study showing $d \approx 77 \pm 31$, ~46 ± 16, and ~45 ± 15 nm after 1/4, 2 and 5 HPT turns, respectively, for the CM CoCrFeNi HEA [4], and the agreement in grain size is resulted in the consistent saturation hardness in the CoCrFeNi HEA as was shown in Fig. 1(a) and (b). It is worth noting that, while the current processing pressure of 6 GPa failed to show phase transformation in the *f.c.c.* CoCrFeNi HEA, an *f.c.c.* CoCrFeNiMn HEA starts to demonstrate *f.c.c.*-to-*h.c.p.* transformations under a high pressure of 14 GPa [51], while the *f.c.c.*-to-*h.c.p.* transition is sluggish in aluminum requiring ~50 GPa pressure [52].

3.3. Micro-mechanical properties of HEA

Nanoindentation was applied to investigate the micro-mechanical properties at the disk edges of the AM HEA in an as-built condition and after HPT for 8 turns and of the CM HEA after HPT for 5 turns. Nanoindentation is an advantageous technique to acquire the mechanical properties from small sample volumes, and it is beneficial to utilize the technique for small bulk samples including the HPT-processed disks [53]. Nanoindentation is even utilized for the advancement of CM HEAs [23,54]. Fig. 4 shows the representative load-displacement curves measured at four equivalent strain rates from 1.25×10^{-4} to 1.0×10^{-3} s^{-1} at the disk edges of (a) the AM sample in an as-built condition and after HPT for 8 turns and (b) the CM HEA after HPT for 5 turns. Each curve is the average of at least 15 separate measurements.

The AM HEA after HPT for 8 turns shows smaller displacements than the HEA in an as-built condition at all strain rates as shown in Fig. 4(a). Thus, the AM HEA after grain refinement demonstrated higher hardness than the as-built HEA. Closer observation shows that the displacements are reasonably similar for both AM and CM HEA after HPT at all strain rates. The result indicates the consistent strength at each indentation strain rate and it is in an excellent agreement with the results from Vickers microhardness testing. All samples in Fig. 4(a) and (b) show positive strain rate dependency before and after grain refinement.
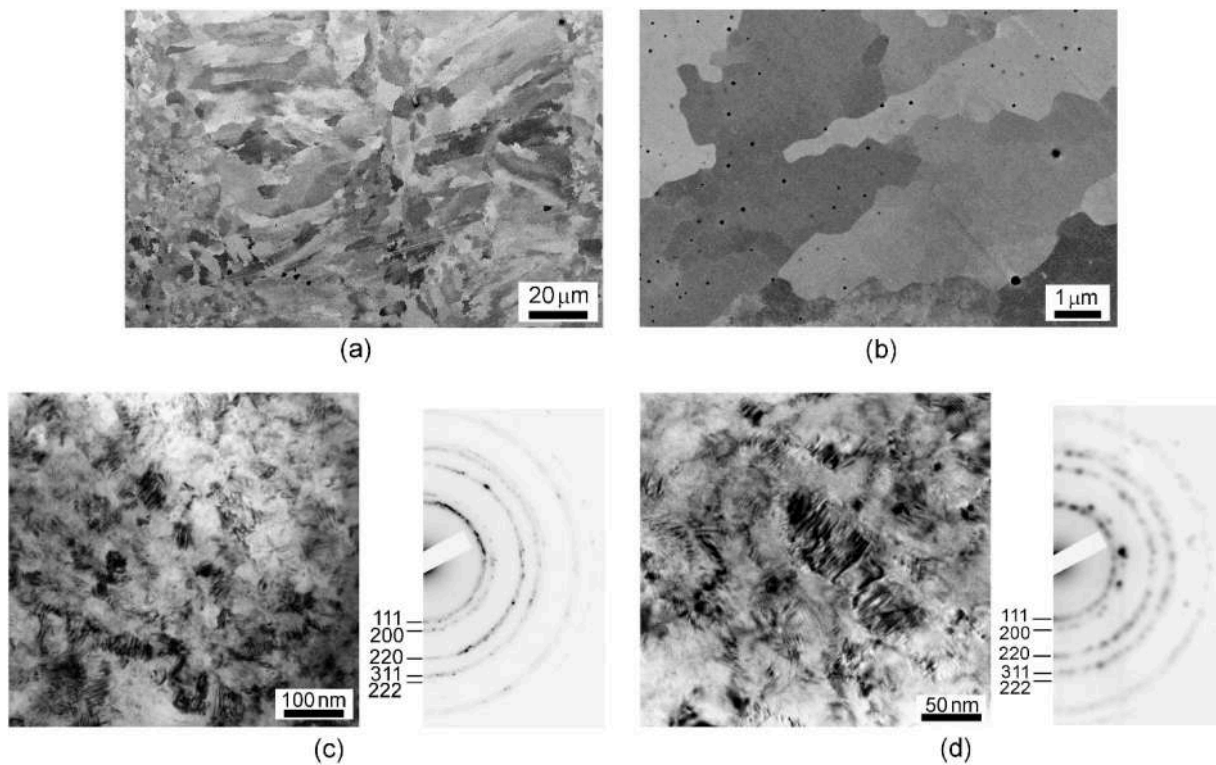

Fig. 3. Representative backscattered electron images in (a) low and (b) high magnifications of the as-built sample, and the TEM bright-field images of the AM CoCrFeNi alloy after HPT for (c) 1 turn and (d) 8 turns by HPT.
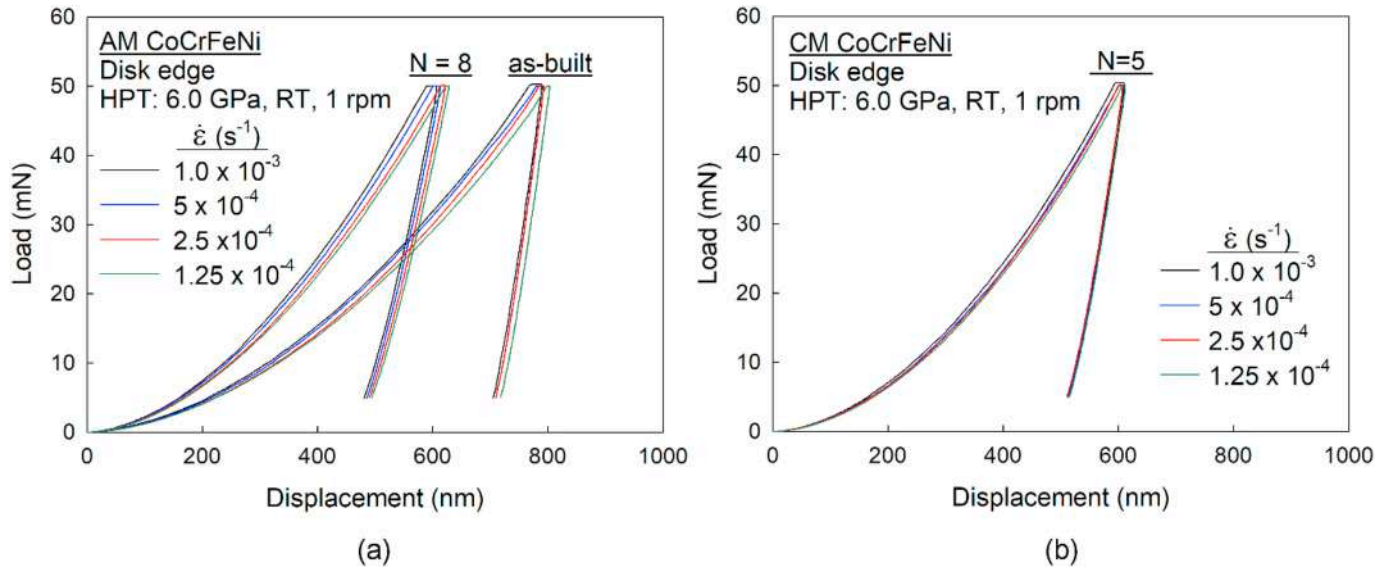
Fig. 4. Representative load-displacement curves measured at four equivalent strain rates from 1.25×10^{-4} to 1.0×10^{-3} s^{-1} at the disk edges of (a) AM sample in an as-built condition and after HPT for 8 turns and (b) CM HEA after HPT for 5 turns.

4. Discussion

4.1. Strain hardening of an AM CoCrFeNi HEA

A hardness increase in polycrystalline materials can be well defined by the Hall-Petch relationship [55,56], and the relationship between grain refinement and hardness was demonstrated earlier for a CM CoCrFeNiMn HEA after HPT up to 2 turns [21]. Specifically, severe torsion straining enabled the activation of atomic diffusion in the CoCrFeNiMn HEA leading to the significant microstructural evolution, while HEAs are well known for their sluggish diffusion [6,57]. Thus, it is anticipated that the microstructural refinement provides a major contribution to an increase in hardness of the present AM CoCrFeNi HEA. In order to understand the hardening behavior of the HEA during grain refinement processing, it is indispensable to apply an approach considering the equivalent strain introduced during HPT processing, $\varepsilon_{eq} = 2\pi Nr/(\sqrt{3}h)$ [45] where h is the thickness of the disk sample. In the present analysis, $h = 0.7$ mm was applied since a small volume of the material flows out under the quasi-constrained HPT set-up during compression and an early torsional stage, thereafter it remains reasonably constant up to 8 turns by HPT.

Fig. 5 shows the relationship between Vickers microhardness and the equivalent strain for the AM HEA after HPT through 8 turns. It is apparent that the hardness drastically increases with increasing equivalent strain in an early stage of HPT up to $\varepsilon_{eq} \approx 12$, thereafter the hardness becomes saturated at the maximum hardness of $H_V = 525$. Such hardness evolution with increasing equivalent strain is defined as a model of strain hardening without recovery during severe plastic deformation [58]. Although the plot is not shown, the CM HEA demonstrated the consistent hardness behavior. It should be emphasized that an equivalent strain of ~12 leading to the upper limit of the saturation hardness is consistent in both AM and CM HEA, while these have different processing routes that cause different initial hardness before HPT.

Further inspection of strain hardening behavior during deformation was conducted quantitatively by estimating the extent of strain hardening through the computation of the hardenability exponent, η. Thus, a linear plot showing hardness versus equivalent strain in Fig. 5 was replotted into a double-natural logarithmic plot and it is shown in Fig. 6 for (a) AM HEA and (b) CM HEA after HPT. The red and blue dotted trend lines describe two separate stages of the hardness developments
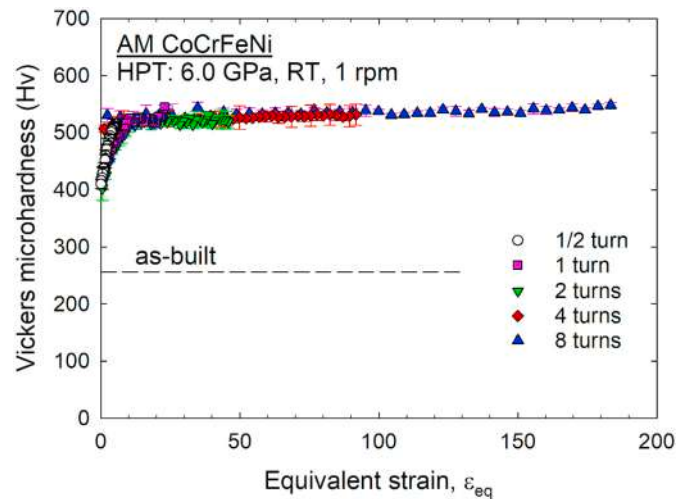
Fig. 5. Plot showing a relationship between Vickers microhardness and the equivalent strain for the AM HEA after HPT through 8 turns.

during grain refinement, and the values of η represent the slopes of those trend lines in the double-natural logarithmic plots. The transitions of strain hardening behaviors where the red and blue dotted lines intersect occur at $\ln(\varepsilon_{eq}) \approx 2.5$, thus $\varepsilon_{eq} \approx 12$, for both HEA. Considering the plots shown in Fig. 5, there is a significant hardness increase with high strain hardening up to $\varepsilon_{eq} \approx 12$.

The red dashed lines in Fig. 6(a) and (b) enable quantitative expressions of strain hardening in the early stage of deformation towards grain refinement. The present CoCrFeNi alloy demonstrated reasonably similar values of strain hardening exponent of $\eta = 0.0859$ and 0.0871 in the AM and CM conditions, respectively, indicating that the processing of the starting material is less relevant in this stage of deformation. It is reasonable to note that a limited number of earlier reports demonstrate the strain hardening exponents of $\eta = 0.08$ for an AZ31 Mg alloy [59], $\eta = 0.07$ for a ZK60 Mg alloy [60], $\eta = 0.031$ for an Ti–6Al–4V alloy [61], and $\eta = 0.017$ for a Zn–3Mg alloy [62] after HPT for $\varepsilon_{eq} <20$ that is equivalent to $\ln(\varepsilon_{eq}) <3.0$. Thus, it is apparent with comparing these reference values that the present HEAs demonstrate significantly high η, thereby exhibiting the high hardenability in an early stage of
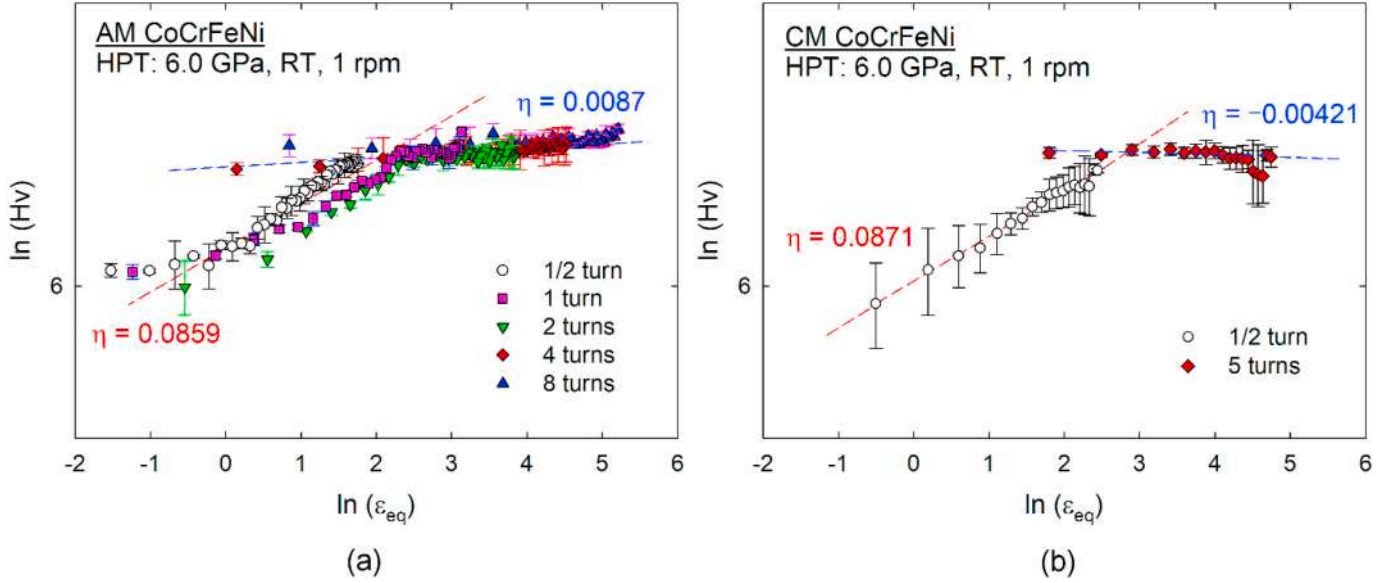
Fig. 6. Double-natural logarithmic plots of hardness versus equivalent strain for (a) AM HEA and (b) CM HEA after HPT.

deformation.

The hardness evolution tends to be stable beyond $\varepsilon_{eq} \approx 12$ according to the hardness measurements in Figs. 1 and 5, but it is notable with this analysis that the AM HEA show a positive strain hardening exponent of $\eta = 0.0087$ at the stable hardness evolution stage, while the CM HEA shows a negative value of $\eta = -0.0042$. It provides an excellent demonstration of the improved strain hardenability under plastic deformation with grain refinement in the AM CoCrFeNi HEA.

4.2. Micro-mechanical properties of an AM CoCrFeNi HEA

The load-displacement curves obtained through nanoindentation are used to analyze two important characteristics of materials, strain rate sensitivity, m, and the activation volume, V^*. Although the measurements were conducted at the disk edges, the hardness homogeneity was achieved after HPT for high numbers of turns as seen in Fig. 1 and it is reasonable to assume that the nanoindentation results represent the mechanical properties of the entire disk volumes of the HEA.

The value of m is calculated at a given strain, ε, and absolute temperature, T, by estimating the uniaxial flow stress, σ_f, by Tabor's empirical relation of $\sigma_f \approx H/C$ where C is a constrain factor of ~3 for fully plastic deformation at constant strain rates, $\dot{\varepsilon}$ [63] and H is the nanoindentation hardness estimated according to the Oliver-Pharr method [64],

$$m = \left(\frac{\partial ln\sigma_f}{\partial ln\dot{\varepsilon}}\right)_{\varepsilon,T} = \left(\frac{\partial ln(H/3)}{\partial ln\dot{\varepsilon}}\right)_{\varepsilon,T} \qquad (1)$$

Thus, the value of m is estimated from the slope of a double logarithmic plot of $H/3$ vs. $\dot{\varepsilon}$. The activation volume, V^*, is calculated by the following equation,

$$V^* = \sqrt{3}kT\left(\frac{\partial ln\dot{\varepsilon}}{\partial \sigma_f}\right)_{\varepsilon,T} = \sqrt{3}kT\left(\frac{\partial ln\dot{\varepsilon}}{\partial (H/3)}\right)_{\varepsilon,T} \qquad (2)$$

where k is Boltzmann's constant.

Fig. 7 shows a double logarithmic plot of $H/3$ vs. $\dot{\varepsilon}$ for the AM HEA in an as-built condition and after HPT for 8 turns. The results for the CM HEA in an as-cast condition [26] and after HPT for 5 turns were shown together for comparison purposes. It is apparent that the m values improved from 0.046 to 0.058 by grain refinement in the AM HEA. The same trend is seen in the CM HEA with m values of 0.026 [26] and 0.031 before and after HPT, respectively, while the values for the CM HEA are
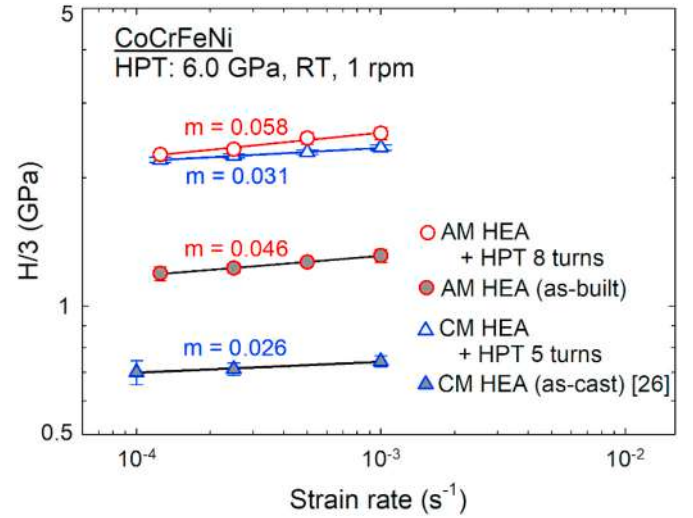
Fig. 7. Double logarithmic plot of $H/3$ vs. $\dot{\varepsilon}$ for the AM HEA in an as-built condition before HPT and after HPT for 8 turns. The results for the CM HEA in an as-cast condition [26] and after HPT for 5 turns were shown together.

lower and the improvement in m is less apparent than the AM samples. The reason may be attributed to the different manufacturing routes leading to the divergent initial bulk structures of the HEA before grain refinement by HPT, and it requires further experiments to identify the reason. Nevertheless, the improved strain rate sensitivity as well as the improved strain hardening capability discussed in an earlier section imply the significant potential of demonstrating high ductility in the AM HEA after grain refinement via HPT, while the HEA exhibits excellent hardness and strength.

It should be noted that the computed m values for both AM and CM CoCrFeNi HEA are valid according to the recent reports estimating the m values for CoCrFeNi alloys as $m = 0.044$ after production by induction melting having a grain size of 21.84 μm [65] and as $m = 0.068$ after manufacturing by magnetron sputtering having a crystallite size of ~7.8 nm [66]. Moreover, several *f.c.c.* HEAs demonstrate the m values between 0.02 and 0.07 [67]. The present AM HEA alloy before grain refinement demonstrates over one order of magnitude higher m value than simple coarse-grained *f.c.c.* metals, such as pure Ni showing $m \approx$

0.0028 [68]. Nevertheless, these simple *f.c.c.* metals increases strain rate sensitivity significantly with grain refinement [52,69] and the present HEAs follow the trend of simple *f.c.c.* metals by increasing *m* values with grain refinement.

The estimated activation volumes are $V^* = 7.64b^3$ and $3.20b^3$ for the AM HEA in an as-built condition and after HPT for 8 turns, respectively, where *b* is the Burgers vector and was calculated by $b = a_0 \times \sqrt{2}/2 \approx 2.25 \times 10^{-10}$ *m* with applying the lattice parameter, a_0, of 3.57 Å for the present HEA powders measured by XRD as well as the reported value for a CoCrFeNi alloy [50,70]. The same way of calculation yielded $V^* = 20.0b^3$ and $6.22b^3$ for the CM CoCrFeNi alloy before and after processing for 5 HPT turns, respectively. Earlier reports discuss the values of V^* vary by three orders of magnitude from $\sim 1b^3$ to $1000b^3$ depending on the different rate-limiting deformation processes of crystalline materials [71–73]. There is a report discussing the chemical short-range ordering of Cr in the atomic structure of HEAs [74], and such ordering may further contribute to the high friction stress in the HEA leading to an influence on the thermal activated process, thereby lowering the V^* value of the HEA in comparison with the defined values for the general *f.c.c.* metals. It is currently under debate in the estimation of V^* and its correlation with *m* for HEAs [67]. Nevertheless, the V^* values for the nanostructured HEA are in a vicinity of $\sim 10b^3$ in the present study and it is anticipated that the deformation mechanism is by grain boundary-mediated dislocation activity.

4.3. Structural evolution during grain refinement

The XRD line profiles were analyzed by applying the Williamson-Hall method for evaluating the structural changes in the AM HEA during additive manufacturing and grain refinement. A Williamson-Hall plot is shown in Fig. 8 where the full width at half maximum (FWHM), *ΔQ*, of the XRD peak profiles are plotted against the scattering vector, *Q*. Thus, microstrain, $\varepsilon = \Delta Q/Q$, and the crystallite size are calculated from the slope and the reciprocal of y-intercept at $Q = 0$ of the fitted line,

respectively [75], for each sample condition. In this procedure, the selected X-ray diffraction data from the available close-packed family planes of 111 and 222 at $Q = 3.05$ and 6.09 Å^{-1} were selected for the samples after grain refinement, so that the coherent crystallite sizes can be estimated by ignoring the smaller coherent sizes yielding larger peak broadening at the out-of-close-packed-plane coordinates of 200, 220 and 311 appearing at $Q = 3.50$, 4.97 and 5.82 Å^{-1}. The latter reveal much wider peaks than the linear regression for the close-packed plane co-ordinates in each sample condition, disclosing significantly reduced coherent crystal sizes and larger strain gradients in those directions. Moreover, the larger broadening of the 200, 220 and 311 peaks for the HPT-processed material testify to reduced coherent crystal sizes due to interception by dislocations and planar faulting, which is consistent with the postulate of large numbers of dislocations showing grain boundary-mediated dislocation activity as the deformation mechanism of the nanocrystalline AM HEA. Four plane coordinates of 111, 200, 220, and 311 are used for the powder and as-built samples.

The estimated crystallite size and micro-strain are summarized in Table 1 for the AM CoCrFeNi in powders, as-built, and after HPT for up to 8 turns. The crystallite size of ~ 460 nm in powders increased to ~ 650 nm after the AM process, and it is influenced by the manufacturing

Table 1
Summary of estimated crystallite size, microstrain and lattice parameters for the AM CoCrFeNi HEA in the conditions of powders, and after additive manufacturing and HPT for up to 8 turns.

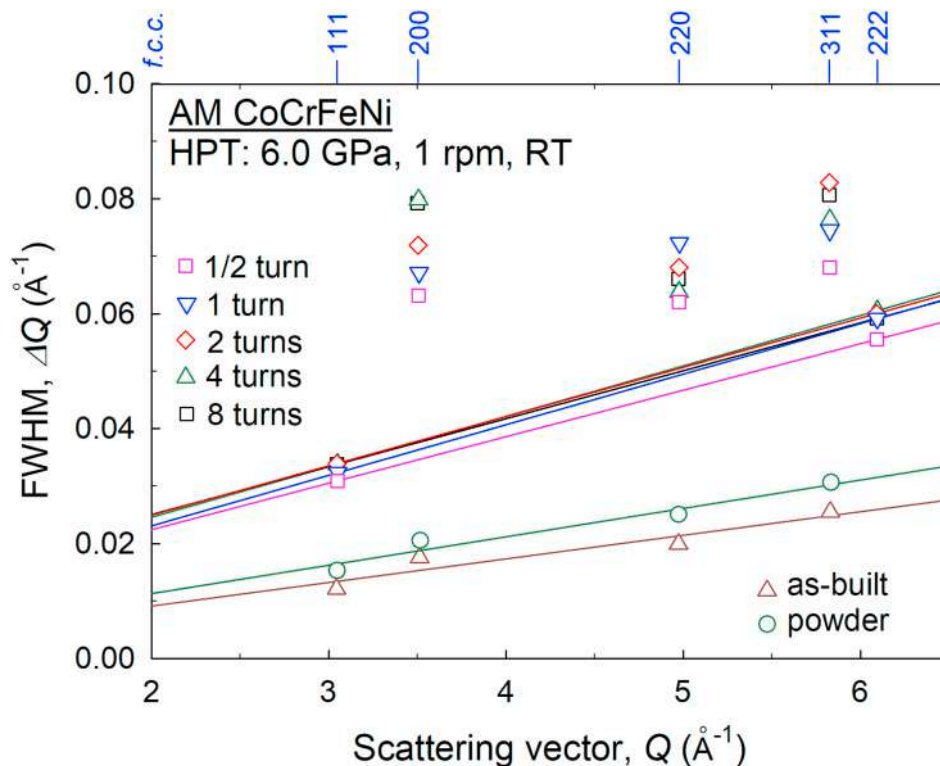|	Crystallite size (nm)	Microstrain	Lattice constant (Å)
Powder	462.54	0.00495	3.5718 ± 0.0007
As-built	652.27	0.00410	3.5744 ± 0.0009
HPT: 1/2 turn	101.25	0.00810	3.5742 ± 0.0048
HPT: 1 turn	116.11	0.00881	3.5728 ± 0.0051
HPT: 2 turns	80.94	0.00858	3.5752 ± 0.0059
HPT: 4 turns	89.65	0.00878	3.5745 ± 0.0059
HPT: 8 turns	75.07	0.00834	3.5771 ± 0.0069

Fig. 8. A Williamson-Hall plot: the full width at half maximum (FWHM), *ΔQ*, of the XRD peak profiles against the scattering vector, *Q*, for the AM CoCrFeNi HEA the conditions of atomized powders, as-built, and after HPT for 1/2, 1, 2, 4 and 8 turns.

process involving lowered dislocation density through remelting, recovery and recrystallization at some local regions having the equiaxed phase structure as shown in Fig. 3(a) and (b). Such change in microstructure is consistent with the decreased microstrain from 0.00495 in powders to 0.00410 after printing. After grain refinement, there is a significant reduction in a crystallite size to ~100 nm by 1/2 HPT turn and it further decreased gradually to ~75 nm though 8 turns. With the grain refinement process, the microstrain significantly increased to ~0.0081 after 1/2 turn and remained reasonably constant though 8 HPT turns. It should be noted that the crystallite size calculated by XRD is often smaller than the actual grain size after severe plastic deformation processes due to the high populations of subgrains and dislocation walls [24,25] and crystallographic direction, measuring the coherent crystallite size. Nevertheless, the crystallite sizes computed using the XRD data are in good agreement with the grain sizes measured directly from the TEM micrographs as shown in Fig. 3(c) and (d) for the AM HEA after HPT.

The changes in the lattice parameter of the CoCrFeNi alloy through printing followed by grain refinement were calculated based on the positions of the diffraction peaks for all five plane coordinates using the XRD profile. The estimated lattice parameters are listed in Table 1 for the HEA in different processing conditions. The pre-alloyed powders having a lattice parameter of 3.572 Å increases slightly after building, and grain refinement increased the value gradually towards 3.577 Å through 8 HPT turns. This increase in lattice parameter may be partly attributed to the dissolution of the minority phases having larger lattice parameters during grain refinement by HPT. The phenomenon is well supported by the recent reports documenting the strong influence of dissolutions and supersaturation of the minority phases into a matrix phase on the XRD peak shifts by compositional straining during a solid-state reaction of Al and Mg by HPT [76,77]. Such expansion in lattice parameter was also shown in a two-phase CoCrFeMnNi alloy produced by HPT-driven mechanically alloying for 1, 10 and 100 turns, where the observed peak shifting between 1 turn and 10 turns involves the dissolution of a *b.c.c.* phase in an *f.c.c.* matrix phase, while additional large shifting of the *f.c.c.* peaks without any phase transformation may be due to an increase of microstrain by grain refinement through 10 to 100 HPT turns [31]. Thus, it is reasonable to anticipate that, beside the mechanical dissolution of the minority phases, there is a contribution of grain refinement to an increase of microstrain and expansion of the lattice parameter in the present AM CoCrFeNi alloy through HPT for 8 turns. The result is in good agreement with an earlier report evaluating theoretically the inherent correlation of microstrain and lattice parameter changes in nanocrystalline materials [78], where both microstrain and lattice parameter tend to increase exponentially with grain (crystallite) refinement, while there are always scatters due to the different grain boundary structures depending on the processing methods. Subsequently, the present study demonstrated the improvement in micro-mechanical properties and structural development in the AM CoCrFeNi HEA, and the results yield comprehensive knowledge of the advantages of grain refinement and structural changes for current development in the AM technology of HEAs.

5. Summary and conclusions

(1) The importance of grain refinement in the micro-mechanical properties and structures of an AM CoCrFeNi HEA was examined after HPT for up to 8 turns under 6 GPa, and the results were compared with those acquired in a CM CoCrFeNi HEA after HPT through 5 turns.

(2) A significant hardness increase was observed up to $\varepsilon_{eq} \approx 12$ and thereafter the hardness saturated at $H_V = 525$ for both AM and CM HEA, while the initial hardness values before the grain refinement process were different due to the separate manufacturing preparations of the alloys. The AM HEA shows the

high strain hardening capability with a tendency of continuous increase in hardness with grain refinement even at $\varepsilon_{eq} > 12$.

(3) Grain refinement improved the strain rate sensitivity of the CoCrFeNi HEA, but the AM HEA demonstrated higher strain rate sensitivity of $m = 0.058$, thus high plasticity, than the CM HEA. Together with the high capability of strain hardening, excellent ductility is anticipated in the AM CoCrFeNi HEA. The estimated activation volume suggested the grain boundary-mediated dislocation activities as the rate-controlling mechanism of the AM HEA and it is consistent with the general nanocrystalline *f.c.c* metals.

(4) XRD analysis demonstrated grain refinement in the AM CoCrFeNi alloy reduced the crystallite size that is well correlated with an increase of microstrain and expansion of the lattice parameter by the combination of mechanical dissolution of the minority phases and severe grain refinement. The out-of-close-packed-plane reflections broaden overemphasized revealing smaller coherent crystal sizes due to interception by large numbers of dislocations and planar faulting that agrees with the estimated rate-controlling mechanism in the nanocrystalline AM HEA.

Data availability

The data that support the findings of this study are available from the corresponding author on reasonable request.

CRediT authorship contribution statement

Wenrui Zhao: Investigation, Formal analysis. **Jae-Kyung Han:** Investigation, Formal analysis. **Yulia O. Kuzminova:** Resources. **Stanislav A. Evlashin:** Resources. **Alexander P. Zhilyaev:** Investigation. **Alexander M. Pesin:** Investigation. **Jae-il Jang:** Investigation, Writing - review & editing. **Klaus-Dieter Liss:** Formal analysis, Writing - review & editing. **Megumi Kawasaki:** Supervision, Writing - original draft.

Declaration of competing interest

The authors declare that they have no known competing financial interests or personal relationships that could have appeared to influence the work reported in this paper.

Acknowledgements

References

[1] B. Cantor, I.T.H. Chang, P. Knight, A.J.B. Vincent, Microstructural development in equiatomic multicomponent alloys, Mater. Sci. Eng. A. 375–377 (2004) 213–218.

[2] J.-W. Yeh, S.-K. Chen, S.-J. Lin, J.-Y. Gan, T.-S. Chin, T.-T. Shun, C.-H. Tsau, S.-Y. Chang, Nanostructured high-entropy alloys with multiple principal elements: novel alloy design concepts and outcomes, Adv. Eng. Mater. 6 (2004) 299–303.

[3] C.-Y. Hsu, J.-W. Yeh, S.-K. Chen, T.-T. Shun, Wear resistance and high-temperature compression strength of fcc CuCoNiCrAl$_{0.5}$Fe alloy with boron addition, Metall. Mater. Trans. A 35 A (2004) 1465–1469.

[4] M.-H. Tsai, Physical properties of high entropy alloys, Entropy 15 (2013) 5338–5345.

[5] M.-H. Tsai, J.-W. Yeh, High-entropy alloys: a critical review, Mater. Res. Lett. 2 (2014) 107–123.

[6] E.J. Pickering, N.G. Jones, High-entropy alloys: a critical assessment of their founding principles and future prospects, Int. Mater. Rev. 61 (2016) 183–202.

[7] D.B. Miracle, O.N. Senkov, A critical review of high entropy alloys and related concepts, Acta Mater. 122 (2017) 448–511.

[8] B. Gludovatz, E.P. George, R.O. Ritchie, Processing, Microstructure and mechanical properties of the CrMnFeCoNi high-entropy alloy, JOM 67 (2015) 2262–2270.

[9] E.P. George, W.A. Curtin, C.C. Tasan, High entropy alloys: a focused review of, Acta Mater. 188 (2020) 435–474.

[10] Y. Zhang, T.T. Zuo, Z. Tang, M.C. Gao, K.A. Dahmen, P.K. Liaw, Z.P. Lu, Microstructures and properties of high-entropy alloys, Prog. Mater. Sci. 61 (2014) 1–93.

[11] Y. Shi, B. Yang, P.K. Liaw, Corrosion-resistant high-entropy alloys: a review, Metals 7 (2017) 43.

[12] P. Sathiyamoorthi, H.S. Kim, High-entropy alloys with heterogeneous microstructure: processing and mechanical properties, Prog. Mater. Sci. (In press) DOI: 10.1016/j.pmatsci.2020.100709.

[13] C.C. Koch, Nanocrystalline high-entropy alloys, J. Mater. Res. 32 (2017) 3435–3444.

[14] M. Vaidya, G.M. Muralikrishna, B.S. Murty, High-entropy alloys by mechanical alloying: a review, J. Mater. Res. 34 (2019) 664–686.

[15] W. Li, P. Liu, P.K. Liaw, Microstructures and properties of high-entropy alloy films and coatings: a review, Mater. Res. Lett. 6 (2018) 199–229.

[16] X.H. Yan, J.S. Li, W.R. Zhang, Y. Zhang, A brief review of high-entropy films, Mater. Chem. Phys. 210 (2018) 12–19.

[17] R.Z. Valiev, R.K. Islamgaliev, I.V. Alexandrov, Bulk nanostructured materials from severe plastic deformation, Prog. Mater. Sci. 45 (2000) 103–189.

[18] H. Shahmir, T. Mousavi, J. He, Z. Lu, M. Kawasaki, T.G. Langdon, Microstructure and properties of a CoCrFeNiMn high-entropy alloy processed by equal-channel angular pressing, Mater. Sci. Eng. A 705 (2017) 411–419.

[19] R. Zheng, J. Chen, W. Xiao, C. Ma, Microstructure and tensile properties of nanocrystalline (FeNiCoCu)$_{1-x}$Ti$_x$Al$_x$ high entropy alloys processed by high pressure torsion, Intermetallics 74 (2016) 38–45.

[20] B. Schuh, F. Mendez-Martin, B. Völker, E.P. George, H. Clemens, R. Pippan, A. Hohenwarter, Mechanical properties, microstructure and thermal stability of a nanocrystalline CoCrFeMnNi high-entropy alloy after severe plastic deformation, Acta Mater. 96 (2015) 258–268.

[21] D.-H. Lee, I.-C. Choi, M.-Y. Seok, J. He, Z. Lu, J.-Y. Suh, M. Kawasaki, T. G. Langdon, J.-i. Jang, Nanomechanical behavior and structural stability of a nanocrystalline CoCrFeNiMn high-entropy alloy processed by high-pressure torsion, J. Mater. Res. 30 (2015) 2804–2815.

[22] H. Shahmir, J. He, Z. Lu, M. Kawasaki, T.G. Langdon, Effect of annealing on mechanical properties of a nanocrystalline CoCrFeNiMn high-entropy alloy processed by high-pressure torsion, Mater. Sci. Eng. A 676 (2016) 294–303.

[23] V. Maier-Kiener, B. Schuh, E.P. George, H. Clemens, A. Hohenwarter, Nanoindentation testing as a powerful screening tool for assessing phase stability of nanocrystalline high-entropy alloys, Mater. Des. 115 (2017) 479–485.

[24] A. Heczel, M. Kawasaki, J.L. Lábár, J.-i. Jang, T.G. Langdon, J. Gubicza, Defect structure and hardness in nanocrystalline CoCrFeMnNi high-entropy alloy processed by high-pressure torsion, J. Alloys Compd. 711 (2017) 143–154.

[25] J. Gubicza, P.T. Hung, M. Kawasaki, J.-K. Han, Y. Zhao, Y. Xue, J.L. Lábár, Influence of severe plastic deformation on the microstructure and hardness of a CoCrFeNi high-entropy alloy: a comparison with CoCrFeNiMn, Mater. Char. 154 (2019) 304–314.

[26] Y. Zhao, X. Wang, T. Cao, J.-K. Han, M. Kawasaki, J.-i. Jang, H.N. Han, U. Ramamurty, L. Wang, Y. Xue, Effect of grain size on the strain rate sensitivity of CoCrFeNi high-entropy alloy, Mater. Sci. Eng. A 782 (2020) 139281.

[27] J.S. Belo, S.C. Marques, A.V. Castilho, L.M. de Oliveira, R.A. Simão, D.S. dos Santos, Hydrogen diffusivity and interaction with Fe$_{20}$Mn$_{20}$Ni$_{20}$Co$_{20}$Cr$_{20}$ and Fe$_{22}$Mn$_{40}$Ni$_{30}$Co$_6$Cr$_2$ high-entropy alloys, J. Alloys Compd. 815 (2020) 152314.

[28] A.V. Podolskiy, Y.O. Shapovalov, E.D. Tabachnikova, A.S. Tortika, M. A. Tikhonovsky, B. Joni, E. Ódor, T. Ungar, S. Maier, C. Rentenberger, M. J. Zehetbauer, E. Schafler, Anomalous evolution of strength and microstructure of high-entropy alloy CoCrFeNiMn after high-pressure torsion at 300 and 77 K, Adv. Eng. Mater. 22 (2020) 1900752.

[29] Q.H. Tang, Y. Huang, Y.Y. Huang, X.Z. Liao, T.G. Langdon, P.Q. Dai, Hardening of an Al$_{0.3}$CoCrFeNi high entropy alloy via high-pressure torsion and thermal annealing, Mater. Lett. 151 (2015) 126–129.

[30] P.F. Yu, H. Cheng, L.J. Zhang, H. Zhang, Q. Jing, M.Z. Ma, P.K. Liaw, G. Li, R.P. Liu, Effects of high pressure torsion on microstructures and properties of an Al$_{0.1}$CoCrFeNi high-entropy alloy, Mater. Sci. Eng. A 655 (2016) 283–291.

[31] A. Kilmametov, R. Kulagin, A. Mazilkin, S. Seils, T. Boll, M. Heilmaier, H. Hahn, High-pressure torsion driven mechanical alloying of CoCrFeMnNi high entropy alloy, Scripta Mater. 158 (2019) 29–33.

[32] M.T. Tsai, J.C. Huang, W.Y. Tsai, T.H. Chou, C.-F. Chen, T.H. Li, J.S.C. Jang, Effects of ultrasonic surface mechanical attrition treatment on microstructures and mechanical properties of high entropy alloys, Intermetallics 93 (2018) 113–121.

[33] T. Fujieda, H. Shiratori, K. Kuwabara, T. Kato, K. Yamanaka, Y. Koizumi, A. Chiba, First demonstration of promising selective electron beam melting method for utilizing high-entropy alloys as engineering materials, Mater. Lett. 159 (2015) 12–15.

[34] Y. Brif, M. Thomas, I. Todd, The use of high-entropy alloys in additive manufacturing, Scripta Mater. 99 (2015) 93–96.

[35] S. Gorsse, C. Hutchinson, M. Gouné, R. Banerjee, Additive manufacturing of metals: a brief review of the characteristic microstructures and properties of steels, Ti-6Al-4V and high-entropy alloys, Sci. Technol. Adv. Mater. 18 (2017) 584–610.

[36] X. Li, Additive manufacturing of advanced multi-component alloys: bulk metallic glasses and high entropy alloys, Adv. Eng. Mater. 20 (2018) 1700874.

[37] S. Chen, Y. Tong, P.K. Liaw, Additive manufacturing of high-entropy alloys: a review, Entropy 20 (2018) 937.

[38] C. Han, Q. Fang, Y. Shi, S.B. Tor, C.K. Chua, K. Zhou, Recent advances on high-entropy alloys for 3D printing, Adv. Mater. 32 (2020) 1903855.

[39] J.M. Torralba, M. Campos, High entropy alloys manufactured by additive manufacturing, Metals 10 (2020) 639.

[40] Z. Tong, H. Liu, J. Jiao, W. Zhou, Y. Yang, X. Ren, Microstructure, microhardness and residual stress of laser additive manufactured CoCrFeMnNi high-entropy alloy subjected to laser shock peening, J. Mater. Process. Technol. 285 (2020) 116806.

[41] T.A. Listyawan, A. Kumar, W. Shin, H. Do, K.-H. Lee, J. Ryu, N. Park, Surface hardening treatment of Fe$_{40}$(CoCrMnNi)$_{60}$ medium entropy alloy via aerosol deposition technique: a new approach, Mater. Lett. 269 (2020) 127633.

[42] P. Wang, P. Huang, F.L. Ng, W.J. Sin, S. Lu, M.L.S. Nai, Z.L. Dong, J. Wei, Additively manufactured CoCrFeNiMn high-entropy alloy via pre-alloyed powder, Mater. Des. 168 (2019) 107576.

[43] Y. Kuzminova, D. Firsov, A. Dudin, S. Sergeev, A.P. Zhilyaev, A. Dyakov, A. Chupeeva, A. Alekseev, D. Martynov, I. Akhatov, S. Evlashin, The effect of the parameters of the powder bed fusion process on the microstructure and mechanical properties of CrFeCoNi medium-entropy alloys, Intermetallics 116 (2020) 106651.

[44] C.L. Wang, Y.H. Lai, J.C. Huang, T.G. Nieh, Creep of nanocrystalline nickel: a direct comparison between uniaxial and nanoindentation creep, Scripta Mater. 62 (2010) 175–178.

[45] A.P. Zhilyaev, T.G. Langdon, Using high-pressure torsion for metal processing: fundamentals and applications, Prog. Mater. Sci. 53 (2008) 893–979.

[46] Z.G. Zhu, Q.B. Nguyen, F.L. Ng, X.H. An, X.Z. Liao, P.K. Liaw, S.M.L. Nai, J. Wei, Hierarchical microstructure and strengthening mechanisms of a CoCrFeNiMn high entropy alloy additively manufactured by selective laser melting, Scripta Mater. 154 (2018) 20–24.

[47] S. Praveen, B.S. Murty, R.S. Kottada, Alloying behavior in multi-component AlCoCrCuFe and NiCoCrCuFe high entropy alloys, Mater. Sci. Eng. A 534 (2012) 83–89.

[48] R.B. Mane, B.B. Panigrahi, Sintering mechanisms of mechanically alloyed CoCrFeNi high-entropy alloy powders, J. Mater. Res. 33 (2018) 3321–3329.

[49] D. Ma, M. Yao, K.G. Pradeep, C.C. Tasan, H. Springer, D. Raabe, Phase stability of non-equiatomic CoCrFeMnNi high entropy alloys, Acta Mater. 98 (2015) 288–296.

[50] Z. Wang, Q. Wu, W. Zhou, F. He, C. Yu, D. Lin, J. Wang, C.T. Liu, Quantitative determination of the lattice constant in high entropy alloys, Scripta Mater. 162 (2019) 468–471.

[51] C.L. Tracy, S. Park, D.R. Rittman, S.J. Zinkle, H. Bei, M. Lang, R.C. Ewing, W. L. Mao, High pressure synthesis of a hexagonal close-packed phase of the high-entropy alloy CrMnFeCoNi, Nat. Commun. 8 (2017) 15634.

[52] Y. Akahama, M. Nishimura, K. Kinoshita, H. Kawamura, Y. Ohishi, Evidence of a fcc-hcp transition in aluminum at multimegabar pressure, Phys. Rev. Lett. 96 (2006), 045505.

[53] M. Kawasaki, B. Ahn, P. Kumar, J.-i. Jang, T.G. Langdon, Nano- and micro-mechanical properties of ultrafine-grained materials processed by severe plastic deformation techniques, Adv. Eng. Mater. 19 (2017) 1600578.

[54] Y. Zou, Nanomechanical studies of high-entropy alloys, J. Mater. Res. 33 (2018) 3035–3054.

[55] E.O. Hall, The deformation and ageing of mild steel: II Characteristics of the Lüders deformation, Proc. Phys. Soc. Sect. B. 64 (1951) 742–747.

[56] N.J. Petch, The cleavage strength of polycrystals, J. Iron Steel Inst. 174 (1953) 25–28.

[57] B.S. Murty, J.W. Yeh, S. Ranganathan, High Entropy Alloys, Elsevier Science & Tech., Butterworth-Heinemann Ltd, Oxford, 2014.

[58] M. Kawasaki, Different models of hardness evolution in ultrafine-grained materials processed by high-pressure torsion, J. Mater. Sci. 49 (2014) 18–34.

[59] M. Kawasaki, R.B. Figueiredo, Y. Huang, T.G. Langdon, Interpretation of hardness evolution in metals processed by high-pressure torsion, J. Mater. Sci. 49 (2014) 6586–6596.

[60] S.A. Torbati-Sarraf, S. Sabbaghianrad, R.B. Figueiredo, T.G. Langdon, Orientation imaging microscopy and microhardness in a ZK60 magnesium alloy processed by high-pressure torsion, J. Alloys Compd. 712 (2017) 185–193.

[61] Y.C. Wang, T.G. Langdon, Effect of heat treatment on microstructure and microhardness evolution in a Ti-6Al-4V alloy processed by high-pressure torsion, J. Mater. Sci. 48 (2013) 4646–4652.

[62] D. Hernández-Escobar, J. Marcus, J.-K. Han, R.R. Unocic, M. Kawasaki, C. J. Boehlert, Effect of post-deformation annealing on the microstructure and micro-mechanical behavior of Zn–Mg hybrids processed by high-pressure torsion, Mater. Sci. Eng. A 771 (2020) 138578.

[63] D. Tabor, Hardness of solids, Rev. Phys. Technol. 1 (1970) 145–179.

[64] W.C. Oliver, G.M. Pharr, An improved technique for determining hardness and elastic modulus using load and displacement sensing indentation experiments, J. Mater. Res. 7 (1992) 1564–1583.

[65] M. Shabani, J. Indeck, K. Hazeli, P.D. Jablonski, G.J. Pataky, Effect of strain rate on the tensile behavior of CoCrFeNi and CoCrFeMnNi high-entropy alloys, J. Mater. Eng. Perform. 28 (2019) 4348–4356.

[66] W. Huo, F. Fang, X. Liu, S. Tan, Z. Xie, J. Jiang, Remarkable strain-rate sensitivity of nanotwinned CoCrFeNi alloys, Appl. Phys. Lett. 114 (2019) 101904.

[67] J. Moon, S.I. Hong, J.B. Seol, J.W. Bae, J.M. Park, H.S. Kim, Strain-rate sensitivity of high-entropy alloys and its significance in deformation, Mater. Res. Lett. 7 (2019) 503–509.

[68] F.D. Torre, P. Spätig, R. Schäublin, M. Victoria, Deformation behaviour and microstructure of nanocrystalline electrodeposited and high pressure torsioned nickel, Acta Mater. 53 (2005) 2337–2349.

[69] Q. Wei, S. Cheng, K.T. Ramesh, E. Ma, Effect of nanocrystalline and ultrafine grain sizes on the strain rate sensitivity and activation volume: fcc versus bcc metals, Mater. Sci. Eng. A 381 (2004) 71–79.

[70] Z. Wu, Y. Gao, H. Bei, Thermal activation mechanisms and Labusch-type strengthening analysis for a family of high-entropy and equiatomic solid-solution alloys, Acta Mater. 120 (2016) 108–119.

[71] T. Zhu, J. Li, A. Samanta, H.G. Kim, S. Suresh, Interfacial plasticity governs strain rate sensitivity and ductility in nanostructured metals, Proc. Natl. Acad. Sci. U.S.A. 104 (2007) 3031–3036.

[72] H. Conrad, Grain size dependence of the plastic deformation kinetics in Cu, Mater. Sci. Eng. A. 341 (2003) 216–228.

[73] H. Conrad, Plastic deformation kinetics in nanocrystalline fcc metals based on the pile-up of dislocations, Nanotechnology 18 (2007) 325701.

[74] C. Niu, A.J. Zaddach, A.A. Oni, X. Sang, J.W. Hurt III, J.M. LeBeau, C.C. Koch, D. L. Irving, Spin-driven ordering of Cr in the equiatomic high entropy alloy NiFeCrCo, Appl. Phys. Lett. 106 (2015) 161906.

[75] X. Li, R. Dippenaar, J.-K. Han, M. Kawasaki, K.-D. Liss, Phase transformation and structure evolution of a Ti-45Al-7.5Nb alloy processed by high-pressure torsion, J. Alloys Compd. 787 (2019) 1149–1157.

[76] J.-K. Han, K.-D. Liss, T.G. Langdon, M. Kawasaki, Synthesis of a bulk nanostructured metastable Al alloy with extreme supersaturation of Mg, Sci. Rep. 9 (2019) 17186.

[77] J.-K. Han, K.-D. Liss, T.G. Langdon, J.-i. Jang, M. Kawasaki, Mechanical properties and structural stability of a bulk nanostructured metastable aluminum-magnesium system, Mater. Sci. Eng. A 796 (2020) 140050.

[78] W. Qin, T. Nagase, Y. Umakoshi, J.A. Szpunar, Relationship between microstrain and lattice parameter change in nanocrystalline materials, Phil. Mag. Lett. 88 (2008) 169–179.

Chapter 6

In Situ Neutron Diffraction Investigating Microstructure and Texture Evolution upon Heating of Nanostructured CoCrFeNi High-Entropy Alloy

This chapter builds upon previous research and explores the microstructural evolution and relaxation of residual stress in CoCrFeNi HEA under heating conditions. The study utilizes nondestructive *in situ* neutron diffraction methods to gain accurate insights into the bulk microstructure, including phase fraction, lattice parameter, and grain reorientation during thermo-mechanical processing. Neutron scattering is a powerful tool for characterizing recovery and recrystallization processes, as well as defect kinetics at high temperatures. *In situ* neutron diffraction offers the advantage of deep penetration into materials, allowing for representative grain statistics in powder-diffraction and texture analyses, even in coarse-grained materials.

In this study, a CoCrFeNi HEA is examined using *in situ* heating experiments with neutron diffraction to investigate microstructural and texture evolu-

tion over time and temperature. The main comparisons are made between as-cast, as-printed, and HPT processed HEA. This chapter provides a detailed analysis of the microstructural and texture evolution of these HEA materials during heating. Temperature-dependent neutron experiments were conducted to analyze the texture and microstresses in the materials.

The findings indicate that after grain refinement through HPT, the material exhibits a typical *f.c.c.* metals texture. Heating ramps reveal three temperature regimes: stress recovery, recrystallization, and normal grain growth. The as-printed material shows higher dislocation density than the as-cast, while residual stress and Bauschinger contributions, dislocation energy, grain boundary amounts, and vacancy contents are elaborated with scenarios of vacancy expulsion leading to recrystallization. Overall, it can be concluded that the fully recrystallized nanostructured material exhibits the lowest dislocation density, which may help alleviate stress in AM materials.

<u>**Contribution**</u>: I contributed to the development of the microstructural analyses and related sample preparation procedures and the editing of the manuscript. I would like to thank all the authors for their valuable contributions to the development of this paper

In Situ Neutron Diffraction Investigating Microstructure and Texture Evolution upon Heating of Nanostructured CoCrFeNi High-Entropy Alloy

Xiaojing Liu, Jae-Kyung Han, Yusuke Onuki, Yulia O. Kuzminova, Stanislav A. Evlashin, Megumi Kawasaki, and Klaus-Dieter Liss*

Herein, in situ temperature-dependent neutron experiments investigate the microstructural evolution of additively and conventionally manufactured CoCrFeNi high-entropy alloys, as-received, and after grain refinement through high-pressure torsion. The evolution of texture after grain refinement and during heating is consistent with typical *fcc* metals. Both conventional and modified Williamson–Hall analyses reveal that major contributions of microstresses stem from dislocations. For the nanostructured material, three temperature regimes are identified on a heating ramp, namely, stress recovery up to 800 K, followed by recrystallization at 850–960 K, and normal grain growth above, in line with the physical change of hardness increase on recovery, decrease on recrystallization, and cutback to the as-manufactured values after grain growth. The as-printed material exposes higher dislocation density than as-cast, reducing slightly upon heating, while there is limited temperature dependence on the lower dislocation density of the as-cast specimen. Stored energies have been elaborated for residual stress and Bauschinger contributions, dislocation energy, grain boundary amounts, and vacancy contents with scenarios of vacancy expulsion leading to recrystallization. Ultimately, the fully recrystallized nanostructured material shows the lowest dislocation density, which may render a recipe for stress release in additively manufactured materials.

1. Introduction

Conventional alloy design principally focuses on admixing one absolute major element with minor elements. In this way, mechanical properties can be tuned by changing both the minor element type and amount as well as the processing history. Usually, a higher number of principal elements in traditional alloys lead to complications in structural phases and the design of processing conditions. A breakthrough came when Yeh et al.[1] and Cantor et al.[2] independently discovered a new type of alloy which includes more than four equiatomic elements but still showing one simple phase structure.[3] According to Yeh's study, the high configuration entropy accounts for a single stable phase,[4] thus named high-entropy alloy (HEA). Over the past decade, there has been a wide interest in the discovery of numerous HEA and their superior mechanical properties, as summarized in some recently published review papers.[5–8]

In addition to the alloy optimization, nanostructuring of materials by severe plastic deformation can further enhance the mechanical properties.[9] Specifically, methods such as high-pressure torsion (HPT),[10] equal-channel angular pressing,[11] and accumulative roll bonding[12] have successfully demonstrated powerful nanostructurization, offering pronounced densification of defects and grain refinement, hence, they largely improve the mechanical properties. However, the thermal stability of severely nanostructured materials, for example, by HPT processing, raises fundamental questions.

X. Liu
Department of Materials Science and Engineering
Technion – Israel Institute of Technology
Haifa 32000, Israel

X. Liu, K.-D. Liss
Department of Materials Science and Engineering, and Guangdong Provincial Key Laboratory of Materials and Technologies for Energy Conversion
Guangdong Technion – Israel Institute of Technology
Shantou, Guangdong 515063, China
E-mail: kdl@gtiit.edu.cn, liss@kdliss.de

The ORCID identification number(s) for the author(s) of this article can be found under https://doi.org/10.1002/adem.202201256.

J.-K. Han, M. Kawasaki
School of Mechanical, Industrial and Manufacturing Engineering
Oregon State University
Corvallis, OR 97331, USA

Y. Onuki
Frontier Research Center for Applied Atomic Sciences
Ibaraki University
Tokai, Ibaraki 319-1106, Japan

Y. O. Kuzminova, S. A. Evlashin
Center for Design, Manufacturing & Materials
Skolkovo Institute of Science and Technology
Moscow 121205, Russia

Post-deformation annealing has been proposed to tune the microstructure of a nanostructured CoCrNi HEA so as to improve the mechanical properties even further by a well-designed annealing procedure, where all examinations were conducted by an ex situ manner.[13] Yet, little has been investigated in situ, leaving indistinct microstructural information during the heating procedure and allowing to ultra-fine-tune the microstructures of severe plastically deformed materials. Indirect investigations of structural evolution and transformations have been obtained by differential scanning calorimetry,[14] as applied to an *fcc* structured HPT-processed CoCrFeNi HEA.[15] However, direct in situ diffraction experiments at high temperatures are necessary to reveal the sequential structural changes enabling mechanistic understanding of thermal behavior of the nanostructured HEA. Such methods have been developed mostly on coarse-grained specimens,[16,17] while the results from nanostructured materials are still in their infancy.[18] Therefore, there is a critical need for in situ characterization of microstructural relaxation and transformation and the thermal stability in bulk nanocrystalline materials.

In recent years, additive manufacturing (AM) for HEA has triggered interest of researchers due to their promising benefits: low cost and waste, high efficiency, and suitability for complex engineering production,[19] including producing structured green specimens for further HPT processing. Substantial progress has been made in the research focusing on the built microstructure and improved mechanical properties of the additively manufactured HEA as compared to the conventionally manufactured HEA.[20–23] However, inherent built defects in AM materials, for example, porosity,[10] cellular structures,[24] and residual stress,[25] greatly influence the final mechanical properties of the products. Thus, post-treatments of additively manufactured materials including HEA are currently a necessity. It is reported that AM materials demonstrate high thermal stability compared to conventional alloys due to a high density of tangled dislocations inside cell walls.[26] While the significance of grain refinement on an AM material has been evaluated recently by applying equal-channel angular pressing on an AM Al–Si alloy at an elevated temperature,[10] the undiscovered behavior of a nanocrystalline microstructure in HEA upon heating motivates the present work.

Nondestructive in situ neutron diffraction methods provide accurate insights to bulk microstructure evolution, such as phase fraction and lattice parameter in HEA[27] and grain reorientation[17,28] during thermo-mechanical processing. Some earlier representative works also demonstrate neutron scattering as a powerful characterization tool to investigate recovery and recrystallization processes[29] as well as defect kinetics at very high temperatures.[30] In situ neutron diffraction bears the advantage of deep penetration into most materials, allowing to probe and integrate over larger volumes to get representative grain statistics for powder-diffraction and texture analyses, even in coarse-grained materials. Particularly at high temperature, it reveals structural changes during sintering[31,32] or for structural investigations of phase diagrams.[33] High-resolution neutron diffraction allows not only to investigate phase composition and lattice parameters but also microstructural investigations through texture and peak-width analysis, as reviewed for example on steel by Tomota et al.[34,35] Because neutrons integrate over the entire (or a large)

volume of the specimen, it is complementary to synchrotron high-energy X-ray diffraction, which likewise penetrates deep into materials but can probe the local structure with a sub-millimeter beam.[36]

In the present study, a CoCrFeNi HEA was examined by an in situ heating experiment illuminated under neutron diffraction to investigate the microstructural and some texture evolution on time and temperature scales. The main comparisons in the microstructural evolution upon heating are made on as-cast, as-printed, and HPT–processed HEA. Applying the novel in situ characterization technique of neutron diffraction, this study demonstrates for the first time the detailed microstructural and texture evolution upon heating of those HEA. The results contribute to bridge the gaps between the important subjects in materials science of metal manufacturing and processing, microstructure and texture, and novel characterization techniques.

2. Experimental Section

Powders of 24Co–26Cr–25Fe–25Ni (at%) HEA with average particle sizes about 35–40 μm were provided by the joint-stock company Polema, Russia, produced by the spraying method. The bulk material was manufactured by a Powder Bed Fusion process with a laser heat source using the metal 3D printer Trumpf TruPrint 1000, Germany. The printing parameters include laser power 150 W, spot diameter 55 μm, spot propagation speed 600 mm s^{-1}, hatch spacing 80 μm, and layer thickness 20 μm. More detailed information can be found in an earlier work.[37] The obtained bulk material is hereby referred to as an as-printed HEA. For comparison purposes, a cast 25Co–25Cr–25Fe–25Ni (at%) HEA was prepared, resulting in an average grain size of around ≈57 ± 22 μm[38] and is referred to as an as-cast HEA. The as-printed billets for the HPT processing were cut perpendicular to the build direction and underwent HPT at room temperature under a compressive pressure of 6.0 GPa at a rotation speed of 1 rpm for 15 turns, and are referred to as an HPT-processed HEA. All these samples were prepared to have a disk shape of 10 mm diameter and ≈0.8 mm thickness for the neutron diffraction characterization.

The specimens were in situ heated in vacuum of about 1–10 Pa at a ramping rate of 4 K min^{-1} from room temperature to specific temperatures of 1000 K for both as–received specimen types and 1273 K for the corresponding HPT-processed HEA, followed by furnace cooling, during neutron diffraction acquisition. The neutron experiments were performed on the Ibaraki diffractometer at the iMATERIA beamline (BL20) at the J–PARC spallation source employing the time-of-flight (TOF) method.[39] Scattering signals were obtained integrated over the entire volume of each sample. Three detector banks labeled 1–3 were positioned at scattering angles $2\theta \in \{155.45°, 90°, 33.88°\}$ with mean orientations of the scattering vector $\vec{G}$ equaling 12.28°, 45°, and 73.06°, toward the back-pointing sample normal direction, as shown in **Figure 1**, allowing to determine the volume-integrated texture components. Instrumental details are referred to literature.[40] Bank 1 corresponds to the highest angle diffractometer where a given scattering vector G satisfies Bragg's law $G = 2 k \sin(\theta)$ by longest TOF τ, where k and θ are the wave vector

ADVANCED
SCIENCE NEWS
www.advancedsciencenews.com

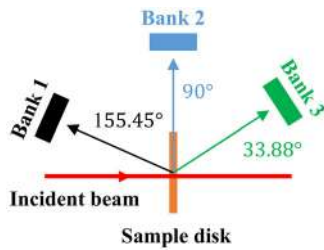ADVANCED
ENGINEERING
MATERIALS
www.aem-journal.com

Figure 1. Position of the three detector banks. Note that the beam is large and integrates over the whole specimen.

and half of the scattering angle 2θ, respectively, since $k \approx \tau^{-1}$. Thus, with given TOF determination $\Delta\tau$ and $|\Delta G/G| = |\Delta\tau/\tau|$, Bank 1 produced the highest resolution while Bank 3 provided the lowest resolution. Recorded intensities were normalized to a vanadium incoherent scatterer and an underlying background stemmed from a quartz sample cell. The instrumental peak broadening was calibrated by the coherent signal of the same vanadium scatterer and subtracted from the specimen peak breaths to correct for further evaluation.

The sample surface perpendicular to the build direction of another set of the as–printed and HPT-processed HEA disks was mechanically polished with 0.25 μm diamond suspension followed by 50 nm silicon oxide suspension. The morphology of the polished samples was then studied by scanning electron microscopy (SEM) at GTIIT using a Zeiss Gemini 450 equipped with an Oxford Ultim Max 100 energy–dispersive X-ray spectrometer (EDS) for chemical composition analysis. The near-surface texture of the samples was measured using a Rigaku SmartLab X-ray diffractometer at GTIIT with Cu-K_α radiation operating at 45 kV and 200 mA in four–circle mode[41] with inner and outer Eulerian cradle angles ϕ and χ. The scanning step sizes were 5° from 0° to 360° and 15° to 90°, respectively. The MTEX tool within MATLAB software is applied to calculate pole figures (PF) and inverse pole figures (IPF).[42] Hardness after heating was tested using a Mitutoyo 200 instrument with applied load of $100\,g_f = 0.98$ N. The specimens were heated to the specific temperature steps at similar heating ramps as used in the neutron experiment, subsequently held for 10 min and quenched.

3. Results

3.1. Microstructural Evolution

Figure 2a displays an SEM image of the as-printed HEA, where the microstructure is normal to the build direction. It exposes a duplex microstructure with elongated grains describing the laser beam width of ≈50 μm with the shorter width of 2 μm, and dispersed equiaxed grains with sizes of about 10 μm between neighboring melt tracks. It is consistent with the previous result.[37] Figure 2b shows the microstructure close to the disk edge along the disk surface of the HPT-processed HEA, which consists of ultrafine grains with sizes of about 50–60 nm. The observed nanostructure presents homogeneous over the disk surface, since processing for even eight turns is sufficient to introduce a homogeneous ultrafine microstructure across the disk diameter,[43] whereas the present process largely surpasses this value by processing 15 turns. Chemical composition of the as-printed HEA was obtained from the EDS experiments and is listed in **Table 1**, together with the as-cast HEA for comparison. It is demonstrated that these two alloys have close chemical contents, and thus, they are comparable.

3.2. Reciprocal Space Evolution

Figure 3 depicts the evolution of neutron-scattering data during the heating–cooling cycles for a) as-printed and b) HPT-processed HEA, in which the three separate rows provide the results from the three banks as sketched in Figure 1. The red curves to the right give the temperature–time cycles. Each line of the diffraction picture represents the diffractogram at a given time, coded in color in which the intensity increases from the blue background through white to red. The more or less vertical acute streaks denote corresponding Laue–Bragg reflections of the HEA, while the very broad distribution stems from the

Table 1. Chemical composition of as-printed and as-cast alloys (at%).

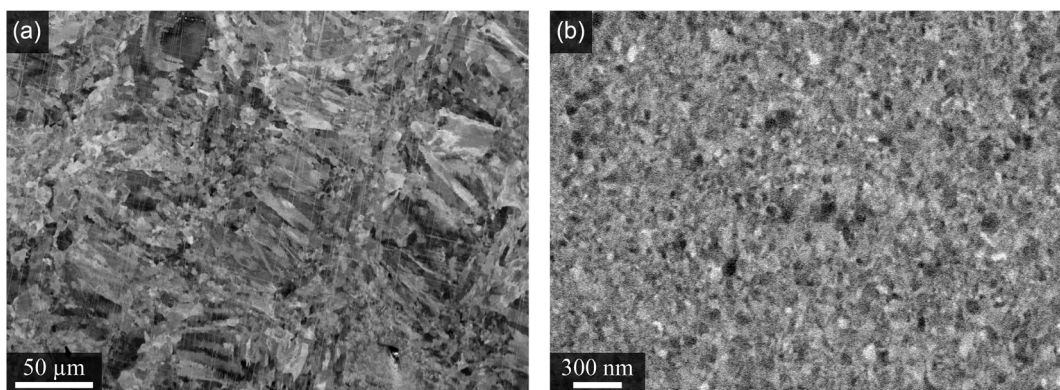|	Co	Cr	Fe	Ni
As-printed HEA	25.44	23.81	25.18	25.57
As-cast HEA	25.13	24.66	24.99	25.22

Figure 2. Scanning electron microscopy (SEM) images of a) as-printed high-entropy alloy (HEA) and b) high-pressure torsion (HPT)-processed HEA.
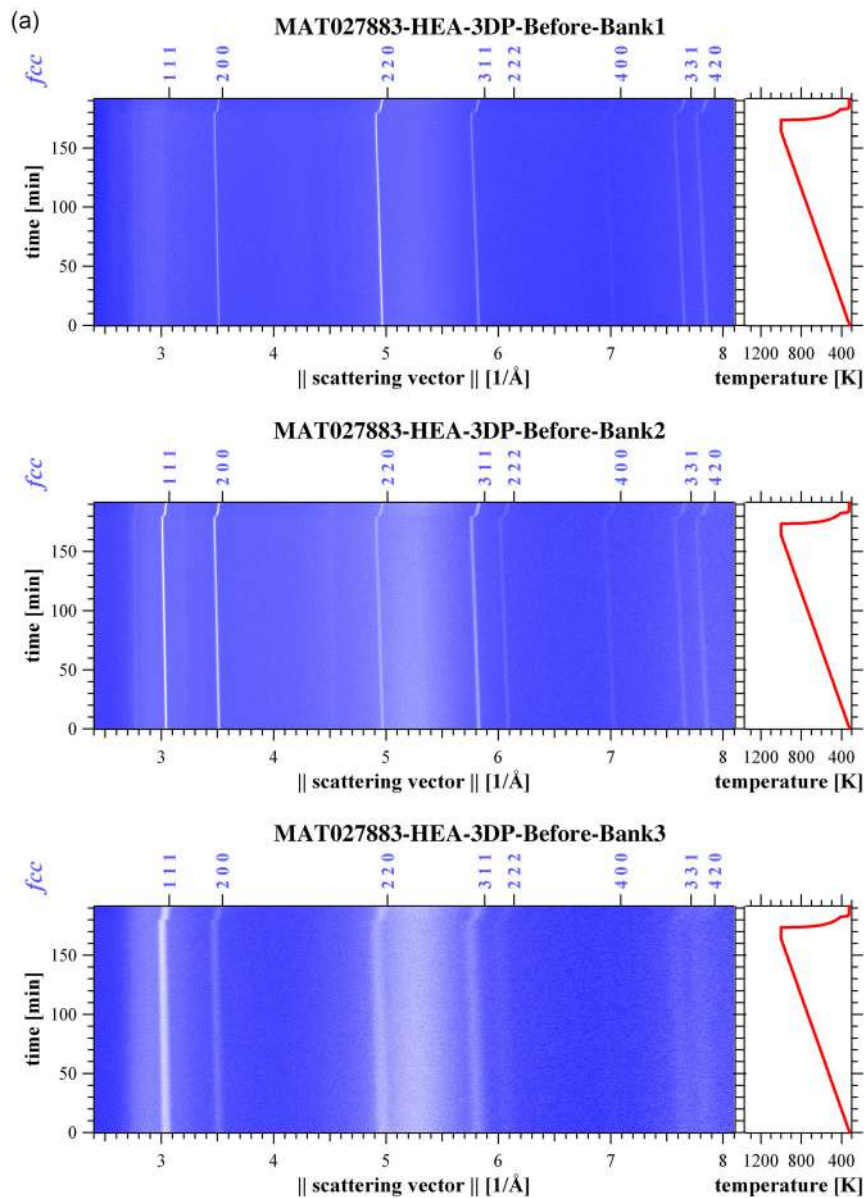
Figure 3. Time evolution of diffractograms in color scale upon thermal annealing of a) as-printed and b) HPT-processed HEA.

amorphous quartz sample holder. It can be seen that both alloys exhibit a single-phase close-packed *fcc* crystal structure without any proof of phase transformation as indexed to the top, which prevails upon annealing, shifting position due to thermal expansion and contraction. From the position of the scattering vector $G_{111} = 3.05\,\text{Å}^{-1}$ at room temperature, we obtain the lattice parameter $a_0 = 3.57\,\text{Å}$ of the *fcc* unit cell.

There are three obvious phenomena yielded in the experiments. First, all peaks deviate to lower scattering vectors upon heating, which is ascribed to the thermal expansion of the alloy. Accordingly, the thermal contraction is apparent during cooling by shifting back the neutron peaks to higher scattering vectors. Second, some peaks are too weak to be visible in specific banks, for example, the 111 reflection in Bank 1 in Figure 3a.

This indicates strong texture and will be discussed in detail in a later section. Third, the intensity and peak widths in Figure 3a show less change upon heating while Figure 3b depicts obvious development, also to be addressed later.

3.3. Peak Width Evolution

The peak width characterized by neutron diffraction comprises two characteristic components, namely finite grain size D and total micro-strain broadening denoted $\Delta\varepsilon$ including inter- and intra-granular type II and type III components, which may stem from vacancy, chemical strain gradient, precipitates, dislocations, misfit, and so on.[44] It evaluates, after instrumental broadening deduction, to

**ADVANCED
SCIENCE NEWS**

www.advancedsciencenews.com

**ADVANCED
ENGINEERING
MATERIALS**

www.aem-journal.com
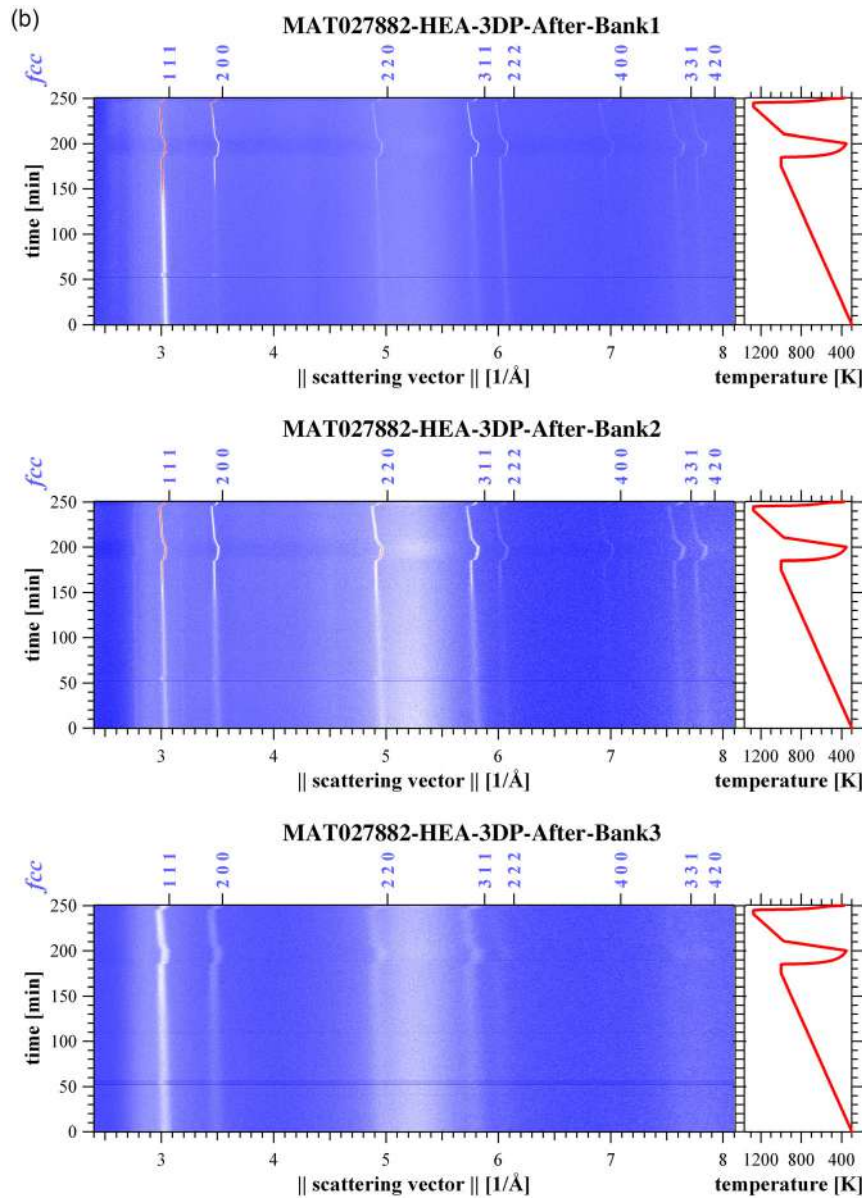
Figure 3. Continued.

$$\Delta Q = K \frac{2\pi}{D} + \Delta\varepsilon G \tag{1}$$

with the modulus of scattering vector $G = 2\,k\,\sin(\theta)$, wave number $k = 2\pi\,\lambda^{-1}$, wavelength λ, grain size D, and a shape factor $K \approx 0.9$ for spherical grains. This relation leads to the conventional Williamson–Hall plot[45] under different temperatures for the as-printed and as-cast HEA. Five peaks (200, 220, 311, 331, 420) are chosen to plot the full width at half maximum, ΔQ against the modulus of the scattering vector G with the results shown in **Figure 4**a.

In Figure 4a, the upper four lines represent peak width of the as-printed HEA at different temperatures from 338 to 1000 K. The middle green line shows the width for the HPT-processed HEA at 1000 K. Finally, the bottom two lines represent the as–cast HEA at 338 and 1000 K. The HPT-processed HEA heated to 1000 K and the as-cast HEA tend to show a reasonably linear relationship between ΔQ and G with lower $\Delta\varepsilon$ as described in Equation (1), which is in contrast to the as-printed HEA. It suggests that heating toward 1000 K introduces structural relaxation, for example full recrystallization, homogeneously over the HPT-processed HEA, which is almost in the same state with the as-cast HEA upon heating as low as 338 K.

For the as-printed HEA, all of them show apparent unsystematic rather than linear behavior which is due to the strain anisotropy caused by dislocations and can be rationalized by a dislocation model. Here, by assuming that dislocations in different slip systems are similar, the modified Williamson–Hall

ADVANCED
SCIENCE NEWS
www.advancedsciencenews.com

ADVANCED
ENGINEERING
MATERIALS
www.aem-journal.com

Figure 4. a) Full width at half maximum at Bank 1 of various *hkl* Laue–Bragg interferences from HEA at different conditions in classical Williamson–Hall plot and b) a modified Williamson–Hall plot. The fit parameters α and β denote axis offsets and slopes of the lines, respectively.

method[46] was applied to calibrate peak width by below equation.[47]

$$\Delta Q = 2\pi \frac{K}{D} + \left(\frac{Mb^2}{4}\right)\rho^{\frac{1}{2}}G^2\overline{C} \tag{2}$$

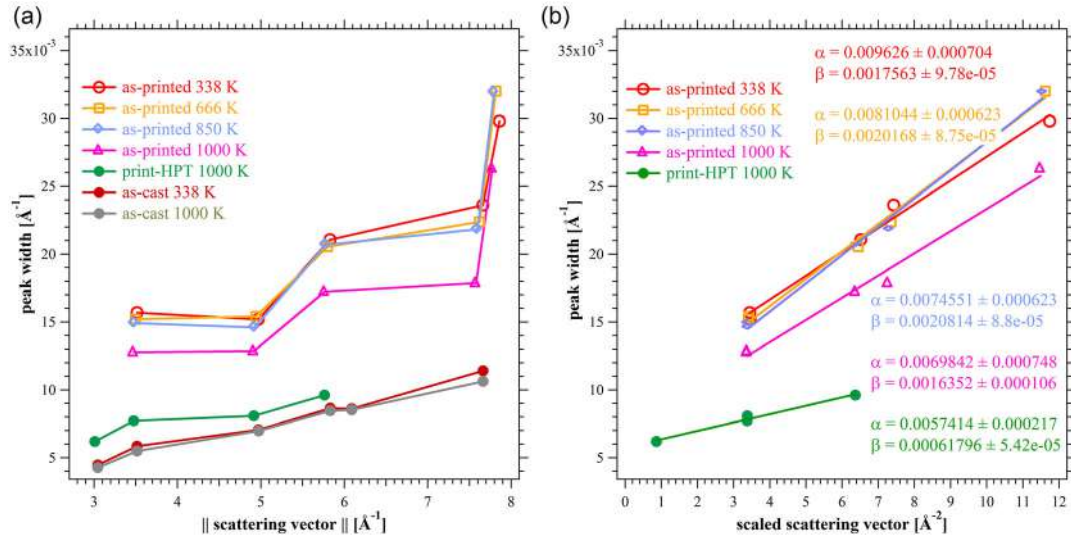where ρ is the dislocation density, $M = R_e\,\rho^{1/2}$ is the dimensionless Wilkens dislocation arrangement parameter depending on the ratio of the effective outer cutoff radius of the dislocations, R_e, and the mean dislocation spacing $\rho^{-1/2}$,[48,49] b is the magnitude of the Burgers vector ($b = a_0/\sqrt{2} = 2.52 \times 10^{-10}$ m), and $\overline{C}$ is the dislocation contrast factor. The presentation of this equation and its derivation in literature are quite complex, for which it makes sense to discuss here briefly its physical interpretation: first of all, conventional and modified Williamson–Hall Equation (1) and (2), respectively, look very similar, so that from the second sum terms, we rewrite and obtain the micro-strain by dislocation components only.

$$\Delta\varepsilon = \frac{1}{4}(R_e\rho^{1/2})(b\rho^{1/2})(b\overline{C}G) \tag{3}$$

Generally, in diffraction, distortions are only seen if the displacement field $\vec{u}$ has a nonvanishing projection $\vec{u}\cdot\vec{G}$ to the scattering vector $\vec{G}$ yielding the term $b\,\overline{C}\,G$, in which $\overline{C}$ denotes an average over the possible orientation distributions of $\vec{b}$ with respect to $\vec{G}$. Because the strain field is anisotropic, the displacement components of $\vec{u}$ along $\vec{G}$ must depend on the stiffness tensor **S**, that is on Poisson's ratio to describe components when $\vec{b}$ is not parallel to $\vec{G}$. The term $\vec{u}\cdot\vec{G}$ would only describe a peak shift, and to obtain a broadening, it has to be integrated over the strain accumulated over the mean spacing between dislocations, yielding the factor $b\,\rho^{1/2}$. Last but not least, the Wilkens arrangement parameter $R_e\,\rho^{1/2}$ ($= M$) scales for the outreach and interaction of dislocation strain fields and is an approximation

depending more detailed on the dislocation arrangements. Altogether, the line width ΔQ is proportional to the square of the scattering vector, one factor is because of strain broadening $\Delta\varepsilon \sim \Delta Q/G$ and the second appears through the contrast factor $\vec{u}\cdot\vec{G}$. Note the factor $M\,\rho^{1/2} = R_e\,\rho$, meaning that the slope of a line in a plot ΔQ versus $G^2\overline{C}$ is directly proportional to the dislocation density. In contrast, when R_e scales with the dislocation spacing, that is, $M = $ constant (≈ 1), and then the slope would be proportional to the square root of the dislocation density.

Thus, we have to distinguish two cases: 1) low and 2) high dislocation density by which the distance between two dislocations, $\rho^{-1/2}$, is larger or smaller, respectively, than a critical maximum dislocation cutoff radius R_e^m. To estimate the latter, dislocation theory approximates the corresponding line energy $U_{el} = 1/2\,\mu\,b^2$, for screw,[50] which is equivalent to $R_e^m = b\,e^{2\pi}$, in which μ is the shear modulus. For $\rho^{-1/2} > R_e^m$ and $\rho^{-1/2} <, R_e^m$ we compute dislocation densities linear (ρ_+) and quadratic (ρ_-) to the regression slope β by

$$\rho_+ = \frac{4\beta}{R_e^m b^2} \text{ and } \rho_- = \left(\frac{4\beta}{b^2}\right)^2 \tag{4}$$

respectively. For the physically realistic result, we take the geometric average

$$\rho = (\rho_+^2 + \rho_-^2)^{1/2} \tag{5}$$

meaning we take into account $R_e \approx \min(R_e^m, \rho^{-1/2})$.

The cited literature reveals that the average contrast factors of individual peaks are used to account for strain anisotropy by the equation

$$\overline{C}_{hkl} = \overline{C}_{h00}(1 - qH^2) \tag{6}$$

with

$$H^2 = \frac{(h^2k^2 + h^2l^2 + k^2l^2)}{(h^2 + k^2 + l^2)^2} \tag{7}$$

where q represents a parameter for the dislocation character, edge, or screw, and $\overline{C}_{h00}$ is the average contrast factor for the $h00$ reflection. Here, we assume a homogeneous model is a sufficient approach for the contrast factor estimation.[51] The average contrast factors for different diffraction vectors depend on the stiffness tensor **S** of the HEA, which enumerate $S_{11} = 172.1$ GPa, $S_{12} = 107.5$ GPa, $S_{44} = 92$ GPa as per reference[27] and come by the software package ANIZC,[52] resulting in $\overline{C}_{h00} = 0.279$ with $q = 1.51$ for edge and $\overline{C}_{h00} = 0.281$ with $q = 2.32$ for screw dislocations. Here, we estimate a reasonable value of $q = 2.0$, close to the average, and describing a mixed character of dislocations. So the average contrast factor equation becomes

$$\overline{C}_{hkl} = 0.279\,(1 - 2.0 H^2) \tag{8}$$

This modified Williamson–Hall evaluation has been applied to the neutron data and results are compiled in **Table 2**. Note, grain sizes are the coherent domain sizes, which may contain larger systematic error due to the relatively poor modeling of the instrument resolution function; however, the trend is clearly seen.

3.3.1. As-Received HEA

Figure 4b shows the modified Williamson–Hall plot for the as-printed HEA at different temperatures, compared to the apparently fully recrystallized HPT-processed specimen at 1000 K. It is clear that all of them fall onto straight lines with the fit parameters α and β denoting axis offsets and slopes of the lines, respectively. The linear behavior in this representation indicates that the main source of stain in the as-printed HEA comes from dislocations (type III micro-stress), which agrees to an earlier report.[53] Four phenomena are observed from Figure 4. First, the slope of the as-printed HEA in Figure 4b remains almost stable up to 850 K and shows a slight decrease up to 1000 K. Based on Equation (2), Table 2 gives the dislocation density of the as-printed HEA at 338 and 1000 K, which are 1.473×10^{14} and 1.307×10^{14} m^{-2}, respectively, indicating that type III residual stress remains almost unchanged at temperatures <1000 K, thereafter a slight annihilation of dislocation occurs at about

1000 K. Second, the Williamson–Hall plot for the as-cast HEA at 338 K fits already a perfect line in Figure 4a and there is no need to apply the modified Williamson–Hall method, meaning it exposes an almost strain-free structure. It also demonstrates that the traditional metal manufacturing method introduces less strain and dislocations as compared to the AM approach. Third, the plot of the as-cast HEA at 338 K almost overlaps with that at 1000 K, demonstrating that heat treatment has a negligible effect in micro-strain release and change of dislocation density on the as-cast alloy. Fourth, the HPT-processed HEA at 1000 K (green line) was compared to the as-printed one at 1000 K (pink line). From the slope, the dislocation density of the former evaluates to 0.3258×10^{14} m^{-2}, which is much smaller than the latter one. The results demonstrate that nanostructuring by severe plastic deformation and subsequent annealing can largely reduce the dislocation density that simple heating on the HEA without nanostructuring failed to achieve. We attribute these observations to the following scenarios: 1) as-cast specimens contain lower dislocation densities than as-printed, because 2) the dislocation density of as-printed material is increased due to the repeated local melting and heat-affected zones inducing thermal stresses and fatigue, and as we show later, 3) the HPT-processed material has already fully recrystallized at 1000 K, exposing dislocation- and stress-free grains in their microstructure.

3.3.2. HPT-Processed HEA

The temperature dependence of the structural evolution in the additively manufactured HEA after HPT was separately evaluated upon heating from room temperature 303 to 1273 K by applying the conventional Williamson–Hall method, as shown in **Figure 5**a. For the severely deformed specimens after heating below 1000 K, only the close-packed habit planes 111 and 222 of the slip systems are used because, in other crystallographic directions, for example, 200, the system has shorter coherence lengths due to the local crystallographic anisotropy of the dislocations, thus relatively emphasized broadening. A recent report demonstrated a consistent analysis procedure on X-ray diffraction data of an HPT-processed 316 L steel.[54] As seen in Figure 3b, some of the other reflections were even difficult to extract due to texture and low counting statistics. For high temperatures at and above

Table 2. Comparison of linear regression parameters α ($\pm 8\%$) and β ($\pm 6\%$), evaluated dislocation densities, coherent domain size ($\pm 8\%$), microscopic grain size ($\pm 10\%$), stored dislocation energy, grain boundary energy, stored energy in vacancies, and residual stress energy for CoCrFeNi under different conditions.

	As-printed at 338 K	As-printed at 1000 K	HPT-processed at 303 K	HPT-processed at 1000 K
α [Å^{-1}]	0.009626	0.0069842	0.030155	0.0057414
β [Å]	0.0017563	0.0016352	0.012385	0.00061796
Dislocation density, ρ [$\times 10^{14}$ m^{-2}]	1.473	1.307	61.13	0.3258
Domain size [nm]	92	126	29	153
Microscopy grain size [nm]	50 000	–	55	–
Stored dislocation energy [J kg^{-1}]	47	42	1322	12
Grain boundary energy [J kg^{-1}]	5	–	4364	–
Stored energy in vacancies [J kg^{-1}]	–	–	2800	–
Residual stress energy [J kg^{-1}]	–	–	1200	–

ADVANCED
SCIENCE NEWS

www.advancedsciencenews.com
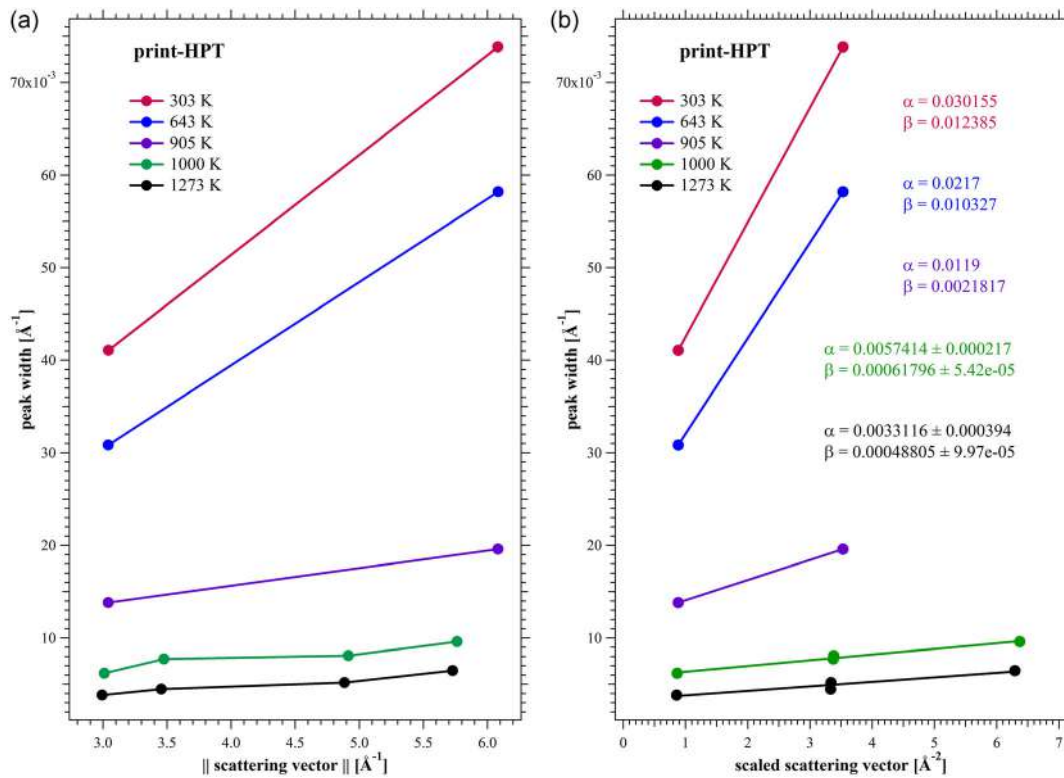
ADVANCED
ENGINEERING
MATERIALS

www.aem-journal.com

Figure 5. Full width at half maximum at Bank 1 of various *hkl* Laue–Bragg interferences from HPT-processed HEA at different temperatures in a) a classical Williamson–Hall plot and b) a modified Williamson–Hall plot. The fit parameters α and β denote axis offsets and slopes of the lines, respectively.

1000 K, four peaks (111, 200, 220, 311) are used to plot the Williamson–Hall lines. Similarly, the modified Williamson–Hall plot can be obtained for the HPT-processed HEA as shown in Figure 5b with the similar parameters of α and β as in Figure 4b. The slopes of the lines have a slight but continuous decrease from 303 to 643 K, while a sudden drop in slope from 10.33×10^{-3} Å at 643 K to 2.18×10^{-3} Å is observed at 905 K. It implies that the lower temperatures have less effect on the dislocation-introduced micro-strain until 905 K, from where micro-strain has a giant reduction. Moreover, a minor slope change between 1000 and 1273 K is observed, indicating that at 1000 K, the micro-strain release is almost finished and further heating has less effect. The dislocation density calculated for the HPT-processed HEA at 303 K was 61.13×10^{14} m^{-2}, and it reduced to 0.3258×10^{14} m^{-2} at 1000 K as summarized in Table 2.

We interpret the behavior of the slope drops in both conventional and modified Williamson–Hall plots to a scenario where 1) both residual- and micro-stresses relax and recover up to 905 K, at which 2) the microstructure recrystallizes to create dislocation-free grains, and thereafter 3) the grains may grow at higher temperatures without introduction of further stresses and dislocations.

3.4. Stored Energy Considerations

Grain refinement and microstructure generally lead to an increase of total energy in the system, where contributing parts are due to the elastic stress field around dislocations, interfacial energies between grains, introduced point defects such as vacancies, intergranular residual stresses such as Bauschinger, and global long-range residual stress.

The dislocation-contributed elastic stored energy can be estimated based on the textbook formulas for the energy per unit length[50]

$$U_{\mathrm{el}} = -\left(f + \frac{1-f}{1-\nu}\right)\frac{\mu b^2}{4\pi}\ln(b\rho^{1/2}) \tag{9}$$

in which f and $(1-f)$ are the fractions of screw and edge dislocations, respectively, $\mu = E/2(1+\nu)$ where E is Young's modulus and ν is Poisson's ratio. $U_{\mathrm{el}}\,\rho$ gives the energy per volume and $W_{el} = U_{\mathrm{el}}\,\rho/\rho_{\mathrm{m}}$ the dislocation stored energy per mass unit, with mass–density ρ_{m}.

We estimate $f = \frac{1}{2}$, $\nu = 0.3$, $\rho_{\mathrm{m}} = 8100$ kg m^{-3},[55] and find $E = 189$ GPa[56] rendering $\mu = 72.7$ GPa to calculate the experimental results added to Table 2.

The grain interface energy is the contribution of high-angle grain boundaries and has been reported to be $\gamma_{\mathrm{GB}} = 0.679$ J m^{-2} at 300 K and 0.787 J m^{-2} at 1000 K.[57] With the total amount of grain boundaries expressed by grain size D, the grain boundary energy per mass amounts to

$$W_{\mathrm{GB}} = \frac{3\gamma_{\mathrm{GB}}}{D\rho_{\mathrm{m}}} \tag{10}$$

Note that D is the grain diameter, which can be much larger than the coherent scattering volume—the latter is more

ADVANCED
SCIENCE NEWS

www.advancedsciencenews.com

ADVANCED
ENGINEERING
MATERIALS

www.aem-journal.com

representing subgrains, or space between dislocation arrangements. Energy contributions are added to Table 2.

After HPT, the concentration c_V of vacancies at room temperature can be very high and their total contributed energy per mass is

$$W_V = c_V E_f N_A M \qquad (11)$$

with an estimated vacancy formation energy from Ni, $E_f \approx 1.75 \, eV$,[58] the molar mass of the alloy $M = 56.4 \times 10^{-3} \, kg \, mol^{-1}$ and Avogadro's number N_A. We establish a simple model of lattice parameter shift, or strain contribution $\Delta \varepsilon_V$, due to vacancies in the following way: based on the local lattice relaxation around a vacancy, we set the linear strain $\Delta \varepsilon_V$ one-third of the volumetric strain, or $3 \Delta \varepsilon_V = (V_f - V_0)/V_0$ where V_f and V_0 are the vacancy formation and atomic volumes, respectively. Assuming the strained volume is over 2 unit cells to each side of the vacancy, affecting 4^3 cells, and applying Vegard's law scaling the number of strained cells to the number of total cells, we obtain

$$c_V = 3 \frac{\varepsilon_V}{(V_f - V_0)/V_0} \qquad (12)$$

With $(V_f - V_0)/V_0 \approx 0.05$[58] and $\Delta \varepsilon_V = 1.0 \times 10^{-3}$ (see further onward) for the HPT-processed specimen, a vacancy concentration of $c_V = 9.4 \times 10^{-4}$ and thus a vacancy stored energy of $W_V = 2800 \, J \, kg^{-1}$ are estimated.

As HPT-processed samples are often observed to crack after crack initiation, for example, by the onset of cutting, huge residual stresses are expected,[59] which we summarize in global stress fields biased by local Bauschinger stress. Assume residual strains $\varepsilon_{res} = 10^{-2}$ being of the order of half the yield elastic strains, the contribution of stored energy is

$$W_{res} = \frac{1}{2} E \varepsilon_{res}^2 / \rho_m \qquad (13)$$

amounting to 1200 J kg^{-1}.

3.5. Texture Evolution

Some texture indication can be obtained from our neutron experimental results as shown in **Figure 6**, since three detector banks locate in different directions toward a test sample surface. Although the orientation coverage is very limited, the study allows to indicate the in situ texture evolution with temperature. Because the scattering signal emerges from the entire specimen, texture components integrate necessarily to fiber textures, as imposed by the sample geometry. The angles between corresponding scattering vector directions of three banks and the sample normal are 12.28°, 45°, and 73.06° respectively, as illustrated in Figure 6d. Moreover, Figure 6 indicates orientations of the three scattering vectors 111, 200, and 220 of the HEA in conditions of a) as-printed, b) HPT-processed, and c) HPT-processed and heated at 950 K. Thicker arrows imply the neutron diffraction peaks with higher intensities as read from Figure 3, while the weaker reflection intensities are depicted by the arrows with thinner lines. Due to a low resolution of detector Bank 3, attention is mainly focused on the results from Banks 1 and 2.

In Figure 6a, the 220 scattering vector alignment peaks close to the sample normal, proving an α–<110> fiber texture of the as-printed HEA. As discussed on Figure 3a, the texture of the as-printed HEA tends to maintain unchanged upon heating. Similarly, Figure 6b supports a strong γ–<111> fiber texture after HPT. The texture change from α–<110> fiber to γ–<111> fiber after HPT processing mainly results from significant grain refinement and grain rotation during severe plastic deformation under HPT. It is consistent with similar studies on the same material[38] and with typical shear textures in *fcc* metals processed by HPT, such as pure Al,[60] an *fcc* CrMnFeCoNi,[61] and an *fcc* CoCuFeMnNi.[62] For the texture after heating at 950 K as depicted in Figure 6c, the anterior γ–<111> fiber retains in Bank 1 but weakened as Banks 2 and 3 also show apparently high 111 intensity. This observation can be explained in two parts. First, the retained <111> deformation
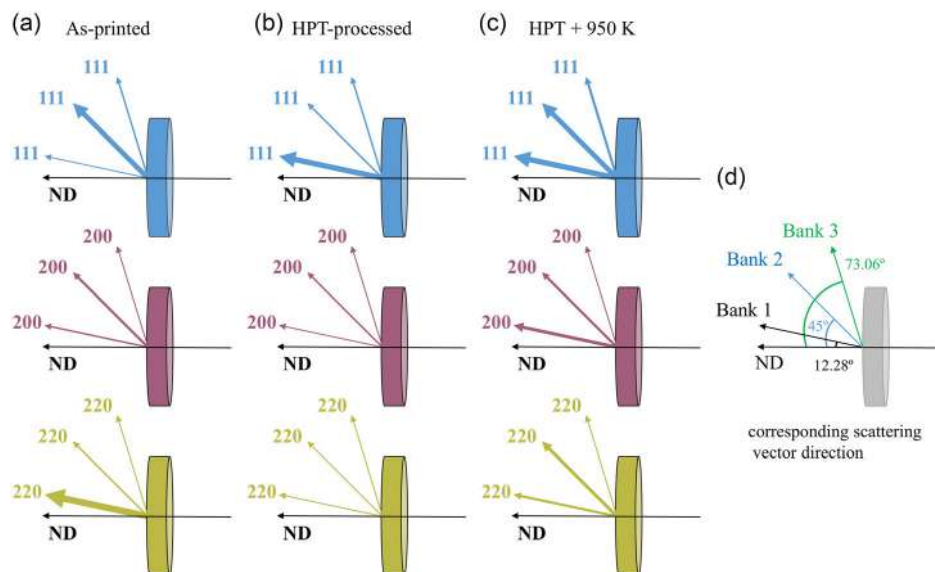

Figure 6. Texture evolution of HEA in a) as-printed, b) HPT–processed, c) HPT–processed and heated at 950 K, and d) the corresponding scattering vector directions. The thickness of the orientation vectors represents qualitatively the observed intensity of the Laue–Bragg interferences.

ADVANCED
SCIENCE NEWS

www.advancedsciencenews.com

ADVANCED
ENGINEERING
MATERIALS

www.aem-journal.com

fiber texture indicates retention of parent grain orientation.[63] The evolution can be interpreted as following: during recrystallization up to 905 K as estimated earlier, new strain-free grains nucleate at grain boundaries and triple junctions. The orientation of the nuclei tends to follow the surrounding deformed grains to some extent, thus leading to the component of retention of the deformation texture. Second, the obvious reappearance of the 111 reflection in all banks indicates the weakened <111> fiber texture after annealing, which is ascribed to a grain reorientation process upon recrystallization.[64] Similar phenomena have also been observed in other *fcc* alloys, such as twinning-induced plasticity steels[65] and copper.[66]

Supporting the neutron diffraction texture, the near-surface texture of the as–printed and HPT-processed HEA without heating was measured by laboratory X-ray diffraction using peaks of 111, 200, 220, 311. **Figure 7**a,b shows the obtained PF and IPF of the as-printed and HPT-processed HEA, respectively. The IPF in Figure 7 show the texture along the normal direction (ND). It is clear that the as–printed HEA mainly possesses an α–<110> fiber texture, and it is consistent with the former neutron data. On the contrary, the HPT-processed HEA exhibits a double-fiber texture with a dominant <111> and weak <100>, which is different from the neutron data. This is because the X-ray measurements only penetrate a few micrometer to sense a near-surface texture while the neutron experiment probes on the entire bulk specimen. This discrepancy is ascribed to the fact that the HPT specimen is highly inhomogeneous in terms of local disorder and localized microstructural processing. For example, such has been demonstrated in a Ti–45Al–7.5Nb alloy processed by HPT, where a removal of several hundred-micron layers has proven the occurrence of heterogeneous phase transformation and order to disorder transformation within the HPT-processed disk.[59]

4. Discussion

4.1. Comparison Between As-Printed and As-Cast HEA

Figure 4a illustrates the peak widths of the as-printed and as-cast HEA, from which the former exhibits strong unsystematic behavior in contrast to the latter fitting almost a straight line, even at room temperature. Such unsystematic behavior in the as-printed HEA is typical for *fcc* crystals that are highly strained and result from the anisotropy in the local crystallographic strain field surrounding dislocations, scaling with their density.[67] Moreover, the heating process has almost no effect on the micro-strain of the as-cast HEA, demonstrating that dislocation activity is small due to an initially low dislocation density.

This is underlined by **Figure 8**, displaying the evolution of the full width at half maximum for a) 200 and b) 220 peaks upon heating of both as-cast (gray lines) and as-printed HEA (red lines). The peak width of the as-cast HEA has no change upon heating, demonstrating again that no recovery or recrystallization happens. Such stable behavior can be attributed to insufficient driving force for recovery and recrystallization, due to a low dislocation density right upon the casting process.

Meanwhile, the breadth of the as-printed HEA keeps unchanged at the beginning of the heating through 850 K (see Figure 8), and is followed by a significant drop after about 850–1000 K. This behavior can be interpreted as sluggish diffusion as an inherent property of HEA at low temperature (<850 K), while at high temperature (850–1000 K), the diffusion coefficient increases and dislocation annihilation becomes accelerated, in parallelism to the literature results for a CoCrFeMnNi alloy.[68] Outcomes from the slopes of the Williamson–Hall plots for as-printed HEA in Figure 4b are consistent, showing less change between 338, 666, and 850 K but experiencing a distinguishable drop at 1000 K. As the peak width involves both grain size and micro-strain effects, here the slope represents the micro-strain evolution. Thus, this small slope drop of the as-printed HEA between 850 and 1000 K indicates a limited amount of continuous dislocation annihilation, and is denoted as grain recovery. Although this dislocation removal occurs in the range of typical recrystallization temperatures of CoCrFeNi HEA of about 773–1000 K,[69] it is ambiguous to identify the occurrence of recrystallization due to the following two reasons. First, even after 1000 K, the conventional Williamson–Hall plot still gives a zigzag line for the as-printed HEA as shown in Figure 4a, implying that simply heating to the
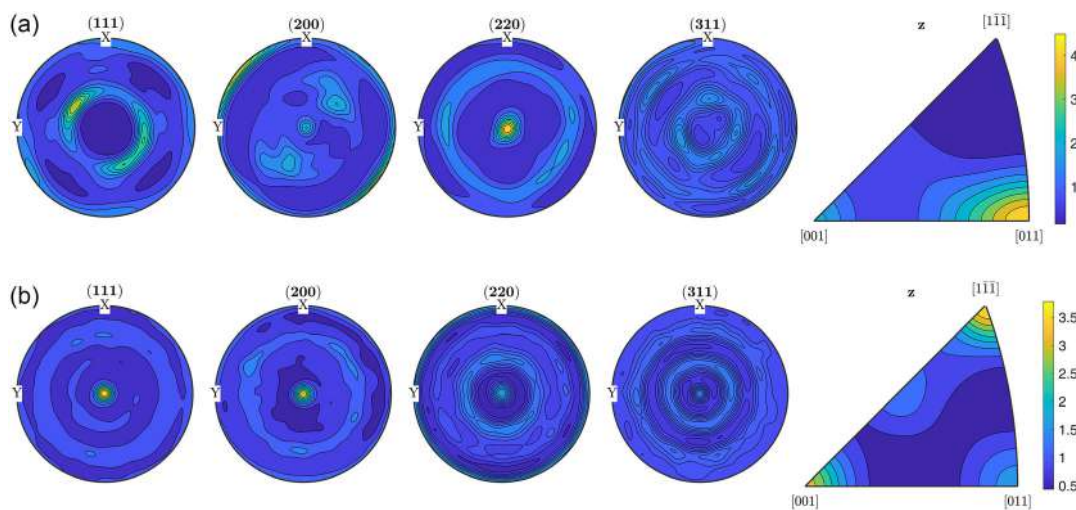

Figure 7. Pole figures and inverse pole figures of a) as-printed and b) HPT-processed HEA.

**ADVANCED
SCIENCE NEWS**

www.advancedsciencenews.com

**ADVANCED
ENGINEERING
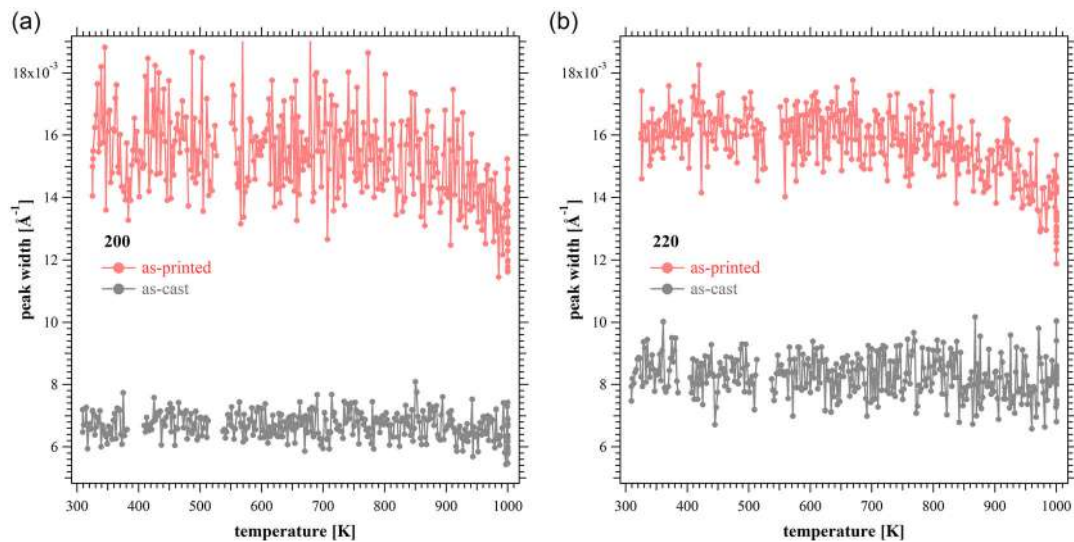MATERIALS**

www.aem-journal.com

Figure 8. Evolution of full peak widths at half maximum from Bank 1 upon thermo-processing for two types of HEA for reflections: a) 200 and b) 220.

sample is not enough to relieve micro-strain. Second, from Figure 3a, the intensity ratios of all peaks in the as-printed HEA seem unchanged and the α-<110> fiber texture remains stable upon heating, whereas for a classical recrystallization process of an *fcc* structure, texture change should be easily detected due to grain reorientation,[69] as shown in the HPT-processed HEA in Figure 6c.

In conclusion, the as-cast HEA exhibits a virtually minor dislocation structure at room temperature, which remains stable even at 1000 K. In contrast, the as-printed HEA has a relatively high dislocation density, leading to dislocation strain and resulting in the distinct unsystematic behavior in the classical Williamson–Hall plot, which can be eliminated by applying the modified Williamson–Hall method on dislocation theory. Meanwhile, upon thermal treatment, the micro-strain undergoes slight reduction but remains still higher than the as-cast HEA, indicating that mere heat treatment of the additively manufactured HEA is not enough for micro-strain relieve.[26]

4.2. Comparison Between HPT-Processed and As-Printed HEA

At the incipient stage of the neutron diffraction experiment in Figure 3b representing the results at room temperature, broad reflections of neutron peaks with wide distributions along the scattering vector can be observed for the printed samples processed by HPT. Such broad peaks arise from lattice distortions and internal micro-strain through micro-stresses, introduced by severe plastic deformation. Upon subsequent heat treatment, the diffraction profiles at all peaks sharpen at about 800 K, which implies a significant reduction of micro-strain. **Figure 9** plots the temperature-dependent evolution of the 111 peak width for both as-printed and further HPT–processed HEA. Herein, the 111 reflection of the as-printed HEA is evaluated from Bank 2, however, the differences in instrumental resolution between the banks can be ignored since they are relatively small as compared to the peak width of the HPT–processed HEA. An earlier

report provides an example of the ignorable instrumental broadening in comparison with the peak broadening due to nanostructuring after severe plastic deformation by HPT.[70]

It is evident in Figure 9 that the peak width of HPT-processed HEA shows a relatively small and linear drop from room temperature to 800 K, followed by a sharp drop ending around 960 K. Since the breadth reflects the micro-strain introduced by dislocations, the first linear decrease can be interpreted as recovery while the sharp drop indicates a large amount of dislocation annihilation, thus ascribed to recrystallization.[63] Moreover, above 960 K, the breadth of the HPT-processed HEA shows almost no variation, supporting that recrystallization ends at about 960 K. All these phenomena are consistent with Figure 5b: at temperatures of 303 and 643 K, the slopes are interpreted as that dislocation density is quite high and shows small decrease with increasing temperature, while a large drop occurs at around 905 K followed by a continuous decrease toward 1000 K, which is almost kept consistent up to 1273 K. It indicates that the residual stress is almost relieved at 1000 K, and further heating has limited effect on the micro-strain evolution.

Although the as-printed HEA without HPT processing experiences slight recovery from 850 to 1000 K as seen in Figure 8, it is incomparable with the severely deformed HEA by HPT as seen in Figure 9, where severe plastic deformation has introduced large amounts of defects incubating high levels of stored energy for recovery and recrystallization. Moreover, from Figure 4b and 5b, the dislocation density upon annealing at 1000 K of the HPT sample becomes even smaller than the as-printed one. This provides strong evidence that HPT followed by the heat treatment can minimize the dislocation density through recrystallization. The work demonstrates important information that for example near-surface bulk treatment by severe plastic deformation and subsequent heat treatment can fully relax internal stresses in additively manufactured materials.

Overall, the various results obtained by diffraction line width of a single peak, change of slope in both conventional and modified Williamson–Hall analysis, and texture evolution
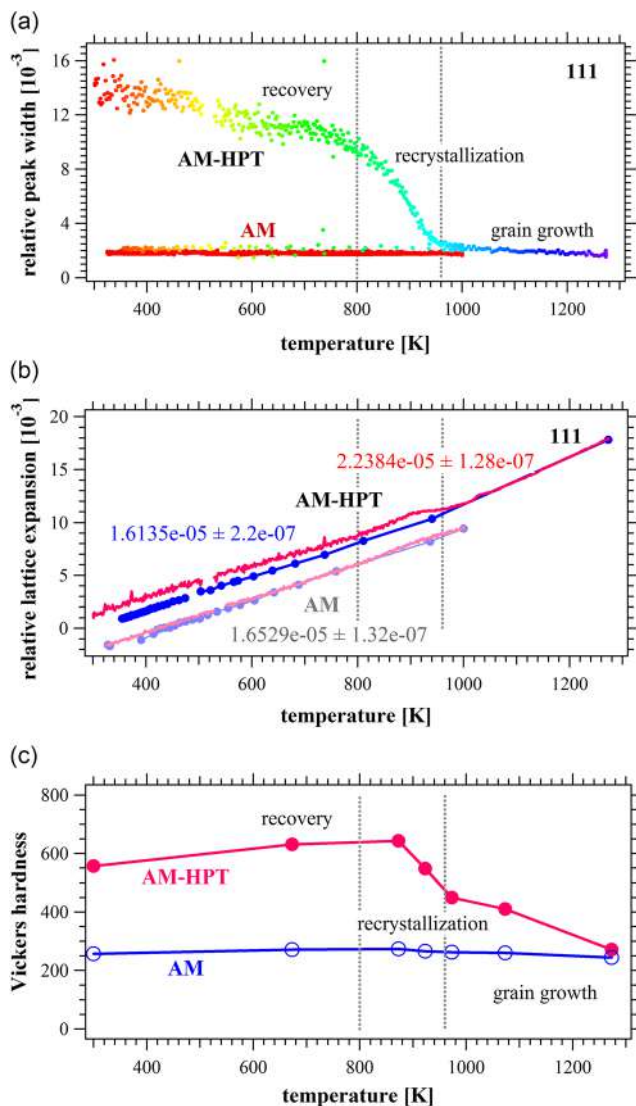
ADVANCED
SCIENCE NEWS
www.advancedsciencenews.com

ADVANCED
ENGINEERING
MATERIALS
www.aem-journal.com

Figure 9. a) Evolution of full width at half maximum of the 111 reflection upon annealing for as-printed (additive manufacturing [AM]) and HPT-processed HEA, Bank 2 and Bank 1, respectively. b) relative lattice expansion upon the heating (reddish) and cooling (bluish) cycles for as-printed (offset by -2×10^{-3}) and HPT-processed materials, measured by the 111 and 200 reflections, respectively. c) Vickers hardness H_v versus annealing temperature for both as-printed and HPT-processed specimens.

underline the following scenarios: 1) the as-cast, as-printed, and HPT–processed specimens show increasing order of dislocation density, which relates to relative smooth manufacturing from the melt, repeated heating- and cooling-induced thermal stress accommodation, and grain breaking by severe plastic deformation, respectively. 2) While dislocation density and stored energy are low, the as-cast material does not show much dislocation annihilation upon heating, whereas the as-printed material recovers slightly above 850 K, and the most serious microstructural changes occur in the HPT-processed specimen. 3) The latter exposes further three regimes of (I) residual stress recovery up to 800 K, (II) a complete recrystallization process to 960 K, and

(III) normal grain growth beyond, leading to a stress- and dislocation-minimized microstructure.

4.3. Thermal Expansion and Vacancy Concentration

Total lattice strain upon heating and cooling is shown in Figure 9b. The main factor is conventional thermal expansion $\eta_{300\,K}$, attributed to the anharmonicity of the atomic binding potentials and can be evaluated at low temperatures, at which diffusion does not play a role, to be $\eta_{300\,K} = 16 \times 10^{-6}\,K^{-1}$ upon cooling, after the system has recrystallized. Upon heating, there is a dramatic change at 900 K, where expansion almost halts and the strain increases faster with $\eta_{1200\,K} = 22 \times 10^{-6}\,K^{-1}$. Upon cooling, the crossover is again near 900 K.

An interpretation of the results is as follows: 1) the holding of thermal expansion during heating occurs due to a decrease of vacancies. The change of strain is $\Delta\varepsilon_V = 1 \times 10^{-3}\,K^{-1}$, giving input to the calculation of vacancies with $c_V = 9.4 \times 10^{-4}$ conducted in Chapter 3.4. and Table 2; 2) At 900 K, diffusion becomes important, thereby starting to recombine the excess vacancies to equilibrium.; 3) Subsequently, new vacancies are being thermally created again, giving raise to faster lattice expansion.

4.4. Hardness Evolution of HPT-Processed HEA

Vickers hardness H_V as a function of annealing temperature is displayed in Figure 9c for the HEA after heating ex situ to given temperatures, followed by quenching. As the material recovers (Figure 9a), hardness even increases beyond the high value obtained directly after HPT due to a relaxation of intergranular stresses, which have biased the material after processing. During recrystallization, the hardness decreases when dislocation-free grains establish and grow, in accordance with the Hall–Patch grain size relationship. In the grain growth regime, hardness approaches the low values of the unprocessed material.

5. The Processing–Microstructure–Property Paradigm

The previous chapters have established and derived the outcomes of the neutron measurements as microstructure evolution and of hardness testing as mechanical properties after HPT and subsequent annealing steps.

Severe plastic deformation by HPT led the material to highly distorted states far beyond thermodynamic equilibrium. It not only creates residual stresses both macroscopically and functionally explained by the Bauschinger effect, but also refines the grains into the tens of nanometers range. While this increases the interfacial energy at grain boundaries, a large density of dislocations is introduced concurrently. The vacancy concentration of the HPT-processed material athermally stored at room temperature can reach the value as high as that at its melting temperature.[71] Vacancy concentrations are usually exponentially enhanced under pressure[71] and further upon shear deformation, while even more vacancies can emit during the HPT treatment, for example, from the large density of edge dislocations

ADVANCED
SCIENCE NEWS

www.advancedsciencenews.com

ADVANCED
ENGINEERING
MATERIALS

www.aem-journal.com

upon depressurizing from processing to ambient pressure and the settlement of local stress fields.

In the HPT-processed CoCrFeNi, the vacancy strain was found to be $\Delta\varepsilon_V \approx 1 \times 10^{-3}$ at the onset of heating (Figure 9b), slightly lower than half of the value upon recovery at 800 K, where residual and Bauschinger stresses reduce and the microstructure settles. Increasing temperature to 900 K re-established a local maximum of vacancy concentration, due to onset of diffusion. In this regime, the athermally created dislocation lines, containing numerous jogs and kinks, can straighten and thus minimize their line energy by diffusion-controlled dislocation climb through emission of vacancies. The latter enhance diffusion and drive the recrystallization process, decreasing all stored energies. Subsequently, further heating allows the grains to grow while thermal vacancies are further created again, enlarging the linear thermal expansion coefficient.

By contrast, for the as-printed material, vacancy concentration, dislocation density, and grain boundary energies are small, keeping the dislocation structure intact while heating to 1000 K. Interestingly, also a bump in expansion upon first heating is seen equally at 900 K, albeit much smaller in magnitude. The as-printed material exposes still a remarkable amount of dislocations (in cells) and some of the previously described effects are visible, but smaller by more than one order of magnitude.

A very similar neutron study as on the present CoCrFeNi HEA has been published by Kawasaki et al. on 316 L Stainless Steel.[72] Therein, Figure 6b of reference,[72] also a systematic strain offset can be recognized between the heating and the cooling curves, about 5× smaller than the present results for HEA. Such scaling can be explained by the fact that thermal vacancy creation is 5× larger in an equiatomic four-species HEA as compared to a (near) monoatomic alloy.[73]

The mechanical properties are inherently linked to the microstructure. After HPT processing at room temperature, hardness has increased dramatically from 256 to 557 H_V. However, the applied stress of the hardness measurement is biased by both residual and Bauschinger stresses as well as a high vacancy density. As they decrease while heating, hardness increases to the measured maximum of 643 H_V after heating to 873 K. Upon recrystallization expressed by both a strong decrease of peak width and reductions in dislocation density and vacancy concentration by thermalization, the hardness diminishes to 410 H_V at 1073 K. Further decrease follows upon grain growth according to the Hall–Petch model toward 271 H_V for the fully recovered material after annealing at 1273 K. In contrast, the hardness of the as-printed HEA basically remains constant upon all different annealing steps, revealing again that the microstructure and dislocation arrangements barely change, due to insufficient stored energies.

The four enumerated contributions of stored energy (Table 2) are all comparable in magnitude for the HPT-processed HEA, amounting in the kilo-Joule per kilogram range, while the corresponding values are at least 2–3 orders of magnitude smaller than for the as-printed material. The obtained energies for the HEA lie in the same order of magnitude as for 316 L Stainless Steel reported by El-Tahawy et al.[74] who have used calorimetric approaches. There is a tendency that El-Tahawy et al. reported a slightly higher dislocation energy, which the present nanocrystalline HEA makes up by a larger grain

boundary energy. At the end, the one can express the other, depending on where grain boundaries are drawn in a coherent scattering volume; and both report on a total stored energy of the HPT-processed materials very close to 10 kJ kg^{-1}.

Given such good agreement renders the neutron-scattering method a reliable technique to obtain not only crystallographic but also microstructural information simultaneously from various aspects including subtle changes of peak width, peak position, and intensities, taken in situ during temperature ramping. Apart from synchrotron high-energy X-ray diffraction,[75] no other method can deliver so much information in a single experiment, particularly from bulk materials.

6. Summary and Conclusions

In this study, in situ heating neutron experiments were conducted on additive manufactured and conventional cast CoCrFeNi HEA before and after HPT processing and subsequent heating. Conclusions of microstructure and internal stress are depicted as follows: 1) The as-printed HEA has significantly higher micro-strain as compared to the as-cast HEA, implying that 3D printing introduces remarkable microstructural stresses, which is anticipated from the examined and reported microstructures, for example, grain sizes. However, both sample conditions fail to recrystallize upon heating to 1000 K as dislocation density and total stored energy are insufficient. In fact, neither recovery nor recrystallization was recognized for the as-cast HEA, while for the as-printed one, the recovery occurs at around 850 K without obvious recrystallization. 2) HPT breaks the grains down to the nanometer scale and introduces large dislocation density into the bulk material. Upon heating of the HPT-processed HEA, three regimes can be identified, namely a) recovery and residual stress relaxation up to 800 K, followed by b) recrystallization up to 960 K, and c) subsequent growth of dislocation-free grains. These temperature ranges define the thermal stability of the HPT-processed material up to under 800 K, indicating an interesting annealing window for partial recrystallization. 3) The texture evolution of the as-printed HEA after HPT and subsequent heating conforms with traditional fcc metals and alloys. The texture evolution can be estimated from the three detector bank orientations during the in situ measurements and has been complemented by X-ray results taken at the surface. 4) The in situ neutron heating measurements distinguishes recovery and recrystallization processes of microstructure by the evolution of diffraction peak width upon heating, which are consistent with texture reorientation. 5) The modified Williamson–Hall method proves the micro-strain fields of the as-printed HEA stem dominantly from dislocations, which are of the highest density after HPT. The temperature ranges of significant changes in dislocation density are consistent with those observed in the evolution of a single peak width. 6) The lowest micro-strain is achieved after complete recrystallization by heating at 1000 K of the HPT-processed specimen, which is even lower than the as-printed without HPT, thereby suggesting an insight for the design of post-printing processing routes to minimize internal stresses. 7) Hardness measurements after annealing reveal an increase up to 873 K, which is ascribed to residual and Bauschinger stress-relaxation as well as a decrease of athermal

ADVANCED
SCIENCE NEWS

www.advancedsciencenews.com

ADVANCED
ENGINEERING
MATERIALS

www.aem-journal.com

vacancies. The hardness decreases upon recrystallization and reaches the values of the as-printed specimen after grain growth. The as-printed material shows negligible dependence of hardness on temperature. 8) Densities of dislocations, grain boundaries, and vacancies are evaluated, where all contribute to the stored energy. For the HPT-processed material, residual and Bauschinger stress energies are added to them. All four components are in the order of a few kilo-Joule per kilogram, summing to $\approx 10\,\mathrm{kJ\,kg^{-1}}$ in total. Such high stored energy leads to recrystallization in the HPT-processed material, while insufficient energy is stored in the as-printed material. 9) A high vacancy concentration has been inferred at room temperature by HPT, which amounts to the values typical or above those at the melting temperature. The relaxation volume of vacancies affects the lattice parameter, which is clearly visible in the neutron diffraction patterns and the relative lattice expansion plot. 10) Vacancy concentration first decreases when heating to 800 K. It peaks again at 900 K, which is attributed to an exceptional emission at dislocations when kinks and jogs climb to straighten the dislocation lines. The large amount of vacancies triggers the recrystallization process. Upon further heating, vacancy concentration decreases until thermalization, which then increases thermally again. 11) As an outlook, the detailed knowledge obtained to distinguish the ranges and onsets of stress relaxation, recovery, recrystallization, and grain growth after HPT will allow to design special microstructures, ultrafine-tuning mechanical and physical properties. 12) In particular, in situ neutron and synchrotron high-energy X-ray studies are of great potential to solve problems directly, which are difficult to access in conventional laboratory–based studies.

Conflict of Interest

The authors declare no conflict of interest.

Data Availability Statement

The data that support the findings of this study are available from the corresponding author upon reasonable request.

[1] J. W. Yeh, S. K. Chen, S. J. Lin, J. Y. Gan, T. S. Chin, T. T. Shun, C. H. Tsau, S. Y. Chang, *Adv. Eng. Mater.* **2004**, *6*, 299.
[2] B. Cantor, I. T. H. Chang, P. Knight, A. J. B. Vincent, *Mater. Sci. Eng. A* **2004**, *375–377*, 213.
[3] J. Yeh, S. Chen, J. Gan, S. Lin, T. Chin, T.-T. Shun, C.-H. Tsau, S. Y. Chang, *Metall. Mater. Trans. A* **2004**, *35A*, 2533.
[4] J.-W. Yeh, S.-J. Lin, T.-S. Chin, J.-Y. Gan, S.-K. Chen, T.-T. Shun, C.-H. Tsau, S.-Y. Chou, *Metall. Mater. Trans. A* **2004**, *35*, 2533.
[5] D. B. Miracle, O. N. Senkov, *Acta Mater.* **2017**, *122*, 448.
[6] E. P. George, D. Raabe, R. O. Ritchie, *Nat. Rev. Mater.* **2019**, *4*, 515.
[7] E. P. George, W. A. Curtin, C. C. Tasan, *Acta Mater.* **2020**, *188*, 435.
[8] J. W. Yeh, *JOM* **2013**, *65*, 1759.
[9] R. Z. Valiev, Y. Estrin, Z. Horita, T. G. Langdon, M. J. Zehetbauer, Y. T. Zhu, *Mater. Res. Lett.* **2016**, *4*, 1.
[10] A. Hosseinzadeh, A. Radi, J. Richter, T. Wegener, S. V. Sajadifar, T. Niendorf, G. G. Yapici, *J. Manuf. Process.* **2021**, *68*, 788.
[11] R. Z. Valiev, T. G. Langdon, *Prog. Mater. Sci.* **2006**, *51*, 881.
[12] N. Tsuji, Y. Saito, H. Utsunomiya, S. Tanigawa, *Scr. Mater.* **1999**, *40*, 795.
[13] S. Praveen, J. W. Bae, P. Asghari-Rad, J. M. Park, H. S. Kim, *Mater. Sci. Eng., A* **2018**, *734*, 338.
[14] N. Gao, *Mater. Sci. Forum* **2008**, *584–586*, 255.
[15] P. T. Hung, M. Kawasaki, J. K. Han, J. L. Lábár, J. Gubicza, *Mater. Character.* **2021**, *171*, 110807.
[16] K. D. Liss, K. Yan, M. Reid, *Mater. Sci. Eng. A* **2014**, *601*, 78.
[17] K. Liss, K. Yan, *Mater. Sci. Eng., A* **2010**, *528*, 11.
[18] K. D. Liss, X. Liu, X. Li, J. K. Han, R. J. Dippenaar, M. Kawasaki, *Mater. Lett.* **2021**, *304*, 4.
[19] C. Han, Q. Fang, Y. Shi, S. B. Tor, C. K. Chua, K. Zhou, *Adv. Mater.* **2020**, *32*, 1.
[20] Y. Brif, M. Thomas, I. Todd, *Scr. Mater.* **2015**, *99*, 93.
[21] J. M. Park, J. Choe, J. G. Kim, J. W. Bae, J. Moon, S. Yang, K. T. Kim, J. Yu, H. S. Kim, J. Min, J. Choe, *Mater. Res. Lett.* **2019**, *0*, 1.
[22] J. M. Torralba, M. Campos, *Metals* **2020**, *10*, 1.
[23] F. Peyrouzet, D. Hachet, R. Soulas, C. Navone, S. Godet, S. Gorsse, *JOM* **2019**, *71*, 3443.
[24] Y. M. Wang, T. Voisin, J. T. McKeown, J. Ye, N. P. Calta, Z. Li, Z. Zeng, Y. Zhang, W. Chen, T. T. Roehling, R. T. Ott, M. K. Santala, P. J. Depond, M. J. Matthews, A. V. Hamza, T. Zhu, *Nat. Mater.* **2018**, *17*, 63.
[25] M. Shiomi, K. Osakada, K. Nakamura, T. Yamashita, F. Abe, *CIRP Ann Manuf. Technol.* **2004**, *53*, 195.
[26] T. Voisin, J. B. Forien, A. Perron, S. Aubry, N. Bertin, A. Samanta, A. Baker, Y. M. Wang, *Acta Mater.* **2021**, *203*.
[27] Y. Wu, W. H. Liu, X. L. Wang, D. Ma, A. D. Stoica, T. G. Nieh, Z. B. He, Z. P. Lu, *Appl. Phys. Lett.* **2014**, *104*.
[28] K. D. Liss, A. Stark, A. Bartels, H. Clemens, T. Buslaps, D. Phelan, L. A. Yeoh, *Adv. Eng. Mater.* **2008**, *10*, 389.
[29] H. Shi, W. Gan, C. Esling, X. Wang, Y. Zhang, E. Maawad, A. Stark, X. Li, L. Wang, *Acta Mater.* **2020**, *200*, 338.
[30] S. Kabra, K. Yan, D. G. Carr, R. P. Harrison, R. J. Dippenaar, M. Reid, K. D. Liss, *J. Appl. Phys.* **2013**, *113*, 063513.
[31] R. E. Whitfield, D. J. Goossens, A. J. Studer, *J. Phys. Conf. Ser.* **2010**, *251*, 4.
[32] G. Chen, K. D. Liss, P. Cao, *Mater. Sci.* **2015**, *46*, 5887.
[33] S. Xu, M. Reid, J. Lin, Y. Liang, L. Yang, J. Zhang, K. D. Liss, *Scr. Mater.* **2022**, *219*, 114841.
[34] Y. Tomota, P. Lukáš, D. Neov, S. Harjo, Y. R. Abe, *Acta Mater.* **2003**, *51*, 805.
[35] Y. Tomota, *Sci. Technol. Adv. Mater.* **2019**, *20*, 1189.
[36] K.-D. Liss, *Quant. Beam Sci.* **2017**, *1*, 1.
[37] Y. Kuzminova, D. Firsov, A. Dudin, S. Sergeev, A. Zhilyaev, A. Dyakov, A. Chupeeva, A. Alekseev, D. Martynov, I. Akhatov, S. Evlashin, *Intermetallics* **2020**, *116*, 106651.

ADVANCED
SCIENCE NEWS

www.advancedsciencenews.com

ADVANCED
ENGINEERING
MATERIALS

www.aem-journal.com

[38] J. Gubicza, P. T. Hung, M. Kawasaki, J. K. Han, Y. Zhao, Y. Xue, J. L. Lábár, *Mater. Character.* **2019**, *154*, 304.

[39] H. Takada, K. Haga, M. Teshigawara, T. Aso, S. Meigo, H. Kogawa, T. Naoe, T. Wakui, M. Ooi, M. Harada, M. Futakawa, *Science* **2017**, *1*, 8.

[40] K. Nakajima, Y. Kawakita, S. Itoh, J. Abe, K. Aizawa, H. Aoki, H. Endo, M. Fujita, K. Funakoshi, W. Gong, M. Harada, S. Harjo, T. Hattori, M. Hino, T. Honda, A. Hoshikawa, K. Ikeda, T. Ino, T. Ishigaki, Y. Ishikawa, H. Iwase, T. Kai, R. Kajimoto, T. Kamiyama, N. Kaneko, D. Kawana, S. Ohira-Kawamura, T. Kawasaki, A. Kimura, R. Kiyanagi, et al., *Science* **2017**, *1*, 9.

[41] W. R. Busing, H. A. Levy, *Acta Crystallograph.* **1967**, *22*, 457.

[42] F. Bachmann, R. Hielscher, H. Schaeben, *Solid State Phenom.* **2010**, *160*, 63.

[43] W. Zhao, J.-K. Han, Y. O. Kuzminova, S. A. Evlashin, A. P. Zhilyaev, A. M. Pesin, J. Jang, K.-D. Liss, M. Kawasaki, *Mater. Sci. Eng. A* **2021**, *807*, 140898.

[44] P. J. Withers, H. K. D. H. Bhadeshia, *Mater. Sci. Technol.* **2001**, *17*, 355.

[45] G. K. Williamson, W. H. Hall, *Acta Metall.* **1953**, *1*, 22.

[46] T. Ungár, I. Dragomir, Á Révész, A. Borbély, *J. Appl. Crystallogr.* **1999**, *32*, 992.

[47] T. Ungar, *Mater. Sci. Eng. A* **2001**, *310*, 14.

[48] M. Wilkens, *Krist. Tech* **1976**, *11*, 1159.

[49] N. Armstrong, M. Leoni, P. Scardi, *Z. Krist. Suppl.* **2006**, *1*, 81.

[50] D. Hull, D. J. Bacon, in *Introduction To Dislocations*, Elsevier, Amsterdam **2011**.

[51] T. H. Simm, P. J. Withers, J. Quinta Da Fonseca, *J. Appl. Crystallogr.* **2014**, *47*, 1535.

[52] A. Borbély, J. Dragomir-Cernatescu, G. Ribárik, T. Ungár, *J. Appl. Crystallogr.* **2003**, *36*, 160.

[53] R. Pokharel, L. Balogh, D. W. Brown, B. Clausen, G. T. Gray, V. Livescu, S. C. Vogel, S. Takajo, *Scr. Mater.* **2018**, *155*, 16.

[54] J. K. Han, X. Liu, I. Lee, Y. O. Kuzminova, S. A. Evlashin, K. D. Liss, M. Kawasaki, *Mater. Lett.* **2021**, *302*, 130364.

[55] G. Laplanche, P. Gadaud, C. Bärsch, K. Demtröder, C. Reinhart, J. Schreuer, E. P. George, *J. Alloys Compd.* **2018**, *746*, 244.

[56] J. Liu, X. Guo, Q. Lin, Z. He, X. An, L. Li, P. K. Liaw, X. Liao, L. Yu, J. Lin, L. Xie, J. Ren, Y. Zhang, *Sci. China Mater.* **2019**, *62*, 853.

[57] M. Vaidya, K. G. Pradeep, B. S. Murty, G. Wilde, S. V. Divinski, *Sci. Rep.* **2017**, *7*, 1.

[58] L. Y. Nemirovich-Danchenko, A. G. Lipnitskiĭ, S. E. Kul'kova, *Phys. Solid State* **2007**, *49*, 1079.

[59] X. Li, R. J. Dippenaar, J. K. Han, M. Kawasaki, K. D. Liss, *J. Alloys Compd.* **2019**, *787*, 1149.

[60] S. Naghdy, L. Kestens, S. Hertelé, P. Verleysen, *Mater. Character.* **2016**, *120*, 285.

[61] W. Skrotzki, A. Pukenas, E. Odor, B. Joni, T. Ungar, B. Völker, A. Hohenwarter, R. Pippan, E. P. George, *Crystals* **2020**, *10*.

[62] R. Sonkusare, K. Biswas, N. Al-hamdany, H. G. Brokmeier, R. Kalsar, N. Schell, N. P. Gurao, *Mater. Sci. Eng. A* **2020**, *782*, 139187.

[63] R. D. Doherty, D. A. Hughes, F. J. Humphreys, J. J. Jonas, D. Juul Jensen, M. E. Kassner, W. E. King, T. R. McNelley, H. J. McQueen, A. D. Rollett, *Mater. Sci. Eng., A* **1997**, *238*, 219.

[64] T. Guo, J. Li, J. Wang, W. Y. Wang, Y. Liu, X. Luo, H. Kou, E. Beaugnon, *Mater. Sci. Eng., A* **2018**, *729*, 141.

[65] L. Bracke, K. Verbeken, L. A. I. Kestens, *Scr. Mater.* **2012**, *66*, 1007.

[66] Q. Chen, D. Y. Shu, J. Lin, Y. Wu, X. S. Xia, S. H. Huang, Z. D. Zhao, O. V. Mishin, G. L. Wu, *J. Mater. Sci. Technol.* **2017**, *33*, 690.

[67] T. Ungár, G. Tichy, *Phys. Status. Solidi Appl. Res.* **1999**, *171*, 425.

[68] W. Woo, E. Huang, J. Yeh, H. Choo, C. Lee, S. Tu, *Intermetallics* **2015**, *62*, 1.

[69] Z. Wu, H. Bei, F. Otto, G. M. Pharr, E. P. George, *Intermetallics* **2014**, *46*, 131.

[70] J. K. Han, K. D. Liss, T. G. Langdon, M. Kawasaki, *Sci. Rep.* **2019**, *9*, 1.

[71] D. Connétable, P. Maugis, *Acta Mater.* **2020**, *200*, 869.

[72] M. Kawasaki, J. K. Han, X. Liu, Y. Onuki, Y. O. Kuzminova, S. A. Evlashin, A. M. Pesin, A. P. Zhilyaev, K. D. Liss, *Adv. Eng. Mater.* **2022**, *24*, 1.

[73] Z. Wang, C. T. Liu, P. Dou, *Phys. Rev. Mater.* **2017**, *1*, 1.

[74] M. El-Tahawy, Y. Huang, T. Um, H. Choe, J. L. Lábár, T. G. Langdon, J. Gubicza, *J. Mater. Res. Technol.* **2017**, *6*, 339.

[75] K.-D. Liss, A. Bartels, A. Schreyer, H. Clemens, *Text. Microstruct.* **2003**, *35*, 219.

Chapter 7

Structural effect of low Al content in the in-situ additive manufactured CrFeCoNiAlx high-entropy alloy

The previous chapters provided a comprehensive analysis of the PBF CrFeCoNi alloy printed with a pre-alloyed powder. Since there is a lot of literature focusing on the CrFeCoNiAl$_x$ composition, with x=0.5 and higher, while studies considering the low aluminum content are limited, this chapter represents the effect of the small aluminum addition (up to 2 wt%) to the CrFeCoNi system through the printing with the CrFeCoNi and Al powder blends. The beginning of the investigation from small volumes allows systematizing the knowledge of the aluminum effect on the CrFeCoNi with a further increase of the aluminum content.

The materials with aluminum presence demonstrate a lower porosity volume compared with a CrFeCoNi alloy for all considered printing parameters while the microhardness results for the as-built materials are contractible. The XRD analysis revealed the lattice parameter growth of the *f.c.c.* crystal structure, which was the only detected phase. It can indicate the incorporation of aluminum atoms into the crystal structure. At the same time, the EDX mapping analysis revealed the inhomogeneous element distribution in the materials containing aluminum. The 1200°C high-temperature annealing was applied to the investigated materials to uniform the element distribution. According to the EDX analysis, it was successful, but the new

precipitates enriched with aluminum and nitrogen were observed, while the XRD analysis did not demonstrate the formation of any additional phases, presumably, due to its small value. The formation of such precipitates is associated with the nitrogen presence in the CrFeCoNi powder. The SME imaging of the annealed samples represented the finer microstructure without annealing twins for the aluminum contained materials opposite to the four-component alloy. This observation is also proved by the microhardness testing reveling the higher results for the aluminum contained samples.

Contribution: I contributed to the development of the structural and phase analyses of the material, the sample preparation process, the formal analysis, the original draft, the final writing, and editing of the manuscript. I would like to thank all the authors for their valuable contributions to the development of this paper.

Contents lists available at ScienceDirect

Materials Letters

Structural effect of low Al content in the in-situ additive manufactured CrFeCoNiAl$_x$ high-entropy alloy

Yulia Kuzminova [a],[*], Anastasia Shibalova [b], Stanislav Evlashin [a], Igor Shishkovsky [a], Pavel Krakhmalev [c]

[a] Center for Design, Manufacturing & Materials, Skolkovo Institute of Science and Technology, Moscow 121205, Russia
[b] Institute of Nanotechnology of Microelectronics of Russian Academy of Science, Moscow 119991, Russia
[c] Karlstad University, SE-651 88 Karlstad, Sweden

ARTICLE INFO

ABSTRACT

The current work considers the effect of the low Al fraction (x = 0.01, 0.05, and 0.1) on the microstructure and phase composition of the CrFeCoNiAl$_x$ high-entropy alloy in-situ manufactured by powder bed fusion additive technique. The influence of a homogenization annealing at 1200 °C is also presented. The presence of Al powder in the pre-mixed blend decreased the porosity in the as-built samples, while the microhardness did not change significantly. All samples with different Al content demonstrated the chemical inhomogeneity, additionally the Al volatilization was observed. The annealing homogenized the material but led to the Al-rich precipitates. Additionally, the microhardness did not drop significantly for annealed CrFeCoNiAl$_x$ samples. The fraction of annealing twins in CrFeCoNiAl$_x$ was much lower than in CrFeCoNi after annealing at 1200 °C. According to XRD analyses, only the fcc phase was determined for all conditions.

1. Introduction

With the growing attention to high-entropy alloys (HEAs) as the prospective class of materials, the interest in their production by additive manufacturing (AM) also increases. The benefit of AM is an opportunity to use in-situ alloying in optimization of the HEAs composition searching for required phase constitution. In-situ additive manufacturing was realized for CoCrFeNiAl$_x$ HEAs using the direct energy deposition technique [1,2]. However, a limited number of studies consider the application of the laser powder bed fusion (L-PBF) technique to the in-situ HEA manufacturing [3,4], while it is an actively used method.

A large number of studies focus on the CrFeCoNiAl$_x$ system, where the fraction of Al impacts the physical and mechanical material properties. The increase of x toward 0.5–1 initiates the structural transformation from fcc to fcc + bcc/B2 and further to bcc structure with x > 1 [2]. Compared to CoCrFeNi alloy, the strength characteristics of CoCrFeNiAl$_{0.7}$ alloy are twice as high while the ductility is five times as low [5,6]. From this point of view, more attention can be paid to the CoCrFeNiAl$_x$ alloy with a low Al fraction (x < 0.5), which guarantees the ductile fcc structure. Moreover, the addition of a low fraction of an extra

element reveals the element mixing during the printing process, which is essential for the investigation of the in-situ additive manufacturing process.

In the study, the structural effect of low fraction of Al (x = 0.01, 0.05, and 0.1) in the CrCoFeNiAl$_x$ system manufactured with L-PBF technique using the pre-mixed blend of the Al and CrCoFeNi alloy powders was studied for understanding of further use of this alloy with potentially better strength-ductility mechanical properties.

2. Materials and methods

In the present work, the Cr$_{24}$Co$_{25}$Fe$_{26}$Ni$_{25}$ at.% alloy [7] and elemental pure Al powders were used. The Al powder with distribution of 5–75 μm and a mean size of 15 μm was provided by RusAL company (Russia). Three blends were performed by mixing the CrCoFeNi alloy powder and the Al powder using a planetary mill.

The 3D printer TruPrint 1000 (Trumpf) was used for printing 12 cylinders (∅ = 12.0 and h = 10.0 mm) with the applied parameters from the earlier study [7] except the laser power and the laser speed which were in the range of 60–175 W and 120–700 mm/s, respectively. The heat treatment was conducted in the air at 1200 °C for 16 h with further

---

* Corresponding author.
  E-mail address: yulia.kuzminova@skoltech.ru (Y. Kuzminova).

Table 1
EDX chemical composition of the as-built CrFeCoNiAl$_x$ samples (scan area is 120×200 μm^2, E = 156 J/mm^3).

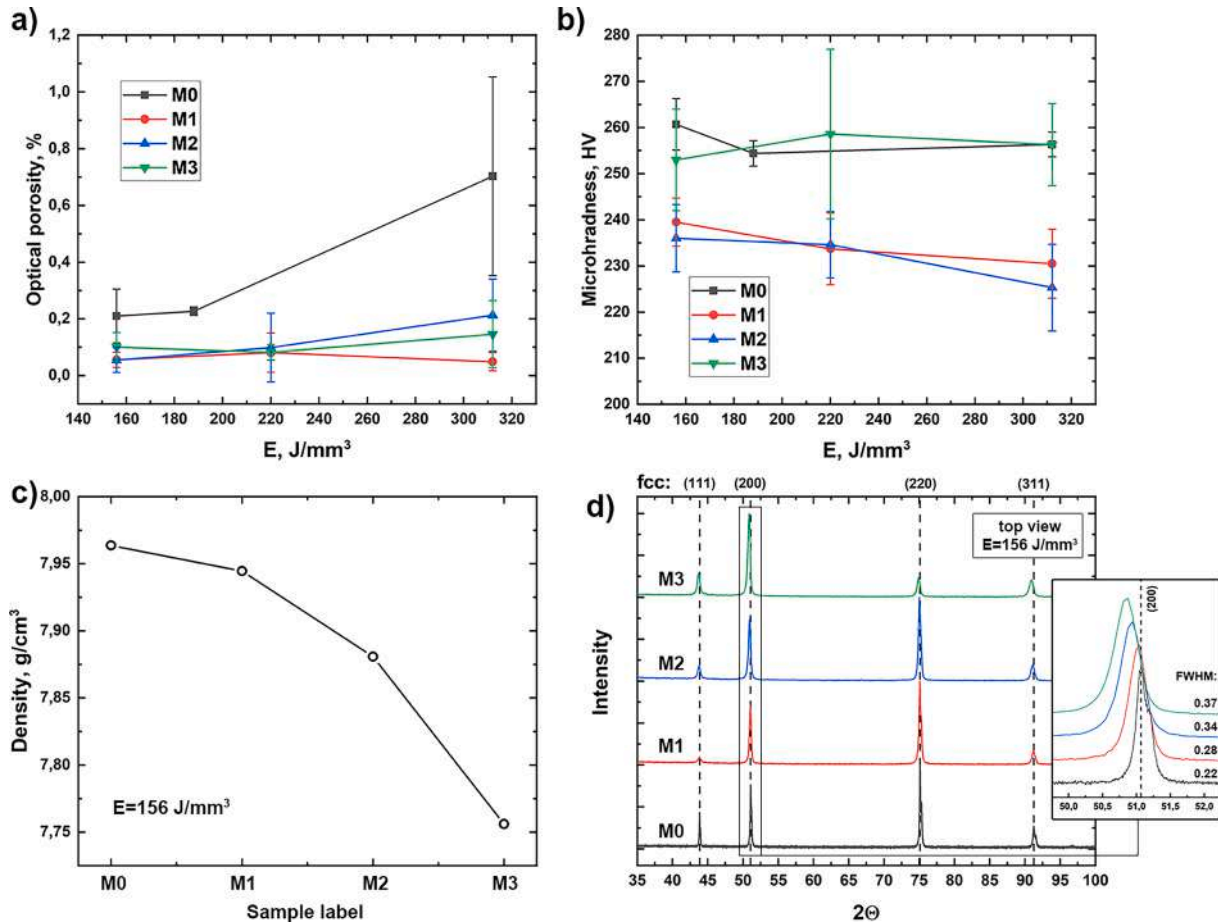|	Al content in the powder blend wt.%	Al wt.%	Al at.%	Cr at.%	Fe at.%	Co at.%	Ni at.%
M0 (x=0)	–	–	–	25.33	25.50	24.36	24.81
M1 (x=0.01)	0.3	0.11	0.22	25.56	25.35	24.91	23.96
M2 (x=0.05)	1.2	0.52	1.09	25.40	25.36	24.56	23.59
M3 (x=0.1)	3.0	1.67	1.98	24.89	24.99	24.33	23.82

Fig. 1. (a) The average porosity and (b) microhardness for the M0-M3 samples; (c) the densities and (d) XRD profiles for the as-built samples.

cooling in water.

The microhardness and porosity were measured in the same way and using the same equipment as in Ref. [7]. The scanning electron microscope, X-ray diffractometer and sample preparation procedures were also the same as in the study [7].

3. Results and discussion

Table 1 summarizes the energy dispersive X-ray (EDX) results for the as-built CrFeCoNi alloy and three mixtures and concentration of Al in the powder blends. Approximately a half of the initial Al content was detected in the printed samples. Correspondingly, Fig. 1a and b present the results of average microhardness and porosity for HEA with different Al additions depending on the volumetric energy (E) calculated according to the equation in Ref. [8]. The average porosity for all CrFeCoNiAl$_x$ alloys remains within 0.25%, which is lower compared with a CrFeCoNi alloy, Fig. 1a. It can be an attribute of the Al presence which changes physical characteristics of the liquid alloy and affects the pore formation. Intangible increase of porosity for higher volumetric energy is observed with increase of Al content. The microhardness drops for M1 and M2 samples and reaches ~235 HV. Only the M3 samples represent

the same microhardness level as for M0 (~255 HV). Fig. 1c demonstrates the decrease of material density measured by Archimedes' method with Al addition which indicates the Al incorporation in the CrFeCoNi alloy. Fig. 1d, containing the X-ray diffraction (XRD) profiles, demonstrates no new phases except the main fcc structure for all considered conditions.

Fig. 2 represents the (a–f) backscattered electron (BSE) images and (g–h) EDX maps of the as-built CrFeCoNiAl$_x$ alloy. A comparison of AM CrFeCoNi alloy [7] and the M1 sample demonstrates no difference in microstructure for the top and front views, Fig. 2a and b. However, in the front view of the M1 sample the heterogeneity of the Al distribution can be seen, Fig. 2g. With the increase of Al content, the new structural features having the homogeneous element distribution appear (dotted regions in Fig. 2d and f). At the top view, the regions with fine equiaxed grains typical for bcc/B2 structure with a high Al content are seen, Fig. 2c and e [1,2]. Presumably, such an inhomogeneous distribution of Al in the material does not provide the solid solution strengthening effect while increasing the microstrains, which can be seen by the broader XRD peaks depicted in Fig. 1d with full widths at half maximum (FWHM). Tensile microstrain may provide slightly lower microhardness for M1 and M2 samples where the Al concentration is too low to form
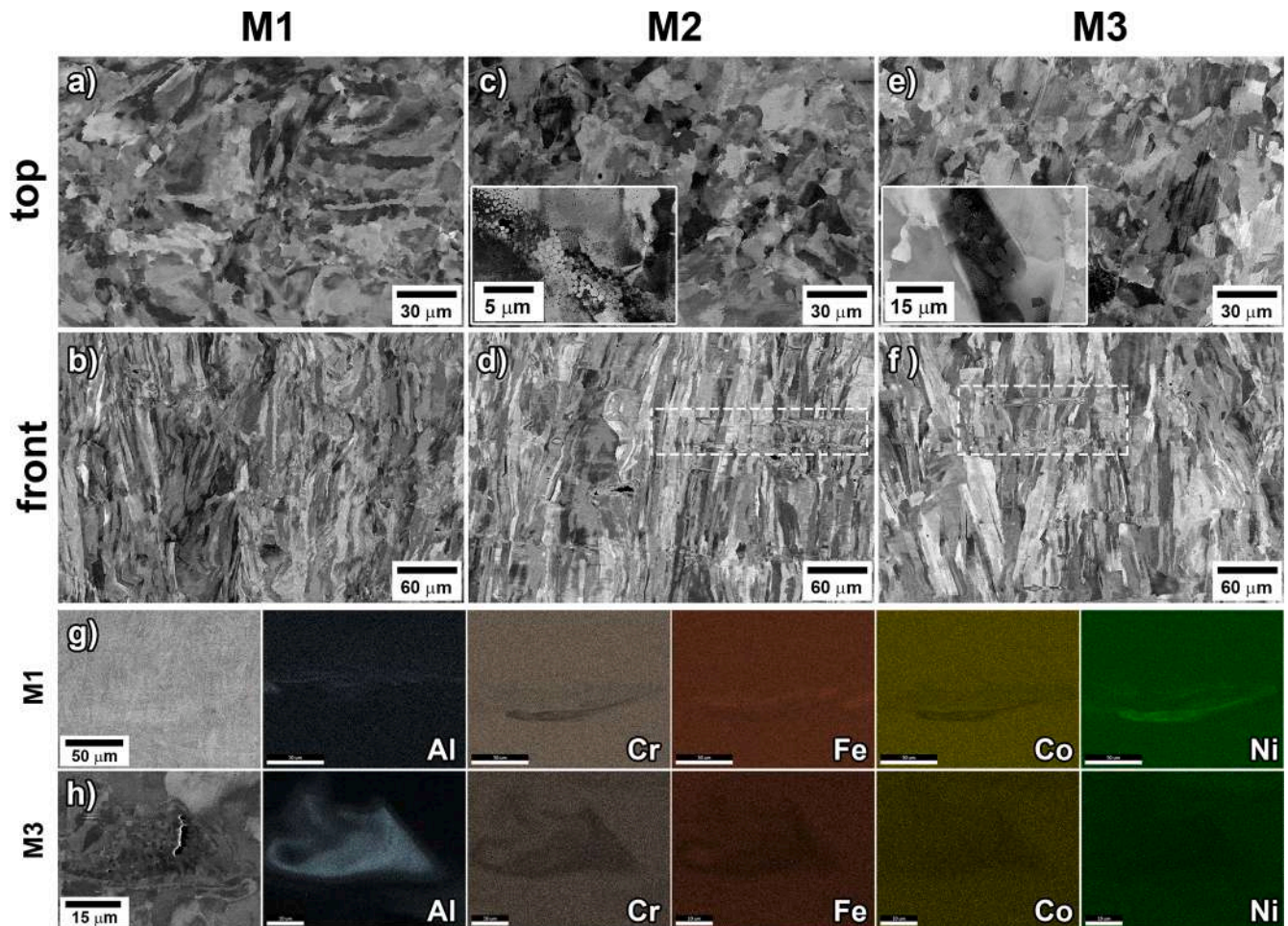
Fig. 2. BSE images of as-built (a, b) M1, (c, d) M2, and (e, f) M3 samples; EDX maps of as-built (g) M1 and (h) M3 samples.

enough fraction of hard B2/bcc phase, which has a higher contribution to microhardness in case of M3 sample. Nevertheless, additional investigations are required. XRD analysis did not indicate presence of any phases in the material except fcc, which means that volume fraction of other phases is below the method sensitivity (~5%).

Fig. 3 illustrates the effect of 1200 °C annealing for 16 h on microstructure and properties of the AM CrFeCoNi and CrFeCoNiAl$_x$ alloys. In Fig. 3a, the annealing twins are clearly seen for CrFeCoNi alloy, which indicates the low stacking fault energy (SFE) of the material (<~32 mJ/m^2) [9]. The annealed M1 sample represents the bimodal structure where the fine structure and coarse grains with annealing twins can be seen, Fig. 3b. The volume fraction of the annealing twins decreases with an increase of Al content, Fig. 3c and d, which indicates the SFE raise, although, for CrFeCoNiAl$_{0.1}$ alloy, SFE less than 34 mJ/m^2 is reported [9]. EDX analysis reveals the same element composition for fine grain areas and for large grains containing annealing twins in the M1 sample. The M2 and M3 samples also have the homogeneous element distribution except for the formed Al- and N-rich precipitates, Fig. 3c. Note, such precipitates can be a result of the high N content (~0.1 wt%) in the initial CrFeCoNi powder.

The microhardness drops from ~260 to ~182 HV for the AM CrFeCoNi alloy after the annealing, Fig. 1b and 3e. For the CrFeCoNiAl$_x$ alloys, the loss of microhardness is less dramatic by ~20–35 HV, which is associated with the finer microstructure. XRD analysis presents the fcc structure for all conditions, Fig. 3f. The lattice parameter (LP) demonstrates the tendency of its increase with an increase of Al content, Fig. 3g, which confirms the incorporation of Al atoms in solid solution. The annealing increases LP for M0 and M1 samples indicating residual

stress removal, while it reduces LP for M2 and M3 samples, which is associated with Al-rich precipitates.

4. Conclusions

- The in-situ production of L-PBF CrFeCoNiAl$_x$ alloy by mixing of two powders did not provide the homogeneous element distribution in the as-built samples, and Al-rich areas were still observed. Annealing led to homogenization of the material.
- Approximately half of the nominal Al content in the powder blend volatilized during manufacturing. The adding of 3 wt% Al powder in the powder mixture resulted in the fully fcc structure, according to XRD analysis, and 1.67 wt% actual content of Al.
- The addition of Al decreased the porosity at the considered volumetric energy range, while the microhardness dropped for ~20 HV or stayed the same. After 1200 °C homogenizing annealing, the microhardness stayed at a higher level for CrFeCoNiAl$_x$ alloy, losing only ~20–35 HV.
- The Al presence in CrFeCoNi alloy increased the SFE, which is indicated by the low amount of annealing twins in CrFeCoNiAl$_x$ alloy after the annealing.

CRediT authorship contribution statement

Yulia Kuzminova: Conceptualization, Methodology, Writing - original draft, Investigation. **Anastasia Shibalova:** Investigation. **Stanislav Evlashin:** Resources, Writing - review & editing. **Igor Shishkovsky:** Resources, Writing - review & editing, Supervision. **Pavel**
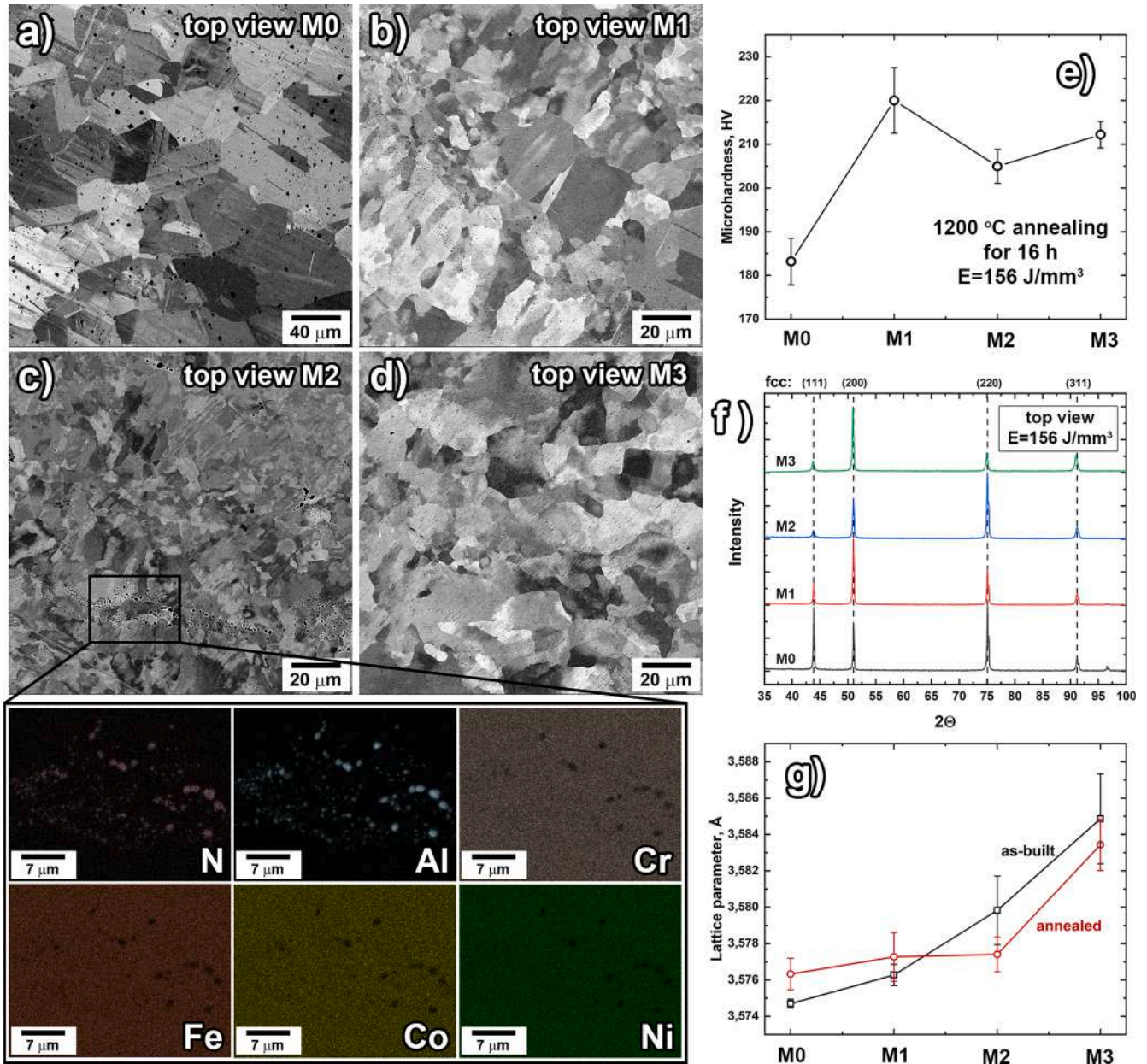
Fig. 3. BSE images of (a–d) M0-M3 samples annealed at 1200 °C. EDX maps represent the picked area in Fig. 3c; (e) the microhardness and (f) the XRD profiles for the annealed M0-M3 samples; (g) LP calculated from XRD profiles.

Krakhmalev: Writing - review & editing, Supervision.

Declaration of Competing Interest

The authors declare that they have no known competing financial interests or personal relationships that could have appeared to influence the work reported in this paper.

Acknowledgements

References

[1] J. Joseph, T. Jarvis, X. Wu, N. Stanford, P. Hodgson, D.M. Fabijanic, Comparative study of the microstructures and mechanical properties of direct laser fabricated and arc-melted AlxCoCrFeNi high entropy alloys, Mater. Sci. Eng. A 633 (2015) 184–193.

[2] M.u. Li, J. Gazquez, A. Borisevich, R. Mishra, K.M. Flores, Evaluation of microstructure and mechanical property variations in AlxCoCrFeNi high entropy alloys produced by a high-throughput laser deposition method, Intermetallics 95 (2018) 110–118.

[3] P. Chen, S. Li, Y. Zhou, M. Yan, M.M. Attallah, Fabricating CoCrFeMnNi high entropy alloy via selective laser melting in-situ alloying, J. Mater. Sci. Technol. 43 (2020) 40–43.

[4] K. Sun, W. Peng, L. Yang, L. Fang, Effect of SLM processing parameters on microstructures and mechanical properties of Al0.5CoCrFeNi high entropy alloys, Metals (Basel) 10 (2) (2020) 292, https://doi.org/10.3390/met10020292.

[5] G.A. Salishchev, M.A. Tikhonovsky, D.G. Shaysultanov, N.D. Stepanov, A. V. Kuznetsov, I.V. Kolodiy, A.S. Tortika, O.N. Senkov, Effect of Mn and V on structure and mechanical properties of high-entropy alloys based on CoCrFeNi system, J. Alloys Compd. 591 (2014) 11–21.

[6] K. Liu, B. Gwalani, M. Komarasamy, S. Shukla, T. Wang, R.S. Mishra, Effect of nano-sized precipitates on the fatigue property of a lamellar structured high entropy alloy, Mater. Sci. Eng. A 760 (2019) 225–230.

[7] Y. Kuzminova, D. Firsov, S. Dagesyan, S. Konev, S. Sergeev, A. Zhilyaev, M. Kawasaki, I. Akhatov, S. Evlashin, Fatigue behavior of additive manufactured CrFeCoNi medium-entropy alloy, J. Alloys Compd. 863 (2021), 158609.

[8] J.A. Cherry, H.M. Davies, S. Mehmood, N.P. Lavery, S.G.R. Brown, J. Sienz, Investigation into the effect of process parameters on microstructural and physical properties of 316L stainless steel parts by selective laser melting, Int. J. Adv. Manuf. Technol. 76 (5-8) (2015) 869–879.

[9] E. George, W. Curtin, C. Tasan, High entropy alloys: a focused review of mechanical properties and deformation mechanisms, Acta Mater. 188 (2020) 435–474.

Chapter 8

The oxidation behavior of the CrFeCoNiAl$_x$ (x = 0, 1.0, and 5.0 wt%) high-entropy alloy synthesized with Al elemental powder via powder bed fusion technique at high temperatures

The active discussion of applying the CrFeCoNi-based systems for high-temperature conditions requires the investigation of the oxidation behavior of the material at such temperatures. In this chapter, the impact of the aluminum concentrations (x=0, 1.0, and 5.0) on the oxidation resistance of the CrFeCoNiAlx system at 800°C and 1000°C is presented.

The compositions were prepared the same way as in the previous chapter, the aluminum and CrFeCoNi powders were blended in required portions and used in the PBF process to print the samples. Further, the three types of samples were annealed at 800°C and 1000°C for 500 hours in the air. It was found that the Al presence in the material prevents the scale delamination of the material by forming Al$_2$O$_3$ pre-

cipitates under the top oxidized layer. Additionally, the formation of the M_2O_3 and M_3O_4 oxides on the oxidized sample surface were discussed, according to the EDX analysis presented below in the Chapter and XRD analysis (Fig.8-1, not included in the publication). Interesting that the diffusion of oxygen primarily occurred homogeneously via the columnar grain boundaries typical of AM materials while the previous study (presented in Chapter 7) demonstrated the inhomogeneous element distribution in the material even with small aluminum content. Additionally, the precipitates enriched with aluminum and nitrogen were detected under the Al_2O_3 layer. Their formation was associated with a high content of nitrogen in the initial powder. The layers enriched with the formed precipitates demonstrate a higher microhardness of 250 HV compared with the inner material with a microhardness of 210 HV.
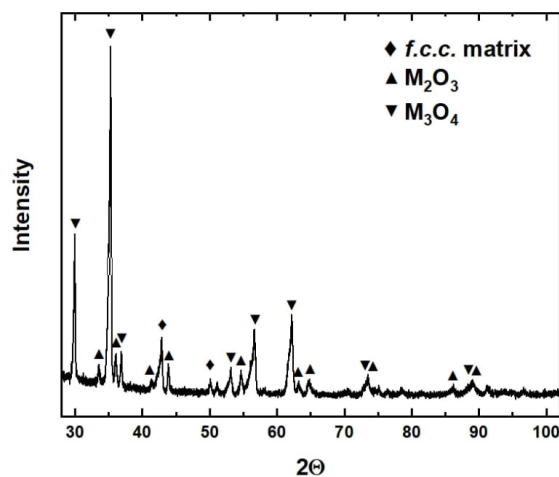
Figure 8-1: XRD pattern obtained with Cu-tube from the oxidized surface of the A5 sample after 500 hours annealing at 1000°C in air.

Contribution: I contributed to the development of the structural and phase analyses of the material, the sample preparation process, the formal analysis, the original draft, the final writing, and editing of the manuscript. I would like to thank all the authors for their valuable contributions to the development of this paper.

The oxidation behavior of the CrFeCoNiAl$_x$ (x = 0, 1.0, and 5.0 wt%) high-entropy alloy synthesized with Al elemental powder via powder bed fusion technique at high temperatures

Yulia O. Kuzminova [a], Denis G. Firsov [a], Anastasia A. Shibalova [c], Stanislav A. Evlashin [a,b], Igor V. Shishkovsky [a], Stanislav S. Dautov [a,*]

[a] Center for Materials Technologies, Skolkovo Institute of Science and Technology, Moscow 121205, Russia
[b] World-Class Research Center, State Marine Technical University, Saint Petersburg 190121, Russia
[c] Institute of Nanotechnology of Microelectronics of Russian Academy of Science, Moscow 119991, Russia

ABSTRACT

High-entropy alloys (HEAs) are promoted as promising materials for various applications, including those dealing with high-temperatures. It requires understanding of the oxidation at different temperatures, especially for such a technological process as additive manufacturing (AM), which is able to produce unique structure. The present work evaluates the oxidation resistance of the CrFeCoNiAl HEAs produced by AM of the blends of CrFeCoNi and Al powders at temperatures of 800 and 1000 °C. Al forms the Al$_2$O$_3$ under the top Cr$_2$O$_3$ layer and prevents the delamination of the oxide scale at considered temperatures. Oxygen diffusion mainly occurs homogeneously through the columnar grain boundaries typical for AM materials. AlN precipitates under the Al$_2$O$_3$ formations were observed for the sample with the highest aluminium concentration due to dissolution of nitrogen in the as-built material.

1. Introduction

Mixing elements in equiatomic or near-equiatomic portions is a new approach to alloy design. High-entropy alloy (HEA) is actively promoted as a class of materials for high-temperature applications (Stepanov et al., 2018). Modern additive manufacturing (AM) is a printing technique which allows producing HEA using metal powder blends (Zhao et al., 2021); Kuzminova et al., 2021).

The CrFeCoNiAl alloy provides a variety of mechanical and physical properties depending on the Al portion, which can change the lattice structure from *f.c.c.* to *b.c.c.* (Li et al., 2018). The AM CrFeCoNiAl alloy possesses comparably high mechanical characteristics at elevated temperatures, the ultimate tensile strength of 679 MPa at 700 °C (Asabre et al., 2019). At such temperatures, it is important to consider the oxidation resistance of the material.

In the present work, the influence of Al content in the CrFeCoNiAl$_x$ on the oxidation resistance properties at 800 and 1000 °C for up to 500 h is studied. HEA is produced by powder bed fusion technique. The weight gains of the AM CrFeCoNiAl$_x$ (x = 0, 1.0, and 5.0 wt%) samples were analyzed. The microstructure and microhardness of the samples after

heat treatments (HT) are discussed.

2. Methods and materials

The metal 3D printer Trumpf TruPrint 1000 was used. The CrFeCoNi (JSC Polema, Russia) powder and Al powder (UC Rusal, Russia) described in (Kuzminova et al., 2021) were preliminarily mixed using a tumbling drum at portions of 99.0/1.0 and 95.5/5.0 wt%, respectively. The earlier analysis of the initial CrFeCoNi powder demonstrated the presence of nitrogen (up to 0.1 wt%) (Kuzminova et al., 2022). The cylindrical rods (ø16 ×50 mm^2) were printed using three types of powder blends (0, 1.0, and 5.0 wt% of Al powder marked as A0, A1, and A5, correspondingly) and using the printing parameters from our previous work (Kuzminova, 2021). Each cylindrical rod was cut into samples with dimensions of ø15 × 4 mm^2. The samples were heat-treated at 800 and 1000 °C in air for up to 500 h. During the heating, samples were removed from the furnace with further air cooling for the weight measurements at room temperature. Three samples were used for each condition. After the HT, samples were cut for microstructural analysis using the scanning electron microscope (SEM) QuattroS (Thermo Fisher

Table 1

The EDX results (wt%) of the as-built samples from the $600 \times 500 \ \mu m^2$ area and the oxidation rates for two temperatures and oxidation rate constant data.

Sample	Cr	Fe	Co	Ni	Al	Cu	Mn	Kp, $g^2cm^{-4}s^{-1}$	
								800 °C	1000 °C
A0	20.36	21.64	23.91	23.49	0	2.41	0.99	-	-
A1	19.98	21.51	23.68	23.30	0.85	2.53	1.06	1.51E-13	6.80E-12*
A5	19.47	20.93	23.35	22.87	2.99	2.25	0.93	1.46E-13	2.65E-11

* Kp calculated without taking into account the last two points due to the weight loss at these durations.
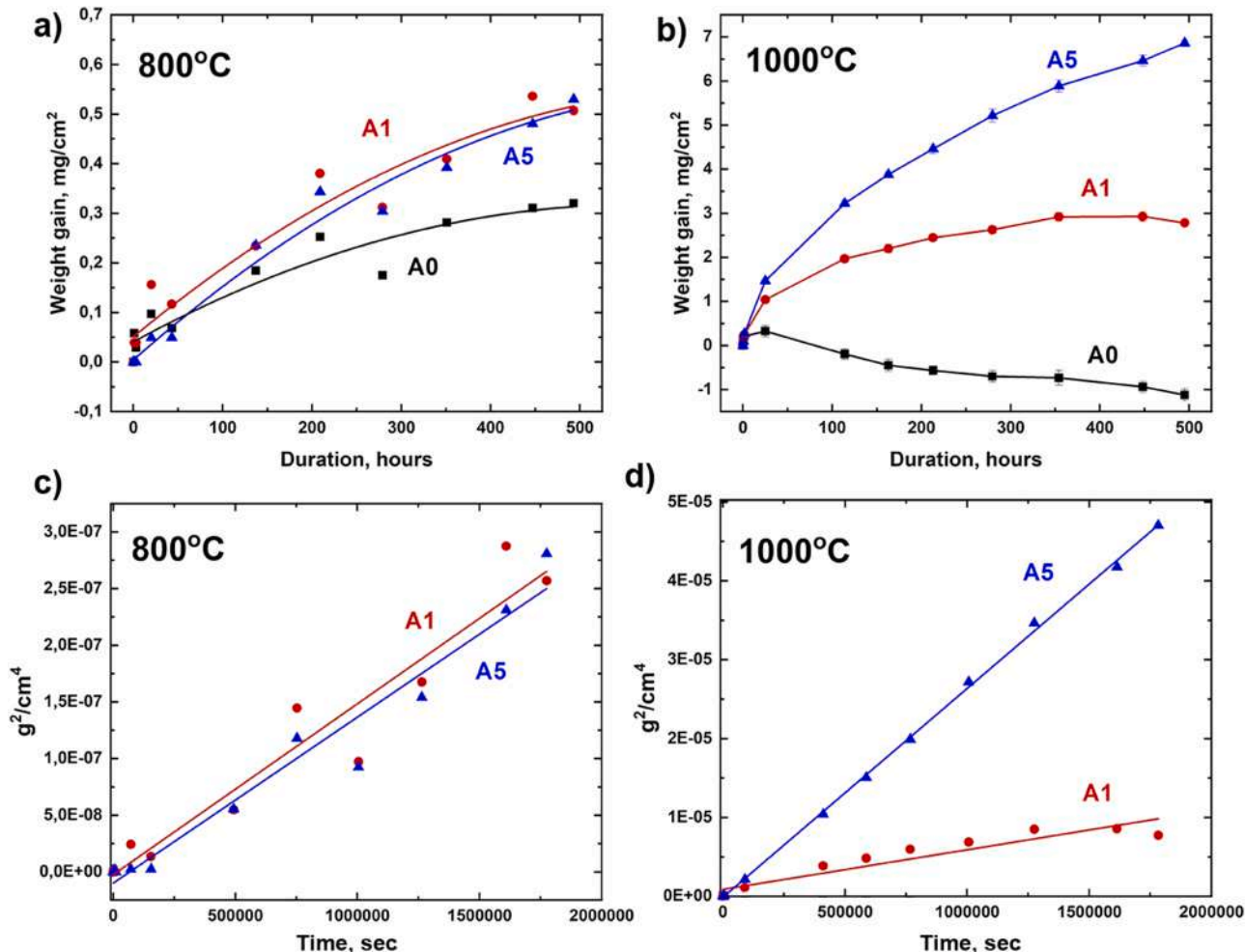

Fig. 1. (a, b) The weight changes and (c, d) the correspondence kinetic curves for the printed CrFeCoNiAl$_x$ samples during the oxidation.

Scientific) equipped with an energy dispersive X-ray (EDX) detector. For the SEM analysis, samples were grinded and polished with the final 40 nm silica suspension. The microhardness was measured using the Micro Vickers hardness testing machine ITV-1-AM (Metrotest) with a load of 300 gf.

3. Results and discussion

The EDX results of the as-built samples are summarized in Table 1 - they reveal the homogeneous distribution of all elements. Mn and Cu were detected in all samples due to their presence in the initial CrFeCoNi powder as impurities. Similarly to previous work (Kuzminova, 2021), the Al content in printed samples is less than in the powder blends, which is associated with the loss of Al on the mix cylinder walls during the mixing.

Fig. 1 demonstrates the results of weight gains and oxidation kinetics of the samples at 800 and 1000 °C. Samples with Al content demonstrate more intense weight increase during heating. It is approximately the same for the samples with different Al content (A1 and A5) at a temperature of 800 °C (Fig. 1a), while the A5 samples increase in weight more rapidly at 1000 °C (Fig. 1b). At the same time, the difference between A1 and A5 samples is barely visible at 800 °C due to slower oxygen diffusion (Fig. 1a). Spalled-off scales have not been collected during the measurements and are not included in weight gain graphs. Fig. 1c and d present the kinetic curves for two temperatures where the linear slopes regard to the parabolic oxidation rate constants (K_p) according to the function (Gorr et al., 2017):

$$\left(\frac{\Delta m}{A}\right)^2 = K_p \times t,$$

where the Δm is a weight change, A is a surface sample area, and t is oxidation time. The kinetic curve for the A0 sample was not included in Fig. 1c and d due to its spallation making the kinetic data irrelevant. The calculated oxidation rate constants are presented in Table 1 for each
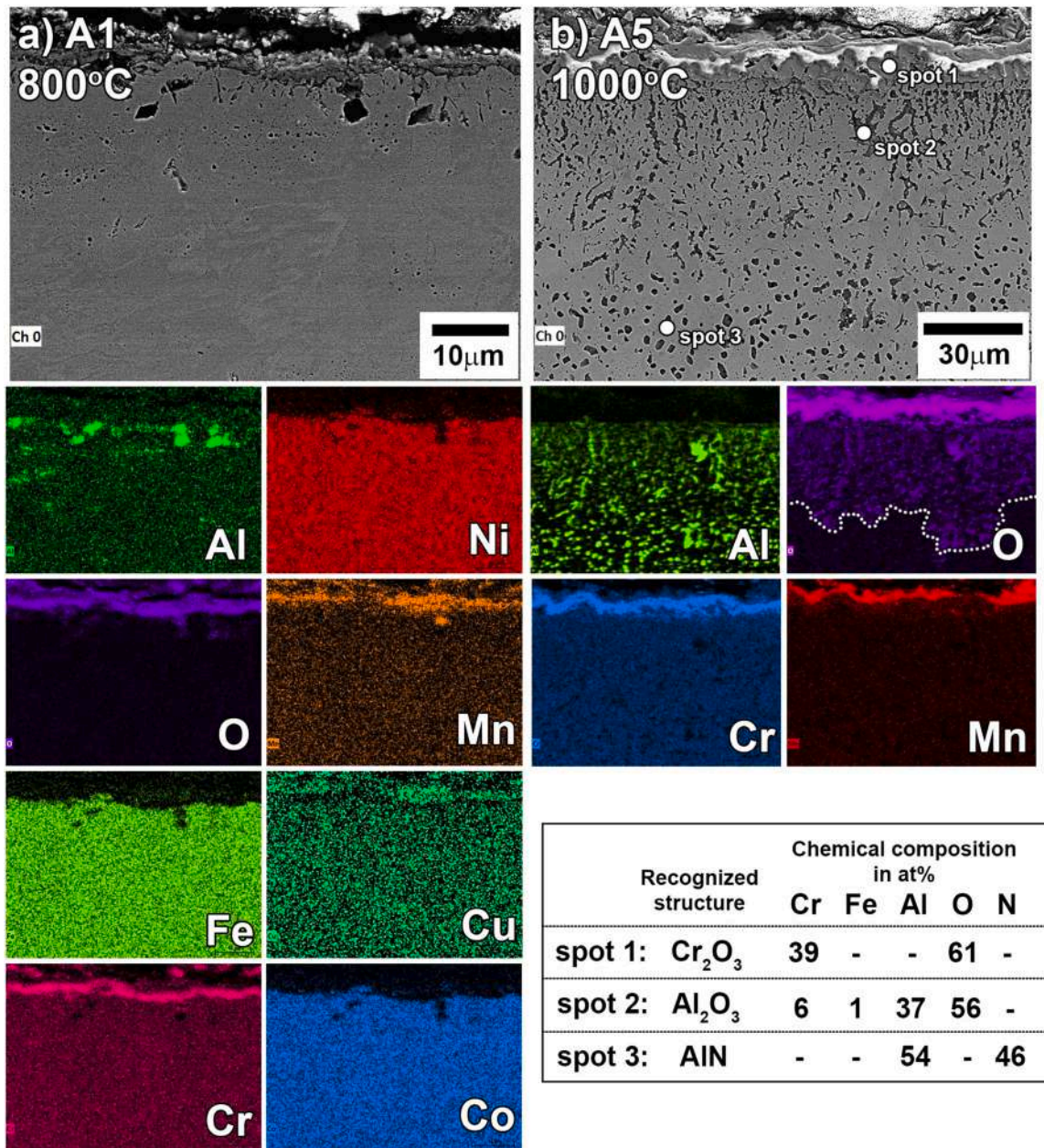
Fig. 2. The SEM images with EDX results: (a) the A1 and (b) A5 samples after HT at 800 and 1000 ℃, respectively.

temperature. This data corresponds to the constants for typical chromia formers (in the range of 10^{-12}- 10^{-11} $g^2cm^{-4}s^{-1}$ for 1000 °C and $5{\cdot}10^{-13}$ - $5{\cdot}10^{-12}$ $g^2cm^{-4}s^{-1}$) for 800 °C, according to (Kofstad, 1988). The calculated constants are several orders of magnitude lower than for alumina formers - even for 800 °C the rate constants of α-alumina and θ-alumina are about 10^{-8} and 10^{-6} $g^2cm^{-4}s^{-1}$ respectively (Kim et al., 2022). However, it is necessary to mention that the delamination of the oxide scale on the A0 sample occurred periodically during the isothermal test at both temperatures. It also explains the comparably slow weight increase at 800 °C and loss at 1000 ℃. Due to that, the oxidation rate constants for A0 samples have not been presented. According to the weight gain curve tendency at 1000 ℃, the oxide delamination for the A1 sample occurred at the last stages of heat treatment (450 and 500 h).

According to the EDX analysis, all samples heat-treated at 800 ℃ for 500 h have a Cr-, Mn- and O-rich layer, which is about 3 μm thick for samples A1 (Fig. 2a) and A5. Similarly to the study of the AlCoCrCuFeNi alloy (Cho et al., 2022), the Al-containing samples additionally demonstrate a thin Al- and O-rich layer under the top Cr-rich layer, which was recognized as the Al_2O_3 oxide. The analysis of the oxidation behavior of the FeCrAl alloys also reveals the formation of the Al-rich oxide layer at the temperatures of 700–900 ℃ (Kim et al., 2022). At higher temperatures (up to 1500 ℃), the thick outermost Fe-, Cr-, and Al-rich oxide layers were formed along with the internal alumina layer at the oxide\metal interface.

The formation of the Mn_2O_3/Mn_3O_4 and Cr_2O_3 oxides on the surface of the CrMnFeCoNi alloy after the oxidation tests was observed in (Laplanche et al., 2016). In the present study, the preliminary powder contains ~1 wt% of Mn, which can be enough for formation of the same oxides on the surface due to the high diffusion rate of Mn (Laplanche et al., 2016). In accordance with the work (Wei and Stottthe, 1988), the oxide scale of the A0 sample could consist of spinel phase $NiCr_2O_4$, NiO, and Cr_2O_3 oxides. Thermal expansion coefficient mismatch and low durability of these oxides lead to thermal stresses in the oxide scale, so, the heating and cooling stages of the isothermal tests provoke crack generation and delamination as a result. Fig. 2b represents the structural
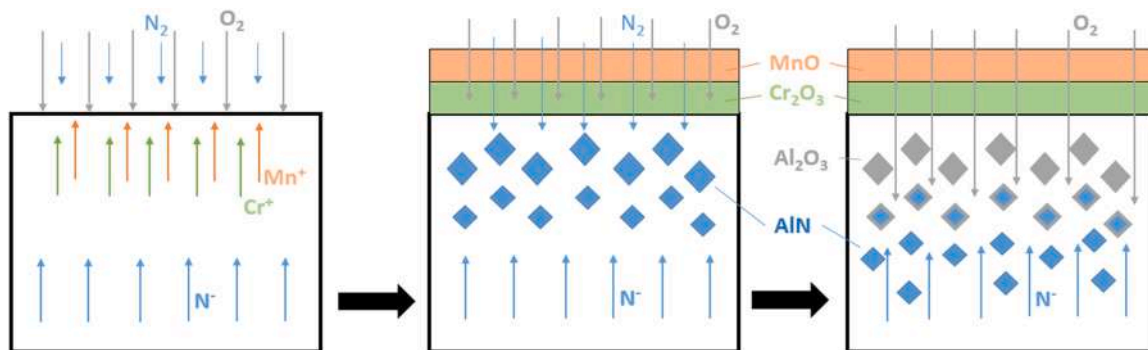
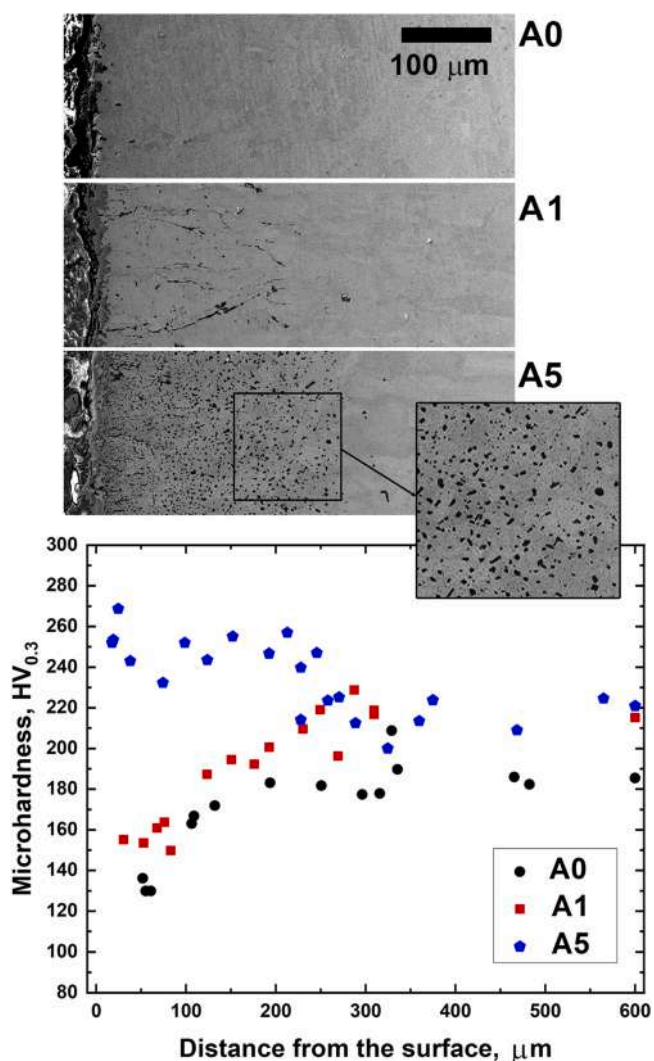**Fig. 3.** Oxidation mechanism of CrFeCoNiAl$_x$ samples.

Fig. 4. SEM images and microhardness response for samples with a different Al content after HT at 1000 ℃.

and chemical features of sample A5 after the HT at 1000 ℃. The point EDX analysis of the sample demonstrates the typical Cr$_2$O$_3$ chemical composition for the oxide layer (Fig. 2b, spot 1). However, the Mn presence was revealed in the top zone of the oxide layer according to the EDX mapping results. The thickness of the top layer enriched with magnesium and chromium oxides is approximately the same for the Al-contained samples. The depth of the layer achieves 30 μm after HT at 1000 ℃. The sublayer marked in oxygen figure is enriched with the

precipitates of the chemical composition typical for Al$_2$O$_3$ (Fig. 2b, spot 2). According to the EDX data, the aluminum nitrides (recognized as AlN) formed in the subsurface zone during HT, especially at 1000 ℃ (Fig. 2b, spot 3). The presence of aluminum nitrides could be explained by their thermodynamic stability in comparison to nitrides of other HEA elements (chromium, nickel, etc.). Presumably, because of the oxygen diffusion into the subsurface zone mostly through the grain boundaries (Wei and Stottthe, 1988), the oxidation of previously formed nitrides occurs. This explains the double aluminum-rich layer - the top one contains the aluminum oxides (about 0–60 μm in the depth of the sample A5) and the bottom one - aluminum nitrides (60–300 μm). At the same time, such high concentrations of homogeneously distributed nitrides were not found in the depth below 300 μm of the 1000 ℃ sample. This fact could be explained by the outward diffusion of nitrogen, which is initially dissolved in the HEA material at high temperatures and occurs mostly through the grain boundaries. Diffusion of nitrogen through the oxide scale could be involved in the formation of nitrides in the bulk alloy because of chromia permeability to nitrogen (Sand et al., 2022). During the nitrogen diffusion, its concentration increased in the grain boundaries of the subsurface zone and became sufficient to form aluminum nitrides. The mechanism of transformation of aluminum nitrides to oxides is depicted in Fig. 3. However, this effect requires additional experiments to clarify the mechanism.

According to SEM data, the oxygen penetration at 1000 ℃ is observed along the columnar grain boundaries for samples A1 and A5, up to ~250 and ~300 μm, respectively (Fig. 4). Such an effect is not observed for sample A0. It should be noted that the previous work demonstrated the formation of M$_2$N precipitates on the grain boundaries in the heat-treated CrFeCoNi alloy containing up to 0.1 wt% of nitrogen (Kuzminova et al., 2022). However, the microhardness decreases from the depths of ~150 and ~250 μm to the sample surface for the A0 and A1 samples, respectively. This effect is associated with the cracked and porous oxide layer and voids in the subsurface zone because of the diffusion processes. The insufficient amount of Al$_2$O$_3$ formed in the A1 is the reason for decreased microhardness at the depths up to 250 μm mentioned above. For the A5 sample, the particles enriched with Al and O or N are seen at the nearest 300 μm to the surface (depicted in Fig. 4), which are associated with an increased microhardness. The thickness of the layer with precipitates is the same along the area surface of the sample no matter the material structure anisotropy.

The Al presence in the CrFeCoNiAl$_x$ leads to formation of the Al$_2$O$_3$ sublayer improving the oxidation resistance by preventing the delamination of the Mn$_2$O$_3$/Cr$_2$O$_3$ top layer. In the case of A0 samples, the oxide scale delamination is observed, while even the small addition of Al (sample A1) helps to avoid the degradation of the surface and forms the Al$_2$O$_3$ predominantly along the columnar grain boundaries. However, high content of Al accelerates the kinetics of the oxidation process, which is clearly observed at 1000 ℃ (Fig. 1d). Additionally, it allows the formation of the Al$_2$O$_3$ and AlN precipitates due to the presence of a small nitrogen amount of ~0.1 wt% as the impurity. The presence of

these precipitates provides higher microhardness of the A5 sample near the surface.

4. Conclusions

- The diffusion of oxygen mainly occurs through the columnar grain boundaries;
- In the aluminium containing samples, the Al2O3 formation under the Mn-/Cr-rich oxide layer along the grain boundaries is observed. The formed alumina prevents the growing and delaminating of the upper oxide layer;
- The thickness of the Mn-/Cr-rich oxide layer depends on the HT temperature rather than on the Al concentration and reaches ∼3 and ∼20 μm for 800 and 1000 °C after 500 h;
- The low concentration of nitrogen in the initial powder is conveyed to the as-built materials. The aluminium addition provokes the formation of the nitrides under the near-surface layer with Al2O3 detected only in the A5 sample after 1000 °C HT.

Declaration of Competing Interest

The authors declare that they have no known competing financial interests or personal relationships that could have appeared to influence the work reported in this paper.

Data Availability

Data will be made available on request.

Acknowledgments

References

Asabre, A., et al., 2019. Effect of Al, Ti and C additions on Widmanstätten microstructure and mechanical properties of cast Al0.6CoCrFeNi compositionally complex alloys. Mater. Des. 184, 108201.

Cho, F.-Y., et al., 2022. High temperature oxidation behavior of high entropy alloy Al4Co3Cr25Cu10Fe25Ni33 in oxygen-containing atmospheres. Mater. Chem. Phys. 278, 125678.

Gorr, B., Müller, F., Azim, M., et al., 2017. High-temperature oxidation behavior of refractory high-entropy alloys: effect of alloy composition. Oxid. Met. 88, 339–349.

Kim, C., Tang, C., Grosse, M., Maeng, Y., Jang, C., Steinbrueck, M., 2022. Oxidation mechanism and kinetics of nuclear-grade FeCrAl alloys in the temperature range of 500–1500 °C in steam. J. Nucl. Mater. 564, 153696.

Kofstad, P., 1988. High Temperature Corrosion. Elsevier Applied Science Publishers Ltd., London, England.

Kuzminova, Y., et al., 2021. Structural effect of low Al content in the in-situ additive manufactured CrFeCoNiAlx high-entropy alloy. Mater. Lett. 303.

Kuzminova, Y.O., Kudryavtsev, E.A., Han, J.K., Kawasaki, M., Evlashin, S.A., 2022. Phase and structural changes during heat treatment of additive manufactured CrFeCoNi high-entropy alloy. J. Alloy. Compd. 889.

Laplanche, G., et al., 2016. Oxidation Behavior of the CrMnFeCoNi high-entropy alloy. Oxid. Met. 85, 629–645.

Li, M., et al., 2018. Evaluation of microstructure and mechanical property variations in Al x CoCrFeNi high entropy alloys produced by a high-throughput laser deposition method. Intermetallics 95, 110–118.

Sand, T., Bigdeli, S., Sattari, M., et al., 2022. Efficacy of an external chromia layer in reducing nitridation of high temperature alloys. Corros. Sci. 197.

Stepanov, N.D., et al., 2018. Structure and high temperature mechanical properties of novel non-equiatomic Fe-(Co, Mn)-Cr-Ni-Al-(Ti) high entropy alloys. Intermetallics 102, 140–151.

Wei, F.I., Stottthe, F.H., 1988. Influence of aluminium on the oxidation of a Cr_2O_3-forming nickel-chromium alloy. React. Solids 6.

Zhao, W., et al., 2021. Significance of grain refinement on micro-mechanical properties and structures of additively-manufactured CoCrFeNi high-entropy alloy. Mater. Sci. Eng. A 807.

Chapter 9

Structural and mechanical properties of the additive manufactured CrFeCoNi(Al,Ti) high-entropy alloys produced using powder blends

Previous chapters have demonstrated that the addition of even a small amount of aluminum to the CrFeCoNi system alters its properties. Therefore, it is crucial to examine the impact of varying aluminum content on the mechanical properties of the CrFeCoNiAl alloy, as well as consider the influence of titanium on the properties of the CrFeCoNiAlTi alloy.

In this chapter, the PBF technique was used to print the CrFeCoNiAl and CrFeCoNiAlTi alloys using powder blends, and they were compared with the PBF CrFeCoNi alloy. Consistent with earlier findings, printing with powder blends did not result in a uniform distribution of elements, but high-temperature treatment proved effective in achieving a homogeneous chemical composition. The presence of aluminum in the CrFeCoNiAl system (up to 4 wt%) induced the formation of a secondary *b.c.c.*/B2 phase from the *f.c.c.* matrix. Annealing at 800°C stabilized the dual-phase composition in the CrFeCoNiAl alloy without the formation of a σ phase. On the other hand, the addition of titanium to the CrFeCoNiAl system led to the simultaneous crystallization of *b.c.c.* and *f.c.c.* phases from the liquid, alter-

ing the microstructural composition of the material. Subsequent annealing at 800°C resulted in the formation of a σ phase in the material. The mechanical properties of the alloys are determined by their phase compositions. It was observed that the strength characteristics increased with an increase in the volume of the *b.c.c.* phase, while ductility decreased. The formation of a σ phase in the CrFeCoNiAlTi alloy significantly reduced its ductility.

Contribution: I contributed to the development of the structural and phase analyses of the material, the sample preparation process, the mechanical testing, the original draft, the final writing, and editing of the manuscript. I would like to thank all the authors for their valuable contributions to the development of this paper.

Structural and mechanical properties of the additive manufactured CrFeCoNi(Al,Ti) high-entropy alloys produced using powder blends

Yulia O. Kuzminova[1]*, Denis G. Firsov[1], Anastasia A. Shibalova[2], Egor A. Kudryavtsev[3], Pavel Krakhmalev[4], Olga G. Klimova-Korsmik[5], Igor V. Shishkovsky[1], Stanislav A. Evlashin[1]

[1] Center for Materials Technologies, Skolkovo Institute of Science and Technology, Moscow 121205, Russia
[2] Institute of Nanotechnology of Microelectronics of Russian Academy of Science, Moscow 119991, Russia
[3] The Joint Research Center of Belgorod State National Research University «Technology and Materials», Belgorod 308015, Russia
[4] Karlstad University, SE-651 88 Karlstad, Sweden
[5] World-class research center, State Marine Technical University, Saint Petersburg 190121, Russia

*Corresponding author: yulia.kuzminova@skoltech.ru
Bolshoy Boulevard 30, bld. 1 Moscow, Russia 121205

ABSTRACT

High-entropy Alloys (HEAs) are considered prospective materials demonstrating the new approach of alloy design creating new compositions for harsh conditions. However, searching for alloy chemical composition providing the best material properties is a costly process. Additive manufacturing (AM) can be an effective technique for adjusting the alloy composition by using several initial materials. The powder bed fusion (PBF) AM process allows the printing of solid parts using powder blends. In the present study, the CrFeCoNi(Al,Ti) HEAs were printed by the PBF technique using the blends of three powders. The structural and phase investigations revealed the chemical inhomogeneity in the materials that led to the new phase formations affecting the mechanical characteristics. The high-temperature annealing at 1200℃ can be considered a post-treatment process for the printed alloys as a homogenization process while the annealing at a lower temperature of 800℃ initiates the decomposition of the initially formed *f.c.c.* phase.

INTRODUCTION

Multi-principal Elemental Alloys (MPEAs), or High-entropy Alloys (HEAs), are considered as a prospective approach to alloy design in Materials Science. Simplifying, it can be said that the MPEA approach suggests the use of several main elements for developing alloy compositions opposite to the traditional approach of alloying one metal [1,2].

The first published CrFeCoNiMn HEA demonstrated exceptional strength-ductility characteristics at cryogenic temperatures [3], while its properties at room temperature and middle temperatures are comparable with the conventional alloys [4,5]. The quaternary CrFeCoNi alloy demonstrates similar properties as the CrFeCoNiMn alloy. It makes sense to pay more attention to the element composition rather than the number of elements in the

alloy. At the moment, the MPEA based on the Cr-Co-Ni-system can be indicated as a prospective playground for alloy design [6]. A recent study reposts the CrCoNi-based GRX-810 alloy demonstrating twice as high ultimate strength at 1093°C compared with nickel superalloy [7]. The alloying with aluminum and\or titanium the CrCoNi-based alloy also presents interesting results at elevated temperatures (tensile strength of 590 MPa and elongation of >40 % at 700°C) [8]. These mechanical characteristics are explained through the formation of the intermetallic *b.c.c.* phases in the *f.c.c.* matrix. Intermetallics demonstrate high strength and low plasticity which limits their application. The combination of hard and brittle phases with a ductile matrix may result in unique material characteristics, especially at elevated temperatures. However, searching for the alloy composition providing the required properties is challenging. This process can be accelerated through additive manufacturing (AM) techniques [9,10,11].

AM technology is the actively exploring modern technique helping to save material and time in the production of items with complex geometry. One of the most popular AM techniques is powder bed fusion (PBF). It uses metal powder as a stock material to print the solid parts. However, due to challenges to produce new materials, the manufacturers of metal powders mainly provide the conventional alloy composition. One of the modern trends in AM field, which actively grows, is to use the metal powder blends or *in situ* printing to build the solid parts. Such technique is actively explored to perform new materials such as MPEAs [9,12,13]. The production of the powder with a final composition as a stock material for the printing process is costly while the mixing of the metal powders with the required element rations allows fast performing the alloy composition in any volume. However, the AM material has its own specifics. The as-printed materials are characterized by the comparably small size of the grains, property anisotropy, and high residual stress due to the high cooling rates and thermal gradient. Therefore, preparing the alloy composition specifically for use in AM may accelerate their application. Particularly, the *in situ* direct laser deposition AM technique for coating the $CrFeCoNiAl_{0.6}$ alloy with 3 at% Ti and 0.25 at% C additions on ferritic H10 tool steel was successfully used [14]. George *et al.* note the Cr-Co-Ni-Al-Ti-based system as one of the prospectives for high-temperature applications due to its high specific strength values [5]. However, there is limited knowledge of the system properties especially those produced with AM techniques. As far as author knowledge, there are no studies of the Cr-Co-Ni-Al-Ti-based alloys synthesized via the PBF AM technique.

This study is focused on the possibility to obtain the CrFeCoNi(Al,Ti) alloys with the PBF technique with laser heat source (PBF-LB) using the blends of aluminum, titanium, and CrFeCoNi powders and analyses of the printed material characteristics and ways their improvements if required. The elemental distribution in the printed alloys was analyzed at an as-built state and in response to the different heat treatments. The phase composition evolution with the change of the chemical composition of the CrFeCoNi(Al,Ti) alloys was considered using X-ray diffraction (XRD) analysis and scanning electron microscopy (SEM) techniques. The microhardness and tensile mechanical properties are presented for the alloys before and after the heat treatment (HT) at 800°C. Additionally, the effects of the different scanning strategies and 1200°C HT on the element distribution in the as-built materials are discussed.

METHODS AND MATERIALS

The blends of powders the CrFeCoNi (Polema Inc., Russia) alloy, Al (RusAl Inc., Russia), and Ti (AP&C Inc., Canada) were used. SEM images of the powders are presented in Fig.1. The CrFeCoNi powder was produced by the spraying technique with cooling in nitrogen. Table 1 shows the chemical composition of the powder provided by the manufacturer. The purities of the aluminum and titanium powders are 99.5 and 99.8 wt.%, respectively.

The four powder blends for printing were prepared using a drum tumbler: 100 wt% of CrFeCoNi powder labeled as "0A"; 99.0/1.0/0 wt% of CrFeCoNi/Al/Ti powders labeled as "1A"; 95.0/5.0/0 wt% of CrFeCoNi/Al/Ti powders labeled as "3A"; and 93.0/5.0/2.0 wt% of CrFeCoNi/Al/Ti powders labeled as "4A1T". The metal 3D printer Trumpf1000 (Trumpf Inc.) was used to build four types of items using powder blends. The printing process parameters were applied the same as in the previous study [15]. To investigate the effect of the residual stress removal and phase stabilization, the HT at 800°C for 30 min and 3 hours with further cooling in water was applied to each type of material.

SEM Quattro S (Thermo Fisher Scientific Inc.) equipped with an energy dispersive X-ray (EDX) detector was applied for microstructural analysis. The samples were preliminarily grinded and polished with 3 μm diamond and 40 nm silica suspensions (Struers Inc.). Electron Backscattered Diffraction (EBSD) analysis was performed with a Nova Nano SEM microscope (FEI Company, Netherlands). For the EBSD analysis, the samples were additionally electropolished with a solution of 90% C_4H_9OH + 10% $HClO_4$. XRD analysis was conducted using the Bruker D8 ADVANCE (Bruker, USA) diffractometer with CuKα radiation on the preliminary sample surfaces polished with 3 μm diamond suspension.

The tensile tests were conducted at room temperature with an Instron tensile machine 5969 (Instron Inc.) with a deformation velocity of $10^{-3}s^{-1}$. The samples with a rectangular geometry were cut from the as-printed and annealed items transversally to the build direction. The geometry with a gauge length of 25.0 mm and a cross-section of 2.0×6.0 mm^2 was applied. Microhardness tests were conducted using the Vickers hardness testing machine ITV-1-AM (Metrotest, Russia) with a load of 300 gf. At least ten measurements per sample were made.

Table 1. The chemical composition of the CrFeCoNi powder provided by the manufacturer (wt%).

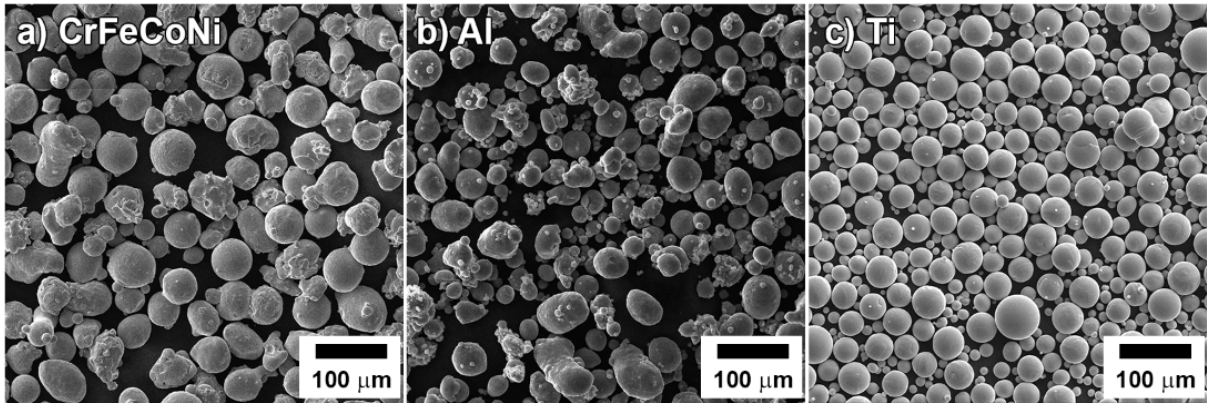| N	Si	Cr	Mn	Fe	Co	Ni	Cu
0.13	0.37	21.57	1.20	22.94	24.98	25.91	2.90

Fig. 1. SEM images of the a) CrFeCoNi, b) Al, and c) Ti powders used to create powder blends for printing.

RESULTS

Chemical composition

The chemical composition of the printed alloys represents a lower Al concentration than expected. The vaporization of light elements such as aluminum is typically observed in the metal printing process [16,17]. Note that the loss of aluminum is less intensive for the CrFeCoNi-Al-Ti blend comparing to the CrFeCoNi-Al. Table 2 summarizes the element compositions for the as-built alloys. EDX mapping demonstrates the inhomogeneous element distribution for the alloys printed using powder blends (Fig. 2a). The observed chemical inhomogeneity is not associated with the phase formation nature since the areas enriched with pure titanium are seen. Interestingly, some areas highly enriched with titanium result in chromium and iron depletions while the Al-rich areas demonstrate the homogeneous composition of other elements (picked with yellow, Fig. 2a). The alloy inhomogeneity is associated with the printing process. The two possible reasons are possible. First, during the spreading of the powder blend on the platform, the heavy particles go down forming a material with higher density at the beginning of the platform. EDX analysis of the 3A sample does not demonstrate the notable difference in aluminum content in the material printed at the beginning and in the middle of the platform (3.94 *vs.* 4.78 wt% Al). However, more precise investigations including process modeling are required in the case of the active using the PBF-LB technique with powder blends. Second, the melted material with higher aluminum concentration (having different surface fluid tension) may be forced to the melt pool boundaries (Fig. 2b). It creates the element of inhomogeneity in the solid tracks. The investigation of single tracks is required for a better understanding of such an effect. Meanwhile, the present work focuses on homogenization options. The double scanning (even with higher laser power up to 175 W) does not provide better titanium and aluminum distribution in the as-built alloys revealing the same EDX results. At the same time, the high-temperature annealing at 1200 $^{\circ}$C (for 24 hours) is more effective. It does not provide the absolute homogenization result while it improves the aluminum distribution in the case of the 3A sample and leads to the Al-Ti-Ni precipitates formations in the element uniform matrix, Fig. 2c and 2d, correspondingly.

Table 2. Chemical composition of the as-built CrFeCoNi(Al,Ti) alloys according to the EDX analysis (wt%) from the area of 600×500 μm².

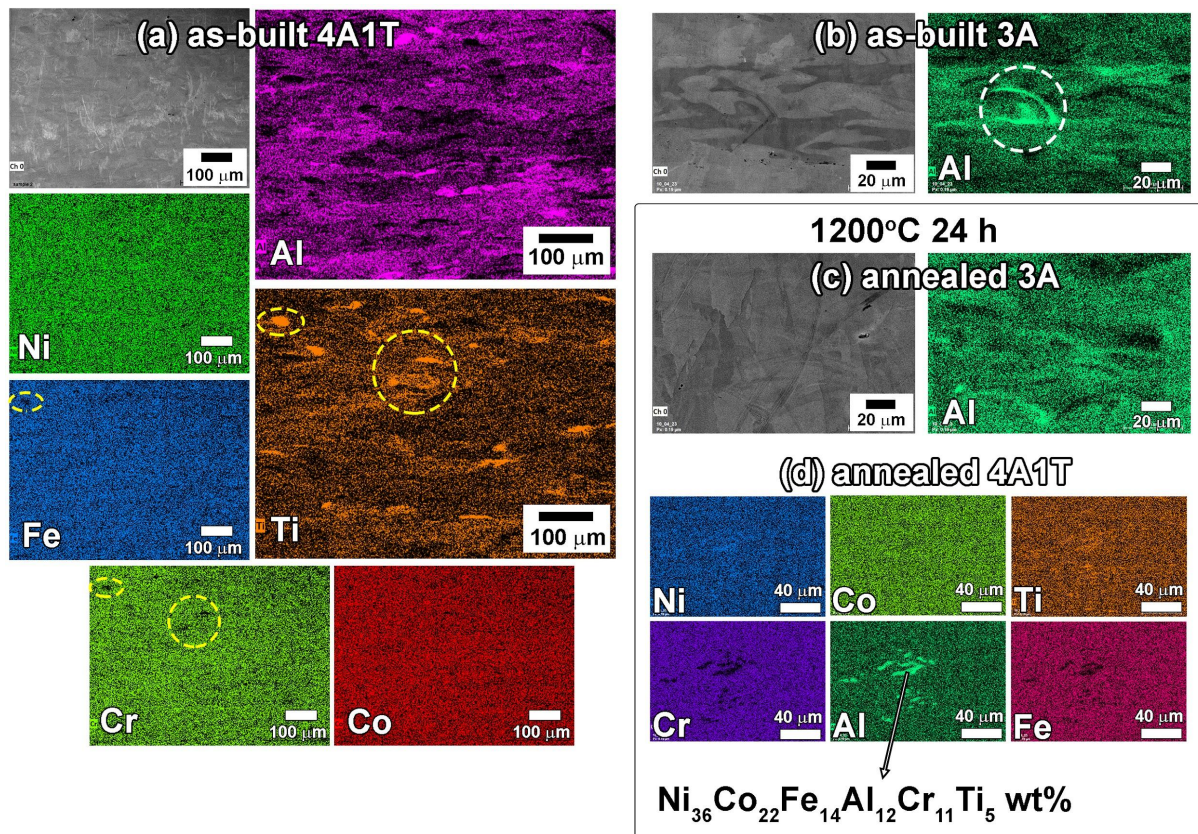|	Cr	Fe	Co	Ni	Al	Ti	Mn	Cu
0A	21.61	23.45	25.84	25.50	0	0	0.95	2.65
1A	21.68	23.09	25.50	25.01	0.76	0	1.13	2.83
3A	20.41	22.39	25.00	24.75	3.62	0	1.02	2.81
4A1T	20.28	22.28	23.98	23.79	4.46	2.63	0	2.58

Fig. 2 (color). EDX maps of the CrFeCoNi(Al,Ti) alloys at (a, b) as-built and (c, d) annealed states (the front view). Fig.a represents the inhomogeneous distribution of Al and Ti in the as-built CrFeCoNiAlTi alloy. The labeled areas enriched with Ti demonstrate the depletion of Cr and Fe. Fig.b represents the inhomogeneity in Al for the as-built CrFeCoNiAl alloy with Al map only since other elements are uniformly distributed. Fig.c and d represent the 1200 ℃ effect on the element distribution for the 3A and 4A1T samples. Specifically, Fig.d represents the formation of the Al-rich precipitates with low Cr and Fe contents.

Microstructure evolution of the printed alloys before and after HT

Figure 3 demonstrates the backscattering electron (BSE) images of the PBF-LB CrFeCoNi(Al,Ti) alloys before and after annealing at 800℃ for 3 hours. The microstructure of the 0A reveals the typical *f.c.c.* structure of ~70 μm grains with a width of ~10 μm elongated transversally to the laser moving direction and fine structure at laser track crossing zones (Fig. 3a) [18]. After the HT, the BSE image demonstrates the same bimodal

microstructural composition (Fig. 3e). The structure stability at such temperatures was also demonstrated for the PBF-LB 316L stainless steel and PBF-LB CrFeCoNi alloy [19,20,15]. At this temperature, the previous results demonstrate the beginning of degradation of the dislocation cellular structure (or, as was concluded in the study, the beginning of recrystallization) and the formation of nitride precipitates in the printed CrFeCoNi alloy [15]. Neutron diffraction analysis indicates that there was no recrystallization process and even changes in dislocation density in the same material up to a temperature of 730℃, while recovery occurred at ~580℃ [21]. It should be noted that differences in heating procedures may lead to variations in structural outcomes.

The noticeable structural difference at as-built conditions is not observed between the 0A, 1A, and 3A samples. The fusion boundaries (labeled with white lines) still can be recognized, Fig.3a-3c. Although, the 800℃ annealing leads to different structural compositions for the aluminum-contained samples, Fig. 3f and 3g. The annealed microstructure looked more fragmented without elongated grains observed for the 0A sample after HT (Fig.3e-3g). The dark areas having up to 29 and 25 at% of Al and Ni reveal the new phase formation, due to another structural composition observed for the 3A sample (Fig. 3g). It indicates the challenge of the elemental homogenization of the alloy since the new phase may have thermodynamic transformation temperatures different from the matrix material.

At high magnification, the effect of the HT is observed even after 30 min of annealing. The as-built alloys consist of the cellular substructure with a cell size of ~600 nm. It was demonstrated earlier that the cell boundaries of the printed CrFeCoNi alloy consist of dislocations [15]. Further, HT leads to the formation of small precipitates enriched with Cr on the high-angle grain boundaries. It was recognized earlier as an M_2N phase [15]. The images of the as-built alloys with aluminum represents similar substructure compositions to the 0A material (Fig. 4a and 4b), while the 3A sample has some regions where the cellular subgrains with a size of ~600-800 nm are surrounded by the new phase (Fig. 4b). The HT effect is different for these two alloys. In the case of the 1A alloy, the short annealing forms the microstructural domains surrounded by the precipitates, Fig. 4d. At the same time, the alloy decomposition forms a new phase on the dislocation boundaries and inside of the cellular grains in the 3A sample after the HT (Fig. 4e).

The titanium addition in the CrFeCoNiAl alloy totally changes the structural composition. The two types of microstructure are observed, the big domains similar to the 0A sample associated with *f.c.c.* structure and regions with fine equiaxial grains with size in the range of ~0.5-1 μm (Fig. 3d). The HT for 3 hours initiates the phase decomposition forming the small precipitates of the new phase around the structural domains. The short HT for 30 min does not lead to notable changes at low magnification while the high magnification reveals the transformation of the cellular substructure to the decomposed phase fine structure (fig. 4c and 4f).
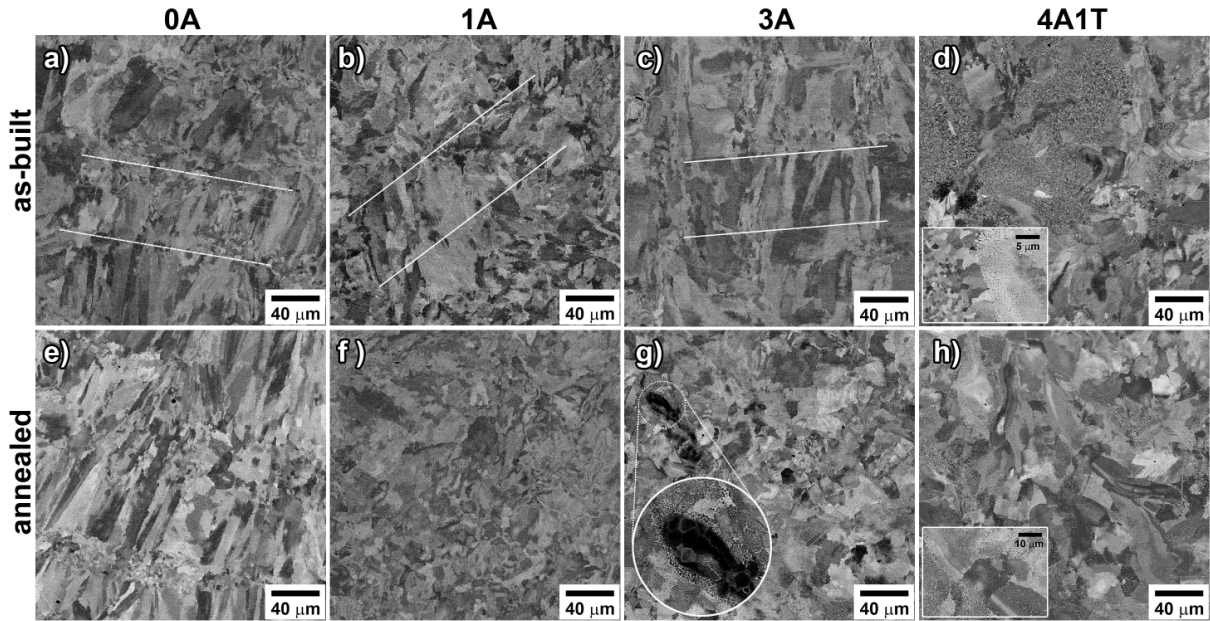
Fig. 3. BSE images of the samples at low magnification at as-built state (a-d) and after 800℃ annealing for 3 hours (e-h) from the top view.
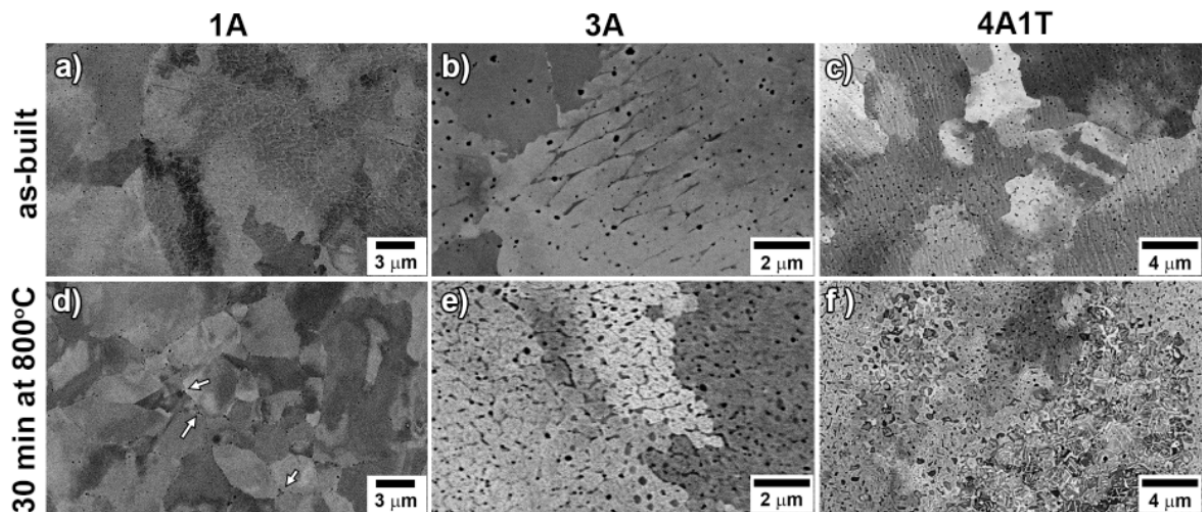

Fig. 4. BSE images of the samples at high magnification before and after annealing at 800℃ for 30 min.

Phase composition evolution

Figure 5 represents the AM CrFeCoNi(Al,Ti) XRD patterns normalized to the 0-1 range at the as-built state and after HT at 800℃ for 0.5 and 3 hours. The XRD analysis reveals the *f.c.c.* structure only for the 0A and 1A samples at as-built and annealed states which is proved by the EBSD analysis. Since the Cu-tube was used, the Ka peaks may contribute to the asymmetry of the main fcc peaks. It can be concluded that no phase transformation occurs in the alloys after applied HT or their low volume (out of the method limits), note the precipitates observed in BSE images. The precise analysis of the (111) *f.c.c.* peaks demonstrates the shifting of the peaks left with Al addition while it moves right after HT. The longer HT does not change significantly the peak position for 0A and 1A alloys. The

increase of the lattice parameter for the *f.c.c.* structure with aluminum addition indicates the embedding of the aluminum atoms in the crystal structure. Table 3 represents the changes in lattice parameters for the detected crystal structures.

The XRD method detects the second *b.c.c.* phase with a lattice parameter of ~2.88 Å for annealed 3A sample (in the *f.c.c.* matrix with a lattice parameter of ~3.59 Å), which agreed with EBSD analysis results (Fig.6a). The *b.c.c.* peak intensity is higher with longer HT indicating the increased volume of *b.c.c.* phase. Note, the recombination of the texture occurs after 3 hours HT (the highest intensity is changed from the (111) peak to the (200) peak). The EBSD analysis reveals the *b.c.c.* phase in the 3A sample (up to 4.1 %) already after the short HT, Fig.6a. The character of the *b.c.c.* phase presented in Fig.6a looks like the decomposition of the supersaturated *b.c.c.* phase (depicted image) since the inner *f.c.c.* grains have a typical form for spinodal decomposition. The fast cooling of the solid solution during the printing does not allow for fully completing the phase transformations. The short heating initiates the diffusion process leading to two simultaneous processes: i) *b.c.c.* phase formation observed at a small portion in the as-built 3A sample, its volume increases with longer HT; and ii) formation of the *f.c.c.* grains in the *b.c.c.* domains. Additionally, the elemental inhomogeneous impacts the phase transformation process. Bloomfield *et al.* show the CrFeCoNiAl$_x$ phase composition evolution with an increase in aluminum content [22]. Since the aluminum distribution in 3A material is not uniform, the different phase transformations can occur locally at different temperatures.

The simultaneous alloying with aluminum and titanium leads to the formation of new phases in the as-built state. The *b.c.c.* phase is observed at the as-built 4A1T sample. The HT leads to the decrease of lattice parameter for the *f.c.c.* phase and an increase in the crystal structure of the *b.c.c.* phase (Table 3). Additionally, the HT at 800℃ leads to the formation of σ-phase having a tetragonal crystal structure [23]. Its peaks started to be well-observed after heating for 3 hours. The precise EBSD analysis of the fine structure observed in the BSE images of the 4A1T sample after short HT concludes that the content of the *b.c.c.* phase is higher for the titanium-contained sample compared with the 3A sample, which is well aligned with XRD patterns observation. The material is characterized by comparably big *f.c.c.* grains and regions consisting of the small *f.c.c.* and *b.c.c.* grains at the ~50/50 volume fraction ratio with an approximate grain size of ~0.8 μm. The same structure is typical for the as-built 4A1T sample as well, Fig. 3d. The size of the fine *f.c.c.+b.c.c.* phases is approximately the same as for the cellular *f.c.c.* subgrains.
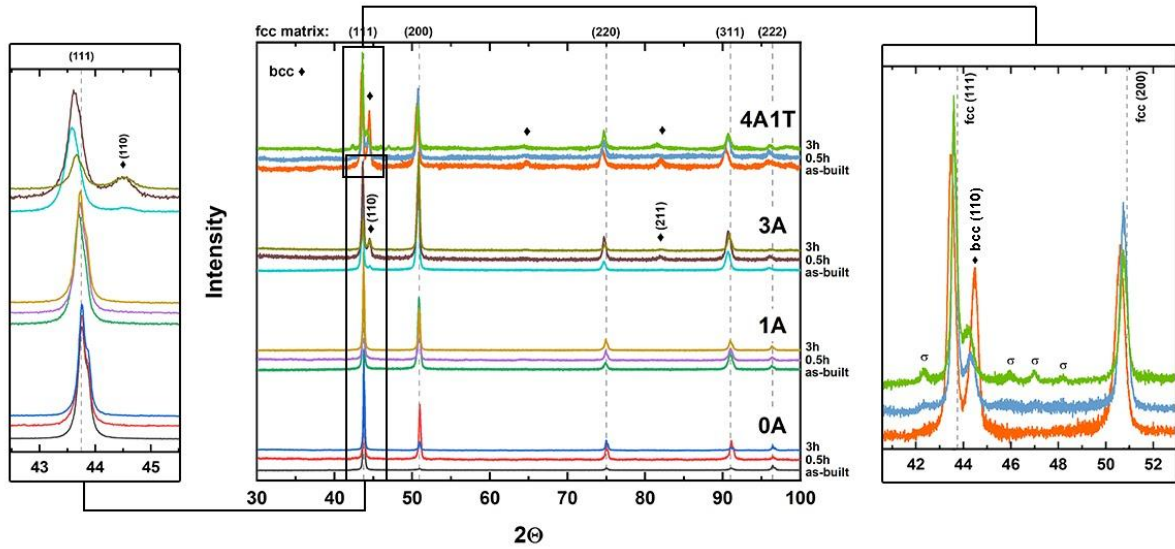
Fig. 5 (color). Normalized XRD patterns for the AM CrFeCoNi(Al,Ti) alloys at different states: as-built, annealed at 800℃ for 0.5, and 3 hours (front view). The 0A and 1A samples demonstrate the *f.c.c.* phase only at any state. The formation of the *b.c.c.* phase in the 3A material is obviously observed only after HT and the 4A1T sample represents the dual phase composition already at the as-built state. The further HT initiates the σ-phase formation in the 4A1T sample only.

Table 3. The calculated lattice parameters (LP) from the XRD results for the detected phases in the CrFeCoNi(Al,Ti) alloys.

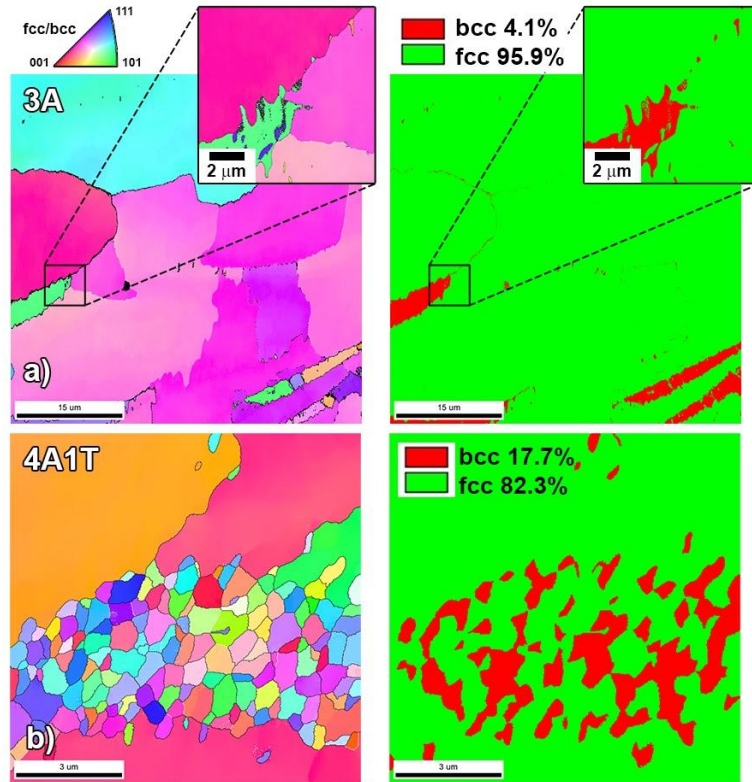|	as-built	after 800℃ annealing for 3 h
0A	*f.c.c.* (LP of ~ 2.584 Å)	*f.c.c.* (LP of ~ 3.583 Å)
1A	*f.c.c.* (LP of ~ 3.587 Å)	*f.c.c.* (LP of ~ 3.586 Å)
3A	*f.c.c.* (LP of ~ 3.597 Å) *b.c.c.* (LP of ~ 2.87 Å)	*f.c.c.* (LP of ~ 3.593 Å) *b.c.c.* (LP of ~ 2.88 Å)
4A1T	*f.c.c.* (LP of ~ 3.605 Å) *b.c.c.* (LP of ~ 2.88 Å)	*f.c.c.* (LP of ~ 3.596 Å) *b.c.c.* (LP of ~ 2.89 Å)

9

Fig. 6 (color). EBSD maps and corresponding phase compositions of the (a) 3A and (b) 4A1T samples after annealing at 800℃ for 30 min.

Microhardness response

Figure 7 demonstrates the effect of the 800℃ annealing duration on the microhardness of the printed CrFeCoNi(Al,Ti) alloys. It is seen that the CrFeCoNi(Al) alloys with different aluminum content provide approximately the same microhardness results at the as-built state (260 HV and 263 HV for 0A and 3A samples, respectively). Only titanium presence initiates the microhardness increase up to ~312 HV in as-built material. The HT initiates the phase decomposition leading to the microhardness increase to 405 and 380 HV for the 3A and 4A1T alloys, respectively. Both alloys demonstrate the wide spread of microhardness values due to structural and phase inhomogeneity. Meanwhile, the materials with zero and low aluminum content (0A and 1A) demonstrate a decrease in microhardness up to ~247 HV. The longer heat treatment does not affect much the microhardness of the A0, A1, and 4A1T materials. At the same time, the drop of microhardness to 378 HV is observed for the 3A sample between the 30 min and 3 hours 800℃ annealing. It is associated with a degradation of the cellular structure. According to the microhardness responses, the following tensile tests were conducted for the materials at the as-built state and after the 30 min heat treatment at 800℃.
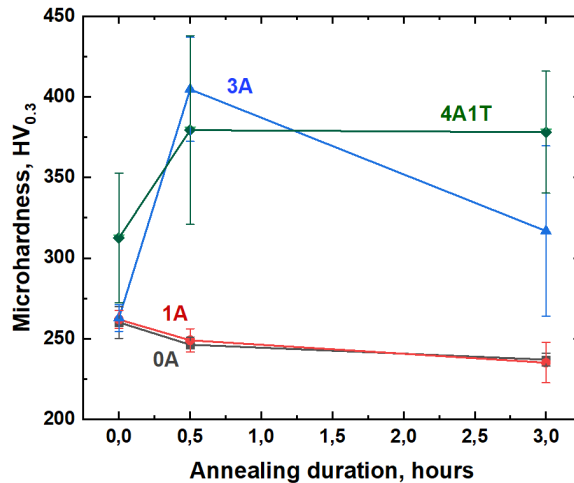
Fig. 7 (color). Microhardness response of the CrFeCoNi(Al,Ti) alloys versus the 800℃ annealing duration. The 0A and 1A samples represent similar microhardness values at the same states. Meanwhile, different microhardness responses are observed for 3A and 4A1T samples with a high standard deviation value. It is explained through the inhomogeneous phase composition in these materials and differences in the phase formation with cooling/heating processes.

Tensile test properties

Figure 8 represents the short HT effect on the tensile test results of the CrFeCoNi(Al,Ti) alloys. Table 4 consists of the full list of the material tensile properties. Similar to the microhardness results, the as-built materials with different aluminum content do not demonstrate significant differences in yield and ultimate strengths, which were in the range of 655-676 MPa and 800-830 MPa, respectively. Only the small titanium addition increases the yield and ultimate strengths up to 850 and 1020 MPa (see Table 4). The elongation decreases only with a relatively high aluminum addition to the CrFeCoNi alloy. It changes from 25% for the 0A and 1A materials to 18% for the 3A material and it dramatically drops with further titanium addition (~3% for 4A1T alloy). The HT decreases the yield strength for the 0A and 1A materials by ~100 MPa and the ultimate strength by ~30 MPa for the 1A material. The heat-treated 3A material demonstrates the same yield strength and increased ultimate strength up to ~901 MPa compared with the as-built state while its ductility drops to ~8 %. The 4A1T alloy also shows the strength increase by ~60-100 MPa after the HT and reduction of already low ductility by ~1%.

The materials with a small Al content represent approximately the same tensile characteristics with a minor strength increase as the CrFeCoNi alloy before and after annealing (Fig. 8a-8b). The difference in the tensile behavior is more obvious for the 3A and 4A1T materials dramatically losing ductility, especially after HT (Fig. 8c). The analysis of the fracture surfaces of the annealed tensile tested samples reveals the similar ductile behavior of the 0A and 1A samples (Fig. 8d and 8e). The deformation involves the twinning mechanism, and the corresponding structural features are observed on the fracture surface of the 0A sample (picked image in Fig.8d). Meanwhile, the 3A and 4A1T samples demonstrate

the ductile matrix with brittle structural features in the fracture surface (Fig. 9f and 9g). These brittle regions are associated with the *b.c.c.* phase.

Table 4. The tensile properties for the PBF-LB CrFeCoNi(Al,Ti) alloys.

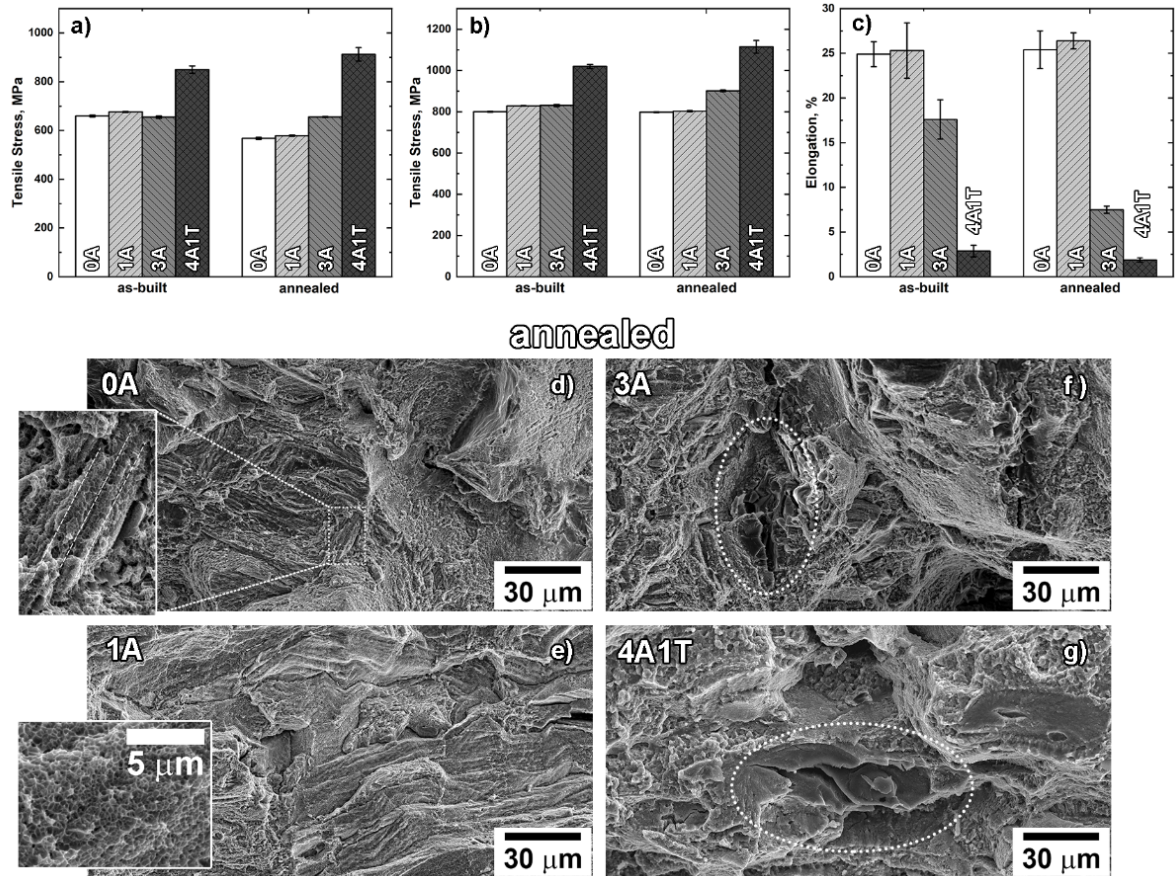|	σ_y, MPa	σ_u, MPa	elongation, %
as-built			
0A	659 ± 4	800 ± 3	25 ± 1
1A	676 ± 3	829 ± 1	25 ± 2
3A	655 ± 5	830 ± 5	18 ± 2
4A1T	850 ± 15	1020 ± 17	3 ± 1
annealed at 800℃ for 30 min			
0A	568 ± 5	798 ± 2	25 ± 2
1A	579 ± 2	803 ± 3	28 ± 3
3A	656 ± 2	901 ± 4	8 ± 0.4
4A1T	912 ± 28	1115 ± 31	2 ± 0.2

Fig. 8. The tensile test results of the CrFeCoNi(Al,Ti) alloys at as-built and 800℃ annealed for 30 min states (a-c). The fracture surfaces of the annealed CrFeCoNi(Al,Ti) alloys after tensile testing (d-g).

DISCUSSION

Printing with powders blend

The EDX analysis revealed the inhomogeneous distribution of aluminum and titanium in the printed samples. The enriched with Al and Ti areas were well-seen in Fig. 2a. Such locally enriched regions initiated the new *b.c.c.* phase formations. The other works considering the PBF-LB alloys printed with powder blends also note the chemical inhomogeneity in the as-built materials [13,24,25]. Karimi *et al.* suggest applying the remelting scan strategy to improve the chemical homogeneity in PBF-LB CrFeCoNiMn alloy [13]. In the present work, the double-scanning (remelting) strategy was applied to the CrFeCoNiAlTi alloy. This approach (even with higher laser power) nevertheless resulted in the same element distribution for the 4A1T sample as for the standard regime resulting. Although, the laser scanning manipulations are more productive in the case of the single-phase CrFeCoNiMn alloy [13,25]. Presumably, the laser scanning approach is more effective for printing with powder blends creating the single-solid solution.

High-temperature annealing at 1200℃ resulted in better homogeneity. However, the phase compositions stable at such temperatures may appear preventing full homogenization (it was seen for the 4A1T sample, Fig. 2d, and presented in Ref.[26]). Moreover, structure recrystallization usually leads to the loss of mechanical characteristics. Mechanical alloying

can be considered an effective solution for improving chemical homogeneity related to the powder-spreading process, but less productive in the case of the element inhomogeneity in the melt pool (noted in the Results section). Additionally, it should be noted that such mechanical application to the powder decreases the quality of the powder which may lead to the quality loss of the printed materials.

Heat treatment impact

According to the XRD and EBSD analyses, the *f.c.c.* structure was detected for the 0A and 1A samples for all considered states. The mechanical properties demonstrated the same characteristics of 0A and 1A materials. The higher aluminum addition (3A sample) initiated the local *b.c.c* phase formation at the subgrain level only which did not significantly impact the strength characteristics but decreased the ductility. The main changes in 3A material properties occured after HT. According to the XRD analysis, the short annealing at 800℃ formed the *b.c.c.* phase. The formation of new phase was observed on the cellular grain boundaries (Fig. 4e). At the same time, the EBSD analysis demonstrated the decomposition of the *b.c.c.* domains, the new *f.c.c.* grains appeared inside. Other studies demonstrate the *b.c.c.* phase formation in CrFeCoNiAl$_x$ alloys consists of two, disordered A2 and ordered B2, crystal structures [9,22,24,27]. Plenty of works demonstrate that the *b.c.c.*/B2 is enriched with aluminum and nickel while *b.c.c.*/A2 has high concentrations of iron and chromium [24,22,28]. Therefore, in this work, the *b.c.c.* phase was associated with B2 structure since the observed *b.c.c.* regions were enriched with Al and Ni (Fig.3g). Additionally, the comprehensive investigation of phase stability of CrFeCoNiAl alloy with aluminum concentration up to 10 at% indicated only three phases (*f.c.c.*, *b.c.c.*/B2, and σ) [22]. The phase diagrams calculated with Thermo-Calc software based on the chemical compositions from Table 2 also resulted in the *b.c.c.*/B2 and σ phase formations in *f.c.c.* matrix (Fig. 9a), while particularly σ-phase was not detected for the 3A material at as-built and annealed states. Longer annealing led to the decomposition of the cellular structure without intensive *b.c.c.* phase formation, which decreased the microhardness response. The XRD pattern of 3 hours annealed 3A sample did not reveal the gain of *b.c.c.* peaks, and EBSD analysis of the 3A sample after short HT demonstrated up to ~5 % of *b.c.c.* phase presence.

The titanium presence in the CrFeCoNiAlTi alloy facilitated the B2 phase formation from the liquid during the cooling (Fig. 9b). According to the Thermo-Calc calculations (the applied database "TCHEA-5: High-Entropy Alloy v.5.1"), it also increased the volume of the σ-phase compared with 3A composition. Indeed, the σ-phase was observed for the 4A1T sample but only after HT (Fig. 5). Note that the ThermoCalc calculations provide the results for the equilibrium structure while the PBF-LB process is related to extremely high cooling rates forming the non-equilibrium state which gives the disparity between the ThermoCalc and XRD results. Other studies also present the *b.c.c.* and σ phase formations in similar alloys [28,29]. The dual-phase formation from the liquid explained the complex structural composition of 4A1T material. In the beginning, the *f.c.c* phase appeared (the huge *f.c.c* zones were observed). Further cooling initiated the formation of *f.c.c.* and *b.c.c.* crystals in unsolidified material. Bloomfield *et al.* conclude the formation of σ phase in the CrFeCoNiAl$_{0.5}$ alloy from the *b.c.c.*/B2 structure supersaturated of the Cr at the temperature range of ~600-900℃ [22], which is well alight with other studies [30,31,32]. The formation

of the σ phase in the 4A1T sample could also occur in the same way. Opposite to the 3A material, the *b.c.c./*B2 structure was formed in the Ti-contained material at high temperatures, but the σ phase did not form (or form at volume out of applied method detect limits) in the material due to the high cooling rate. Following HT at 800℃ provided the required temperature conditions for the σ phase from the *b.c.c./*B2 structure.
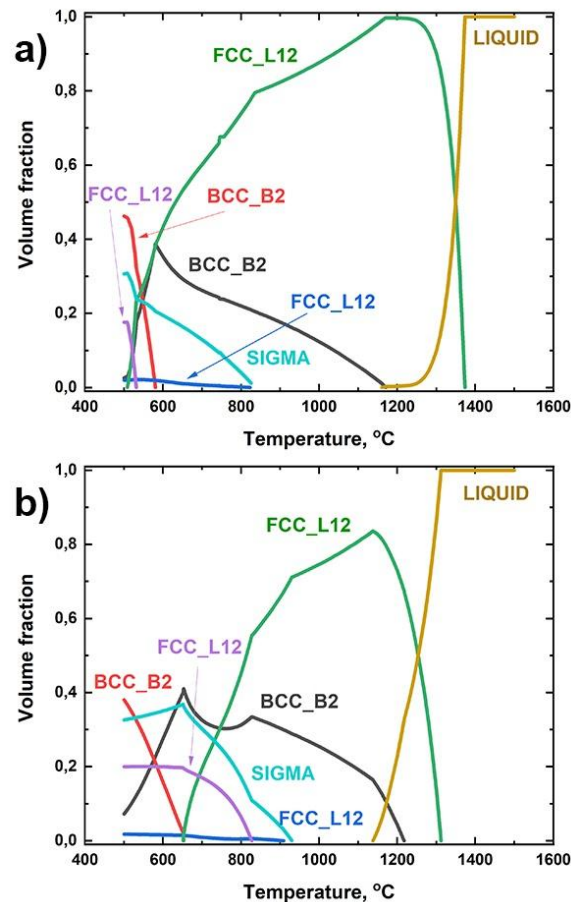

Fig. 9 (color). ThermoCalc phase diagrams were calculated for the (a) 3A and (b) 4A1T materials based on their chemical composition from Table 2.

Structural application prospectives

The small concentration of aluminum in the CrFeCoNiAl alloy did not provide a noticeable improvement in mechanical properties. Even the precipitates formed after HT at the grain boundaries did not contribute to the microhardness properties, while they can lead to ductility loss at cryogenic temperatures [15,33]. The main aluminum effect on mechanical behavior appeared with the *b.c.c.* phase formation which occurred from ~10 at% of aluminum (with an equal concentration of other elements) [9,34]. In the current work, the ~7.5 at% of aluminum related to the 3A sample where the *b.c.c.* phase was still observed. It was explained through the chemical inhomogeneity forming the *b.c.c.* phase at the areas with high aluminum concentrations. It led to the loss of plasticity without benefits in strength since the deformation could occur through the soft *f.c.c.* matrix while the *b.c.c.* regions became the crack sites (Fig. 8f). Figure 10 represents the microstructures of the tensile-tested annealed

samples with different aluminum and titanium contents (the microstructure for the PBF-LB CrFeCoNi alloy can be observed in the earlier study [35]). The slip lines crossing over the grains are well-seen for the 1A sample with the lowest Al content, Fig. 10a. They are the same as for the four- and five-component CrFeCoNi(Mn) systems [35,36]. They were recognized as twins in Cantor's alloy and observed at a later deformation stage [37]. At the same time, the 3A sample had a hard but brittle *b.c.c.* area becoming crack sites, Fig.10b. The crack was initiated in *b.c.c.* areas and rapidly moved across the phase and stopped on the *b.c.c./f.c.c.* border where it relaxed in the *f.c.c.* grains. However, the plasticity of the as-built 3A sample was high enough to provide the fully solid parts appropriate for the tensile test. Moreover, the as-built 3A sample can be mechanically processed and a following HT may fix the obtained structural composition. As was demonstrated in the present study, the short HT led to phase decomposition with the formation of the *b.c.c.* phase on the cellular grain boundaries. It provided the microhardness increase with ductility loss while the tensile strength did not show such growth. The prevention of hot tearing with aluminum addition was not observed in the present study as it is demonstrated in the study [24]. Sun *et al.* present the lowest hot crack volume for the composition with 5 wt% aluminum content. The lower and higher aluminum contents drastically increase the hot crack volume. However, in the present study, the notable hot tearing formation was not observed even for the PBF-LB CrFeCoNi alloy. The attempt to create the same $Al_{0.5}CoCrFeNi$ composition as in the work [24] was not successful due to the delamination of the printed items. As the explanation, the thermal history may play a significant role in the PBF-LB $Al_xCoCrFeNi$ structure formation. Despite the similar AM process and alloy composition, the thermal history difference may be significant, since the size of the observed cellular structure is twice as high in the referenced work (~1.5 μm) than in this study (~0.8 μm). The titanium contained 4A1T material demonstrated the higher strength characteristics at the as-built state due to the *b.c.c.* phase formation. The further increase of strength (microhardness and tensile strength) and loss of tensile ductility of the material after the HT were the results of the σ phase formation. Compared with the 3A sample, the *f.c.c.* phase fraction was lower in the 4A1T material (Fig. 5 and 6) and it was seen that the damage occurred mostly through the brittle *b.c.c.* phase, Fig.10c. Moreover, the hot tears for the 4A1T sample were more typical. These two factors together facilitated the crack formation in the material and crack propagation during the deformation. The arc-melted AlCoCrFeNiTi alloy also represents low ductility while the strength properties are higher compared to the PBF-LB 4A1T alloy in the present study, Table 5 [8]. The fine structure typical for PBF-LB materials provides higher strength properties compared with conventional methods. As was said above, the elemental and structural inhomogeneities led to the mechanical property inhomogeneity demonstrated by the microhardness dispersion and hot tears facilitating the crack formation (Fig. 8g). It makes the homogenization process of the material printed with powder blends an important task. Additionally, the chemical composition should be adjusted. Consideration of the arc-melted Cr-Fe-Co-Ni-Al-Ti system under the compressive load demonstrates promising mechanical test results with higher content of aluminum and titanium, while the current printing parameters do not allow building the undamaged material.
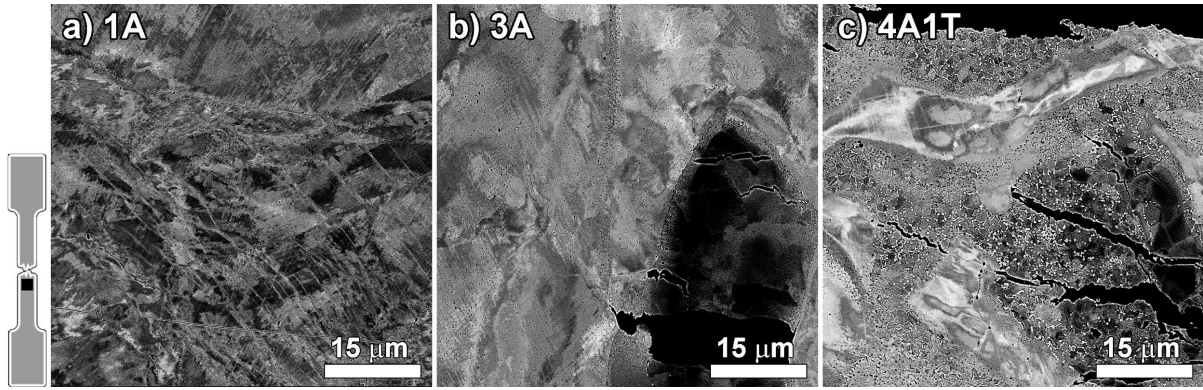
Fig. 10. BSE images of the microstructures of the tensile tested (a) 1A, (b) 3A, and (c) 4A1T samples after 800℃ HT near the damaged zone.

Table. 5. The comparison of the mechanical test results obtained under the compressive (C) and tensile (T) loads at room temperature.

Composition (in molar portions)	Load	$\sigma_{0.2}$, MPa	$\sigma_{max/ult}$, MPa	ε, %	Ref.
PBF-LB CrFeCoNiAl$_{0.4}$Ti$_{0.14}$	T	850	1020	3	This study
Arc-melted Al$_{0.5}$CoCrFeNiTi$_{0.15}$	T	1098	1415	5	[8]
Arc-melted CrFeCoNiAl	C	1500	2830	27	[38]
Arc-melted CrFeCoNiAlTi$_{0.5}$	C	2260	3140	23	[38]
Arc-melted CrFeCoNiTi$_{0.25}$	C	1310	2621	9	[39]
Arc-melted CrFeCoNiTi$_{0.25}$Al$_{0.5}$	C	1880	3475	10	[39]

CONCLUSIONS

The present work considers the PBF-LB CrFeCoNi(Al,Ti) alloys printed using powder blends. The following conclusions can be made:

- The PBF-LB printing of the CrFeCoNi(Al,Ti) alloys using powder blends does not provide a homogeneous element distribution. The scanning strategy manipulations do not improve the elemental distribution associated with new phase formations;

- The high-temperature annealing at 1200℃ may be an effective procedure to homogenize the chemical composition of the alloys printed using the powder blend. The PBF-LB CrFeCoNiAlTi alloy demonstrated the Ni- and Al-rich precipitates within the matrix having a uniform elemental distribution;

- The XRD analysis reveals the small volume of *b.c.c.*/B2 phase in the 3A sample formed from the *f.c.c.* matrix. Its volume increases with further HT at 800℃

stabilizing the dual phase composition in the material. At the beginning of HT, the secondary *b.c.c.*/B2 phase appears at the cellular grain boundaries while the longer HT leads to the decomposition of the cellular substructure.

- The titanium addition to the Cr-Fe-Co-Ni-Al system changes the crystallization process forming simultaneously both *f.c.c.* and *b.c.c.* phase formations from the liquid. It leads to the complex structural composition consisting of the big domains of *f.c.c.* grains and fine grain regions with a mix of two phases. Following HT at 800℃ leads to the σ phase formation.

- The phase composition is the main factor affecting the mechanical characteristics of the printed CrFeCoNi(Al,Ti) alloys. The newly formed *b.c.c.*/B2 phase is a main contributor to the strength properties of the 3A material appearing after HT at 800℃. The 4A1T demonstrates the comparable high strength characteristics at the as-built state which additionally increase after the HT. However, for both materials presenting additional phases, the loss of ductility is observed. Additionally, the phase inhomogeneity in the materials leads to the limited gain of strength characteristics.

CRediT AUTHOR STATEMENT

Y. Kuzminova: Conceptualization, Methodology, Investigation, Formal analysis, Visualization, Writing - Original Draft; **D. Firsov:** Investigation; **A. Shibalova:** Investigation, Formal analysis; **E. Kudryavtsev:** Investigation; **P. Krakhmalev:** Supervision, Writing - Review & Editing; **O. Klimova-Korsmik:** Investigation, Formal analysis; **I. Shishkovsky:** Resources, Supervision, Writing - Review & Editing; **S. Evlashin:** Resources, Writing - Review & Editing.

ACKNOWLEDGMENTS

DECLARATION OF INTERESTS

The authors declare that they have no known competing financial interests or personal relationships that could have appeared to influence the work reported in this paper.

REFERENCES

[1] Cantor, B., Chang, I. T. H., Knight, P., & Vincent, A. J. B. (2004). Microstructural development in equiatomic multicomponent alloys. *Materials Science Engineering A*, *375–377*, 213–218. https://doi.org/10.1016/j.msea.2003.10.257

[2] Yeh, J. W., Chen, S. K., Lin, S. J., Gan, J. Y., Chin, T. S., Shun, T. T., Tsau, C. H., & Chang, S. Y. (2004). Nanostructured high-entropy alloys with multiple principal elements: Novel alloy design concepts and outcomes. *Advanced Engineering Materials*, *6*(5), 299-303+274. https://doi.org/10.1002/adem.200300567

[3] Gali, A., & George, E. P. (2013). Tensile properties of high- and medium-entropy alloys. *Intermetallics*, *39*, 74–78. https://doi.org/10.1016/j.intermet.2013.03.018

[4] Salishchev, G. A., Tikhonovsky, M. A., Shaysultanov, D. G., Stepanov, N. D., Kuznetsov, A. V., Kolodiy, I. V., Tortika, A. S., & Senkov, O. N. (2014). Effect of Mn and V on structure and mechanical properties of high-entropy alloys based on CoCrFeNi system. *Journal of Alloys and Compounds*, *591*, 11–24. https://doi.org/10.1016/j.jallcom.2013.12.210

[5] George, E. P., Curtin, W. A., & Tasan, C. C. (2020). High entropy alloys: A focused review of mechanical properties and deformation mechanisms. *Acta Materialia*, *188*, 435–474. https://doi.org/10.1016/j.actamat.2019.12.015

[6] Gludovatz, B., Hohenwarter, A., Thurston, K. V. S., Bei, H., Wu, Z., George, E. P., & Ritchie, R. O. (2016). Exceptional damage-tolerance of a medium-entropy alloy CrCoNi at cryogenic temperatures. Nature Communications, 7. https://doi.org/10.1038/ncomms10602

[7] Smith, T.M., Kantzos, C.A., Zarkevich, N.A. et al. A 3D printable alloy designed for extreme environments. Nature 617, 513–518 (2023). https://doi.org/10.1038/s41586-023-05893-0

[8] Asabre, A., Kostka, A., Stryzhyboroda, O., Pfetzing-micklich, J., & Hecht, U. (2019). Effect of Al , Ti and C additions on Widmanstatten microstructures and mechanical properties of cast Al0.6CoCrFeNi compositionally complex alloys. *Materials & Design*, *184*, 108201. https://doi.org/10.1016/j.matdes.2019.108201

[9] Li, M., Gazquez, J., Borisevich, A., Mishra, R., & Flores, K. M. (2018). *Evaluation of microstructure and mechanical property variations in AlxCoCrFeNi high entropy alloys produced by a high-throughput laser deposition method. Intermetallics, 95(January)*, 110–118. https://doi.org/10.1016/j.intermet.2018.01.021

[10] George, E. P., Raabe, D., & Ritchie, R. O. (2019). High-entropy alloys. *Nature Reviews Materials*, *4*(8), 515–534. https://doi.org/10.1038/s41578-019-0121-4

[11] Haase, C., Tang, F., Wilms, M. B., Weisheit, A., & Hallstedt, B. (2017). Combining thermodynamic modeling and 3D printing of elemental powder blends for high-throughput investigation of high-entropy alloys – Towards rapid alloy screening and design. *Materials Science and Engineering A*, *688*, 180–189. https://doi.org/10.1016/j.msea.2017.01.099

[12] Chen, P., Yao, X., Attallah, M. M., & Yan, M. (2022). In-situ alloyed CoCrFeMnNi high entropy alloy: microstructural development in laser powder bed fusion. *Journal of Materials Science & Technology*. https://doi.org/10.1016/J.JMST.2021.11.083

[13] Karimi, J., Kollo, L., Rahmani, R., Ma, P., Jia, Y. D., & Prashanth, K. G. (2022). Selective laser melting of in-situ CoCrFeMnNi high entropy alloy: Effect of remelting. *Journal of Manufacturing Processes*, *84*, 55–63. https://doi.org/10.1016/j.jmapro.2022.09.056

[14] Asabre, A., Wilms, M. B., Kostka, A., Gemagami, P., Weisheit, A., & Laplanche, G. (2021). Laser metal deposition of Al0.6CoCrFeNi with Ti & C additions using elemental powder blends. *Surface and Coatings Technology*, *418*, 127233. https://doi.org/10.1016/J.SURFCOAT.2021.127233

[15] Y.O. Kuzminova, E.A. Kudryavtsev, J.-K. Han, M. Kawasaki, S.A. Evlashin, Phase and structural changes during heat treatment of additive manufactured CrFeCoNi high-entropy alloy, J. Alloys Compd. 889 (2021) 161495. doi:https://doi.org/10.1016/j.jallcom.2021.161495

[16] Gaytan, S. M., Murr, L. E., Medina, F., Martinez, E., Lopez, M. I., & Wicker, R. B. (2009). Advanced metal powder based manufacturing of complex components by electron beam melting. *Materials Technology*, *24*(3), 180–190. https://doi.org/10.1179/106678509X12475882446133

[17] Mukherjee, T., Zuback, J. S., De, A., & DebRoy, T. (2016). Printability of alloys for additive manufacturing. *Scientific Reports*, *6*. https://doi.org/10.1038/srep19717

[18] DebRoy, T., Wei, H. L., Zuback, J. S., Mukherjee, T., Elmer, J. W., Milewski, J. O., Beese, A. M., Wilson-Heid, A., De, A., & Zhang, W. (2018). Additive manufacturing of metallic components – Process, structure and properties. Progress in Materials Science, 92, 112–224. https://doi.org/10.1016/j.pmatsci.2017.10.001

[19] Krakhmalev P, Fredriksson G, Svensson K, Yadroitsev I, Yadroitsava I, Thuvander M, Peng R. Microstructure, Solidification Texture, and Thermal Stability of 316 L Stainless Steel Manufactured by Laser Powder Bed Fusion. Metals. 2018; 8(8):643. https://doi.org/10.3390/met8080643

[20] Voisin, T., Forien, J.-B., Perron, A., Aubry, S., Bertin, N., Samanta, A., Baker, A., & Wang, Y. M. (2021). New insights on cellular structures strengthening mechanisms and thermal stability of an austenitic stainless steel fabricated by laser powder-bed-fusion. *Acta Materialia*, *203*, 116476. https://doi.org/https://doi.org/10.1016/j.actamat.2020.11.018

[21] Liu, X., Han, J. K., Onuki, Y., Kuzminova, Y. O., Evlashin, S. A., Kawasaki, M., & Liss, K. D. (2022). In Situ Neutron Diffraction Investigating Microstructure and Texture Evolution upon Heating of Nanostructured CoCrFeNi High-Entropy Alloy. *Advanced Engineering Materials*. https://doi.org/10.1002/adem.202201256

[22] Bloomfield, M. E., Christofidou, K. A., Mignanelli, P. M., Reponen, A.-P. M., Stone, H. J., & Jones, N. G. (2022). Phase stability of the AlxCrFeCoNi alloy system. *Journal of Alloys and Compounds*, *926*, 166734. https://doi.org/10.1016/J.JALLCOM.2022.166734

[23] G. Bergman, D.P. Shoemaker, The determination of the crystal structure of the σ phase in the iron-chromium and iron-molybdenum systems, Acta Crystallogr. 7 (1954) 857–865. doi:10.1107/S0365110X54002605

[24] Sun, Z., Tan, X., Wang, C., Descoins, M., Mangelinck, D., Tor, S. B., Jägle, E. A., Zaefferer, S., & Raabe, D. (2021). Reducing hot tearing by grain boundary segregation engineering in additive manufacturing: example of an AlxCoCrFeNi high-entropy alloy. *Acta Materialia*, *204*. https://doi.org/10.1016/j.actamat.2020.116505

[25] Chen, P., Li, S., Zhou, Y., Yan, M., & Attallah, M. M. (2020). Fabricating CoCrFeMnNi high entropy alloy via selective laser melting in-situ alloying. *Journal of Materials Science & Technology*, *43*, 40–43. https://doi.org/https://doi.org/10.1016/j.jmst.2020.01.002

[26] Kuzminova, Y., Shibalova, A., Evlashin, S., Shishkovsky, I., & Krakhmalev, P. (2021). Structural effect of low Al content in the in-situ additive manufactured CrFeCoNiAlx high-entropy alloy. *Materials Letters*, *303*. https://doi.org/10.1016/j.matlet.2021.130487

[27] Jasiewicz, K., Cieslak, J., Kaprzyk, S., & Tobola, J. (2015). Relative crystal stability of AlxFeNiCrCo high entropy alloys from XRD analysis and formation energy calculation. *Journal of Alloys and Compounds*, *648*, 307–312. https://doi.org/10.1016/j.jallcom.2015.06.260

[28] Y. Yu, J. Wang, J. Li, H. Kou, W. Liu, Characterization of BCC phases in AlCoCrFeNiTix high entropy alloys, Mater. Lett. 138 (2015) 78–80. doi:10.1016/J.MATLET.2014.09.100

[29] C.E. Slone, E.P. George, M.J. Mills, Elevated temperature microstructure evolution of a medium-entropy CrCoNi superalloy containing Al , Ti, J. Alloys Compd. 817 (2020) 152777. doi:10.1016/j.jallcom.2019.152777

[30] Strumza, E., & Hayun, S. (2021). Comprehensive study of phase transitions in equiatomic AlCoCrFeNi high-entropy alloy. *Journal of Alloys and Compounds*, *856*. https://doi.org/10.1016/j.jallcom.2020.158220

[31] Butler, T. M., & Weaver, M. L. (2017). Investigation of the phase stabilities in AlNiCoCrFe high entropy alloys. *Journal of Alloys and Compounds*, *691*, 119–129. https://doi.org/10.1016/j.jallcom.2016.08.121

[32] Chen, M., Lan, L., Shi, X., Yang, H., Zhang, M., & Qiao, J. (2019). The tribological properties of Al0.6CoCrFeNi high-entropy alloy with the σ phase precipitation at elevated temperature. *Journal of Alloys and Compounds*, *777*, 180–189. https://doi.org/10.1016/j.jallcom.2018.10.393

[33] Kuzminova, Y., Firsov, D., Dudin, A., Sergeev, S., Zhilyaev, A., Dyakov, A., & Chupeeva, A. (2020). The effect of the parameters of the powder bed fusion process on the microstructure and mechanical properties of CrFeCoNi medium-entropy alloys. *Intermetallics*, *116*(July 2019), 106651. https://doi.org/10.1016/j.intermet.2019.106651

[34] Wang, W., Wang, W., & Yeh, J. (2014). Phases, microstructure and mechanical properties of AlxCoCrFeNi high-entropy alloys at elevated temperatures. *Journal of Alloys and Compounds*, *589*, 143–152. https://doi.org/10.1016/j.jallcom.2013.11.084

[35] Kuzminova, Y. O., Firsov, D. G., Dagesyan, S. A., Konev, S. D., Sergeev, S. N., Zhilyaev, A. P., Kawasaki, M., Akhatov, I. S., & Evlashin, S. A. (2021). Fatigue behavior of additive manufactured CrFeCoNi medium-entropy alloy. *Journal of Alloys and Compounds*, *863*, 158609. https://doi.org/10.1016/j.jallcom.2021.158609

[36] Schuh, B., Mendez-Martin, F., Völker, B., George, E. P., Clemens, H., Pippan, R., & Hohenwarter, A. (2015). Mechanical properties, microstructure and thermal stability of a nanocrystalline CoCrFeMnNi high-entropy alloy after severe plastic deformation. *Acta Materialia*, *96*, 258–268. https://doi.org/10.1016/J.ACTAMAT.2015.06.025

[37] Laplanche, G., Kostka, A., Horst, O. M., Eggeler, G., & George, E. P. (2016). Microstructure evolution and critical stress for twinning in the CrMnFeCoNi high-entropy alloy. *Acta Materialia*, *118*, 152–163. https://doi.org/10.1016/j.actamat.2016.07.038

[38] Zhou, Y. J., Zhang, Y., Wang, Y. L., & Chen, G. L. (2007). Solid solution alloys of AlCoCrFeNi Tix with excellent room-temperature mechanical properties. *Applied Physics Letters*, *90*(18). https://doi.org/10.1063/1.2734517

[39] Zhang, K. B., Fu, Z. Y., Zhang, J. Y., Wang, W. M., Wang, H., Wang, Y. C., Zhang, Q. J., & Shi, J. (2009). Microstructure and mechanical properties of CoCrFeNiTiAlx high-entropy alloys. *Materials Science and Engineering A*, *508*(1–2), 214–219. https://doi.org/10.1016/j.msea.2008.12.053

Chapter 10

Conclusions and Outlooks

- The CrFeCoNi alloy exhibits great potential as a material for 3D printing applications. Optimizing printing parameters can effectively reduce defects and its high ductility allows for the printing of large items and complex geometries without cracks. In its as-built state, the PBF CrFeCoNi alloy displays a homogenous element distribution and a single solid solution. The AM process imparts high-strength properties to the printed alloy. At the as-built state, the ultimate strength characteristics are equivalent to hot-rolled materials and the yield strength properties are even higher. Numerous publications have highlighted the advantage of the CrFeCoNi alloy is its ability to exhibit improved mechanical properties at lower temperatures, making it an attractive option for use in cryogenic environments. It was also revealed for the PBF CrFeCoNi alloy.

- During cycling loading, there is a notable dependency of the fatigue strength of the PBF CrFeCoNi alloy on near-surface defects that are typical in AM materials. This highlights the issue of defect presence in AM materials under cycling loading conditions and emphasizes the need for defect removal processes. One way to handle this problem is by implementing surface machining, which can significantly improve fatigue strength multiple times over. Moreover, structural analysis indicates that the PBF CrFeCoNi alloy exhibits distinct deformation mechanisms for different load types. The dislocation slips only are

observed at lower cycling loads without twinning appearing. The twinning may be involved during tensile loading of the material at later deformation stages nonetheless this statement requires additional proof.

- The PBF CrFeCoNi alloy demonstrated phase stability in the wide temperature (up to 1000°C). However, in the present work, the nitride precipitates (with a M_2N crystal structure enriched with Cr) were detected on the grain boundaries after heat treatment at the temperature range of 700-800°C. Its formation was related to the presence of nitrogen in the initial powder material up to 0.1 wt%. The nitrogen effect on the material mechanical properties is controversial. On the one hand, nitrogen may provide a solid solution hardening of the material. Additionally, it may prevent grain growth during the recrystallization process due to fixing the grain boundaries. However, the present work demonstrated the mechanical properties degradation of the annealed PBF CrFeCoNi alloy associated with the formation of the nitrides. Particularly, the annealed material does not demonstrate the expected ductility growth with a temperature decrease. Additionally, the annealed material does not reveal the improved fatigue strength properties at a high-cycling fatigue regime, which may be also associated with the formation of the brittle phase on the grain boundaries. The nitrides riched with Al are observed after the aluminum addition to the CrFeCoNi alloy. Note that only the main *f.c.c.* phase is observed in the as-built PBF CrFeCoNi alloy due to the high cooling rate. Therefore, the alloying of the PBF CrFeCoNi alloy with nitrogen may be considered only in the case of the as-built state use. The increase in temperature leads to the formation of the brittle phase on the grain boundaries decreasing the material mechanical characteristics.

- An *in situ* neutron diffraction analysis showed that 3D printing results in a high micro-strain due to high dislocation density in the CrFeCoNi alloy. Additionally, the analysis revealed the recovery process of the as-printed material at 850 K (577°C), which does not occur in the as-cast material up to 1000 K (727°C). The DSC analysis demonstrated the endothermic peak associated with recov-

ery process beginning at the temperature of 400°C with a peak maximum at 500°C, which particularly is associated with the recovery of point defects. At the same time, the neutron diffraction analysis revealed the beginning of the dislocation movement at the temperature of 850 K. The cellular substructure remains stable even after long heat treatment at 600°C for up to 21 days. The transmission electron microscopy revealed that the cellular microstructure degrades and coalesces after 24 hours of annealing at 700°C leading to a drop in microhardness. The continuous recrystallization process may occur starting from the temperature of 800°C. Subsequent structural analyses of printed CrFeCoNi alloy showed dislocation-free grain growth at 1000°C, while the texture of the material remained unchanged at this temperature. Such material behavior indicates the application of the PBF CrFeCoNi alloy at elevated temperatures is limited. Only further chemical modification may increase the possible temperature application range. Although, the as-built alloy can be effective for structural applications at room temperature and below 600°C.

- During the HPT process, the PBF CrFeCoNi HEA exhibits greater strain hardening capability and sensitivity to strain rate compared to the cast alloy. An *in situ* neutron diffraction analysis reveals that the HPT process reduces the recovery and stress relaxation temperature to below 800 K. Recrystallization in the HPT material also begins at lower temperatures of 960 K, while higher temperatures initiate dislocation-free grain growth. Interestingly, the lowest micro-strain is achieved after complete recrystallization by heating the HPT-processed specimen at 1000 K, which is even lower than the as-printed material without HPT. Hardness measurements after annealing show an increase up to 873 K, followed by a decrease with increasing temperature. This is attributed to residual and Bauschinger stress-relaxation, as well as a decrease in athermal vacancies before the material begins to soften due to recrystallization. As an insight, the deformation process of printed material may be adjusted for the post-printing processes focusing on internal stress minimization.

- The PBF printing with the aluminum and CrFeCoNi powder blends does not

provide the homogeneous element distribution. The material even with a small aluminum addition reveals the aluminum reached areas at the front view while the XRD analysis indicates the initial *f.c.c.* phase only. The high-temperature annealing at 1200°C homogenizes the element distribution but may lead to precipitate formation in case of the low purity of the initial materials. The microstructural analysis of the annealed CrFeCoNiAl and microhardness response demonstrated the structure stabilization at high temperatures with even small aluminum addition. It indicates the increase of the stalking fault energy by aluminum adding. However, the effect of the small aluminum addition to the system on the tensile properties was not observed compared to the four-component system. Aluminum addition prevents the material from delaminating at elevated temperatures (800°C and 1000°C) by forming the Al_2O_3 oxides along the columnar grains, the main oxygen penetrating "channels". The oxidized layer enriched with Cr is still observed as a top layer. The presence of nitrogen in the initial powder also affects the near-surface chemical composition forming the Al-N precipitates under the Al_2O_3 oxide zone. Generally, the oxygen effect on the near-surface layers was observed till the depth of 300 μm at the 1000°C annealing for 500 hours. It makes the aluminum effect on the oxygen resistance properties of the CrFeCoNiAl alloy ambiguous. There is no absolute prevention to the oxidizing process with aluminum addition while the positive effect on the material delaminating is observed. However, since the CrFeCoNiAl alloy is considered the material for elevated temperatures applications, further investigations at high temperatures are required.

- The PBF CrFeCoNiAl printed using the powder blends with the aluminum content up to 7.5 at% allows the *b.c.c.*/B2 phase formation even at the as-built material state. The HT at 800°C increases the volume of the secondary phase. The new phase mostly occurs on the cellular grain boundaries leading to the material strength increase and the ductility loss. The formation of σ-phase was not observed for this material even after the HT at 800°C. The using of the blend of the CrFeCoNi, Al, and Ti powders also does not lead to the homogeneous element distribution in the as-built material while

the high-temperature HT at 1200℃ may uniform the element distribution. The titanium presence (up to 3 at%) initiates the simultaneous formation of the *f.c.c.* and *b.c.c.* phases from the liquid during the crystallization affecting the microstructural composition. It significantly increases the strength properties and dramatically decreases ductility. The HT at 800℃ additionally increases the strength characteristics due to the σ-phase formation in the CrFeCoNiAlTi alloy. Although, the comparison with the arc-melted material having a similar composition reveals the lower tensile properties of the printed material. It indicates the specifics of the PBF material printed with powder blend. Since the as-built material has an inhomogeneous element distribution the phase formations and transformations occur locally. It provides some martial specifics. First, the temperature ranges of material phase transformations extend which can require a more careful choice of HT. Second, the mechanical properties are not uniform in the material. It simplifies the crack formation in the brittle zones and further material damage at lower loads. Comparison of the PBF CrFeCoNiAlTi alloy printed with powder blends with the arc-melted CrFeCoNiAlTi alloy having similar chemical composition reveals the lower strength-ductile characteristics. It makes the post-treatment of material printed with the powder blend an essential step in improving material properties. The development of high-temperature heat treatment processes (including HIP) looks like the most prospective for this purpose. Additionally, intensive deformation can also be effective, in the case of material properties investigations without a goal keeping the initially printed form of the item.

- The application of HEA for the AM process reveals the same specifics of the printed material as for bulk printed materials. Therefore, it is possible to use the solutions applied for the printing with well-known materials to the printing with HEAs. At the same time, the modification of the HEA chemical composition through printing with powder blends is limited. Presumably, printing with a pre-alloyed powder provides uniform material properties, which provide better mechanical characteristics, similar to or higher to the HEA produced with a conventional technique. However, the development of the post-process

to homogenize the material properties is a new challenge for further printing with powder blends.

Bibliography

[1] A. Arabi-hashemi, X. Maeder, R. Figi, C. Schreiner, S. Griffiths, and C. Leinen-bach. 3D magnetic patterning in additive manufacturing via site-specific in-situ alloy modification. *Applied Materials Today*, 18:100512, 2020.

[2] A. Asabre, A. Kostka, O. Stryzhyboroda, J. Pfetzing-micklich, and U. Hecht. Effect of Al , Ti and C additions on Widmanst a mechanical properties of cast Al0.6CoCrFeNi compositionally complex alloys. *Materials & Design*, 184:108201, 2019.

[3] A. Asabre, M. B. Wilms, A. Kostka, P. Gemagami, A. Weisheit, and G. La-planche. Laser metal deposition of Al0.6CoCrFeNi with Ti & C additions using elemental powder blends. *Surface and Coatings Technology*, 418:127233, 7 2021.

[4] P. Bajaj, A. Hariharan, A. Kini, P. Kürnsteiner, D. Raabe, and E. A. J. Materials Science & Engineering A Steels in additive manufacturing : A review of their microstructure and properties. 772(November 2019), 2020.

[5] M. Bloomfield, K. Christofidou, P. Mignanelli, A.-P. Reponen, H. Stone, and N. Jones. Phase stability of the AlxCrFeCoNi alloy system. *Journal of Alloys and Compounds*, 926:166734, 12 2022.

[6] C. Brice, R. Shenoy, M. Kral, and K. Buchannan. Precipitation behavior of aluminum alloy 2139 fabricated using additive manufacturing. *Materials Science and Engineering: A*, 648:9–14, 2015.

[7] Y. Brif, M. Thomas, and I. Todd. The use of high-entropy alloys in additive manufacturing. *Scripta Materialia*, 99(April):93–96, 2015.

[8] B. Cantor, I. T. H. Chang, P. Knight, and A. J. B. Vincent. Microstructural development in equiatomic multicomponent alloys. *Materials Science Engineering A*, 375-377:213–218, 2004.

[9] H. D. Carlton, A. Haboub, G. F. Gallegos, D. Y. Parkinson, and A. A. Mac-Dowell. Damage evolution and failure mechanisms in additively manufactured stainless steel. *Materials Science and Engineering A*, 651:406–414, 1 2016.

[10] S. Chen, G. Guillemot, and C.-A. Gandin. Three-dimensional cellular automaton-finite element modeling of solidification grain structures for arc-welding processes. *Acta Materialia*, 115:448–467, 8 2016.

[11] J. A. Cherry, H. M. Davies, S. Mehmood, N. P. Lavery, S. G. R. Brown, and J. Sienz. Investigation into the effect of process parameters on microstructural and physical properties of 316L stainless steel parts by selective laser melting. *The International Journal of Advanced Manufacturing Technology*, 76(5):869–879, 2015.

[12] H.-P. Chou, Y.-S. Chang, S.-K. Chen, and J.-W. Yeh. Microstructure, thermo-physical and electrical properties in AlxCoCrFeNi (0 x 2) high-entropy alloys. *Materials Science and Engineering: B*, 163(3):184–189, 7 2009.

[13] Q. Chu, M. Wu, C. Chang, L. Sheng, M. Liu, and X. Yan. Study of the microstructure and wear properties of Ti-12Mo-6Zr-2Fe alloy fabricated via selective laser melting. *Materials Letters*, 342, 7 2023.

[14] T. DebRoy, H. L. Wei, J. S. Zuback, T. Mukherjee, J. W. Elmer, J. O. Milewski, A. M. Beese, A. Wilson-Heid, A. De, and W. Zhang. Additive manufacturing of metallic components – Process, structure and properties. *Progress in Materials Science*, 92:112–224, 2018.

[15] G. Dirras, L. Lilensten, P. Djemia, M. Laurent-Brocq, D. Tingaud, J.-P. Couzinié, L. Perrière, T. Chauveau, and I. Guillot. Elastic and plastic properties of as-cast equimolar TiHfZrTaNb high-entropy alloy. *Materials Science and Engineering: A*, 654:30–38, 2016.

[16] A. Fedorenko, B. Fedulov, Y. Kuzminova, S. Evlashin, O. Staroverov, M. Tretyakov, E. Lomakin, and I. Akhatov. Anisotropy of mechanical properties and residual stress in additively manufactured 316l specimens. *Materials*, 14(23), 12 2021.

[17] T. Fujieda, M. Chen, H. Shiratori, K. Kuwabara, K. Yamanaka, Y. Koizumi, A. Chiba, and S. Watanabe. Mechanical and corrosion properties of CoCrFeNiTi-based high-entropy alloy additive manufactured using selective laser melting. *Additive Manufacturing*, 25:412–420, 1 2019.

[18] A. Gali and E. P. George. Tensile properties of high- and medium-entropy alloys. *Intermetallics*, 39:74–78, 2013.

[19] S. M. Gaytan, L. E. Murr, F. Medina, E. Martinez, M. I. Lopez, and R. B. Wicker. Advanced metal powder based manufacturing of complex components by electron beam melting. *Materials Technology*, 24(3):180–190, 2009.

[20] E. P. George, W. A. Curtin, and C. C. Tasan. High entropy alloys : A focused review of mechanical properties and deformation mechanisms . *Acta Materialia*, 188:435–474, 2020.

[21] E. P. George, D. Raabe, and R. O. Ritchie. High-entropy alloys. *Nature Reviews Materials*, 4(8):515–534, 2019.

[22] B. Gludovatz, A. Hohenwarter, K. V. Thurston, H. Bei, Z. Wu, E. P. George, and R. O. Ritchie. Exceptional damage-tolerance of a medium-entropy alloy CrCoNi at cryogenic temperatures. *Nature Communications*, 7, 2 2016.

[23] S. Gorsse and O. N. Senkov. About the reliability of CALPHAD predictions in multicomponent systems. *Entropy*, 20(12), 12 2018.

[24] C. Han, Q. Fang, Y. Shi, S. Tor, C. K. Chua, and K. Zhou. Recent Advances on High-Entropy Alloys for 3D Printing. 1903855:1–41, 2020.

[25] Y. He, H. Zhang, H. Su, P. Shen, Y. Hou, and D. Zhou. In Situ Alloying of Fe-Cr-Co Permanent Magnet by Selective Laser Melting of Elemental Iron, Chromium and Cobalt Mixed Powders. *Metals*, 12(10), 10 2022.

[26] M. A. Hemphill, T. Yuan, G. Y. Wang, J. W. Yeh, C. W. Tsai, A. Chuang, and P. K. Liaw. Fatigue behavior of Al 0 . 5 CoCrCuFeNi high entropy alloys. *Acta Materialia*, 60(16):5723–5734, 2012.

[27] D. Herzog, V. Seyda, E. Wycisk, and C. Emmelmann. Additive manufacturing of metals. *Acta Materialia*, 117:371–392, 9 2016.

[28] O. Hunziker, D. Dye, and R. C. Reed. On the formation of a centreline grain boundary during fusion welding. *Acta Materialia*, 48(17):4191–4201, 2000.

[29] J. Joseph, T. Jarvis, X. Wu, N. Stanford, P. Hodgson, and D. M. Fabijanic. Comparative study of the microstructures and mechanical properties of direct laser fabricated and arc-melted AlxCoCrFeNi high entropy alloys. *Materials Science and Engineering A*, 633:184–193, 2015.

[30] Y.-F. Kao, S.-K. Chen, T.-J. Chen, P.-C. Chu, J.-W. Yeh, and S.-J. Lin. Electrical, magnetic, and Hall properties of AlxCoCrFeNi high-entropy alloys. *Journal of Alloys and Compounds*, 509(5):1607–1614, 2 2011.

[31] Karen Taminger. Electron beam additive manufacturing: state-of-the-technology, challenges & opportunities. Technical report, NASA Langley Research Center, Direct digital manufacturing workshop. Solomons (MD), 2010.

[32] J. Karimi, L. Kollo, R. Rahmani, P. Ma, Y. D. Jia, and K. G. Prashanth. Selective laser melting of in-situ CoCrFeMnNi high entropy alloy: Effect of remelting. *Journal of Manufacturing Processes*, 84:55–63, 12 2022.

[33] A. Katz-Demyanetz, A. Koptyug, and V. V. Popov. In-situ Alloying as a Novel Methodology in Additive Manufacturing. In *Proceedings of the 2020 IEEE 10th International Conference on "Nanomaterials: Applications and Properties", NAP 2020*. Institute of Electrical and Electronics Engineers Inc., 11 2020.

[34] W. E. King, H. D. Barth, V. M. Castillo, G. F. Gallegos, J. W. Gibbs, D. E. Hahn, C. Kamath, and A. M. Rubenchik. Observation of keyhole-mode laser melting in laser powder-bed fusion additive manufacturing. *Journal of Materials Processing Technology*, 214(12):2915–2925, 2014.

[35] H. Knoll, S. Ocylok, A. Weisheit, H. Springer, E. Jägle, and D. Raabe. Combinatorial Alloy Design by Laser Additive Manufacturing. *Steel Research International*, 88(8), 8 2017.

[36] R. Korsmik, I. Tsybulskiy, A. Rodionov, O. Klimova-Korsmik, M. Gogolukhina, S. Ivanov, G. Zadykyan, and R. Mendagaliev. The approaches to design and manufacturing of large-sized marine machinery parts by direct laser deposition. *Procedia CIRP*, 94:298–303, 2020.

[37] Kou S. *Welding metallurgy.* NJ: John Wiley & Sons, 2nd ed. hoboken edition, 2003.

[38] I. Kunce, M. Polanski, and J. Bystrzycki. Microstructure and hydrogen storage properties of a TiZrNbMoV high entropy alloy synthesized using Laser Engineered Net Shaping (LENS). *International Journal of Hydrogen Energy*, 39(18):9904–9910, 2014.

[39] Y. O. Kuzminova, D. G. Firsov, S. D. Konev, A. A. Dudin, S. A. Dagesyan, I. S. Akhatov, and S. A. Evlashin. Structure control of 316L stainless steel through an additive manufacturing. 9:551–555, 2019.

[40] G. Laplanche, A. Kostka, O. M. Horst, G. Eggeler, and E. P. George. Microstructure evolution and critical stress for twinning in the CrMnFeCoNi high-entropy alloy. *Acta Materialia*, 118:152–163, 10 2016.

[41] S. Leuders, T. Lieneke, S. Lammers, T. Tröster, and T. Niendorf. On the fatigue properties of metals manufactured by selective laser melting - The role of ductility. *Journal of Materials Research*, 29(17):1911–1919, 6 2014.

[42] M. Li, J. Gazquez, A. Borisevich, R. Mishra, and K. M. Flores. Intermetallics Evaluation of microstructure and mechanical property variations in Al x CoCrFeNi high entropy alloys produced by a high-throughput laser deposition method. 95(January):110–118, 2018.

[43] S. Liu and Y. C. Shin. Additive manufacturing of Ti6Al4V alloy: A review. *Materials & Design*, 164:107552, 2 2019.

[44] S. G. Ma, S. F. Zhang, J. W. Qiao, Z. H. Wang, M. C. Gao, Z. M. Jiao, H. J. Yang, and Y. Zhang. Superior high tensile elongation of a single-crystal CoCrFeNiAl 0.3 high-entropy alloy by Bridgman solidification. *Intermetallics*, 54:104–109, 2014.

[45] A. A. Martin, N. P. Calta, S. A. Khairallah, J. Wang, P. J. Depond, A. Y. Fong, V. Thampy, G. M. Guss, A. M. Kiss, K. H. Stone, C. J. Tassone, J. Nelson Weker, M. F. Toney, T. van Buuren, and M. J. Matthews. Dynamics of pore formation during laser powder bed fusion additive manufacturing. *Nature Communications*, 10(1):1–10, 2019.

[46] D. B. Miracle, J. D. Miller, O. N. Senkov, C. Woodward, M. D. Uchic, and J. Tiley. Exploration and development of high entropy alloys for structural applications. *Entropy*, 16(1):494–525, 2014.

[47] D. B. Miracle and O. N. Senkov. A critical review of high entropy alloys and related concepts. *Acta Materialia*, 122:448–511, 2017.

[48] M. Moorehead, K. Bertsch, M. Niezgoda, C. Parkin, M. Elbakhshwan, K. Sridharan, C. Zhang, D. Thoma, and A. Couet. High-throughput synthesis of Mo-Nb-Ta-W high-entropy alloys via additive manufacturing. *Materials and Design*, 187, 2 2020.

[49] T. Mukherjee, J. S. Zuback, A. De, and T. DebRoy. Printability of alloys for additive manufacturing. *Scientific Reports*, 6, 1 2016.

[50] A. A. Nepapushev, D. O. Moskovskikh, and K. V. Vorotilo. TiAl-Based Materials by In Situ Selective Laser Melting of Ti / Al Reactive Composites. *Metals*, pages 1–8, 2020.

[51] F. Otto, A. Dlouhý, K. G. Pradeep, M. Kuběnová, D. Raabe, G. Eggeler, and E. P. George. Decomposition of the single-phase high-entropy alloy CrMnFe-CoNi after prolonged anneals at intermediate temperatures. *Acta Materialia*, 112:40–52, 2016.

[52] D. Panov, O. Oreshkin, B. Voloskov, V. Petrovskiy, and I. Shishkovsky. Pore healing effect of laser polishing and its influence on fatigue properties of 316L stainless steel parts fabricated by laser powder bed fusion. *Optics & Laser Technology*, 156:108535, 2022.

[53] Z. Pei, J. Yin, P. K. Liaw, and D. Raabe. Toward the design of ultrahigh-entropy alloys via mining six million texts. *Nature Communications*, 14(1), 12 2023.

[54] D. Raabe, C. C. Tasan, H. Springer, and M. Bausch. From high-entropy alloys to high-entropy steels. *Steel Research International*, 86(10):1127–1138, 10 2015.

[55] A. Riemer, S. Leuders, M. Thöne, H. A. Richard, T. Tröster, and T. Niendorf. On the fatigue crack growth behavior in 316L stainless steel manufactured by selective laser melting. *Engineering Fracture Mechanics*, 120:15–25, 2014.

[56] M. Rittiruam, J. Noppakhun, S. Setasuban, N. Aumnongpho, A. Sriwattana, S. Boonchuay, T. Saelee, C. Wangphon, A. Ektarawong, P. Chammingkwan, T. Taniike, S. Praserthdam, and P. Praserthdam. High-throughput materials screening algorithm based on first-principles density functional theory and artificial neural network for high-entropy alloys. *Scientific Reports*, 12(1), 12 2022.

[57] G. A. Salishchev, M. A. Tikhonovsky, D. G. Shaysultanov, N. D. Stepanov, A. V. Kuznetsov, I. V. Kolodiy, A. S. Tortika, and O. N. Senkov. Effect of Mn and v on structure and mechanical properties of high-entropy alloys based on CoCrFeNi system. *Journal of Alloys and Compounds*, 591:11–24, 2014.

[58] B. Schuh, F. Mendez-Martin, B. Völker, E. George, H. Clemens, R. Pippan, and A. Hohenwarter. Mechanical properties, microstructure and thermal stability of a nanocrystalline CoCrFeMnNi high-entropy alloy after severe plastic deformation. *Acta Materialia*, 96:258–268, 9 2015.

[59] S. L. Semiatin, V. G. Ivanchenko, and O. M. Ivasishin. Diffusion models for evaporation losses during electron-beam melting of alpha/beta-titanium alloys. *Metallurgical and Materials Transactions B*, 35(2):235–245, 2004.

[60] O. N. Senkov and S. L. Semiatin. Microstructure and properties of a refractory high-entropy alloy after cold working. *Journal of Alloys and Compounds*, 649:1110–1123, 2015.

[61] M. Shamsujjoha, S. R. Agnew, J. M. Fitz-Gerald, W. R. Moore, and T. A. Newman. High Strength and Ductility of Additively Manufactured 316L Stainless Steel Explained. *Metallurgical and Materials Transactions A: Physical Metallurgy and Materials Science*, 49(7):3011–3027, 2018.

[62] A. Simchi. Direct laser sintering of metal powders: Mechanism, kinetics and microstructural features. *Materials Science and Engineering: A*, 428(1-2):148–158, 7 2006.

[63] S. Singh, N. K. Katiyar, S. Goel, and S. N. Joshi. Phase prediction and experimental realisation of a new high entropy alloy using machine learning. *Scientific reports*, 13(1):4811, 12 2023.

[64] C. E. Slone, E. P. George, and M. J. Mills. Elevated temperature microstructure evolution of a medium-entropy CrCoNi superalloy containing Al , Ti. *Journal of Alloys and Compounds*, 817:152777, 2020.

[65] T. M. Smith, C. A. Kantzos, N. A. Zarkevich, B. J. Harder, M. Heczko, P. R. Gradl, A. C. Thompson, M. J. Mills, T. P. Gabb, and J. W. Lawson. A 3D printable alloy designed for extreme environments. *Nature*, 4 2023.

[66] H. Springer and D. Raabe. Rapid alloy prototyping: Compositional and thermo-mechanical high throughput bulk combinatorial design of structural materials based on the example of 30Mn–1.2C–xAl triplex steels. *Acta Materialia*, 60(12):4950–4959, 2012.

[67] K. Sun, W. Peng, L. Yang, and L. Fang. Effect of SLM Processing Parameters on Microstructures and Mechanical Properties of Al0.5CoCrFeNi High Entropy Alloys. *Metals*, 10(2), 2020.

[68] Z. Sun, X. Tan, C. Wang, M. Descoins, D. Mangelinck, S. B. Tor, E. A. Jägle, S. Zaefferer, and D. Raabe. Reducing hot tearing by grain boundary segregation engineering in additive manufacturing: example of an AlxCoCrFeNi high-entropy alloy. *Acta Materialia*, 204:116505, 2021.

[69] T. DebRoy and S. A. David. Physical processes in fusion welding. *Rev. Mod. Phys.*, 67:85–112, 1995.

[70] Z. Tang, T. Yuan, C. W. Tsai, J. W. Yeh, C. D. Lundin, and P. K. Liaw. Fatigue behavior of a wrought Al<inf>0.5</inf>CoCrCuFeNi two-phase high-entropy alloy. *Acta Materialia*, 99:247–258, 2015.

[71] T. Voisin, J.-b. Forien, A. Perron, S. Aubry, N. Bertin, A. Samanta, A. Baker, and Y. M. Wang. New insights on cellular structures strengthening mechanisms and thermal stability of an austenitic stainless steel fabricated by laser powder-bed-fusion. 203, 2021.

[72] B. Voloskov, T. Mishurova, S. Evlashin, I. Akhatov, G. Bruno, and I. Serge-ichev. Artificial Defects in 316L Stainless Steel Produced by Laser Powder Bed Fusion: Printability, Microstructure, and Effects on the Very-High-Cycle Fatigue Behavior. *Advanced Engineering Materials*, 25(1), 1 2023.

[73] C. Wang, X. P. Tan, Z. Du, S. Chandra, Z. Sun, C. W. Lim, S. B. Tor, C. S. Lim, and C. H. Wong. Additive manufacturing of NiTi shape memory alloys using pre-mixed powders. *Journal of Materials Processing Technology*, 271:152–161, 9 2019.

[74] W.-r. Wang, W.-l. Wang, and J.-w. Yeh. Phases , microstructure and mechanical properties of Al x CoCrFeNi high-entropy alloys at elevated temperatures. *Journal of Alloys and Compounds*, 589:143–152, 2014.

[75] Y. M. Wang, T. Voisin, J. T. Mckeown, J. Ye, N. P. Calta, Z. Li, Z. Zeng, Y. Zhang, W. Chen, T. T. Roehling, R. T. Ott, M. K. Santala, P. J. Depond, M. J. Matthews, A. V. Hamza, and T. Zhu. steels with high strength and ductility. 17(January), 2018.

[76] Z. Wu, H. Bei, G. M. Pharr, and E. P. George. Temperature dependence of the mechanical properties of equiatomic solid solution alloys with face-centered cubic crystal structures. *Acta Materialia*, 81:428–441, 2014.

[77] A. Yadollahi, M. J. Mahtabi, A. Khalili, H. R. Doude, and J. C. Newman. Fatigue life prediction of additively manufactured material: Effects of surface roughness, defect size, and shape. *Fatigue and Fracture of Engineering Materials and Structures*, 41(7):1602–1614, 2018.

[78] A. Yadollahi and N. Shamsaei. Additive manufacturing of fatigue resistant materials: Challenges and opportunities. *International Journal of Fatigue*, 98:14–31, 5 2017.

[79] A. Yadollahi, N. Shamsaei, S. M. Thompson, A. Elwany, and L. Bian. Effects of building orientation and heat treatment on fatigue behavior of selective laser melted 17-4 PH stainless steel. *INTERNATIONAL JOURNAL OF FATIGUE*, pages 1–18, 2016.

[80] J. W. Yeh, S. K. Chen, S. J. Lin, J. Y. Gan, T. S. Chin, T. T. Shun, C. H. Tsau, and S. Y. Chang. Nanostructured high-entropy alloys with multiple principal elements: Novel alloy design concepts and outcomes. *Advanced Engineering Materials*, 6(5):299–303, 2004.

[81] Y. Yu, J. Wang, J. Li, H. Kou, and W. Liu. Characterization of BCC phases in AlCoCrFeNiTix high entropy alloys. *Materials Letters*, 138:78–80, 1 2015.

[82] N. Yurchenko, E. Panina, M. Tikhonovsky, G. Salishchev, S. Zherebtsov, and N. Stepanov. Structure and mechanical properties of an in situ refractory Al20Cr10Nb15Ti20V25Zr10 high entropy alloy composite. *Materials Letters*, 264, 4 2020.

[83] N. Yurchenko, N. D. Stepanov, D. G. Shaysultanov, M. A. Tikhonovsky, and G. A. Salishchev. Effect of Al content on structure and mechanical properties of the AlxCrNbTiVZr (x=0; 0.25; 0.5; 1) high-entropy alloys. *Materials Characterization*, 121:125–134, 2016.

[84] J.-C. Zhao. Combinatorial approaches as effective tools in the study of phase diagrams and composition–structure–property relationships. *Progress in Materials Science*, 51(5):557–631, 2006.

[85] P. F. Zhou, D. H. Xiao, Z. Wu, and X. Q. Ou. Al0.5FeCoCrNi high entropy alloy prepared by selective laser melting with gas-atomized pre-alloy powders. *Materials Science and Engineering A*, 739:86–89, 1 2019.